THESIS

TIMING AND GENESIS OF FRACTURES IN THE NIOBRARA FORMATION, NORTHEASTERN FRONT RANGE AND DENVER BASIN, COLORADO

Submitted by

Cody Lee Allen

Department of Geosciences

In partial fulfillment of the requirements

For the Degree of Master of Science

Colorado State University

Fort Collins, Colorado

Summer 2010

COLORADO STATE UNIVERSITY

April 30th, 2010

WE HEREBY RECOMMEND THAT THE THESIS PREPARED UNDER OUR SUPERVISION BY CODY L. ALLEN ENTITLED TIMING AND GENESIS OF FRACTURES IN THE NIOBRARA FORMATION, NORTHEASTERN FRONT RANGE AND DENVER BASIN, COLORADO BE ACCEPTED AS FULFILLING IN PART REQUIREMENTS FOR THE DEGREE OF MASTER OF SCIENCE.

Committee on Graduate Work

____

Wayne Charlie

____

Sven Egenhoff

____

Bryan Richter

____

Advisor: Eric Erslev

____

Department Head: Sally Sutton

ABSTRACT OF THESIS

TIMING AND GENESIS OF FRACTURES IN THE NIOBRARA FORMATION, NORTHEASTERN FRONT RANGE AND DENVER BASIN, COLORADO

Naturally-occurring fractures in foreland basins, particularly in self-sourced resource plays, are critical to the production of hydrocarbons from low permeability reservoirs. Both shear and extensional fractures commonly cause reservoir anisotropy as well as providing critical tests of tectonic hypotheses. The objective of this research is to determine the mechanisms and timing of naturally-occurring fractures in the upper Cretaceous Niobrara Formation along the northeastern Front Range and in the Denver Basin of the Rocky Mountain Foreland.

Previous hypotheses for the origin of fractures within the Denver Basin have focused largely on mechanisms invoking basement reactivation either by vertical block motion or by Laramide subhorizontal shortening. Contrasting hypotheses include multidirectional slip, regional and/or local detachment, and post-Laramide extension in the direction of previous compression. This study analyzes the kinematics, modes and mechanisms of deformation in the Niobrara Formation from fractures examined along the northeastern Front Range and from faults identified in 3D seismic data from the Denver Basin. Surface fracture data collected from 61 locations include minor faults, joints, calcite-filled fractures, and pressure solution stylolites. Subsurface data includes two 3D seismic surveys (Sooner Field and Dana Point) were fault geometries were examined.

In outcrops, ideal σ_1 analysis of strike–slip and thrust fault data document a subhorizontal Laramide compression with an average attitude of 086°-08°. Normal faults identified through the study are highly variable with an average slip direction of 183°-73°. Normal dip-slip reactivation of right-lateral shear planes indicates normal faults are younger. Two joint systems are observed throughout the study area with J_1 joints averaging 078° and later J_2 joints averaging 171°. Subsurface 3D seismic data show listric and planar normal fault sets cut the Niobrara and lower Pierre formations. Calculated fault dip angles at Sooner Field average 8°, and those at Dana Point average 27°. These low fault dip angles suggest layer-parallel detachment, but diverse fault strikes are problematic and suggest multiple slip directions. No basement-to-Cretaceous faults were identified in either volume, casting doubt on basement reactivation hypotheses.

Fracture sets in the Niobrara Formation show evidence for four different fracture mechanisms. Initial faulting generated by Laramide subhorizontal compression (086°) was followed by later, but still Laramide, ENE- to E-W-striking J_1 splitting joints. Post-Laramide extension is indicated by NNW to N-S-striking J_2 joints. Lastly, low-angle listric and planar normal faults in seismic data are interpreted to be post-Laramide. They were probably caused by local detachment, but their mechanisms and timing require further investigation.

Cody Lee Allen
Department of Geosciences
Colorado State University
Fort Collins, CO 80523
Summer 2010

ACKNOWLEDGMENTS

This project was supported by a research assistantship through Noble Energy Inc., and the Duncan A. McNaughton memorial grant from the American Association of Petroleum Geologists. Echo Geophysical Inc. graciously donated access to the Dana Point 3D seismic survey.

I would like to express my sincere gratitude and thanks to my advisor, Dr. Eric Erslev, for his patience and guidance throughout my graduate studies at Colorado State University. Eric, your expertise and scientific enthusiasm greatly enhanced my ability to test complex geologic hypotheses, and fostered a renewed appreciation for field research, and the Colorado outdoors. I would also like to thank Dr. Sven Egenhoff and Dr. Wayne Charlie for being on my graduate committee, as well as fellow students and staff at Colorado State University for their instruction, and friendship. Special thanks go to Dr. Bryan Richter of Noble Energy Inc. who was also on my committee, for being a great mentor, friend, and sounding board for new ideas and hypotheses.

Field data presented in this thesis could not have been collected without the permission of many public and private landowners. I would like to thank Holcim Inc, Cemex Inc., and the many private land owners who allowed access to outcrop along the northeastern Front Range.

Last but not least, I would like to express my sincere gratitude and appreciation to my mother Jacqi and father Terry for their support and encouragement. To my wife Charity, thank you for your emotional and financial support, understanding, patience, and bright smile after long field days. I couldn't have done it without you.

TABLE OF CONTENTS

Page

Title Page …………………………………………………………………………. i
Signature Page………………………………………………………………………..ii
Abstract of Thesis………………………………………………………………….iii
Acknowledgements………………………………………………………………….. v
Table of Contents……………………………………………………………………vi

1. INTRODUCTION…………………………………………………………….….... 1

2. STRATIGRAPHIC SUMMARY……………………………………………………….8
Precambrian…………………………………………………………………8
Paleozoic……………………………………………………………………10
Mesozoic……………………………………………………………………12
Cenozoic……………………………………………………………………18

3. PREVIOUS WORK……………………………………………………………….20
Laramide Tectonic and kinematic Models…………………………………20
Post-Laramide Tectonic and Kinematic Models…………………………...26
Previous Structural Interpretations of the Northeastern Front Range……...28
Subsurface Denver Basin Fracture Studies………………………………...32

4. METHODS OF DATA COLLECTION, SURFACE FRACTURE OBSERVATIONS AND ANALYSIS…………………………………………….....40
Fault and Shear Sense Data Collection Methods…………………………...41
Fracture and Bedding Data Collection Methods……………………………42
Methods of Analysis of Minor Fault Data………………………………....42
Methods of Analysis of Joint, Calcite Fracture, Stylolite, and Pencil Cleavage Data…………………………………………………………………………44
Geologic Observations…………………………………….......................44
Livermore Quadrangle…………………………………………...53
Laporte Quadrangle……………………..56
Horsetooth Reservoir Quadrangle…………………………………..63
Masonville Quadrangle……………………………………………..67
Carter Lake Reservoir Quadrangle…………………………………73
Hygiene Quadrangle………………………………………………...76
Boulder Quadrangle……………………………………………....81
Observations Summary……………………………………………...88

5. DETAILED FRACTURE ANALYSIS……………………………………...90
Minor Fault Slickenlines and Ideal σ_1 Axes…………………………………..90
Stylolite Data Analysis……………………………………………………...98
Joint Data and Analysis……………………………………………………..99
Calcite filled Fracture Analysis……………………………………………..104
Conclusions from Fracture Analysis………………………………………..105

TABLE OF CONTENTS (CONT.)

Page

6. 3D SEISMIC FAULT ANALYSIS……………………………………………….….107

Previous Subsurface studies and hypotheses………………………………..107

Methods of 3D Seismic Fault Analysis…………………………………..111

Sooner Field 3D Seismic Observations and Fault Analysis………………...113

Dana Point 3D Seismic Observations and Fault Analysis…………………..120

Conclusions……………………………………………………………….128

7. CONCLUSIONS…………………………………………………………...132

Questions for Future Research……………………………………………137

References Cited……………………………………………………………139

Appendices…………………………………………………………………153

Appendix One: Shear Fracture Data Tables..154

Appendix Two: Extensional Fracture Data Tables…………………………....159

Appendix Three: Calcite-Filled Fracture Data Tables……………………..…...165

Appendix Four: Stylolite Data Table……………………………………........169

Appendix Five: Pencil-Cleavage Data Table…………………………………...170

Appendix Six: Borehole Breakout Data Table …………………………..…....171

Appendix Seven: Formation Micro-Image Log Fracture Data Tables………....172

Appendix Eight: Sooner Field 3D Seismic Fault Data Tables……… ……..…...175

Appendix Nine: Dana Point 3D Seismic Fault Data Tables………………...……186

Chapter 1

Introduction

Foreland basins develop on continental crust along the length of collisional plate margins or along compressional destructive margins (Beaumont, 1981; Blackstone, 1986; Jordan, 1981; 1995; DeCelles and Giles, 1996; Leeder, 1999). They are the most studied type of sedimentary basin because they lie adjacent to Earth's major mountain chains and contain geological data with which orogenic belts can be reconstructed. Retro-arc foreland basins such as the active basins east of the Andes and the eastern forelands of the Rocky Mountains lie on continental crust of the overriding plate at destructive margins on the continental side of orogenic belts away from the subducting plate (Leeder, 1999; Allen and Allen, 1990, Ramos et al., 2002; Prezzi et al. 2009).

The problems addressed by this study are the mechanisms and timing of naturally-occurring fractures in foreland basins, particularly in self-sourced resource plays where fractures are critical to the production of hydrocarbons from low permeability reservoirs. The primary objective of this research is to constrain mechanisms responsible for extensional fractures and shear fractures occurring within upper Cretaceous sediments of the foreland Denver Basin through the determination of strain and stress axes across the study area. This study focuses on the asymmetrical foreland Denver Basin east of the

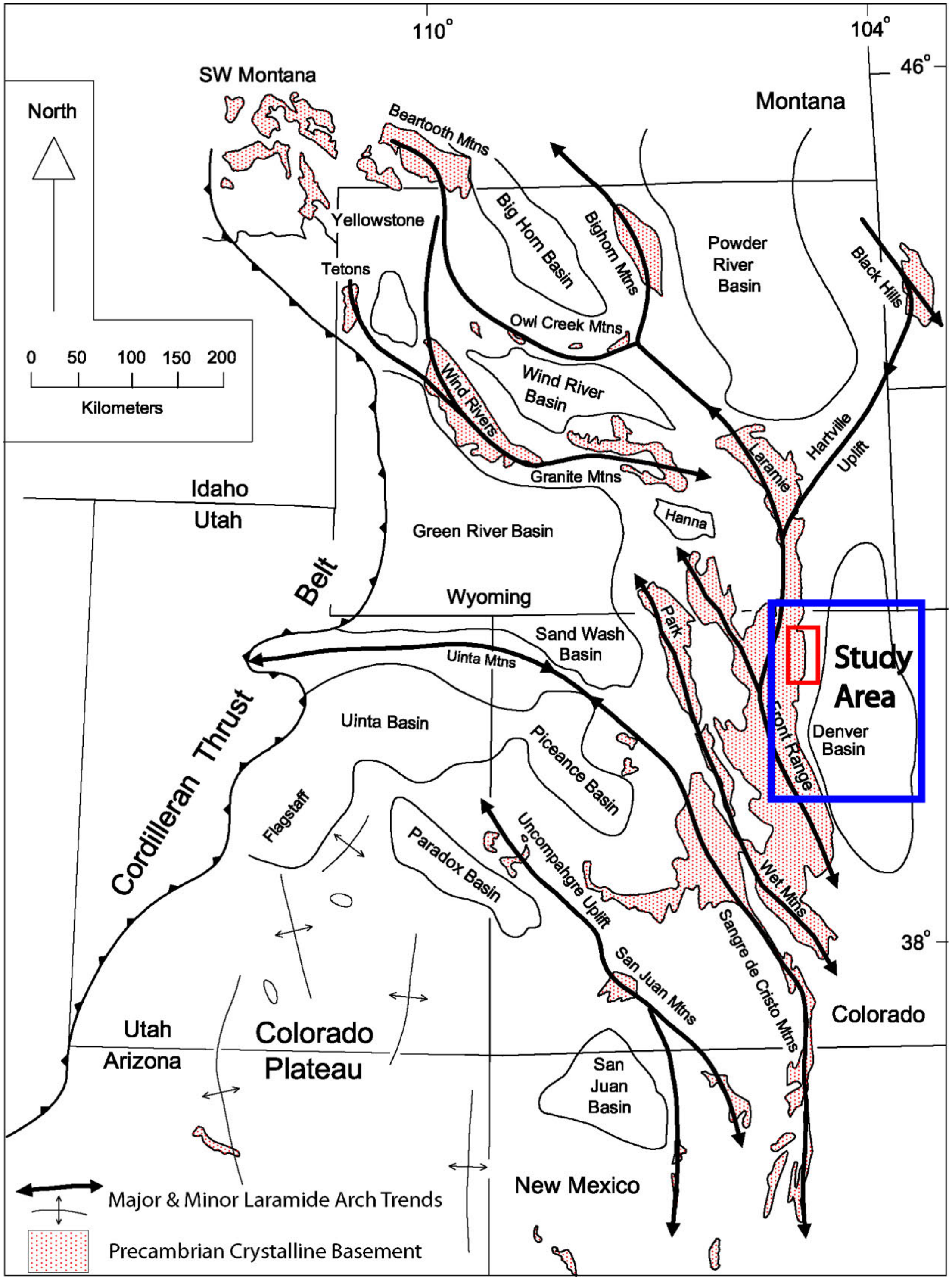

Figure 1.1. Map of the Rocky Mountains showing Precambrian basement rocks in relation to Laramide basins and trends of major and minor Laramide arches (Erslev and Koenig, 2009). The red and blue boxes approximate surface and subsurface study areas respectively.

Rocky Mountains in Colorado and Wyoming and the upper Cretaceous Niobrara Formation (Fig 1.1). The Denver Basin contains prolific hydrocarbon reserves, including 4 TCF of natural gas in the Wattenberg Field (Weimer et al., 1998). The upper Cretaceous Niobrara Formation, which contains intervals of fine-grained, organic-carbon-rich strata (up to 9 % TOC), has produced economic quantities of natural gas from facies of negligible porosity and permeability (Gustason and Deacon, 2008). Mechanisms responsible for fractures in the Denver Basin and the Niobrara Formation have generated intense debate because of their variable orientations and complex tectonic histories.

Industry 3D seismic surveys from the Denver Basin show that the Niobrara Formation is faulted at depth and may compartmentalize reservoirs. Interpretations for fault origins include Cretaceous wrench faulting reactivating Precambrian faults (Haberman, 1983; Davis, 1985; Pritchett, 1993; Weimer et al., 1998) and normal faults that sole into underlying thrust faults or detachment surfaces (Oldman, 1996; Kittleson, 1988; 2004). These studies focused primarily on subsurface fracture mechanisms within the Denver Basin without examining fractures expressed at the surface, where one can directly observe kinematic indicators such as minor faults associated with their development. Surface fracture analysis of the Niobrara Formation has extended Rocky Mountain surface fracture studies (Erslev et al., 2004; Erslev and Larson, 2006; Erslev, 2005; Erslev and Koenig, 2009) and linked them to the subsurface.

The following questions address the major structural problems regarding our understanding of natural fracture mechanisms in foreland basins and their association with hydrocarbon reservoirs.

- What are the kinematics of foreland orogens during basin development? Hypotheses include: a) unidirectional, subhorizontal shortening on basement involved thrust faults; and b) multidirectional slip.
- How do foreland basins document upper crustal strain? Hypotheses include; a) homogeneously across basins, overprinting earlier orogenic events; b) heterogeneously across basins, reactivating pre-existing structures; and c) strain partitioning; d) local variation.
- What is the timing of fracturing relative to one another and the orogeny? Timing relative to the orogeny include: a) pre-orogenic; b) syn-orogenic and; c) post orogenic.
- What kinds of brittle deformation mechanisms occur in foreland basin centered hydrocarbon reservoirs? Hypotheses include: a) shear fracturing; b) extensional fracturing; c) frictional sliding; and d) pressure solution.
- What are the modes of deformation responsible for foreland basin fracturing? Hypotheses include: a) trishear fault propagation folding; b) strike-slip reactivation of pre-existing basement faults; c) fault-bend folding; d) folding of crystalline basement; e) bedding-parallel detachment from flexural slip; f) basement arch collapse; g) erosional unroofing and elastic rebound; h) backsliding and gravitational collapse of the foreland; i) crustal uplift associated with regional extension; and j) variable localized extension.
- How do natural fractures affect hydrocarbon production? Are there preferred fracture orientations for hydrocarbon migration? Hypotheses

include a) fractures are natural conduits to fluids; b) fractures are natural seals to fluids; c) certain orientations are preferred for fluid migration; d) certain fracture orientations are mineralized.

This investigation analyzes the kinematics and the modes and mechanisms of deformation in the Niobrara Formation exposed along the northeastern Front Range, and fault geometries observed in upper Cretaceous strata from subsurface datasets in the Denver Basin (Figs. 1.1, 1.2). In order to test the aforementioned hypotheses, the following objectives were pursued:

- Constrain mechanisms responsible for extensional fractures and shear fractures occurring within upper Cretaceous sediments of the foreland Denver Basin through the determination of strain and stress axes across the study area.
- Determine relative timing of surface extensional and shear fractures based on observations of cross-cutting and abutting relationships.
- Identify orientations of healed fractures and determine whether preferred mineralization trends are present.
- Compare calculated strain and stress axes to previous authors observations (Matthews and Work, 1978; Braddock et al., 1988; Erslev, 1993; Holdaway, 1998; Erslev et al., 2004; Erslev and Larson, 2006; Larson, 2009).
- Quantify subsurface fracturing in the Denver Basin from 3D seismic surveys and compare fault geometries to surface minor fault observations.

- Summarize and integrate fracture data into a geospatial database using ArcGIS, and identify local or regional patterns in the Niobrara Formation and the Denver Basin.

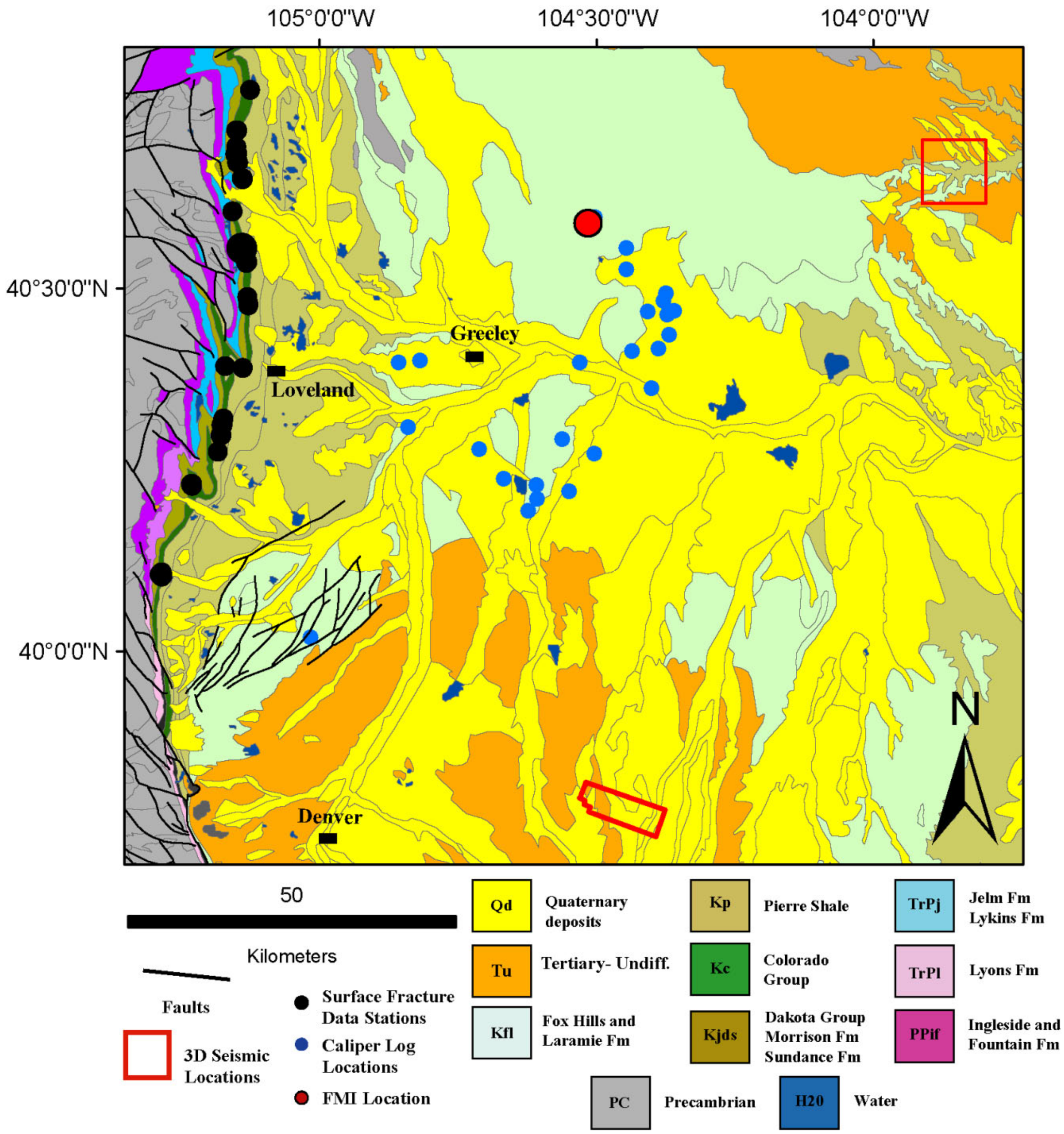

Figure 1.2. Bedrock geologic map of the study area with surface field locations, industry subsurface fracture investigations, and 3D seismic survey locations.

The 16,250 km^2 study area includes the eastern margin of the Front Range and Denver Basin in northern Colorado. Surface fracture data was collected over seven 7.5 minute geologic quadrangles along the northeastern Front Range (Wrucke and Wilson, 1967; Braddock et al., 1970; 1988b; 1988c; 1988d; 1989; Madole et al., 1998). Surface data collected consist of minor faults (shear fractures), extensional fractures (joints), calcite-filled fractures, stylolites, pencil cleavage, and bedding. Subsurface data used in this thesis include: public well data, proprietary borehole breakout data obtained from six arm caliper logs, proprietary Formation Micro-Image (FMI) logs, and 3D seismic surveys of the Niobrara Formation from the Denver Basin. Induced fracture orientations (Birmingham et al., 2001) aided in understanding current stress and strain axes in the basin.

This investigation is important to understanding the structural geology in the Front Range and fractures in subsurface hydrocarbon reservoirs. Self-sourced hydrocarbon resource plays like the Niobrara Formation can be economically significant if hydrocarbons are stored and migrate through open fracture networks (Oldman, 1996). Recent exploration success in the Denver Basin by EOG Resources Inc. has shown productions rates exceeding 1,500 barrels of oil per day from a stimulated, lateral well in the Niobrara Formation and makes predicting fracture orientations an important objective for petroleum companies. Determinations of open fractures orientations allow wells to be planned at optimum angles to fracture anisotropy, and prevent cross-well communications during infill drilling. Identifying fracture mechanisms allows prediction of fracture orientations, and may be useful in identifying fracture permeability and density.

Chapter 2

Stratigraphic Summary

Rocks exposed in the study area range in age from early Proterozoic to late Miocene (Peterman et al., 1968; DePaolo, 1981; Courtwright and Braddock, 1989; Sonnenberg and Bolyard, 1997) (Fig. 2.1). Paleozoic sediments identified in Devonian intrusives northwest of the study area provide evidence that lower Paleozoic strata once covered portions of the study area (McCallum and Mabarak, 1976; Smith, 1977).
Early Paleozoic strata were eroded prior to deposition of Pennsylvanian rocks and formed the subplanar Pennsylvanian nonconformity upon which upper Paleozoic and Mesozoic strata were deposited (Kluth, 1997). Stratigraphic thickness of upper Paleozoic and Mesozoic strata gradually change across the study area (Braddock et al. 1988c; 1988d; 1989a) other than areas where Laramide deformation has tectonically thinned or thickened strata.

Precambrian

The northern Colorado Front Range contains Proterozoic rocks belonging to the Yavapai tectonic province that accreted onto the Archean Wyoming province approximately 1700 Ma (Selverstone et al., 2000). Northwest of the study area in the Livermore Mountain quadrangle, excellent exposures of early Proterozoic metasedimentary and metavolcanic rocks are present. Assorted metasediments,

ERA	PERIOD	FORMATION	THICKNESS (ft)	MAP SYMBOL
CENOZOIC	Holocene Pleistocene	Alluvium, Colluvium, Landslide Deposits, & Terrace Gravels	0-??	Qal, Qc, Qls, Qtg
	Miocene	Ogallala / Arikaree	300-350	No, Na
	Oligocene	White River Group	0-240	PeW
MESOZOIC	Cretaceous	Fox Hills SS	450	Kfh
		Pierre Shale	>4435	Kp
		Niobrara Fort Hays Limestone	290-350 10-15	Kn, Knf
		Benton Group	495-570	Kcgm
		Dakota Group	245-320	Kd
	Jurassic	Morrison	300-330	Jm
		Sundance / Jelm	152-200	JTrsj
	Triassic	Lykins	700-800	TrPl
PALEOZOIC	Permian	Lyons	3-30	
		Owl Canyon	200-350	Plo
		Ingleside	200-240	Pi
	Penn.	Fountain	650-800	PPf
Middle to Early Proterozoic Crystalline Basement				XYu,Xg, PC

Figure 2.1 Generalized stratigraphic column of the northeastern Front Range from Braddock et al. (1988a, 1988b, 1988c, 1988d, Wrucke and Wilson (1967), and Madole et al. (1998).

leucocratic gneisses, metaplutonics and amphibolites are present (Braddock and Connor, 1988). Rb-Sr studies concluded that regional metamorphism occurred at 1.71 Ga (Peterman et al., 1968). A Sm-Nd model age of 1.8 Ga for the formation of continental crust in Colorado is consistent with Peterman's (1968) results (DePaolo, 1981; Braddock and Connor, 1988).

Three major periods of batholithic intrusion occurred in the Front Range, beginning with the Boulder Creek Granite at 1.7 Ga (Selverstone et al., 1997) and followed by widespread plutonism beginning with the 1.43 Ga Sherman Granite (Zielinski et al., 1981), and the 1.42 Ga Silver Plume Granite (Peterman et al., 1968). These middle Proterozoic granites underwent local mylonization along the NE- striking Moose Mountain, Skin Gulch, and Poudre River shear zones west of the study area (Selverstone, 2000). Igneous intrusive rocks including the Pikes Peak batholith represent the third period of intrusion at approximately 1.0 Ga (Tweto, 1979).

Paleozoic

Lower Paleozoic sediments are absent in outcrops along the Front Range and in the subsurface of northeast Colorado over the Transcontinental Arch (Sonnenberg and Bolyard, 1997). Remnants of Cambrian, Ordovician, Devonian and Mississippian rocks are present in the Southern Colorado Sag, and in the Central Colorado Trough (Kluth, 1997; Hoy and Ridgeway, 2002). Massive blocks of lower Paleozoic strata are present in the Devonian-Silurian kimberlite diatremes of the State-Line Diamond District (McCallum and Mabarak, 1976; Smith, 1977). Prior to the discovery of these diatremes, there was no evidence of lower Paleozoic strata being deposited in the northern part of the Colorado Front Range. Erosion of Frontrangia removed early Paleozoic strata and formed the subplanar Pennsylvanian nonconformity, upon which a thick sequence of Pennsylvanian and Permian red arkosic sandstones and conglomerates were deposited on the flanks of the ancestral Front Range uplift (Kluth, 1997).

The Fountain Formation was deposited during the Middle Pennsylvanian to early Permian and ranges in thickness from 224 to 354 m, thinning to the north of the study area (Wrucke and Wilson, 1957; Braddock et al., 1970, 1988, 1989; Madole et al. 1998). The Fountain Formation is a reddish-brown to purplish-gray arkosic conglomerate with medium- to coarse-grained feldspathic sandstones that are interbedded with siltstone, shale and minor amounts of limestone. The Fountain Formation is typically non-resistant to erosion and poorly exposed, but to the north it becomes more calcareous, forming prominent hogbacks. The Fountain Formation preserves minor faults in stream cuts and road cuts where sandstone and limestone beds dip >10º (Larson, 2009).

The lower Permian Ingleside Formation is a reddish-pink, fine-grained quartz sandstone, commonly well-cemented with quartz and/or calcite. Formation thickness ranges from 5 to 73 m across the study area (Wrucke and Wilson, 1957; Braddock et al., 1970; 1988; 1989; Madole et al. 1998). The variable lithologies of the Ingleside Formation were interpreted as the product of depositional environments fluctuating from near-shore beach to shallow marine environments (Rhoads, 1987). Previous fracture studies (Larson, 2009) identified cataclasite on minor fault surfaces and slickenlines on bedding planes in sandstones. Faults occurring in limestones are seldom preserved.

The lower Permian Owl Canyon Formation is a red, fine-grained, ripple-laminated sandstone which pinches out to the south in the Carter Lake geologic quadrangle and thickens to the north, ranging between 61-107 m (Braddock et al., 1970, 1988, 1989; Madole et al. 1998). This red siltstone and fine-grained sandstone is named the Satanka Formation in the Masonville geologic quadrangle (Braddock et al., 1970). The Owl Canyon Formation forms valleys between the resistant Ingleside and Lyons sandstones.

The lower Permian Lyons Sandstone is an orange to pinkish-gray, well-sorted, cross-stratified quartzose (Wrucke and Wilson, 1957; Braddock et al., 1970, 1988, 1989; Madole et al. 1998). Formation thickness ranges from 9 m to > 76 m across the study area. North of the study area, the Lyons Sandstone progressively thins to < 1 m in thickness near the Wyoming border. In the northeastern portion of the Denver Basin, Permian evaporate sequences of Leonardian and Guadalupian ages were identified and correlated into southeastern Wyoming, southwestern Nebraska and eastern Kansas (Oldham, 1996). Proposed Permian salt edges occurring in Silo Field, Wyoming have been debated as causing increased fracture densities in Cretaceous hydrocarbon reservoirs (Longman et al., 1998). Silica-cemented sandstone and siltstone beds preserve slickensided minor faults where dipping >10º. Two prominent gypsum beds have been described capping the upper Permian strata adjacent to the study area (Braddock et al., 1988).

Mesozoic

The Upper Permian to Lower Triassic Lykins Formation is dominated by red to reddish-brown siltstone and fine-grained sandstone containing several thin carbonate beds (Braddock et al., 1970, 1988, 1989; Madole et al., 1998). It ranges in thickness from 154 to 227 m through the study area (Wrucke and Wilson, 1957; Braddock et al., 1970, 1988, 1989; Madole et al., 1998). The Lykins Formation is poorly exposed and is located in valleys between the Lyons Formation and Dakota Group hogbacks.

The upper Triassic Jelm and upper to middle Jurassic Sundance formations are mapped together as one unit in the study area. The Jelm Formation unconformably overlies the Lykins Formation and is orange-pink or reddish-brown, fine-grained crossbedded calcareous sandstones (Wrucke and Wilson, 1957; Braddock et al., 1970, 1988, 1989; Madole et al., 1998). The Upper to Middle Jurassic Sundance Formation unconformably overlies the Jelm Formation and is a very light-gray to yellowish-gray, fine-grained, partially cross-laminated sandstone equivalent to the Canyon Springs Sandstone Member (Wrucke and Wilson, 1957). The Jelm and Sundance formations range in combined thickness from < 1 m adjacent to Boulder, CO, to nearly 60 m west of Laporte, CO (Wrucke and Wilson, 1957; Braddock et al., 1970, 1988, 1989; Madole et al. 1998). It is typically poorly exposed, and covered by vegetation and landslide debris from the overlying Lykins Formation.

The upper Jurassic Morrison Formation consists of green, red, yellow and white, weathered claystones and siltstone with interbedded gray micrite, and fine-grained sandstones (Braddock et al., 1970, 1988, 1989; Madole et al. 1998). In the southern study area, the Morrison Formation is further divided into upper and lower members, distinguished by gray, fine-grained, cross-stratified sandstone occurring in the lower member (Wrucke and Wilson, 1957). It is typically poorly exposed and masked by Dakota Group landslides. The abundant claystone allows the unit to change thickness dramatically within folds and act as a detachment surface for glide-block landslides of the lower Dakota Group (Braddock, 1978).

Cretaceous sediments are complex due to flooding of the foreland Denver Basin by discrete northern and southern epicontinental seaways during the Neocomian through late Albian periods (Gustason and Deacon, 2008). The basal Cretaceous sequence is composed of interbedded shales and sandstones of the Dakota Group, which are regionally variable in thickness from 45 to 120 meters (Weimer, et al., 1989; Weimer, et al. 1990; Graham, 2000). The Dakota Group crops out as a narrow belt of east dipping resistant sandstones from northern Douglas County, Colorado to the Wyoming state line (Mackenzie, 1971). The Dakota Group contains the Lytle and South Platte formations. The South Platte Formation is further divided into the Plainview, Skull Creek, Fort Collins, and Horsetooth members (Braddock et al. 1988). Weimer et al. (1972) hypothesized that during the early Cretaceous, clastic sediments sourced from thrust belts deposited alluvial, floodplain, and deltaic deposits on the western margin of the Western Interior Cretaceous Seaway.

The lower Cretaceous Dakota Group is a marine transgressive package where fluvial-deltaic deposits are overlain by sub-tidal deposits. These shallow marine/sub-tidal deposits grade into deeper marine shales that quickly regress back into low energy shoreline and shoreface sediments. These sediments are abruptly overlain by higher-energy, coarser sediments which cap the succession (Weimer et al., 1990). The Fort Collins and Horsetooth members collectively form the lower, eastern Dakota Hogback and contain slickensided minor faults (Holdaway, 1998; Erslev and Larson 2006).

The Benton Group and the Colorado Group consist of middle and upper Cretaceous sediments (Wrucke and Wilson, 1957; Tweto, 1979; Braddock et al., 1970, 1988, 1989; Madole et al. 1998). The middle Cretaceous Mowry Shale, upper

Cretaceous Graneros Shale, Greenhorn Limestone, Carlile Shale, and Codell Sandstone collectively are known as the Benton Group for this study. The Benton Group ranges in thickness from 125 to 174 m across the study area (Wrucke and Wilson, 1957; Braddock et al., 1970, 1988, 1989; Madole et al., 1998). Subsurface fracture data from micro-resistivity image well logs indicate the Graneros Shale is highly fractured (Richter, personal communication, 2009). Except for the Codell Sandstone which caps the Carlile Shale, the Benton Group is poorly exposed across the study area. The Codell Sandstone is a buff to light-gray, clay-rich sandstone that contains various fossil fragments and has a minimal amount of preserved slickensided minor fault surfaces.

The upper Cretaceous Niobrara Formation consists of two members, the Fort Hays Limestone and the Smokey Hill Shale, which range in combined thickness from 107 to 122 m across the study area (Wrucke and Wilson, 1957; Braddock et al., 1970, 1988, 1989; Madole et al. 1998). The Fort Hays Limestone is consistently 5 m of light-gray, thick-bedded micrite with abundant *Inoceramus* and *Psuedoperna congesta* fossil fragments (Braddock et al., 1970; 1988; 1989; Madole et al., 1998). It marks the base of the Niobrara Formation and forms a low-relief hogback. The Fort Hays Limestone contains a variety of kinematic indicators. Interlocking, perpendicular-to-bedding stylolites are sparsely identified in the study area. Calcite-filled fractures can contain strain hardened slickensided surfaces but are not pervasively preserved. Calcite-filled fractures often parallel strike-slip fault trends, as well as extensional fracture trends.

The Smokey Hill Shale is 102 to 122 m of interbedded calcareous shale, marl, and shaley fossiliferous limestone (Wrucke and Wilson, 1957; Braddock et al., 1970; 1988; 1989; Madole et al. 1998). Lithofacies, Total Organic Carbon (%), and $CaCO_3$ (%)

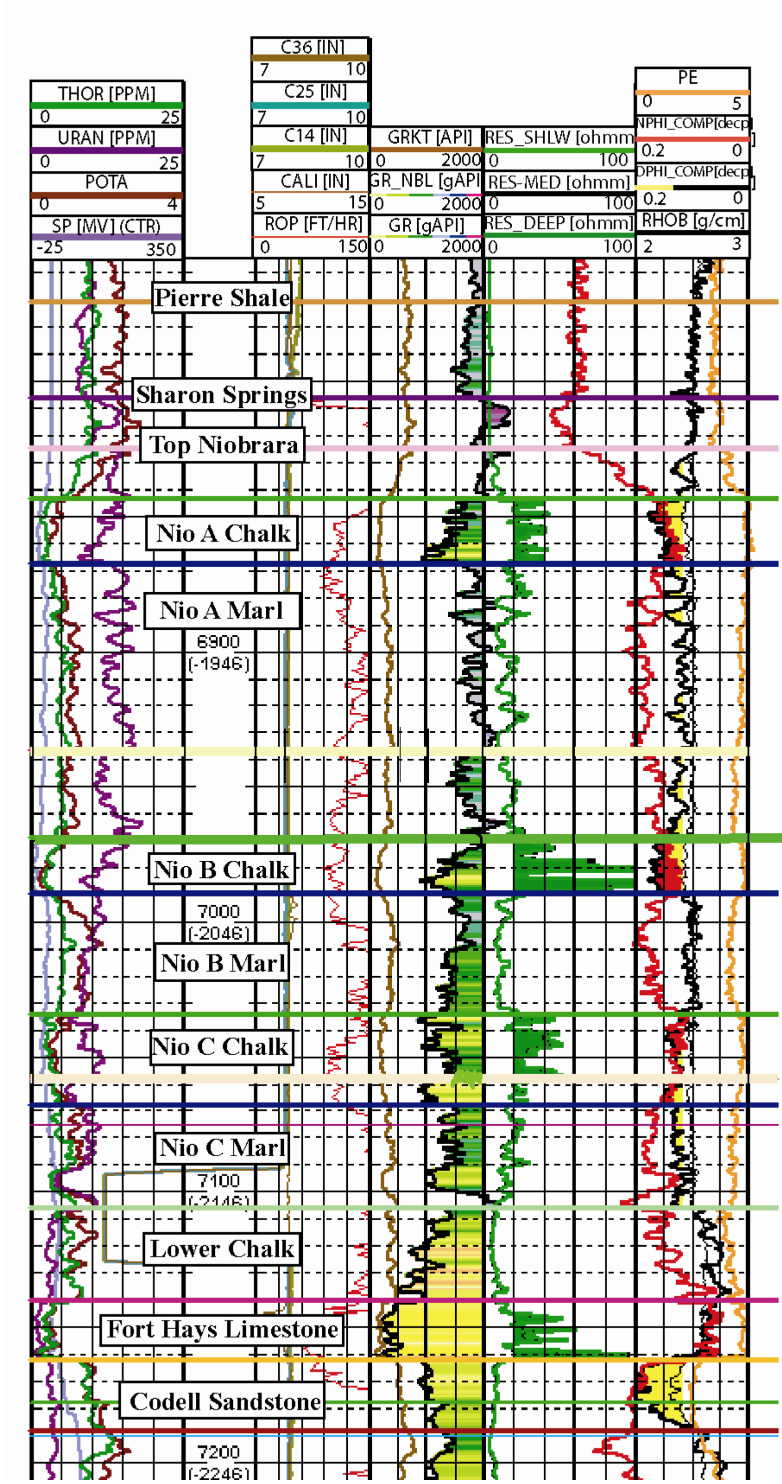

Log Key:

THOR= Thorium (ppm)
URAN= Uranium (ppm)
POTA= Potassium (%)
SP = Spontaneous Potential
C36= Caliper 3-6 (inches)
C25= Caliper 2-5 (inches)
C14= Caliper 1-4 (inches)
CAL1= Caliper 1(inches)
ROP= Rate of Penetration (Feet/ Hour)
GRKT= Gamma KT (gAPI)
GR= Gamma Ray (gAPI)
RES_SHLW=Shallow Resistivity (ohm.m)
RES_MED= Medium Resistivity (ohm.m)
RES_DEEP= Deep Resistivity (ohm.m)
PE= Photo Electric Factor
NPHI= Neutron Porosity (100 pu)
DPHI= Density Porosity (100 pu)
RHOB= Bulk Density (g/cm3)

Figure 2.2. Industry provided type log through the upper Benton Group, the Niobrara Formation, and the lower Pierre Shale (Richter, personal communication, 2009).

studies within the Denver Basin have further subdivided the Smokey Hill into four benches, the lower chalk, the C marl overlain by the C chalk, the B marl overlain by the B chalk, and the upper A marl overlain by the A chalk (Gustafson, and Deacon, 2008) (Fig. 2.2). Observations of surface outcrops and cores available through the USGS Core library show these chalk-marl transitions are often gradational from marly chalks to chalky marls, with thin interbedded lenses of shaley limestone and calcareous shale. Like the Fort Hays Limestone, abundant *Inoceramus* and *Psuedoperna congesta* fossil fragments are present. The Niobrara Formation contained the majority of slickensided minor fault data collected for this study.

The upper Cretaceous Pierre Shale consists of predominantly dark olive-gray shale, and sandy shale containing limestone, ironstone concretions, and several sandstone members (Braddock et al., 1970, 1988, 1989; Madole et al., 1998). Across the northern Front Range, 10 members collectively make up the Pierre Shale and are approximately 1350 m in total thickness (Scott and Cobban, 1965, 1986). An incomplete exposure of tan, medium-grained sandstone of the upper Cretaceous Fox Hills Formation lies to the northeast of the study area (Scott and Cobban, 1986). Near Golden, CO, the Fox Hills Sandstone is in gradational contact with the Pierre Shale (Covington, 1966). Complete sections of the unit averaged 137 m in thickness (Nibbelink, 1983). Subsurface aquifer studies investigating the Fox Hill sands discovered repeated lithofacies sections hypothesized to be the result of layer-parallel detachment and basin-directed thrusting (Kittleson, 1988; 2004).

Cenozoic

Throughout the study area, much of the lower Cenozoic is not exposed. Paleocene sills of light-gray, very-fine-grained dacite porphyry containing phenocryst of quartz, plagioclase, and biotite were identified west of Lyons, CO and dated at 62.2 +/- 3 Ma (Hoblitt and Larson, 1975; Braddock et al., 1988). North of the study area, the Oligocene Chadron and Brule formations of the White River Group are angularly unconformable to east-dipping Mesozoic strata (Courtwright and Braddock, 1989). Near the Colorado-Wyoming Border, the White River Group is about 75 m thick, but measurements were confined to a paleovalley of eroded Mesozoic strata (Courtwright and Braddock, 1989). The Miocene Arikaree Formation, consisting of siltstones and fine-grained sandstone, ranges in thickness from 0 to 15 m. The Arikaree Formation is exposed on steep slopes below a remnant alluvial apron known as the Gangplank west of Cheyenne, WY (Courtwright and Braddock, 1989).

The late Miocene to early Pliocene Ogallala Formation is an olive-gray, coarse grained sandstone and conglomerate that unconformably onlaps Precambrian basement of the Laramie Range in Wyoming and Permian, Triassic, Jurassic, and Cretaceous strata in western Nebraska, Kansas, and eastern Colorado (Courtwright and Braddock, 1989). Clastic source material for the Ogallala Formation was shed eastward from Laramide arches during regional uplift associated with the Rio Grande Rift in the late Miocene (Raynolds, 1997; McMillan et al., 2002, 2006). Up to 1800 m of Cenozoic sediments have been stripped away adjacent to the northeastern Front Range (McMillan et al., 2006).

Assorted terrace gravels, pediments, landslide remnants, and alluvium/colluvium deposits from Pleistocene to present are scattered east of the Front Range (Wrucke and Wilson, 1957; Braddock et al., 1970, 1988, 1989; Madole et al., 1998).

Chapter 3

Previous Work

Foreland basins form as the result of the migration of thrust belts, and are modified by processes such as crustal thickening, mass transport by erosion-sedimentation and regional isostatic subsidence (Jordan and Flemings, 1991; DeCelles and Giles, 1996; Catuneanu, 2004). The evolution of the associated orogen is recorded by the architecture of different stratigraphic units that constitute the infill of the foreland basin (Jordan, 1995) and by the kinematic framework of faults, folds, arches, and basement fabrics (Erslev and Koenig, 2009) associated with foreland deformation. To better understand the Denver Basin of the Rocky Mountain foreland and its associated fracture mechanisms, it is helpful to review previous researchers' observations and hypotheses concerning Laramide tectonic models, post-Laramide tectonic models, northeastern Front Range structural interpretations, and subsurface Denver Basin fracture studies.

Laramide Tectonic and Kinematic Models

Diverse fault strikes and fold trends in basement-cored arches of the Rocky Mountain foreland have led to a variety of hypotheses attempting to explain their origin. Beginning in the late 1960's, geologists have vigorously debated the relative dominance of horizontal compression and vertical tectonic motions, and were polarized into two schools of thought. Observations of steep-dipping faults in the Rocky Mountains led to several vertical tectonic models including: uplift from intrusive basaltic magma deep within the crust (Eardley, 1963); fault steepening at depth causing vertical uplift (Prucha et al., 1965), and other block uplift models (Stearns, 1971, 1978; Matthews and Work, 1978).

Since then, several researchers have presented compelling evidence supporting horizontal compression hypotheses for the Laramide Orogeny. By the late 1970's seismic refection profiles transecting the southeast end of the Wind River Mountains revealed Precambrian basement thrusted over Cretaceous sediments on a low-angle fault (Smithson et al., 1979). Early 1980's oil prospecting in the Rocky Mountains drilled through several kilometers of Precambrian hanging-wall basement before penetrating Phanerozoic footwall strata (Gries, 19883a; 1983b). Material mass balance arguments (Erslev, 1986) questioned the validity of vertical motions and modern geological, geophysical, and kinematic data clearly showed the dominance of horizontal slip and compression during the Laramide Orogeny (Stone, 1984, 2005; Erslev, 1986, 1993, 2005; Holdaway, 1998; Erslev et al., 2004; Erslev and Larson, 2006; Larson, 2009).

Previous debates of Laramide tectonics have focused on the kinematic evolution of the orogen (Wise, 1963; Sales, 1968; Stone, 1969), the rotation of the Colorado Plateau (Hamilton, 1981; Gries, 1983; Chapin and Cather, 1983; Karlstrom and Daniel, 1993) as well as hypotheses linking plate kinematics to diverse Laramide structural trends (Bird, 1988, 1998; Breitsprecher et al., 2003; Saleeby, 2003).

Laramide arch trends vary greatly from N-S (Front Range and Sangre de Cristo arches) NE-SW (Hartville Arch), NW-SE (Wind River and Black Hills arches), and E-W (Uinta, Owl Creek, and Sweetwater arches) (Fig. 1.1). To explain various orientations of

Laramide structures without invoking vertical uplift models, Wise (1963) and Sales (1968) proposed transpression causing regional-scale simple shear. Stone's (1969) observation of NW-trending arches led to hypotheses of regional northeast-southwest horizontal compression. Stone (1969) expanded on these ideas and applied the concept of "wrench faults" to explain much of the deformation observed within the Rocky Mountain Foreland. First order structures such as the Nash Fork-Hartsville uplift were presumed to be NE-SW striking right-lateral wrench faults, whereas NW-SE striking left-lateral wrench faults controlled the Tensleep and Seminole structures (Stone, 1969).

The diversity of arch trends became the basis for rotational hypotheses for Laramide stresses. Gries (1983) noted that seismic and wellbore data document low-angle thrusting of Precambrian basement over Phanerozoic rocks in both-west trending and north-northwest-trending arches. Gries (1983) suggested that arches formed as the result of a counterclockwise rotation of Laramide compressive stress that was oriented E-W during the Late Cretaceous, NE-SW compression during the Paleocene and N-S during the Eocene (Fig 3.1). Chapin and Cather (1983) hypothesized that internal geometries and an *en echelon* arraignments of basins along the east side of the Colorado Plateau were evidence of ENE-WSW compression during the Late Cretaceous, and NE-SW in the late Paleocene to middle Eocene. Chapin and Cather (1983) hypothesized that the latest event was the result of the NNE translation of the Colorado Plateau. Observations of right-lateral slip on north-striking faults in northern New Mexico by Karlstrom and Daniel (1993) supported this hypothesis, but Bauer and Ralser's (1995) study of the Picuris Pecos fault suggested that at least some of the right lateral offset occurred prior to Laramide deformation. Aeromagnetic maps from north-central New Mexico show north-

northeast trending linear features with dextral offsets across the Picuris-Pecos, Tusas-Picuris and Nacimiento fault systems (Cather et al., 2006). The exact timing in which dextral offset occurred remains highly contested (Cather and Harrison, 2002; Frankhauser and Erslev, 2004; Cather et al., 2006).

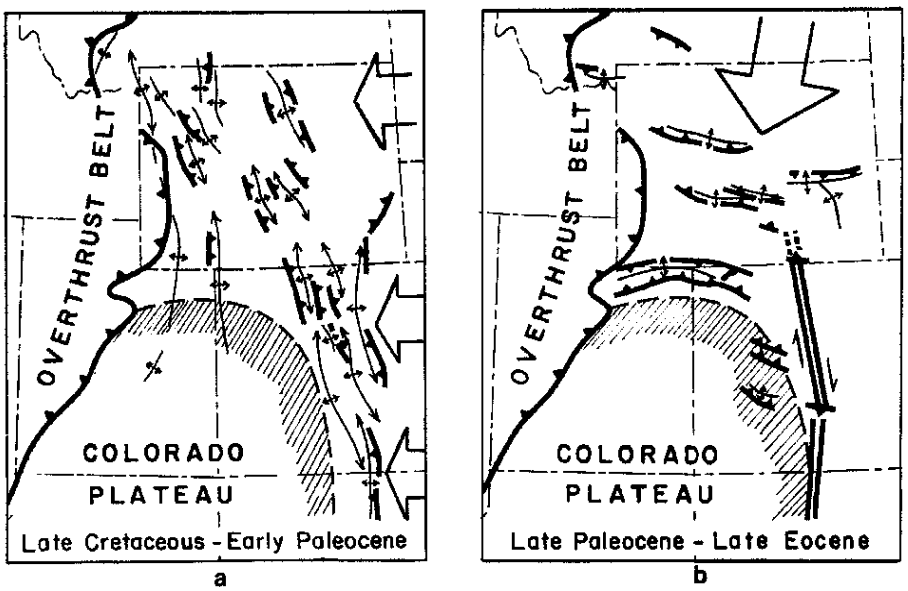

Figure 3.1. Gries's (1983a) model of multi-directional deformation and predicted compression directions during a) early and b) late Laramide time.

Hypotheses linking plate kinematics to Laramide arch trends have also invoked rotating stress field models. Bird (1988, 1998) predicted a 15°difference in the motion of the Kula and Farallon plates relative to the North American plate and hypothesized a 15° clockwise rotation of Laramide compression. But geochemical analysis conducted by Breitsprecher et al. (2003) of igneous rocks in the Pacific Northwest suggested that the Kula/ Farallon plate boundary was located near the U.S.–Canada border during the Eocene, and questioned the idea of multiple shortening directions driven by different vector motions of the Farallon and Kula Plates during flat slab subduction.

Saleeby (2003) recognized that the subbatholith mantle lithosphere of the southern Sierra Nevada batholith was missing in southern California and replaced by the Rand Schist, a schist similar in age to the Franciscan complex. Saleeby (2003) hypothesized that the Laramide shallow slab segment was due to the subduction of a fragment of an aseismic ridge that was the counterpart of the Hess-Shatsky large igneous province of the northwest Pacific basin. The thickened mafic crustal section relative to the abyssal lithosphere is presumed to have had greater buoyancy, leading to slab segmentation (Saleeby, 2003). The sheared-off segment of the subbatholith mantle lithosphere was replaced by tectonically underplated greywacke-basalt lithologies. The assemblage was derived from the Franciscan subduction complex as well as possible forearc basin material that was displaced down-dip into the shallow subduction zone (Saleeby, 2003). Using an interpretive plate trajectory model, Saleeby (2003) hypothesized that end-loading of the North American plate during subduction of an aseismic ridge drove Laramide deformation and a 30° clockwise rotation of stresses.

Recent researchers have focused on the analysis of minor fault data and ideal compression axes in syn-Laramide strata of the Rocky Mountain region (Varga, 1993; Selvig, 1994; Molzer and Erslev, 1995; Jurista, 1996; Fryer, 1996; Erslev, 1997, 2001, 2008; Gregson and Erslev, 1997; Holdaway, 1998; Ehrlich, 1999; Ruf and Erslev, 2000; Hager, 2001; Bump, 2003; Fisher, 2003; Erslev et al., 2004; Magnanai et al., 2005; Erslev and Larson, 2006, Neeley, 2006). Minor fault analysis of (n=18,963) of Laramide faults throughout the Rocky Mountains were collectively analyzed by Erslev (2005) and Erslev and Koenig (2009) (Fig. 3.3). Their regional analysis showed the average slip (N67E-01) and compression (N67E-02) directions indicated unimodal, ENE-WSW

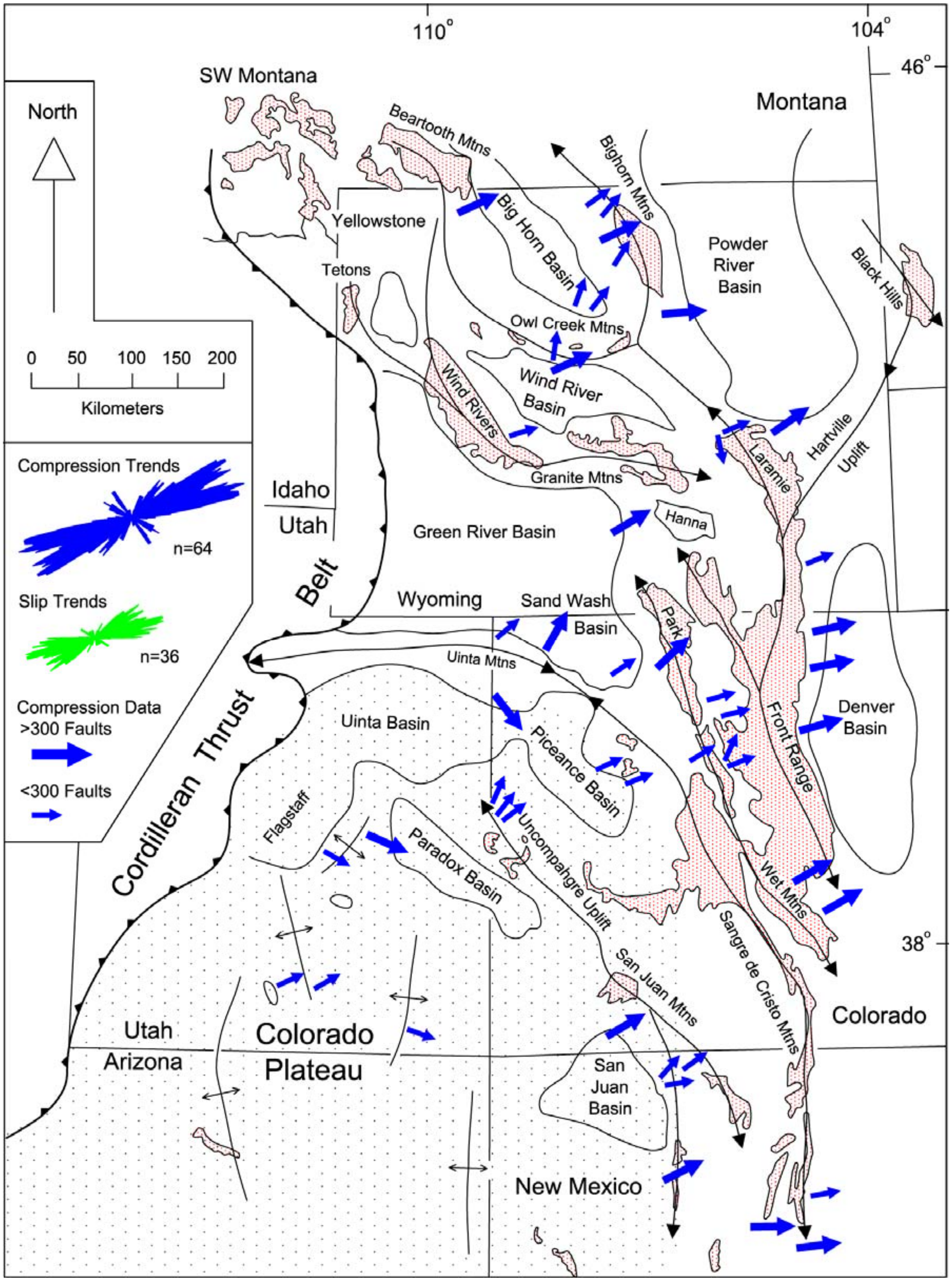

Figure 3.2. Tectonic map of the Laramide Foreland showing trends of major and minor Laramide arches. Arrows indicate average shortening directions from published and unpublished minor fault data (Erslev and Koenig, 2009).

shortening and compression, which is nearly identical to shortening directions predicted by Laramide arches (N67E) and folds (N66E). The absence of regular multidirectional fold trends contradicts hypotheses of rotated compression directions due to plate convergence changes (Erslev and Koenig, 2009).

Post-Laramide Tectonic and Kinematic Models

Continued debates regarding post-Laramide fracture mechanisms are commonly linked to the effect and boundary of deformation associated with Rio Grande Rifting. The Rio Grande rift was described by Tweto (1980) as a continuous graben system that extends from New Mexico through the San Luis and Upper Arkansas valleys to Leadville, CO. Daggett et al. (1986) used gravity and seismic data to examine the southern extent of the Rio Grande Rift and concluded that the southern margin was underlain by anomalous mantle which penetrated or replaced the lowermost crust. Daggett et al. (1986) hypothesized that 2-3 km of crustal thinning relative to the adjacent Basin and Range province occurred, which was consistent with extension estimates of the time.

Aldrich et al. (1986) observed NW-SE dike swarms in the southwestern U.S. and hypothesized that least principal stress directions were perpendicular to dike trends and thus parallel with regional extension trends. Aldrich et al. (1996) used K-Ar dating of elongate dikes to constrain the timing of extension which led to hypotheses of regional extension in an ENE-WSW direction during the mid-Tertiary (~32 to 15-10 Ma) and rotating clockwise 45° to a WNW-ESE direction sometime between 15 and 7 Ma.

Kellogg (1999) observed the close proximity of Neogene normal faults with Laramide thrust faults, and suggested that the two fault types were genetically linked by reactivation. Deep seismic profiles across Laramide uplifts such as the Wind River Mountains in Wyoming and the Manzano uplift in New Mexico indicate listric thrusts, flattening at depth into the middle crust at about 15-16 km bound the uplifts (Sharry et al., 1986; Russell and Snelson, 1994). The bounding thrusts may have controlled the position of Tertiary normal faults by offering zones of weakness that can be reactivated during crustal extension (Kellogg et al., 1995).

McMillan et al. (2006) investigated late Cenozoic relief development in the Rocky Mountain orogenic plateau by reconstructing aggradational surfaces at the top of the basin fill and by measuring subsequent incision relative to reference surfaces. McMillan et al. (2006) hypothesized that localized extension is associated with the projection of the Rio Grande Rift into the central Rockies, and the domed uplift generally coincides with the position of buoyant mantle anomalies interpreted at depth.

Fault and fold data from the Rio Grande rift dataset of Erslev and Koenig (2009) showed a trimodal distribution of NNW-SSE, N-S and less abundant NE-SW orientations. The average fault strike (N06W) and fold trends (N13W) were hypothesized to be related by either reverse drag folding adjacent to curved normal faults or extensional fault-propagation folds above blind normal faults (Erslev and Koenig, 2009). The overall state-to-state bimodality of fault rose diagrams supports dual stage extension histories as proposed by Aldrich et al. (1986), or reactivation of pre-existing N-S and NNW-SSE Laramide faults proposed by Kellogg (1999) (Erslev and Koenig, 2009).

Previous Structural Interpretations of the Northeastern Front Range

The Hayden Survey conducted the first geologic, topographic, and structural investigations of the northeastern Front Range from field studies in the late 1860's. Hayden (1874; 1877) showed vertical-offsets in faults from cross-sections through SSE-plunging anticlines, and NW-striking faults in the northeastern Front Range.

Ziegler (1917) recognized that repeated stratigraphic sequences were occurring along range-parallel fault systems. Ziegler's (1917) cross sections through Golden, CO showed steep, westward-dipping reverse faults overturning the Dakota, Morrison, Lykens, and Lyons formations. Ziegler (1917) identified similar geometries through Boulder, CO, where westward-dipping reverse faults cut Morrison and Dakota stratigraphic sequences nearly bedding parallel to the upturned formations. However, farther to the north, west of Loveland, CO, Ziegler's (1917) cross sections presented the Big Thompson Anticline as an asymmetric fold cored by a blind, subplanar ENE-dipping reverse fault that cut into basement.

Boos and Boos (1957) mapped the eastern flank of the Front Range in detail from the Colorado-Wyoming border to the Canyon City Basin. They proposed that northeast trending structures of the Colorado Mineral Belt had Precambrian ancestry and were rejuvenated in Tertiary time. Boos and Boos (1957) described fifteen separate structures varying in complexity including east-dipping monoclines, north-south folds parallel to the mountain front, normal faults with substantial throw, step-like platforms bordered by drape folds, *en echelon* fault blocks, thrust faults, wedge-shaped grabens, and more. Diverse trends of faults and folds through the study area led Boos and Boos (1957) to conclude that the varied structures represented reactions of sedimentary rocks resting on metamorphic and igneous basement to compressive forces and differential uplift during Laramide mountain building.

Matthews and Sherman (1976) published cross-sections and 3D structural interpretations for variably-striking monoclonal folds in the northeastern Front Range. Their model showed drape folding of sedimentary strata over differentially uplifted basement blocks. Matthews and Sherman (1976) suggested that the variable trends observed for monoclinal fold axes were evidence favoring differential basement block uplift over horizontal compression during the Laramide. Later structural interpretations of the northeastern Front Range by Matthews and Work (1978) included the Livermore model and hypothesized that regional tectonism resulted from vertical motions associated with high-angle, variably-striking reverse and normal faults.

Cross sections published with USGS geologic maps (Braddock et al., 1970; 1988a-e; 1989; Courtwright and Braddock, 1989: Madole et al. 1998) invoke dip-slip motion on planar to concave-down, subvertical faults with basement folding near faults and parallel folding of the sedimentary strata. The diversity of structural interpretations is summarized by various cross-sections that transect Milner Mountain Anticline west of Loveland, CO (Fig. 3.3).

Erslev and Gregson (1996) used kinematic analyses of minor fault data to test hypotheses of Laramide deformation in the northeastern Front Range. Erslev and Gregson (1996) recognized unidirectional, horizontal shortening oriented approximately 080° in the Horsetooth Reservoir area west of Fort Collins, Colorado. They documented a southeastward deflection of stress from the upper hinge to the forelimb of Grayback Monocline, a major NE-striking monocline in the Livermore Embayment northwest of Fort Collins, Colorado. They hypothesized that the clockwise deflection of stress could be due to stress refraction by strain partitioning, fault reactivation, or clockwise, vertical axis rotations by right-lateral strike-slip movement (Erslev and Gregson, 1996).

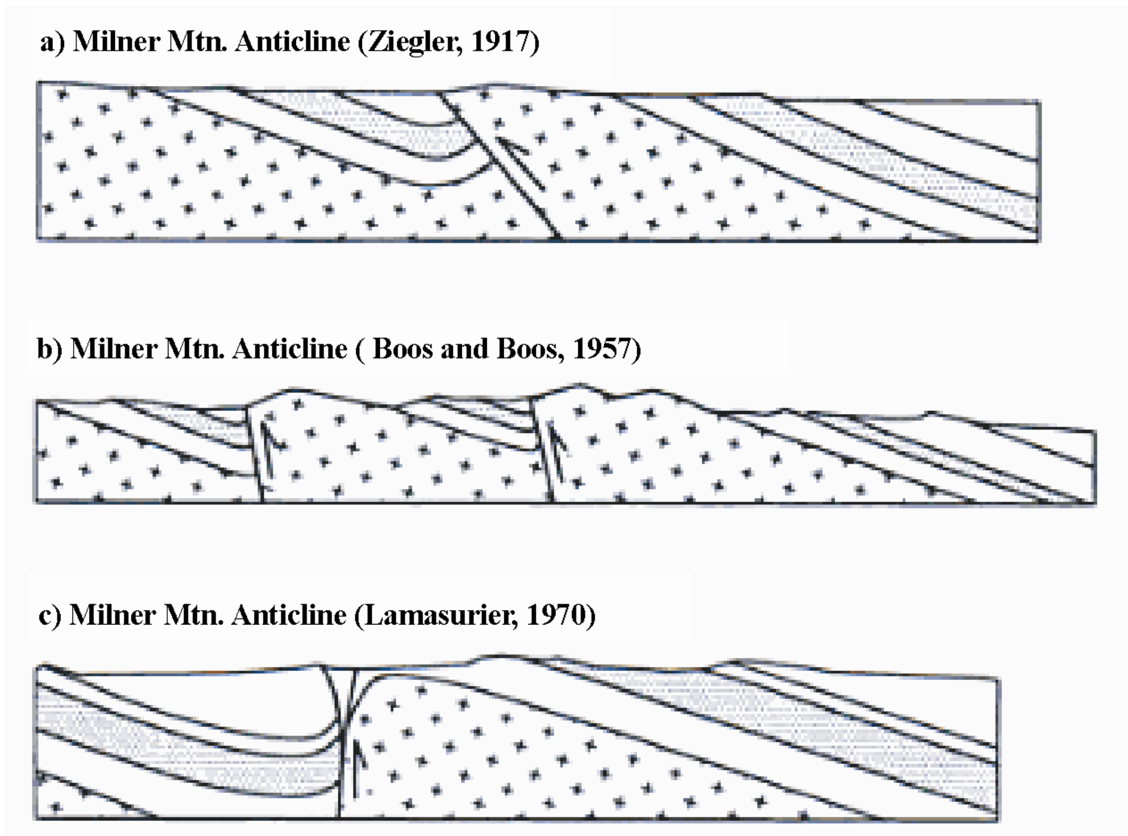

Figure 3.3. The evolution of structural interpretations across the northeastern Front Range as summarized by cross-sections transecting Milner Mountain Anticline. Figure from Erslev and Holdaway (1999).

Holdaway (1998) analyzed minor fault data west of Fort Collins, Colorado, and paleomagnetic data from two sites along the Grayback monocline northwest of Fort Collins, Colorado. Using slickenline and Compton’s (1966) ideal compression analysis of minor fault data (n=2231), Holdaway (1998) documented that regional Laramide shortening was unidirectional and oriented 79°. Paleomagnetic analyses of the two sites revealed clockwise vertical-axis rotations of 39° in the forelimb of the Grayback monocline but no rotations in the anticlinal zone of the Grayback monocline (Holdaway, 1998). Clockwise paleomagnetic and stress directions presented by Holdaway (1998) were evidence of right-lateral shear in the forelimb of Grayback monocline.

Tetreault et al. (2008) performed detailed paleomagnetic analyses at various locations within the forelimb of the Grayback Monocline to identify fold-axis parallel deformation and to observe paleostress deflections within fault related folds. Tetreault et al. (2008) confirmed that maximum rotations occurred within steeply dipping strata of the forelimb. They suggest the Grayback monocline was formed by transpressional trishear fault-propagation folding and occurred above a reactivated, NW-dipping, right-lateral / reverse fault, and refuted the hypothesis that local stress rotations were responsible for paleostress deflections in fault-related folds.

Erslev and Larson (2006) and Larson (2009) analyzed minor fault data (n=3150) collected in syn-Laramide strata west and northwest of Fort Collins, CO. Erslev and Larson (2006) showed that Laramide compression was subhorizontal, unidirectional and oriented at 085°. Minor fault and paleomagnetic data were hypothesized to have clockwise vertical axis rotations where strain partitioning occurred in the forelimbs of NE-trending monoclines formed by right-lateral transpression. Erslev and Larson (2006) hypothesized that trishear fault-propagation folding was the locally dominant mode of deformation near oblique-slip and dip-slip reverse faults, and Larson (2009) stated that the structural low of the Livermore Embayment north west of Fort Collins, CO, was due to the local dominance of oblique, right-lateral slip on reactivated, NE-trending faults.

Subsurface Denver Basin Fracture Studies

Subsurface structural studies in the Denver Basin have generated several hypotheses from diverse datasets including geophysical well logs from vertical wellbores, limited 2D and 3D seismic surveys, and well-to-well cross-communication maps. Weimer (1980) used stratigraphic isopachs to identify Cretaceous disparities in stratigraphic thickness across the northern Denver Basin. Weimer (1980) postulated that stratigraphic thicks and thins were associated with three northwest-trending and nine northeast-trending paleostructures which were active during the Cretaceous. These paleostructural elements were thought to have been controlled by recurrent basement fault-block movement along the Transcontinental Arch (Weimer, 1978, 1980; Sonnenberg and Weimer, 1981). A problem persisted in explaining the occurrence of normal faults in the Niobrara Formation. Davis and Weimer (1976) concluded that the normal faulting observed in seismic lines of the Niobrara Formation and younger intervals were the result of growth faulting associated with recurrent movement during the Laramide.

Haberman (1983), and Davis (1974, 1985) investigated seven, 2D seismic lines southwest of Greeley, CO, in Hambert Field and one, N-S 2D seismic line which transected the Greeley-Wattenberg Lineament mapped by Weimer and Sonnenberg (1982) east of the Wattenberg Field. Haberman (1983) and Davis (1985) observed low-angle listric, normal fault geometries in upper Cretaceous rocks including the Niobrara-Carlile, Lower Pierre, and Middle Pierre Hygiene formations. Davis (1985) noted that listric normal faults were concentrated near NE-trending lineaments as described by Weimer (1980), and detached away from axes of proposed structural highs. Davis (1985) concluded that listric normal faults observed on seismic data supported interpretations of paleostructural highs even though basement faults were not seen in seismic profiles. Davis (1985) suggested that basement faults with opposite senses of motion relative to upper Cretaceous fault systems could be located by indirect evidence such as the position of listric normal faults. Listric normal faults were hypothesized to occur above the corners of basement fault blocks (Davis, 1985).

In 1992, the U.S. Department of Energy contracted the acquisition of 3D seismic data over a 20 km^2 area in Sooner Field (T8N, 58W) to provide better reservoir characterization of the "D" sand, and other hydrocarbon bearing reservoirs (Pritchett, 1993). Pritchett (1993), on the basis of detailed fault mapping of the Sooner Field 3D seismic volume used illustrations of amplitude anomalies to show listric normal faults soled into the Graneros Shale, normal and growth faults were subvertical but had shallowing dips at depth, and basement faults showed both normal and reverse motions. Pritchett (1993) concluded that potential fault mechanisms included regional basement wrench faulting and regional uplift coincident with sedimentation

Weimer (1996) and Weimer et al. (1998) expanded on the recurrent movement on basement faults model using seismic and well control data. By hand contouring Cretaceous intervals, Weimer et al. (1998) identified strike and dip anomalies in relation to regional thickness patterns. Weimer (1996) hypothesized that offsets in strata and abrupt changes in strike and dip were the result of rigid block rotation and movement along basement-cored faults. He suggested that several wrench fault zones (WFZ) in the Denver Basin explains primary NE-SW fault systems with secondary synthetic and antithetic faults compartmentalizing Cretaceous reservoirs (Weimer, 1996; Weimer et al. 1998).

Kittleson (1988; 2004) used well control to examine the hydrogeology of the Laramie- Fox Hills Aquifer in Weld County, Colorado and showed evidence of repeated stratigraphic sections and variable water quality in wells penetrating the Laramie-Fox Hills Formation. Well-log cross-sections constructed by Kittleson (1988) showed frequent folding above repeated sections of the Laramie-Fox Hills sands. Theses cross-sections also showed a previously unrecognized *decollement* fault zones in the Kp2 marker horizon of the Pierre Shale. Kittleson (2004) hypothesized that sedimentary packages overlying the Kp2 horizon of the Pierre Shale migrated basinward on bedding-parallel detachment surfaces. This discovery contradicted hypotheses of growth faulting in the area since the deformation was hypothesized to be post deposition and thickening of strata was caused by thrust faulting.

Oldman (1996) identified “salt pinch outs” from well control in southwestern Nebraska and concluded that salt dissolution led to the collapse and related normal faulting of upper Cretaceous sedimentary rocks. However, isopach maps show Permian salts are limited to eastern portions of the Denver Basin and are unlikely to cause fracturing near the basin center.

Longman et al. (1998) investigated stratigraphic disparities in the Niobrara Formation across the Denver Basin using well log data. Isopach maps revealed thinning of the uppermost Niobrara Formation and were used to support hypotheses of basement fault-block movements during the Laramide Orogeny along NE-SW and NW-SE trending faults which cross cut the Denver Basin. Thins of the uppermost Niobrara Formation were attributed to sub-aerial exposure over basement highs consistent with basement arches such as the Transcontinental Arch and Hartville uplift.

Birmingham (1998) observed varied hydrocarbon production characteristics in Codell well completions, which led to hypotheses that upper Cretaceous reservoirs were structurally compartmentalized. Using well logs and Formation Micro-Imaging (FMI) logs, Birmingham (1998) showed sub-vertical and listric normal faults in the Niobrara and Codell stratigraphic sequences.

Another source of fracture information was recorded by Birmingham et al. (2001) from observations of hydraulic fracturing techniques on recently drilled wellbores and their associated interference with older wells' production rates in the Denver Basin. Birmingham et al. (2001) mapped "frac'ed into" wells and documented the general direction in which hydraulic fluids had to flow to intercept previously existing wells. Numerous "frac into" problems led to dividing the Wattenberg Field into two structural areas. Area 1 consists of N-S "frac into" directions, whereas area 2 consists of E-W "frac into" directions. Borders between the two separate areas were hypothesized to parallel basement fault trends as identified by Weimer (1996). Birmingham et al. (2001) concluded that area 1 was bound to the north by the Windsor wrench fault zone, to the south by the Longmont wrench fault zone, and to the west by the N-S trending synclinal hinge of the Denver Basin.

Current observations from more recent well completion programs south of Greeley, CO, confirm fracture complexity suggested by "frac into" orientations. However N-S "frac into" directions clearly cross proposed wrench fault boundaries, and dominantly occur west of the proposed synclinal hinge in the Denver Basin (B. Richter, personal communication, 2009). This suggests other mechanisms are contributing to induced fractures orientations along the western Denver Basin. One of the most puzzling structural problems of the Denver Basin lies in explaining N-S fracture development along the proposed synclinal hinge.

Current technical studies by Noble Energy Inc. have focused on the *in situ* state of stress and strain relationships observed in the Wattenberg Field and Denver Basin. A caliper logging program was instituted by Noble Energy Inc. in 2008 to investigate borehole stability and borehole breakouts. Breakouts are the zone of compressive failure that results from stress concentration around the wellbore. The max horizontal stress (S_{Hmax}) squeezes the borehole, causing the borehole to elongate parallel to the minimum horizontal stress (S_{hmin}) direction and fail (Zoback, 2007). 26 wells were logged across the Wattenberg Field from 2008 to 2009 with the six arm caliper, but only 13 wells showed statistically significant breakout data (B. Richter, personal communication 2009) (Fig.3.4).

The 13 wells with breakout data revealed a complicated arrangement of varied S_{Hmax} directions (Fig3.4). Breakouts were only observed in the Pierre Formation and could easily be mistaken for wellbore rugosity associated with drilling through interbedded shales and sand.

The 13 wells with no wellbore failures were hypothesized to be the result of an isotropic horizontal stress state for many portions of the field (B. Richter, personal communication, 2009). The lack of considerable horizontal stress influence and the presence of N-S borehole breakouts and “frac into” directions adjacent to the Front

Range suggest Laramide horizontal compression ended and was replaced either by regional uplift and erosion of overburden, or by post-Laramide extension.

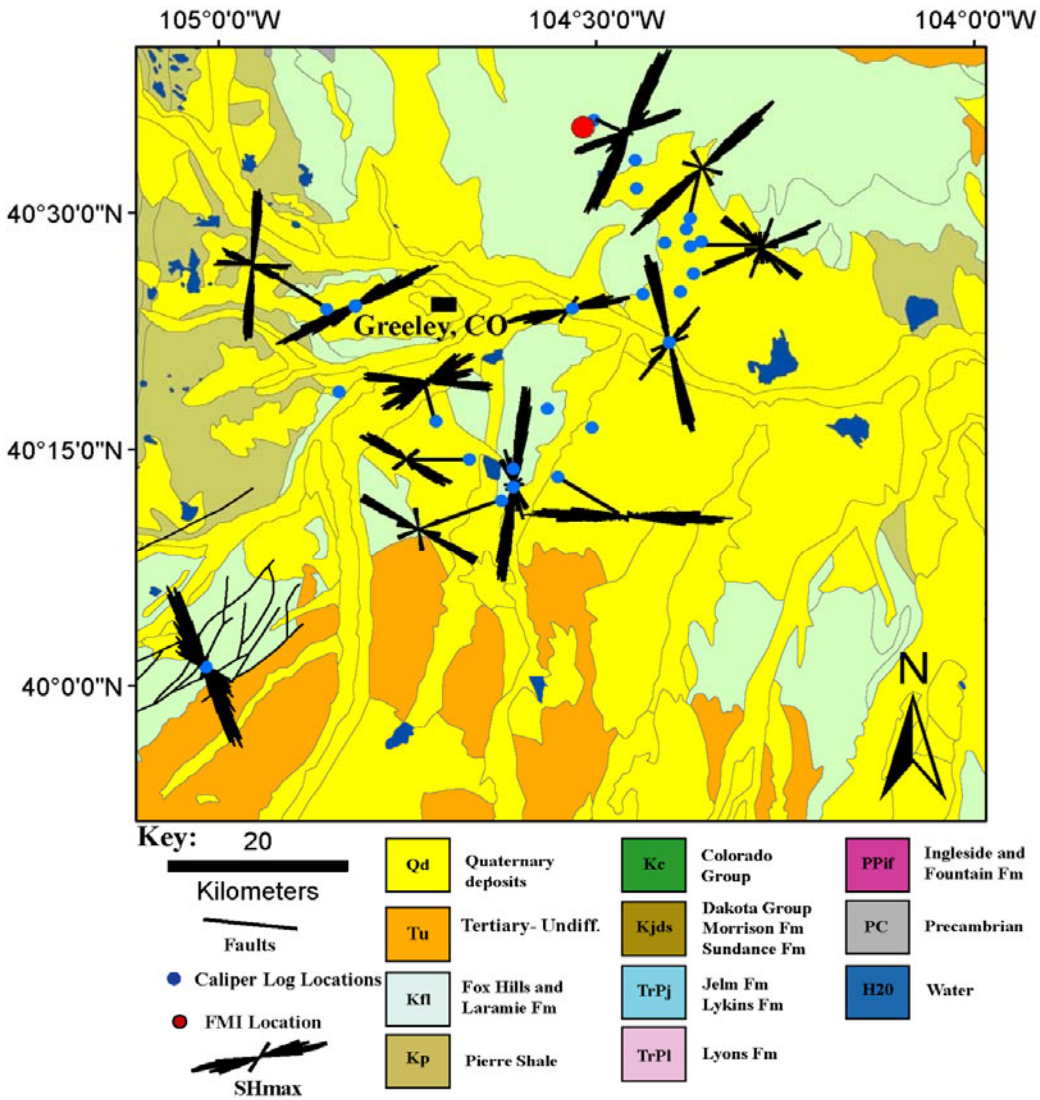

Figure 3.4. Simplified bedrock geologic map with roseplots of S_{Hmax} directions calculated from borehole breakouts. S_{Hmax} axes are normal to observed borehole breakout directions in 13 of 26 wells included in the six arm caliper *in situ* stress study of the Wattenberg Field. S_{Hmax} directions also predict frac into orientations (B. Richter, personal communication, 2009).

A Formation Micro-Image Log (FMI) was run in a vertical wellbore north of Wattenberg Field to gain a better understanding of natural and induced wellbore fractures in 2009 (B. Richter, personal communication 2009). The image revealed that fracture orientations in upper Cretaceous sediments differed from lower stratigraphic intervals (Fig. 3.5). Upper Cretaceous fracture orientations averaged a 33.28 vector mean, whereas the Lyons and Lykins formations averaged 80.85 vector mean and higher dispersion values. The vector means of natural, healed, and induced fractures are also highly variable (Fig. 3.5). Faults through the well bore are highly variable, with a mean vector orientation of 67.5. Hypotheses for fracture heterogeneity include counterclockwise rotation of Laramide stress during basin development, strain refraction due to detachment of overpressured Cretaceous intervals, and local counterclockwise vertical axis rotation causing strain partitioning.

Isopach maps of the Niobrara Formation based on of over 5000 wells in the greater Wattenberg Field area reveal interesting depositional trends between chalk and marl benches (B. Richter, personal communication, 2009). The Wattenberg High parallels the Transcontinental Arch where stratigraphic thinning is prominent in the Codell Sandstone, Fort Hays Limestone and lower Smokey Hill sequences. However, stratigraphic thinning is not observed in upper Niobrara sequences. Depth structure maps over the same areas and intervals reveal long multi-mile inferred fault trends comparable to NE faults described by previous workers (Stone, 1969; Weimer, 1986; Weimer et al., 1998).

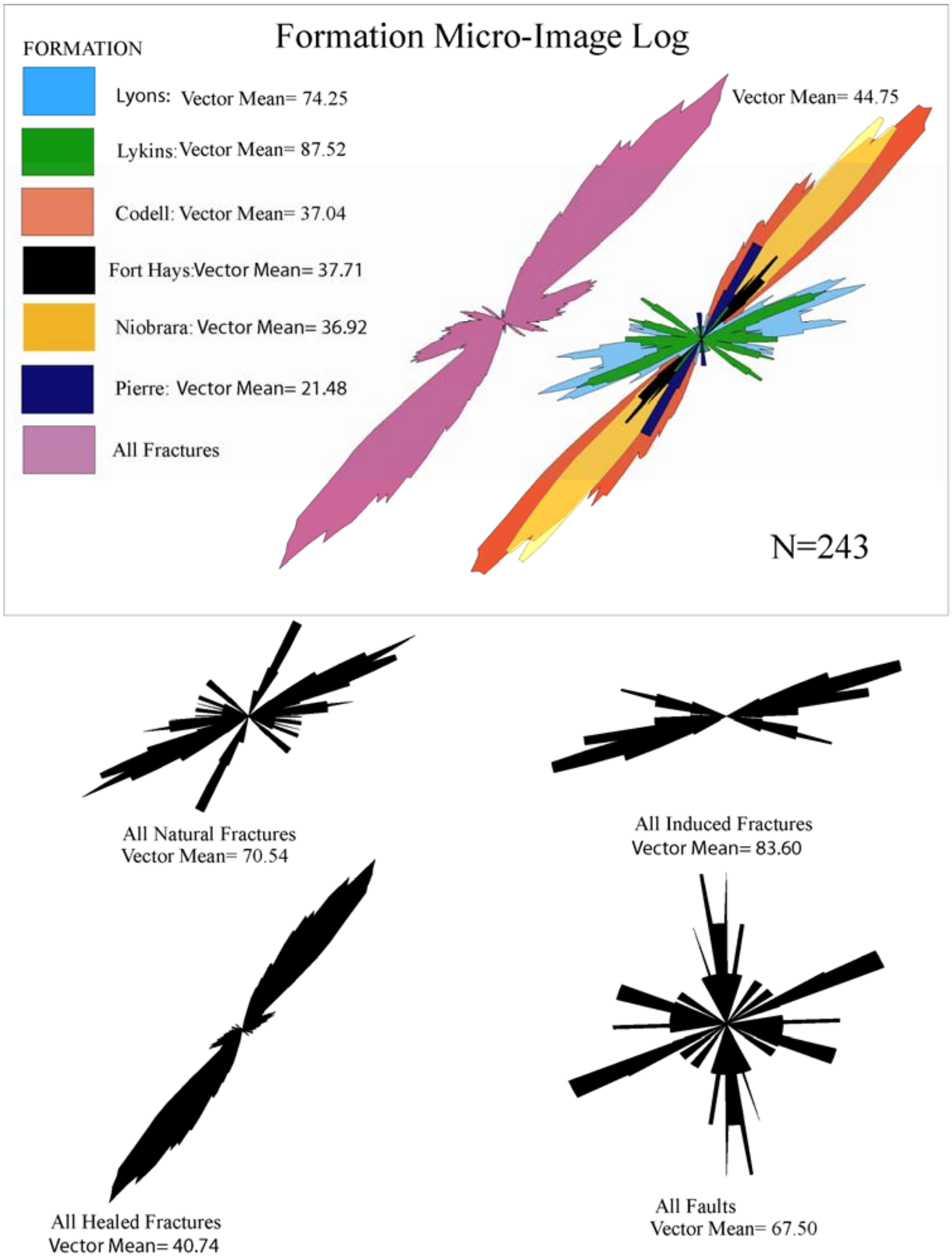

Figure 3.5. Industry provided fracture orientations observed from a Formation Micro-Image log collected in T7N, R64W (Fig. 3.4.). Fractures observed in the Niobrara Formation strike NE- and are commonly healed by vein mineralization fill (B. Richter, personal communication, 2009).

Chapter 4

Methods of Data Collection, Surface Fracture Observations and Analysis

The primary objective of this research was to constrain mechanisms responsible for extensional and shear fractures occurring within upper Cretaceous sediments of the foreland Denver Basin through the determination of the directions of strain and stress axes across the study area. Stress and strain directions for shear fractures can be determined through the analysis of slickensided minor faults (Angelier, 1984, 1990). Minor fault kinematic data consists of fault plane strike and dip, the trend and plunge of slickenlines, and fault shear sense (Compton, 1966, Angelier, 1990). The analysis of minor faulting will be used to compare with past minor fault studies of early Cretaceous rocks within the study area and to further test various hypotheses of Laramide kinematics proposed for the region. Extensional fracture, or joint, data consist of plane strike and dip, where crosscutting and/or abutting relationships are recorded. Analysis of joint data will test hypothesis of fracture heterogeneity across the study area and relative timing of joint sets. Calcite-filled fracture data consists of plane strike and dip, and will test hypothesis of preferred healed fracture orientations. Bedding, vertical solution stylolites, and pencil cleavage were also analyzed in this study. Appendix A contains the results of all stress and strain analyses and the geographic coordinates, formation, and bedding attitude for all stations.

Fault and Shear Sense Data Collection Methods

Minor fault (n=216) data were collected from 21 stations within the upper Cretaceous Fort Hays Limestone and Smokey Hill members of the Niobrara Formation. Shear sense of minor faults were determined using RM and RO criteria of Petit (1987) (Fig. 4.1.). One fault plane and slickenline measurement was collected from each fault with the exception of faults showing reactivated surfaces such as the case of station BD-17. All minor fault data is summarized in Appendix 1.

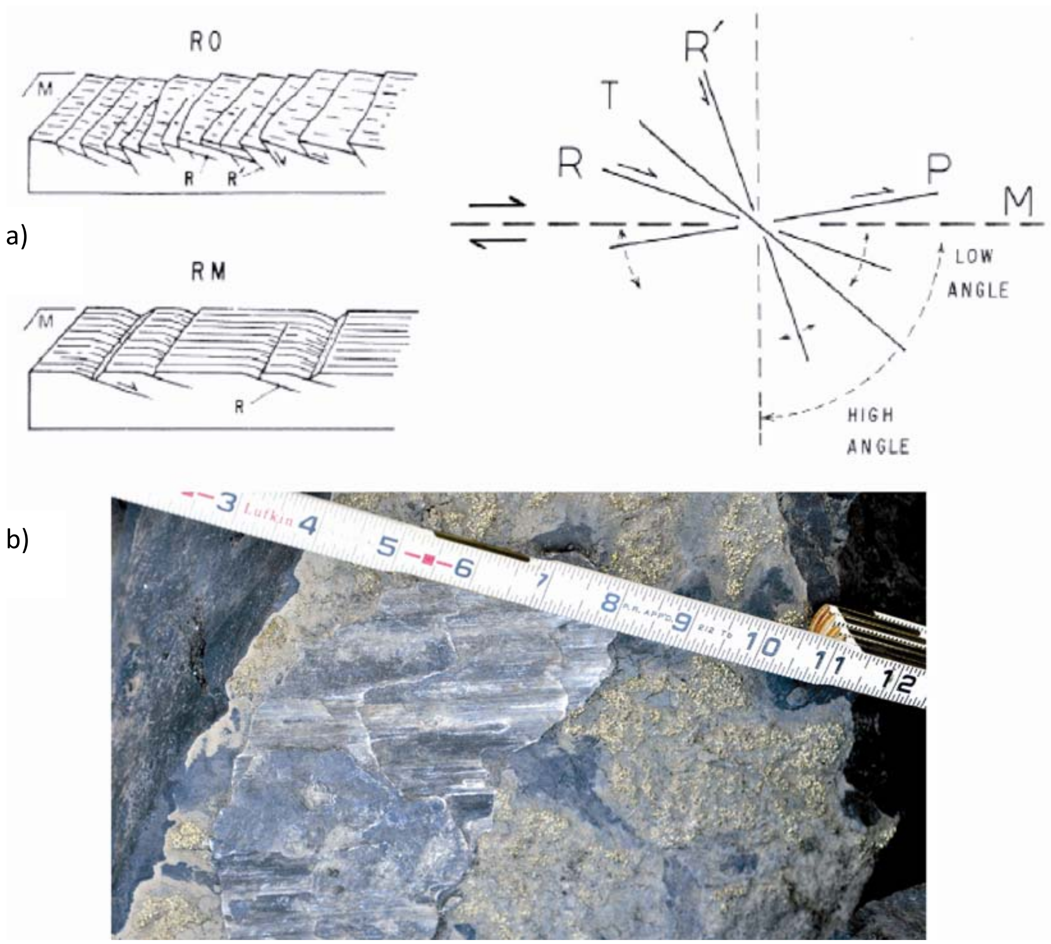

Figure 4.1. a) Block diagrams of RO, RM type faults and the orientations of synthetic Riedel shears (R), P-shears (P), antithetic Riedel shears (R'), and tensile fractures (T) (Petit, 1987). b) RM fabrics on a left lateral strike slip fault in the Niobrara Formation.

Fracture and Bedding Data Collection Methods

Joint data (n=1162) were collected from 63 data stations in the upper Benton Group through the Niobrara Formation. The relative timing of jointing was recorded by abutting and cross-cutting relationships of joints, minor faults, and calcite-filled fractures. Bedding attitude data (n=337) were recorded for upper Cretaceous strata throughout the study area.

Calcite-filled fracture data (n=244) were collected from 29 stations in the upper Cretaceous Benton Group through the upper Niobrara Formation. Vertical solution stylolites (n=97), pencil cleavages (n=20), and fold axis orientations were observed and recorded in the Fort Hays Limestone and Lower C chalk and marl sequences of the Niobrara Formation at three study locations. All fracture data is summarized in Appendices (1-7).

Methods of Analysis of Minor Fault Data

Methods employed for kinematic analysis across the study area were eigenvector analysis of slickenline attitudes and the ideal σ_1 method of Compton (1966) to quantify clustering of stress and strain axes. Eigenvector analysis of slickenlines was used to calculate the average slip directions during deformation. The ideal σ_1 method of Compton (1966) calculates an ideal σ_1 direction assuming σ_1 is on the plane perpendicular to a slickenlined fault that contains the slickenline, and that an angle α lies between the slickenline and the σ_1 axis. This provides two possible orientations of σ_1, where only one is consistent with the observed shear sense. The Compton (1966) ideal σ_1 method assumes faulting occurs on ideal planes without the influence of mechanical anisotropy, like bedding planes. Contoured stereoplots of ideal σ_1 axes can be used to distinguish single vs. multiple compression directions and suggest vertical axis rotations (Erslev et al., 2004).The ideal σ_1 method has been used for the conjugate minor faults common in the Phanerozoic strata of the Front Range and Laramide foreland (Erslev et al., 2004; Tetreault et al., 2008). Holdaway (1998) and Larson (2009) have shown that conjugate minor faults in Permian through Cretaceous strata were formed by Laramide compression and did not form on reactivated planes. Strike-slip and thrust fault data across the study area were analyzed separately from normal fault data. Field observations showed normal fault slickenline trends crosscut or overprinted earlier strike-slip fault slickenlines.

Raw minor fault data were entered into the SELECT (Erslev, 1998a) spreadsheet which can be used to correct slickenlines attitudes which plot off fault planes due to field observation errors. Slickenline trends on high-angle faults (>45° dip) were corrected using plunge and plunge direction. Slickenline plunges on low-angle faults (<45° dip) were corrected to honor their trend. SELECT created files of the attitudes of fault planes, slickenlines, and ideal σ_1 compression axes using reasonable α angles (Byerlee, 1978). α angles ranged between 9° and 36° and were measured in the plane perpendicular to the conjugate intersection and checked using SELECT2 (Erslev, 1998a).

Fault data were plotted and summarized using STEREOWIN (Almendinger, 2002) and ORIENT (Vollmer, 1992), creating stereoplots of fault planes, slickenlines, ideal σ_1 axes, as well as generating eigenvalues of average trend and plunge attitudes of slickenlines and ideal σ_1 axes for each fault data station. Data stations that have a significant amount of conjugate fractures were used to calculate α angles. All data stations were separated by stratigraphic member, and then averaged to find the best average fit α angle (Appendix 1). The Niobrara Formation's angle between conjugate shear fractures (2α) ranges between 25-68° across the entire study area, yielding an average α angle of 20°. The Fort Hays Limestone's angle between conjugate shear fractures (2α), range between 18-46° across the entire study area, yielding an average α angle of 15°. Eigenvector and eigenvalues of ideal σ_1 axes were recorded for the best average fit α angle (+/- 1°) for each stratigraphic unit. The best fit α angle used for the entire minor fault dataset is 17.5°. Nearby field studies have concluded that α= 20° is a good fit for ideal σ_1 analyses in sandstones across the Rocky Mountains (Erslev and Larson, 2006; Erslev and Koenig, 2009; Larson, 2009).

Methods of Analysis of Joint, Calcite-Filled Fracture, Stylolite, and Pencil Cleavage Data

Fracture plane measurements were sorted based on observed abutting or cross cutting relationships, fracture type, and location into separate files where SELECT. EXE (Erslev, unpublished) was used to create fracture plane files. Each file was analyzed in STEREOWIN, calculating eigenvectors of poles to planes and plotting fracture planes in stereoplots. Fracture attitudes were rotated about bedding strike to restore bedding to horizontal. Roseplots of joint strikes were created using 10° smoothing to best represent the data and scaled based on the size of the data set using LDIS (Erslev, 1998b).

Geologic Observations:

Field fracture studies include observations of mapped structural features, their geometry and orientation, as well as their relationships to fracture data collected throughout the study area. The study area is divided into areas based on the 1:24000 scale geologic maps published by the USGS (Figs.4.2-4.9). In some instances, field data stations are closely spaced and require maps to be further subdivided into subareas (Figs 4.2-4.19).

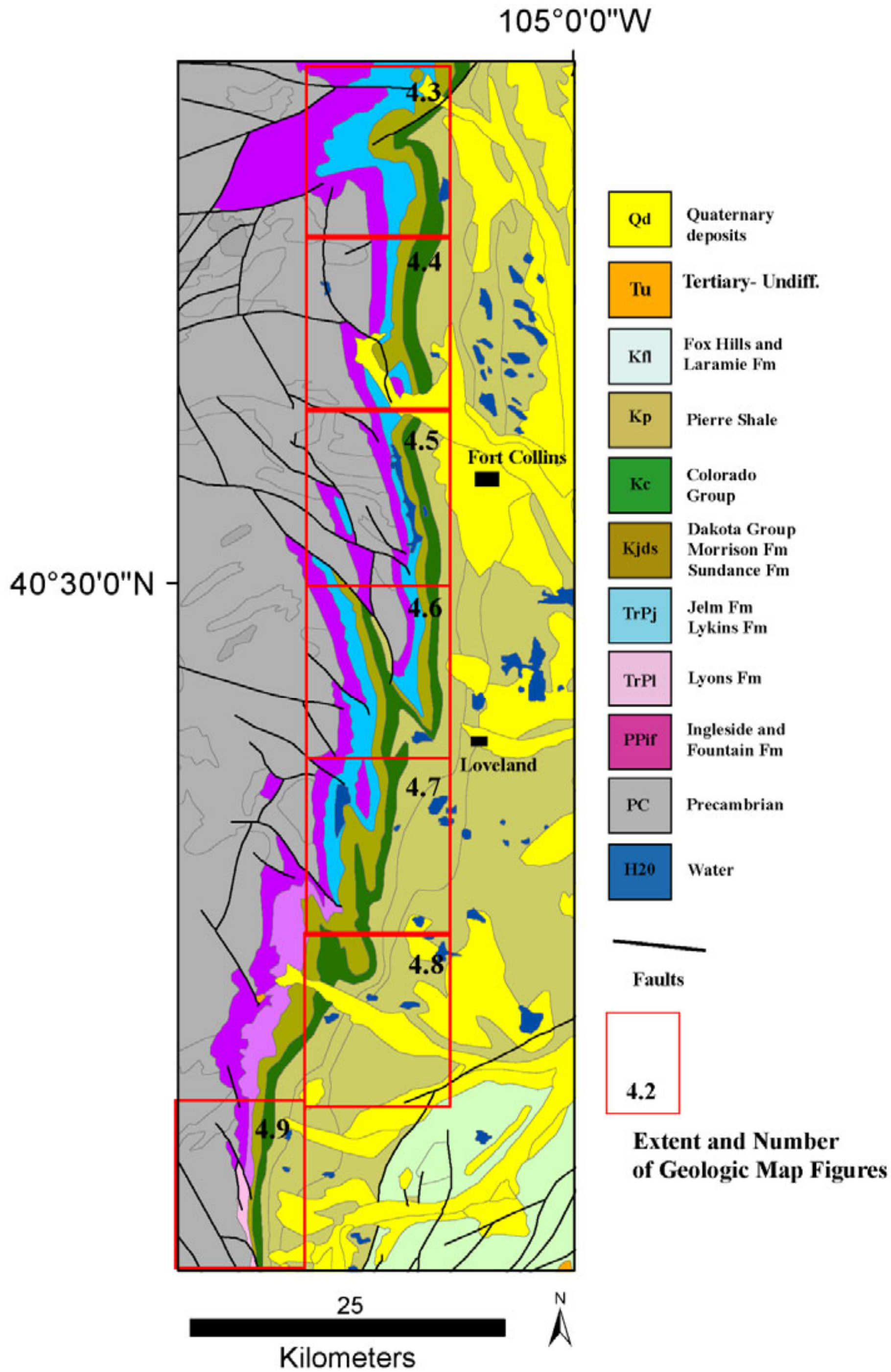

Figure 4.2. Simplified bedrock geologic map of the northeastern Front Range. Red boxes show the extent of larger-scale geologic maps. Figure adapted from Tweto (1979) and Brandt et al. (2003a, 2003b).

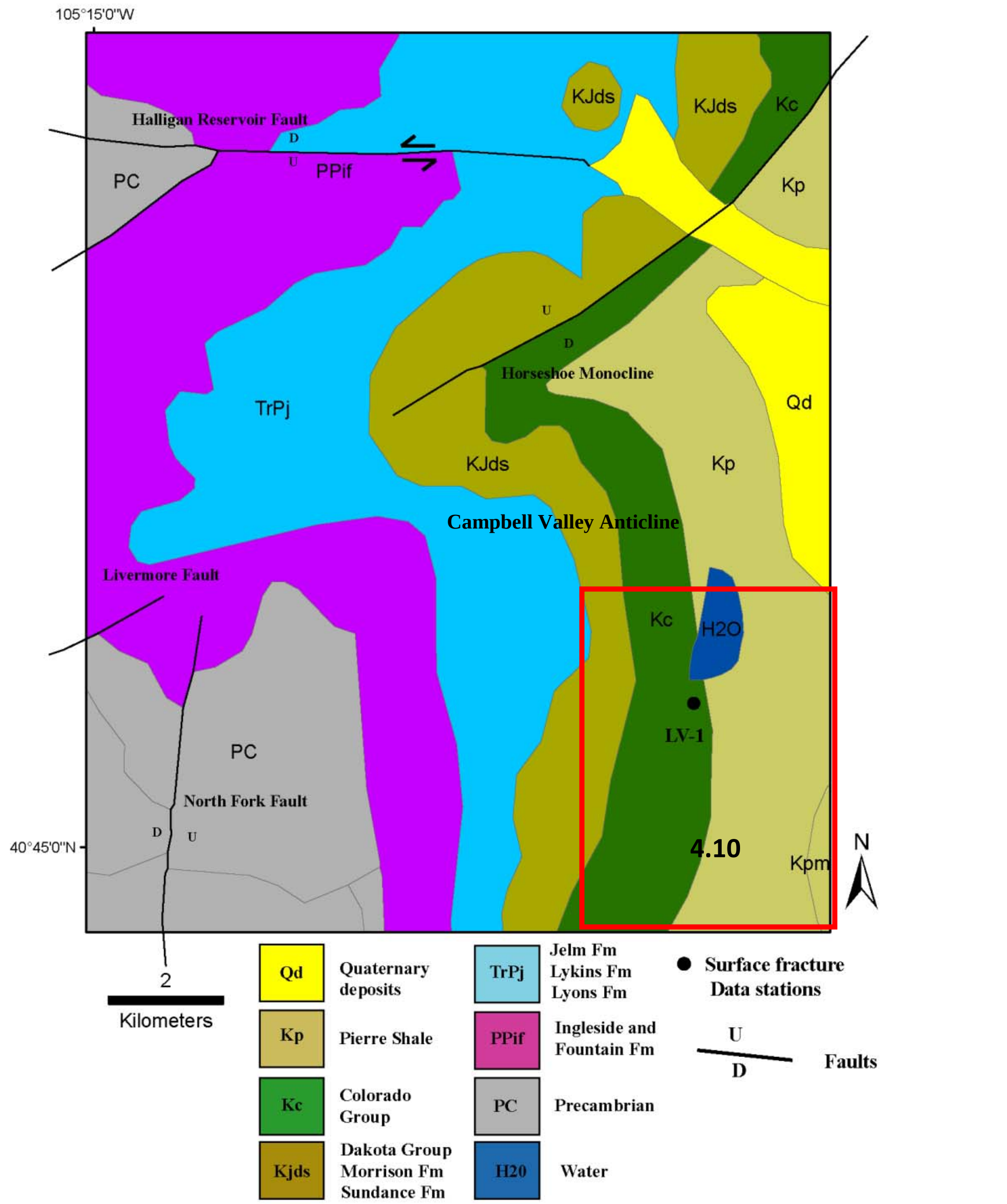

Figure 4.3. Bedrock geologic map of the Livermore Quadrangle with station locations and more detailed maps located as a red box. Adapted from Brandt et al. (2003a).

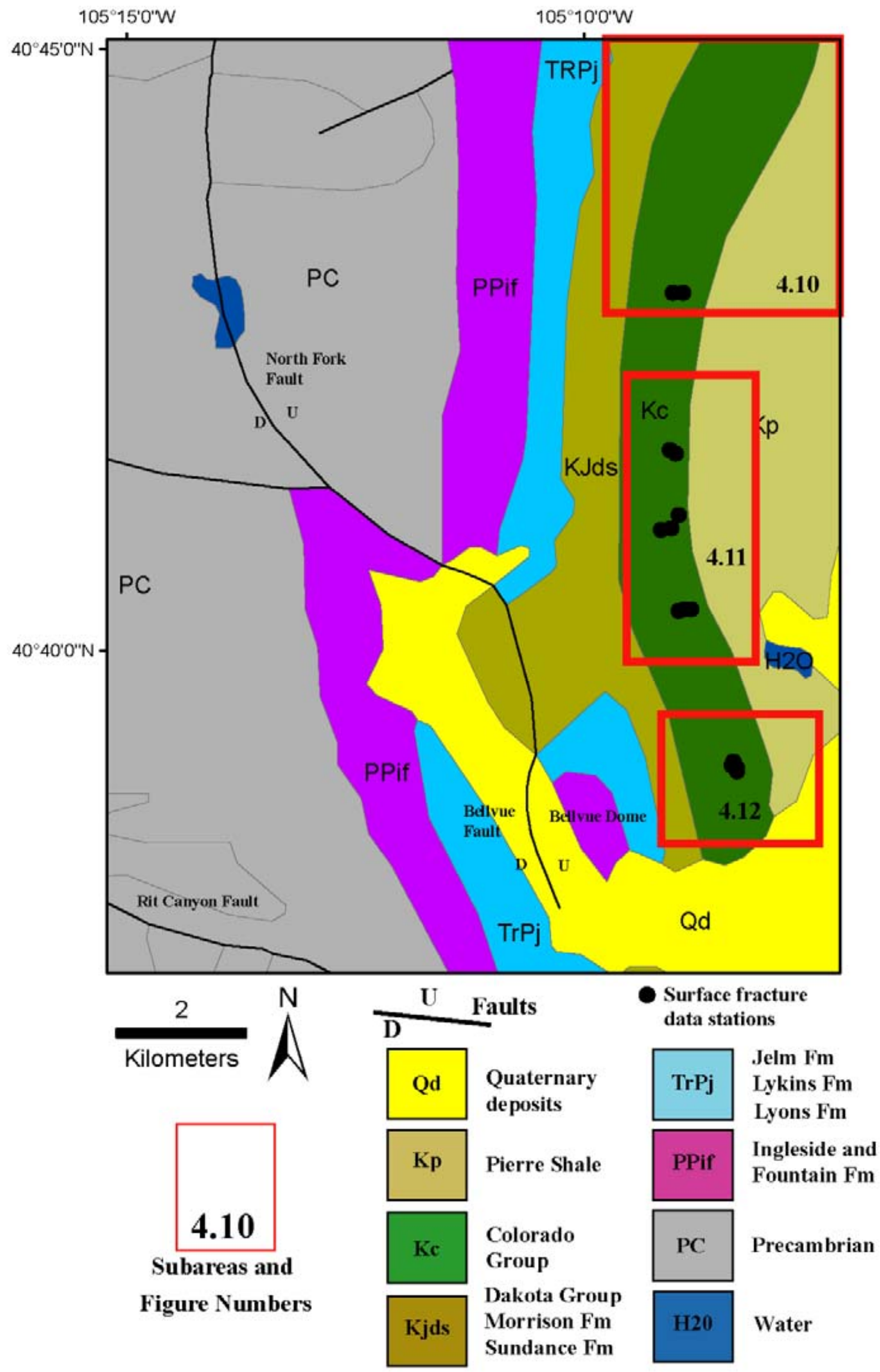

Figure 4.4. Bedrock geologic map of the Laporte Quadrangle with station locations and more detailed maps located as red boxes. Adapted from Brandt et al. (2003a), and Braddock et al. (1988c).

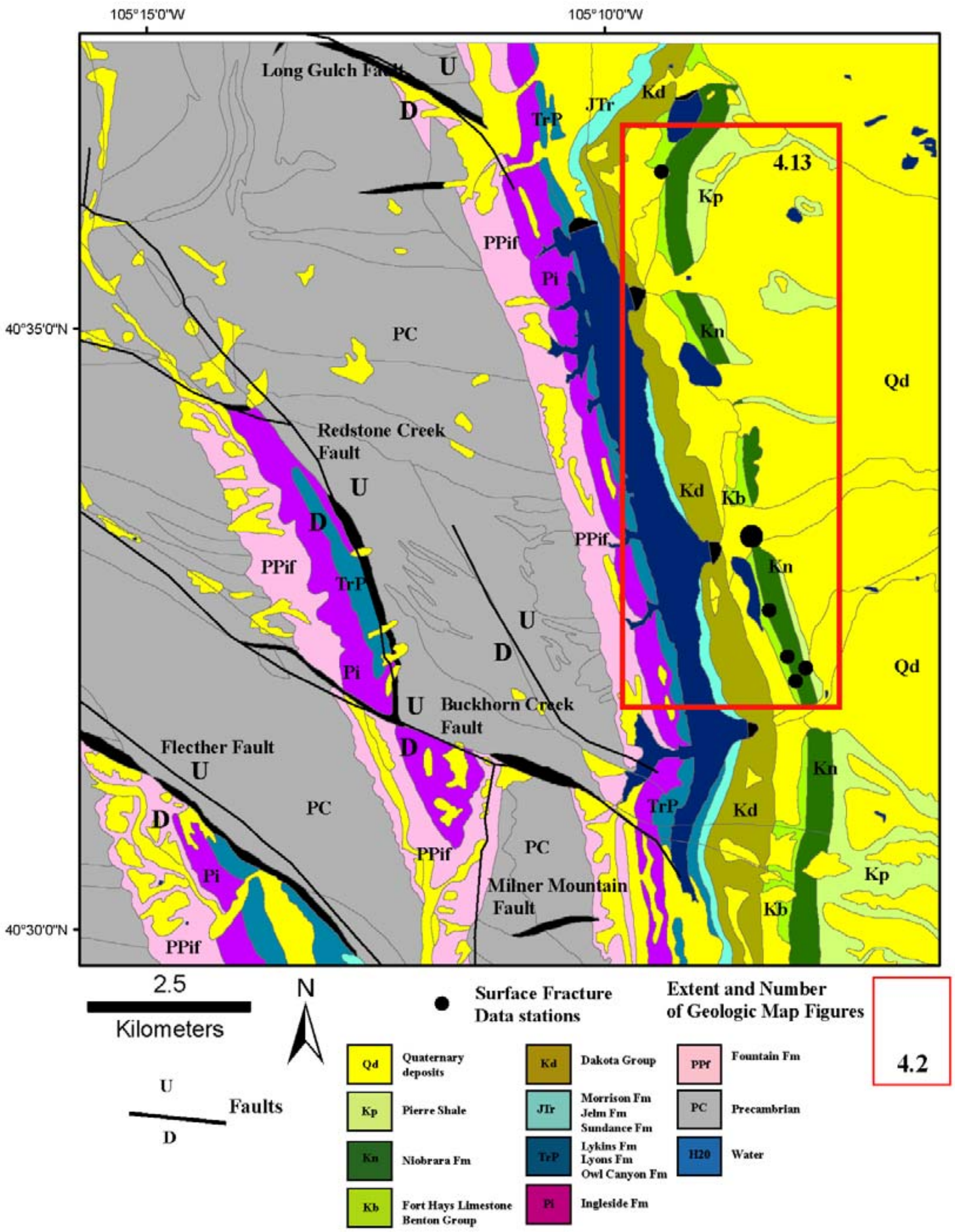

Figure 4.5. Bedrock geologic map of the Horsetooth Reservoir Quadrangle with station locations and more detailed maps located as a red box. Adapted from Brandt et al., (2003a), and Braddock et al. (1988a).

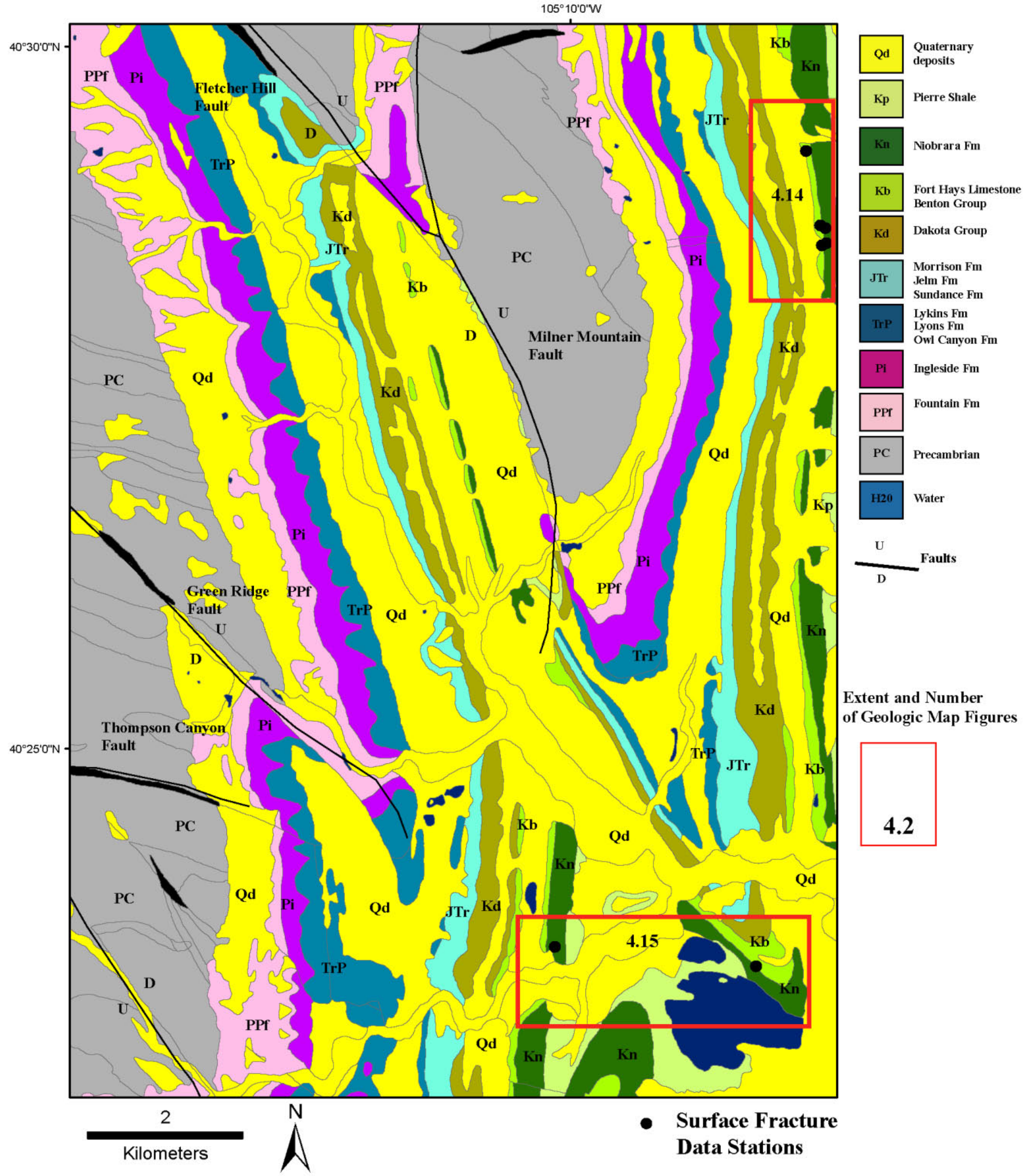

Figure 4.6. Bedrock geologic map of the Masonville Quadrangle with station locations and more detailed maps located in red boxes. Adapted from Brandt et al. (2003) and Braddock et al. (1970).

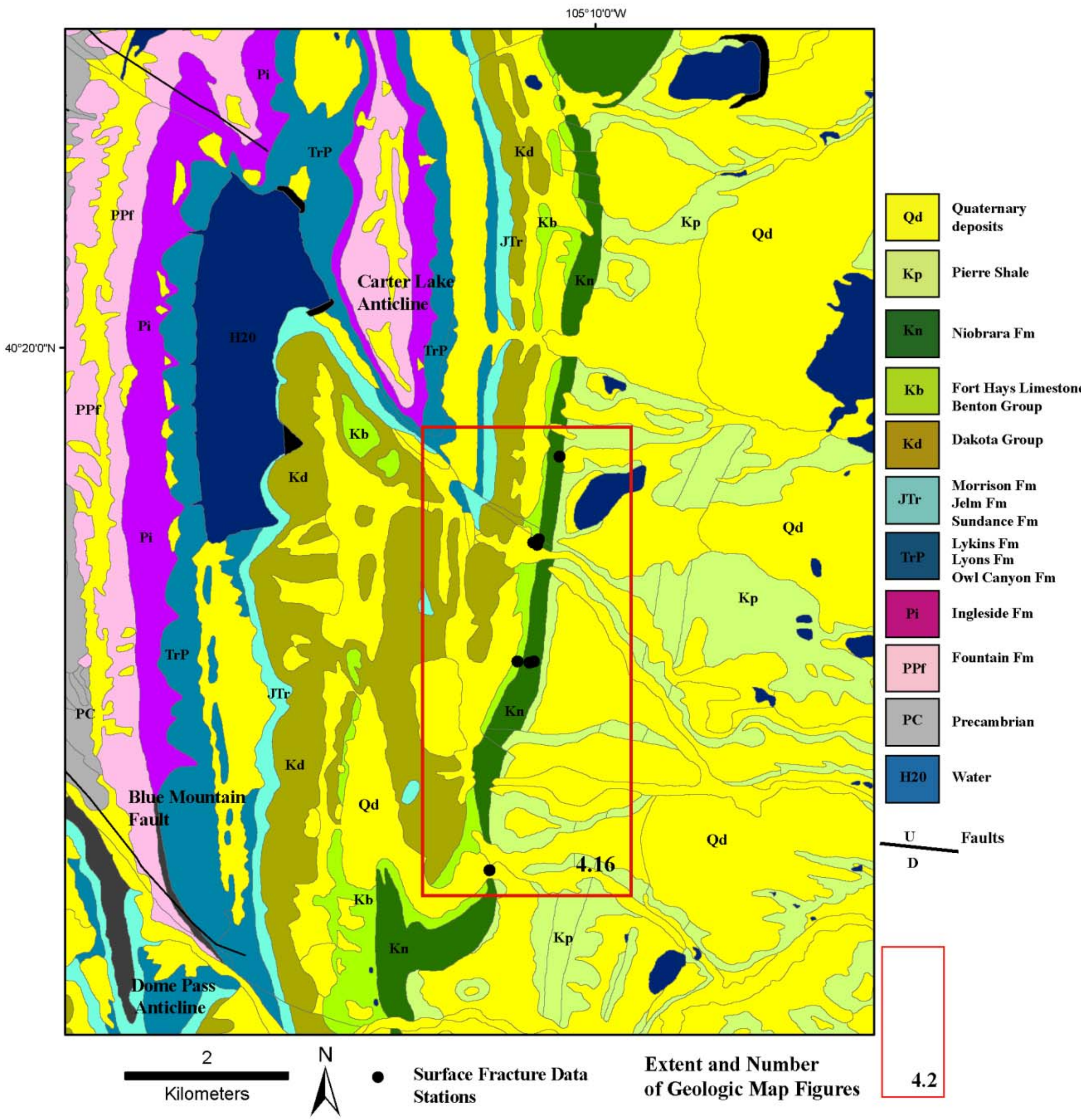

Figure 4.7. Bedrock geologic map of the Carter Lake Reservoir Quadrangle with station locations and more detailed maps located by a red box. Adapted from Brandt et al. (2003) and Braddock et al. (1988).

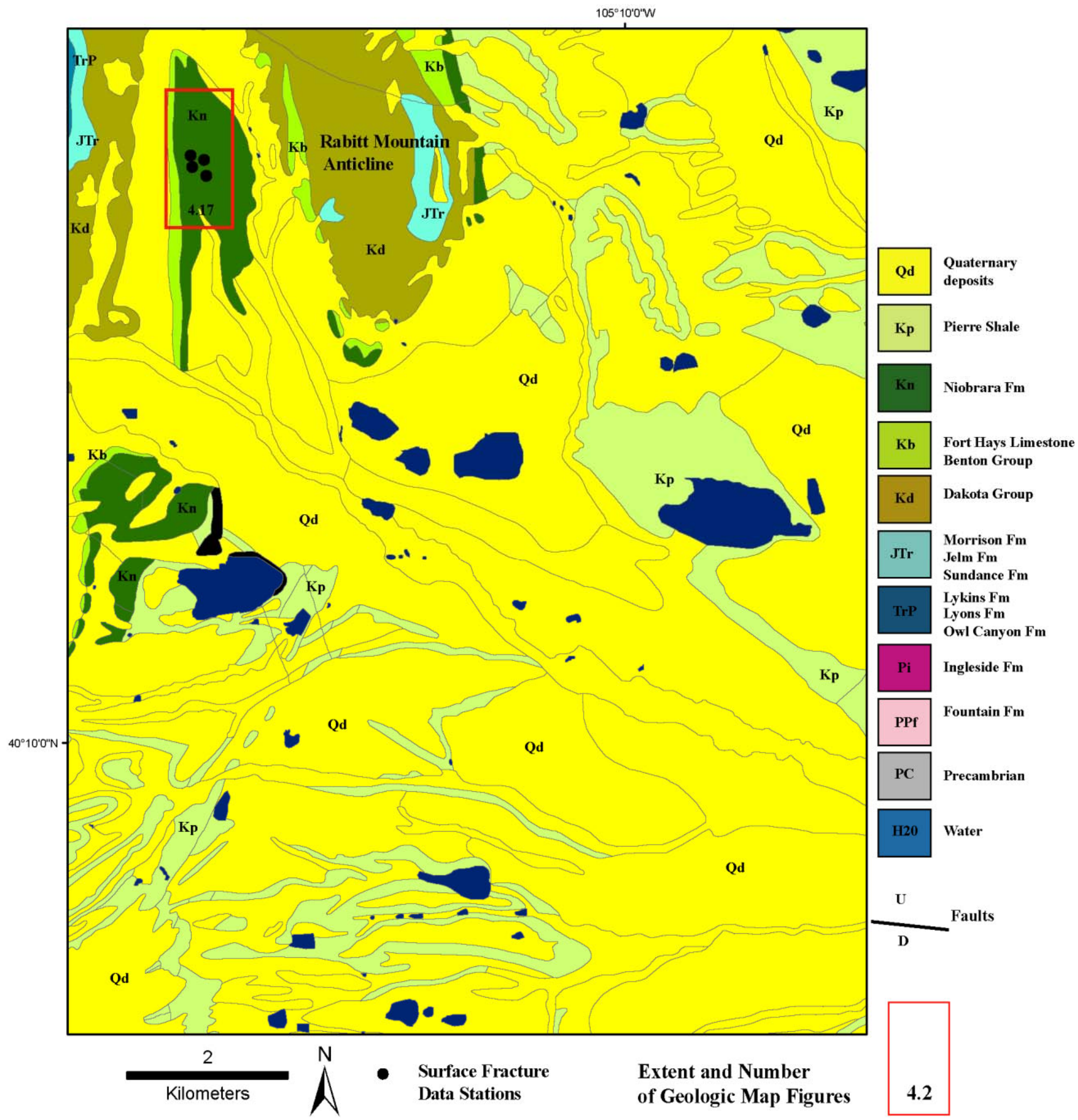

Figure 4.8. Bedrock geologic map of the Hygiene Quadrangle with station locations and more detailed maps located as a red box. Adapted from Brandt et al. (2003), and Madole et al. (1998).

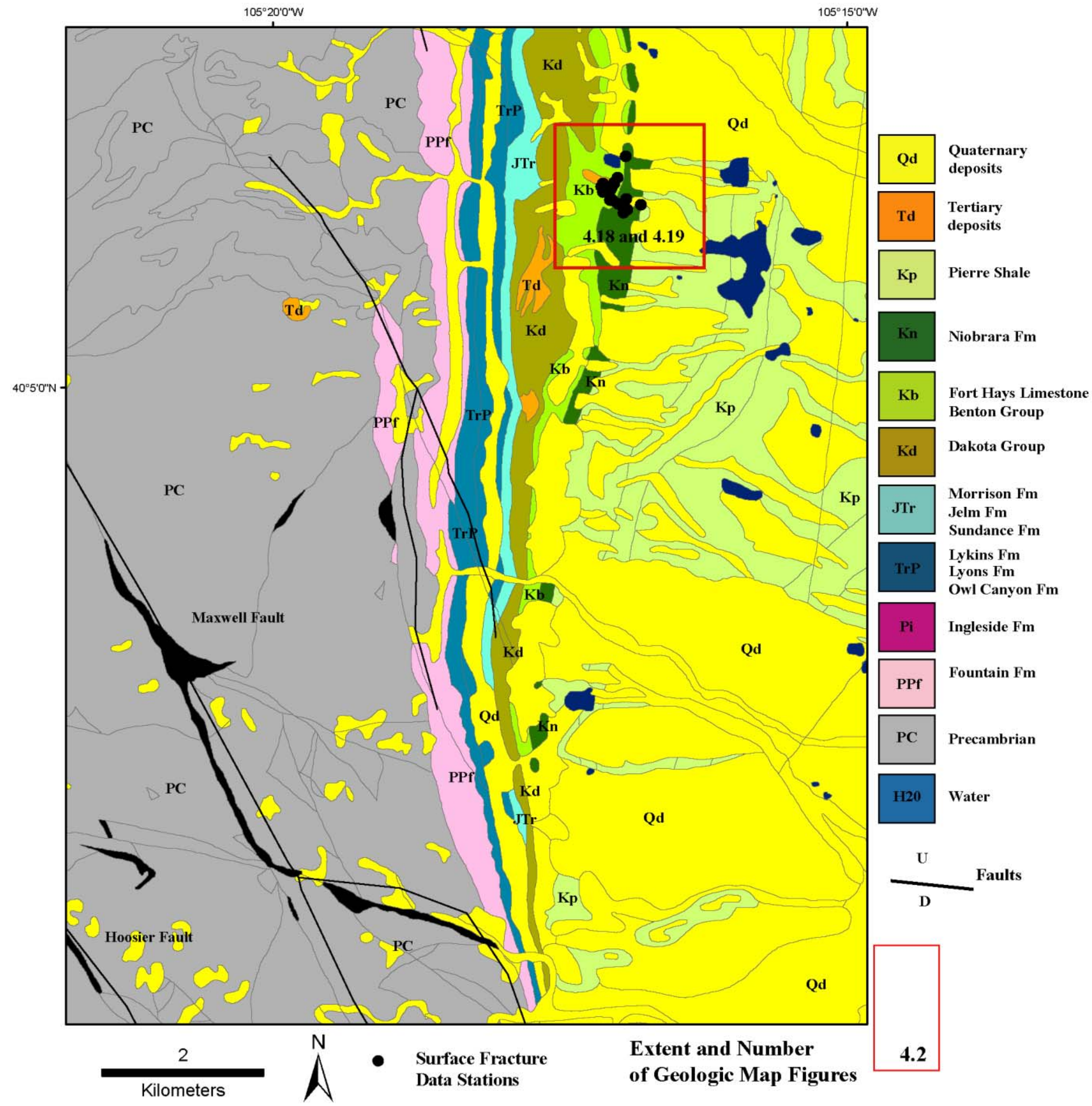

Figure 4.9. Bedrock geologic map of the Boulder Quadrangle with station locations and more detailed maps located as red boxes. Adapted from Brandt et al (2003) and Wrucke and Wilson (1957).

Livermore Quadrangle:

The Livermore Quadrangle's southeastern corner marks the northern extent of the study area (Fig 4.3). Recent geologic studies conducted in the area include Matthews and Sherman's (1976) cross-sections and 3D interpretations of variable striking monoclinal folds, Braddock et al. (1988) surface geologic mapping, and Larson's (2009) minor fault and fracture investigations of syn-Laramide strata. Larson (2009) collected fracture data just north of the study area along the Horseshoe Monocline and the Campbell Valley Anticline on the eastern side of the Livermore Quadrangle. Larson (2009) documented extensive E-W and NNW-trending Laramide minor faults in early Cretaceous strata with an average σ_1 trend of 101°.

One station of fracture data (LV-1) was collected at a road cut exposure of the Niobrara Formation where bedding dips 10° to ENE (Fig. 4.10a, 4.10b). Fractures are vertical to subvertical and have a trimodal distribution of orientations. No evidence of minor faulting was observed at this station. Cross-cutting relationships suggest that ENE-trending fractures are the earliest fractures present, with an average strike of 82°. These fractures are perpendicular to bedding strikes and are faced with calcite crystal growth with no observable shearing, and with no conjugate pairings. The NNE and NNW-trending fractures abut into ENE-fracture sets unless entirely calcite healed, allowing continued fracture propagation. Relative timing relationships are indistinguishable between the NNE and NNW-fracture systems. The average orientation of these fractures is 173°.

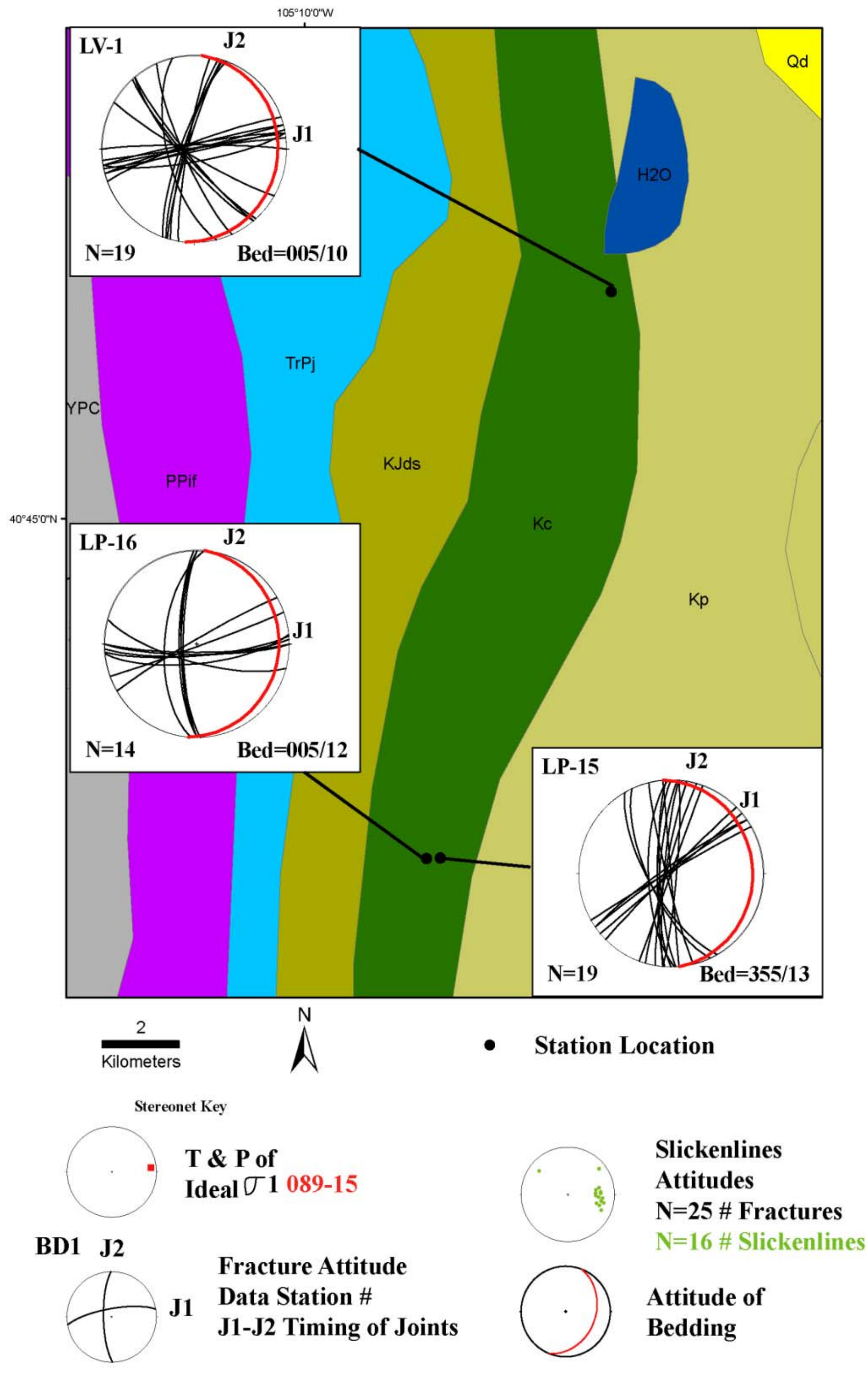

Figure 4.10a. Stereonets of fracture planes, slickenlines and the best fit ideal σ_1 axis measured in the southeastern Livermore quadrangle and northeastern Laporte quadrangle.

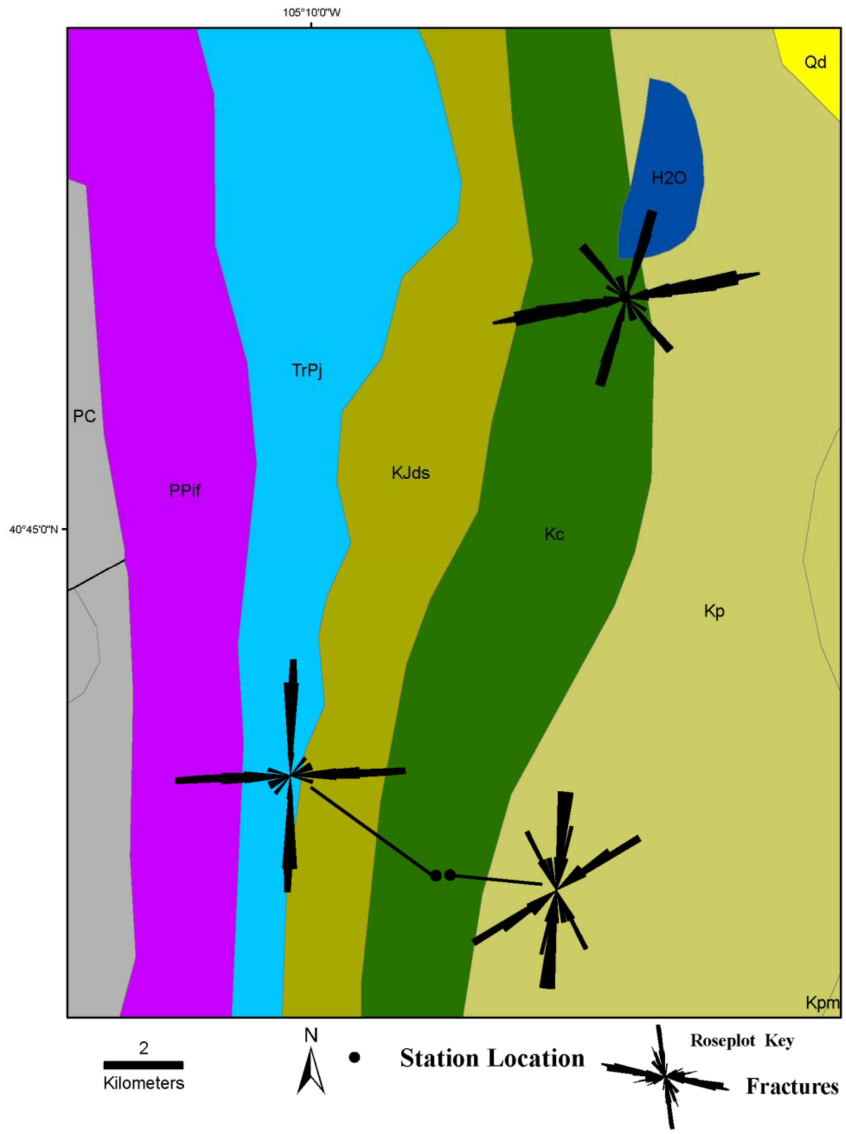

Figure 4.10b. Roseplots of fracture strikes measured in the southeastern Livermore and northeastern Laporte quadrangles.

Though ENE-trending fractures showed no observable offset, they are oriented 19° away from average Laramide σ_1 trends (101°) of the area calculated by Larson (2009) in the Dakota Group. ENE-trending fractures are either mode one splitting fractures from slightly deviated Laramide stress fields in the Niobrara Formation, or mode two Laramide shear fractures which are later reactivated by regional extension or uplift. Since no conjugate pair fractures or minor faults were identified at LV-1 in the Niobrara Formation, ENE-trending fractures are inferred to be J_1 joints. NNE and NNW-fractures are incompatible with ESE-oriented σ_1 trends calculated by Larson (2009), and abutting relationships suggest these fractures are probably related to post-Laramide tectonic processes and are identified as J_2 joints.

Laporte Quadrangle

The Laporte quadrangle contains 16 fracture data stations primarily located within the Carlile Shale, Fort Hays Limestone and the Niobrara Formation on the east side of the Laporte Quadrangle (Fig. 4.4). All stations are located within the inactive Holnam Quarry where bedding dips of the Niobrara Formation range between 15 and 20° to the east. Exposures include road cuts and water canals where the mine has not been reclaimed. Due to station proximity the eastern Laporte Quadrangle fracture data is subdivided into north, central and south subareas.

The north subarea of the Livermore quadrangle shows Permian to Cretaceous strata that shallow in dip from west to east. Early to late Cretaceous strata strike NNE and dip ESE- 10-15° (Fig. 4.10a). Due west of the study area, fracture investigations by Larson (2009) in the N-striking Dakota Group showed faulting was dominantly thrusting, with slickenline and σ_1 axes trending nearly due east (89°). Larson (2009) also identified perpendicular-to-bedding J_1 joints with an average strike of 236°, and abutting J_2 joints striking 136°.

Fractures observed in the Niobrara Formation appear bimodal and trimodal in distribution, with abutting relationships indicating E-W to ENE- trending fractures are older than N-striking fractures (Figs. 4.10a, 4.10b). Fractures observed at station LP-16 show ENE and ESE-fractures are probably conjugate strike-slip minor faults bisected by E-W trending J_1 joints, but no slickenlines or offsets were observed. The average strike for these fractures is 87°. These orientations are consistent with local Laramide ideal σ_1 trends (89°) recorded by Larson (2009) from minor fault data collected in the Dakota Group. Younger fractures (J_2) identified at station LP-16 strike on average 180°. Fractures collected at station LP-15 show NE-trending fractures strike on average 233° and are older than N-striking facture sets (J_2). J_2 joints at station LP-15 strike on average 356°. J_1 joints in the Niobrara Formation at station LP -15 parallel local J_1 orientations observed by Larson (2009) in the Dakota Group.

The central subarea of the Livermore quadrangle consists of Permian to Cretaceous strata striking north with eastward dips ranging from 10 to 25° before being truncated and folded south of the North Fork Fault. Fractures observed within the Niobrara Formation become continually more consistent to the south where cross cutting relationships indicate NNW-trending J_2 abut against NE-striking J_1 joint sets (Fig 4.11a, 4.11b). The average J_1 joint strike is 245°, with J_2 joints striking 160° for the subarea. Fracture orientations are consistent between the Carlile Shale and Niobrara Formations except at station LP-13. No minor faults were observed in this subarea. Both J_1 and J_2 orientations are comparable to joint observations made by Larson (2009) west of the study area in the Dakota Group.

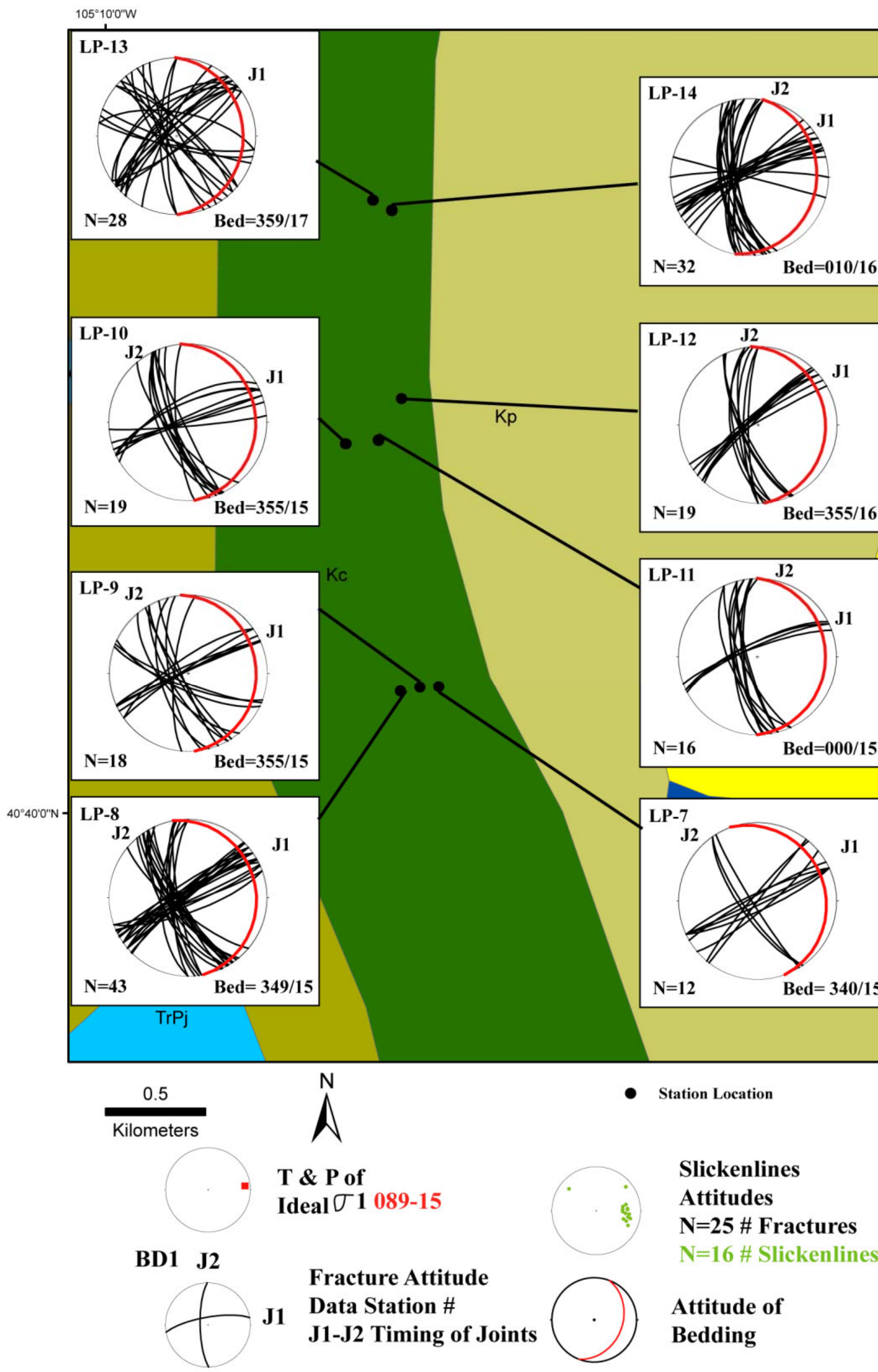

Figure 4.11a. Stereonets of fracture planes measured in the central subarea of the eastern Laporte Quadrangle.

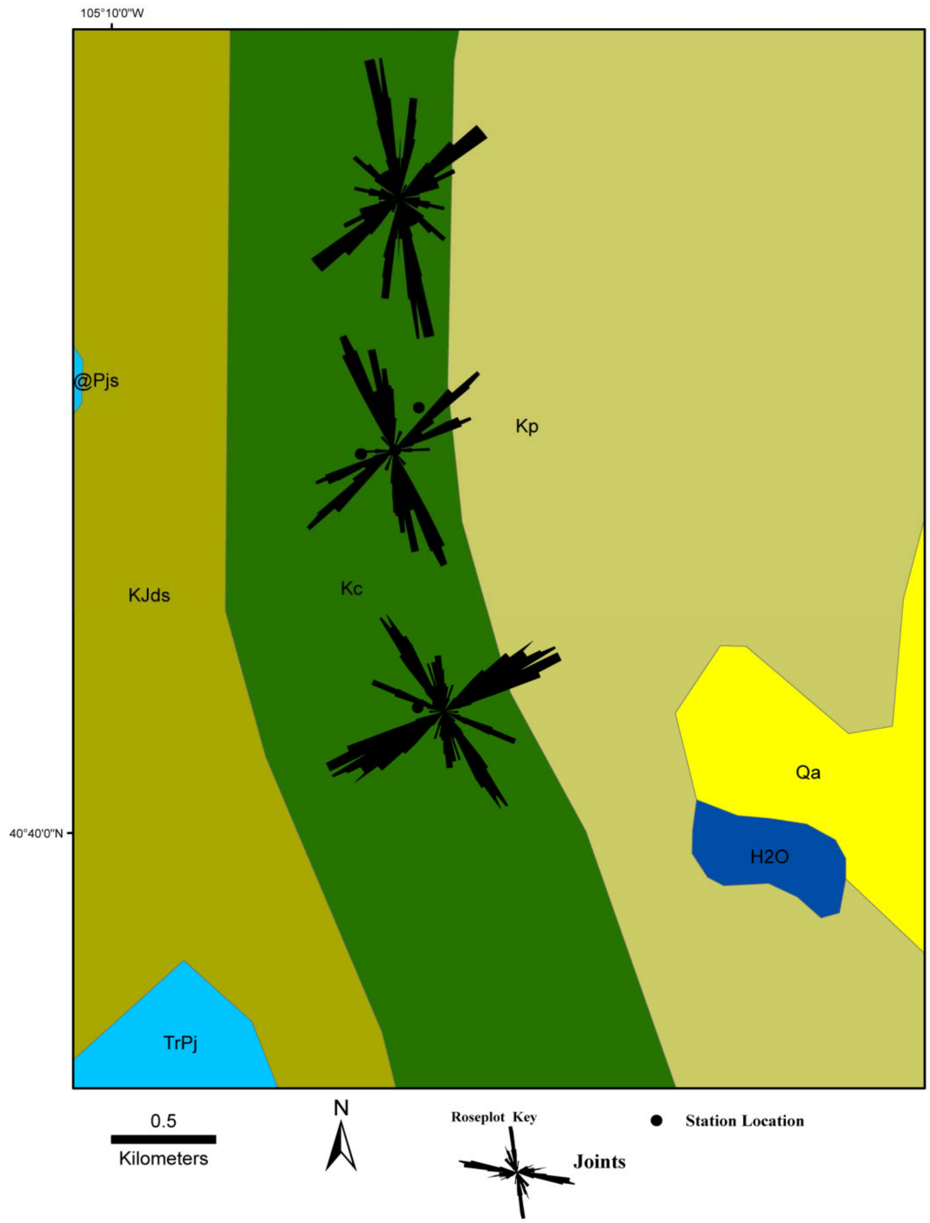

Figure 4.11b. Roseplots of fracture strikes measured in the central subarea of the Laporte quadrangle.

The southern subarea consists of a large 20° eastward-dipping panel of the Fort Hays Limestone overlain by the lower Niobrara Formation exposed by previous mining activity. West of the subarea is the ENE-dipping Bellvue Fault that bounds the western Bellvue syncline and Bellvue Dome, and abuts against the North Fork Fault to the north. Minor fault data collected by Larson (2009) documented synthetic minor thrusts in the footwall of the Bellvue Fault with ideal σ_1 axes trending 76°. Fracture data collected in the Fort Hays Limestone and lower members of the Niobrara Formation showed weakly trimodal distributions (Fig. 4.12a, 4.12b). ENE and ESE-striking calcite filled fractures observed at station LP-1 showed right-lateral and left-lateral offsets respectively, though no slickenlines were identified. Vertical solution stylolites identified at station LP-1 strike N-S with average poles trending 086° with a 19° plunge. The poles of stylolites bisect conjugate fractures observed at station LP-1. N-striking fractures abut both fault orientations, and roughly parallel stylolite trends but do not appear related (Fig. 4.12b). Fracture observations along the lower Niobrara Formation show no clear minor faulting, but have fairly consistent J_1 and J_2 joint strikes. The average J_1 strike is 74° and the average J_2 strike is 178°.

Conjugate fractures and stylolite poles appear compatible with Laramide ideal σ_1 axes of 89° north of the study area, but are oblique to 76° trending ideal σ_1 axes calculated from thrusts in the footwall of the Bellvue Fault by Larson (2009). J_1 orientations observed along the Niobrara Formation east of the Bellvue fault parallel ideal σ_1 axes calculated at the Bellevue Fault by Larson (2009) with an average trend of 74°. This is either a striking coincidence, or evidence of multiple stress axes locally affecting fracturing in the Niobrara Formation. Larson (2009) hypothesized from observations of

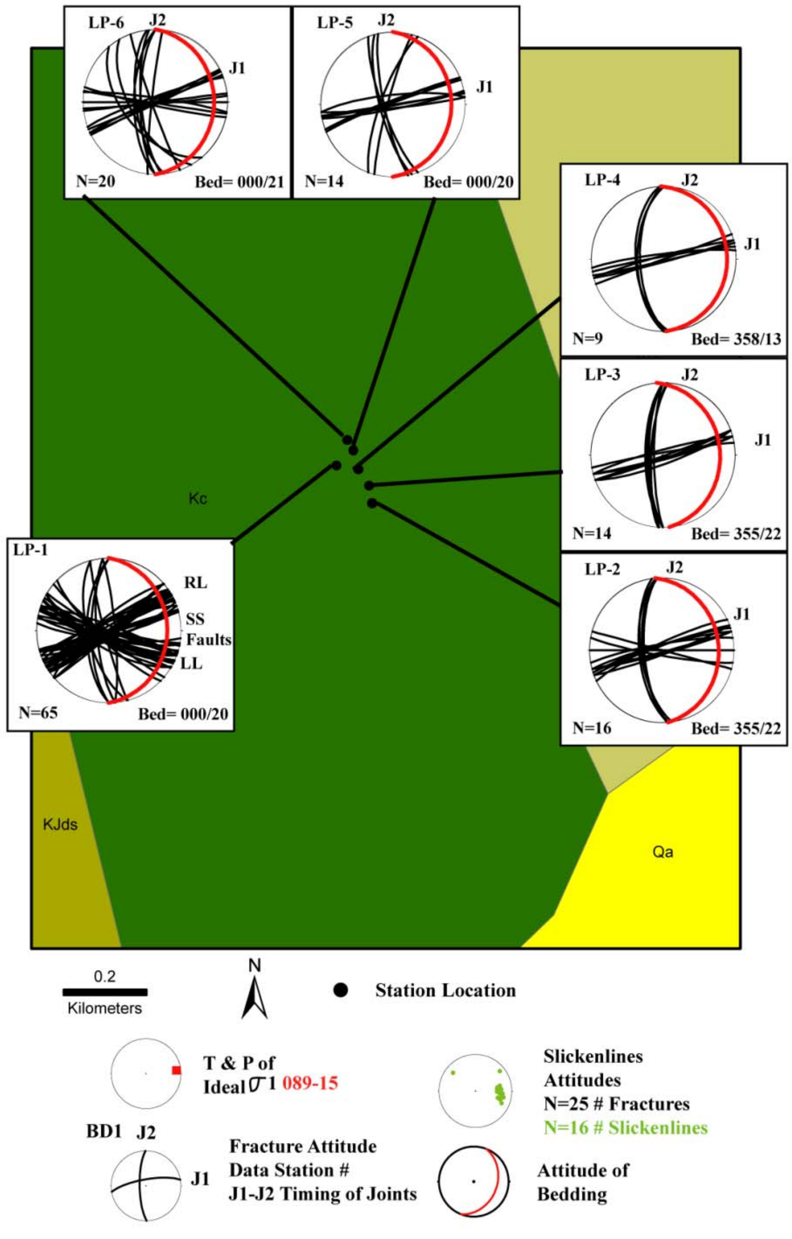

Figure 4.12a. Stereonets of fracture planes measured in the southeastern Laporte quadrangle.

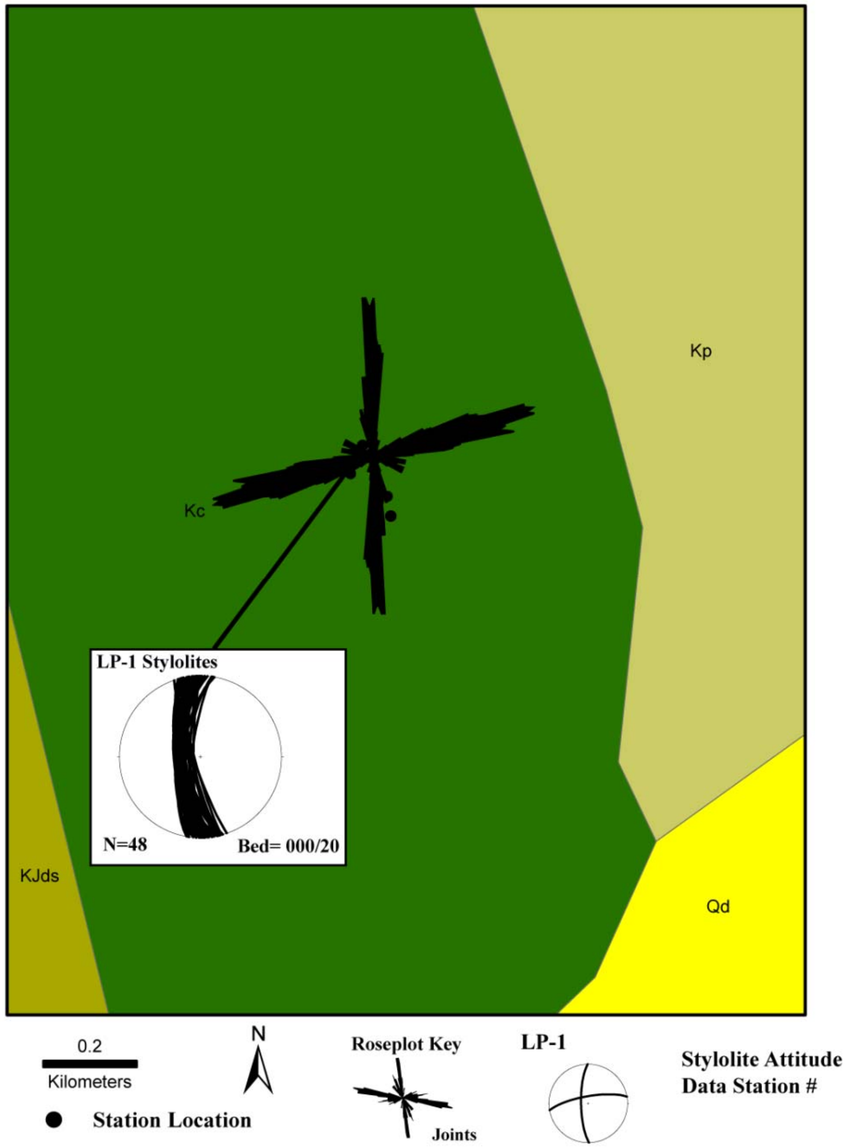

Figure 4.12b. Roseplots of fracture strikes and stereonets of stylolite planes measured in the southeastern Laporte quadrangle.

master joints cross-cutting minor thrust faults, and the abrupt loss of slip on the Bellvue Fault between the Bellvue dome and syncline is likely due to the interaction of multiple deformation modes. Fracture data collected in the southern subarea in the Niobrara Formation supports this hypothesis. J_2 fracture orientations in the southern subarea are remarkably consistent with high first eigenvalues. Analysis of J_2 eigenvalues show consistently higher first eigenvalues than J_1 joints sets. This suggests that some J_1 joints are faults and also suggests that J_2 joints are not cross-joints, which would be typically associated with uplift.

Horsetooth Reservoir Quadrangle

The Horsetooth Reservoir Quadrangle has been the focus of substantial research into local Laramide kinematics and structural analyses from several different stratigraphic units (Prucha et al., 1965; Erslev and Rogers, 1993; Erslev and Gregson, 1996; Holdaway, 1998; Erslev et al., 2004, Erslev and Larson, 2004; Larson, 2009).

Prucha et al. (1965) investigated geometries of faults and adjacent structures southwest of the study area, in particular the triangle syncline immediately south of the Buckhorn Creek Fault and west of the Milner Mountain Fault. Prucha et al. (1965) concluded that the local complexity could not be explained by regional horizontal compression. However, horizontal compression is seen in minor fault studies throughout the entire quadrangle. Erslev and Gregson (1996) utilized kinematic analyses of minor fault data to test hypotheses of Laramide deformation in the northeastern Front Range. Erslev and Gregson (1996) documented unidirectional, horizontal shortening oriented approximately 080° in the Horsetooth Reservoir area. Similar methods employed by Holdaway (1998) identified faults in Permian to Lower Cretaceous rocks and documented horizontal shortening oriented approximately 073° in the Horsetooth Reservoir area with regional Laramide stress and strain oriented 79° . Erslev and Larson (2006) found minor faults were dominantly thrusts which strike subparallel to the Buckhorn Creek Fault with σ_1 trends varying from NE to ENE. Master and cross joints observed by Erslev and Larson (2006) cross-cut minor thrusts and master joint strikes were consistently deviated 10° -15° from ideal σ1 trends. Larson (2009) noted that strike-slip minor faults and conjugate NE and ENE-striking fractures in the southern Horsetooth Reservoir area had identical trends and suggested that NE and ENE-striking fractures in the Dakota Group are strike-slip minor faults.

The Niobrara Formation dips 15° to 20° ENE throughout the Horsetooth Reservoir Quadrangle and overlies the low relief hogback of Fort Hays Limestone. Fracture data was taken from road cuts primarily within the Fort Hays Limestone, as much of the Niobrara Formation is poorly exposed (Fig. 4.13a). At station HT-1, conjugate fracture trends are nearly identical to strike-slip faults observed by Larson (2009) in the Dakota Group, though no slickenlines were observed. The observed fractures are likely strike-slip faults reactivated in tension during regional uplift.

Average J_1 trends for this subarea observed at station HT-2 through HT-5 are 236°. Average Laramide ideal σ_1 trends of 80° calculated by previous workers are 33° clockwise from average J_1 trends observed at these station in the Niobrara Formation. HT-6 shows a J_1 orientation that is parallel to Erslev and Larson's (2006) calculated Laramide stress axes of the area at 78°. J_2 orientations vary slightly from N to NW and appear roughly parallel to bedding strike of the Niobrara Formation, and nearly perpendicular to ideal σ_1 trends identified by Holdaway (1998) and Erslev and Larson (2006) (Figs. 4.13a, 4.13b).

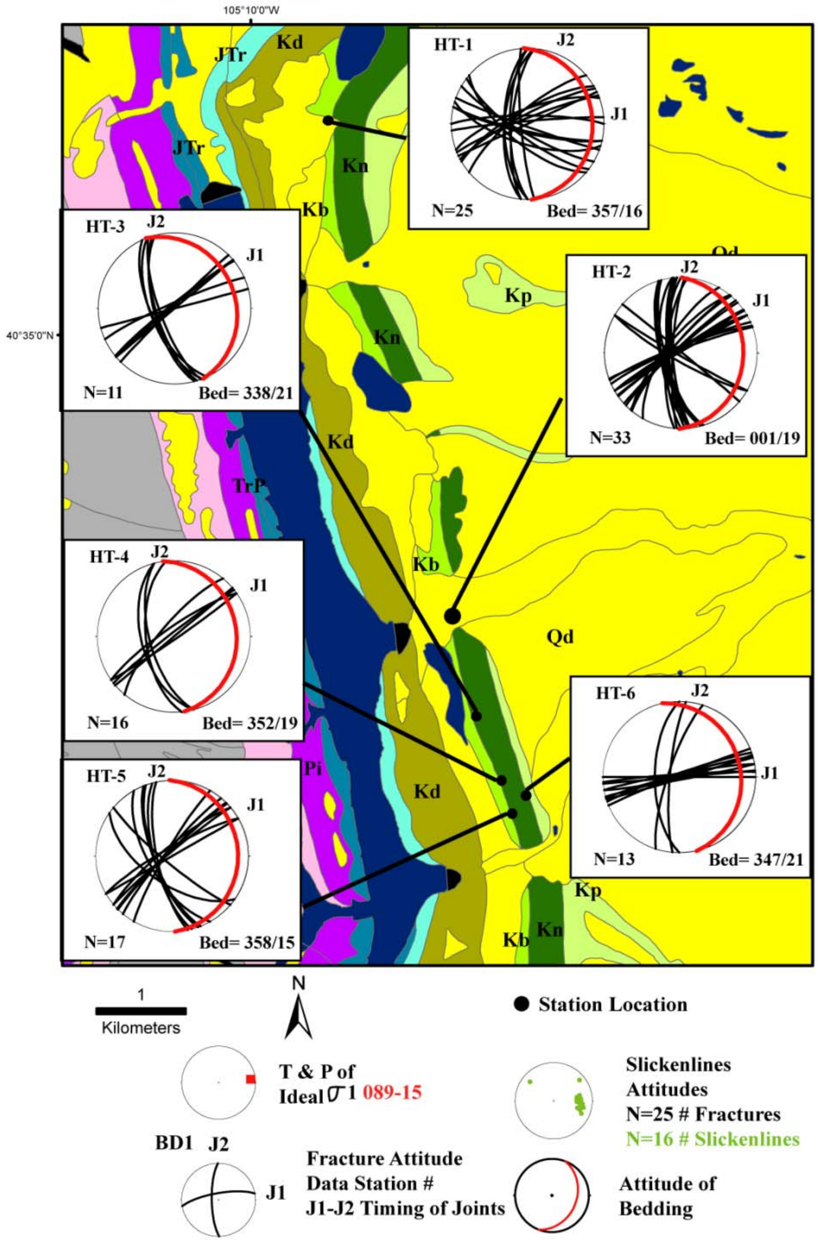

Figure 4.13a. Stereonets of fracture planes measured in the Horsetooth Reservoir quadrangle.

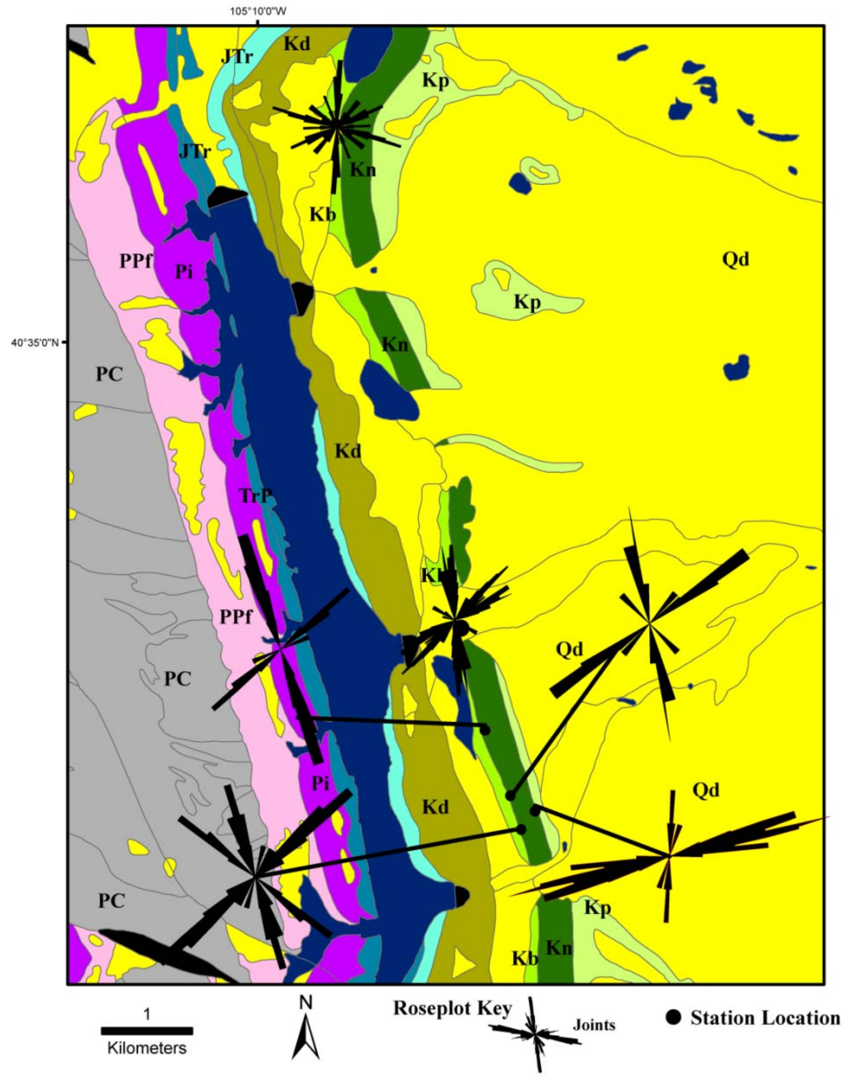

Figure 4.13b. Roseplots of fracture strikes measured in the Horsetooth Reservoir quadrangle.

Conjugate fractures that parallel strike-slip faults in the Dakota Group and ENE-striking J_1 joints observed at HT-6 show Laramide stresses have acted on the Niobrara Formation. However the majority of fractures result from a slightly deviated Laramide stress field as evidenced by J_1 joints in stations HT-2 through HT-5, and by post-Laramide extension as evidenced by the remarkably consistent NNW-striking J_2 joints.

Masonville Quadrangle

The Masonville Quadrangle has also received considerable attention to structural deformation styles occurring along the northeastern Front Range due to its accessibility to academic institutions and the Denver petroleum industry. Early structural interpretations in the area by Ziegler (1917) based on field geometries were initially discounted by advocates of vertical tectonics, but have since been verified as the primary importance of horizontal shortening and compression during the Laramide Orogeny (Erslev et al., 2004).

The Milner Mountain Anticline is the largest structure in the study area. Geologic maps of the region by Braddock et al. (1970) show planar basement contacts offset by faults with minimal folding in the vicinity of these faults. Erslev and Rodgers (1993) observed that these faults in strata surrounding Milner Mountain progressively lose displacement upward in sedimentary strata. Erslev and Rodgers (1993) trenched these faults and showed fault dips 20-70° NE, consistent with earlier interpretation by Ziegler (1917). These fault dip and displacement observations led Erslev and Rodgers (1993) to conclude that Milner Mountain was the result of fault-propagation folding on NW-striking faults.

Much of the structural studies conducted through the Masonville Quadrangle have since focused on minor faults occurring within Permian to lower Cretaceous rocks. Minor fault investigations by Holdaway (1998) on the east flank of the Milner Mountain showed dominantly conjugate strike-slip faults with few conjugate thrusts. Ideal σ_1 analysis by Holdaway (1998) showed compression and slip directions varied between 71° and 87°, which is more easterly than previous studies to the north. Holdaway (1998) noted that some data stations did not display well-defined conjugate strike-slip faults, but instead showed a mass of near vertical faults, some with oblique-slip +\- normal motion. Fault data collected from this area, with exception of rare thrust faults, were observed to be consistent with extension parallel to the axis of the Milner Mountain, east-west near horizontal shortening indicated by data in the Dakota Group, and north-south extension shown by normal fault data from the Ingleside Formation.

Fracture studies of the Niobrara Formation require the Masonville Quadrangle to be broken into the Coyote Ridge northern subarea, which flanks the eastern backlimb of the Milner Mountain Anticline, and the Boedecker Reservoir southern subarea, which is located near the southeast tip of the SE-plunging Big Thompson Anticline. Coyote Ridge is due east of Milner Mountain and exposes the upper Carlile and lower Niobrara formations in steep v-shaped valleys that cross-cut the N-striking sedimentary rocks E-W. J_1 joint sets strike 075°, with J_2 joints striking NW to NNW with an average strike of 171° (Fig. 4.14a). Bedding attitudes dip easterly 30-35°, which is about 10 degrees steeper than strata to the north. J_1 joints observed in the Niobrara Formation subparallel ideal σ_1 trends calculated by Holdaway (1998) west of the study area. Only five strike slip faults were identified in this subarea with an ideal σ_1 axes trending 82° at station MV-3 of the Lower Niobrara C Member and 58° in the Fort Hays Limestone. For the first

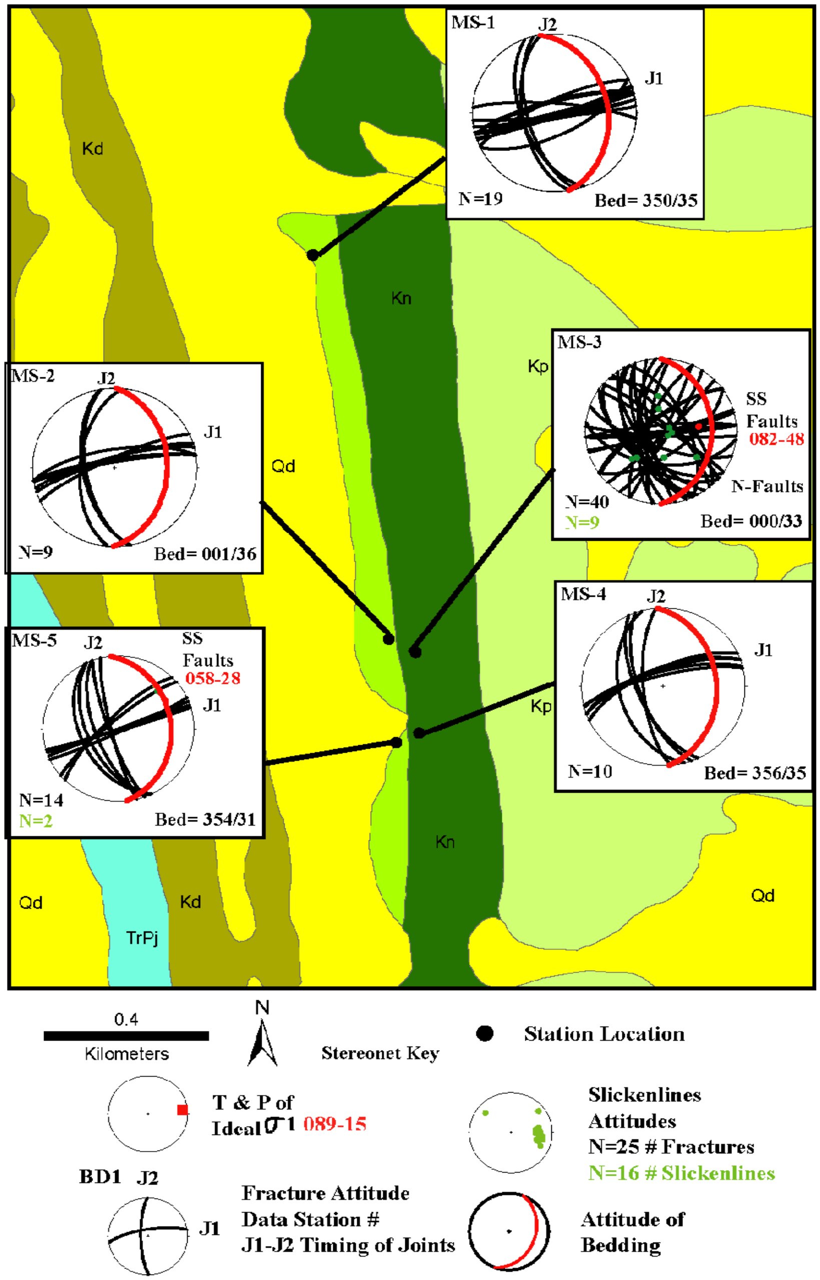

Figure 4.14a. Stereonets of fracture planes, slickenlines and the best fit ideal σ_1 axis measured in the eastern Masonville quadrangle.

time through the study area, six normal faults offset strike-slip faults and J_1 joints at station MV-3. Orientations for normal faults are quite variable, with an average strike of N68E.

No evidence of strike slip reactivation was observed at MV-3, but extensional faulting observed within the Niobrara suggests late-Laramide or post-Laramide local extension. Normal faults observed in outcrop appear to sole out into shalier sequences of the lower Niobrara C Member. Vertical displacement generally did not exceed 10-20cm and was commonly isolated between shale units in chalk marl sequences (Fig 4.14a, 4.14b).

The southern subarea of the Masonville Quadrangle includes two data stations on opposite sides of the asymmetric syncline that separates the Big Thompson Anticline from Precambrian basement to the west. Bedding attitudes steeply dip SW 60-70° in the Niobrara Formation adjacent to Boedecker Reservoir at station MV-6, and dip 10-15° ESE at station MV-7. No outcrop data was collected farther to the north and west of Milner Mountain since the Niobrara Formation forms the valley bottom to the west and is poorly exposed. Faults observed at MV-6 show normal displacement trending N36E and steeply dip to the SE.

By rotating bedding to horizontal, observed faults appear to be strike slip faults associated with outer-arc extension near a fold axis. J_1 joints strike SE, but when bedding is restored to horizontal, they strike 80°, which is subparallel to σ_1 trends identified from minor faults in the Niobrara Formation to the north and σ_1 analysis conducted by Holdaway (1998) in lower Cretaceous rocks to the north and west. No definitive evidence of timing was observed between J_1 joints and minor faults at MV-6. J_1 joints observed at station MV-7 strike E-W and are near vertical. J_2 joints abut into J_1 fractures and strike NNW. No evidence of faulting was observed at MV-7 (Fig. 4.15).

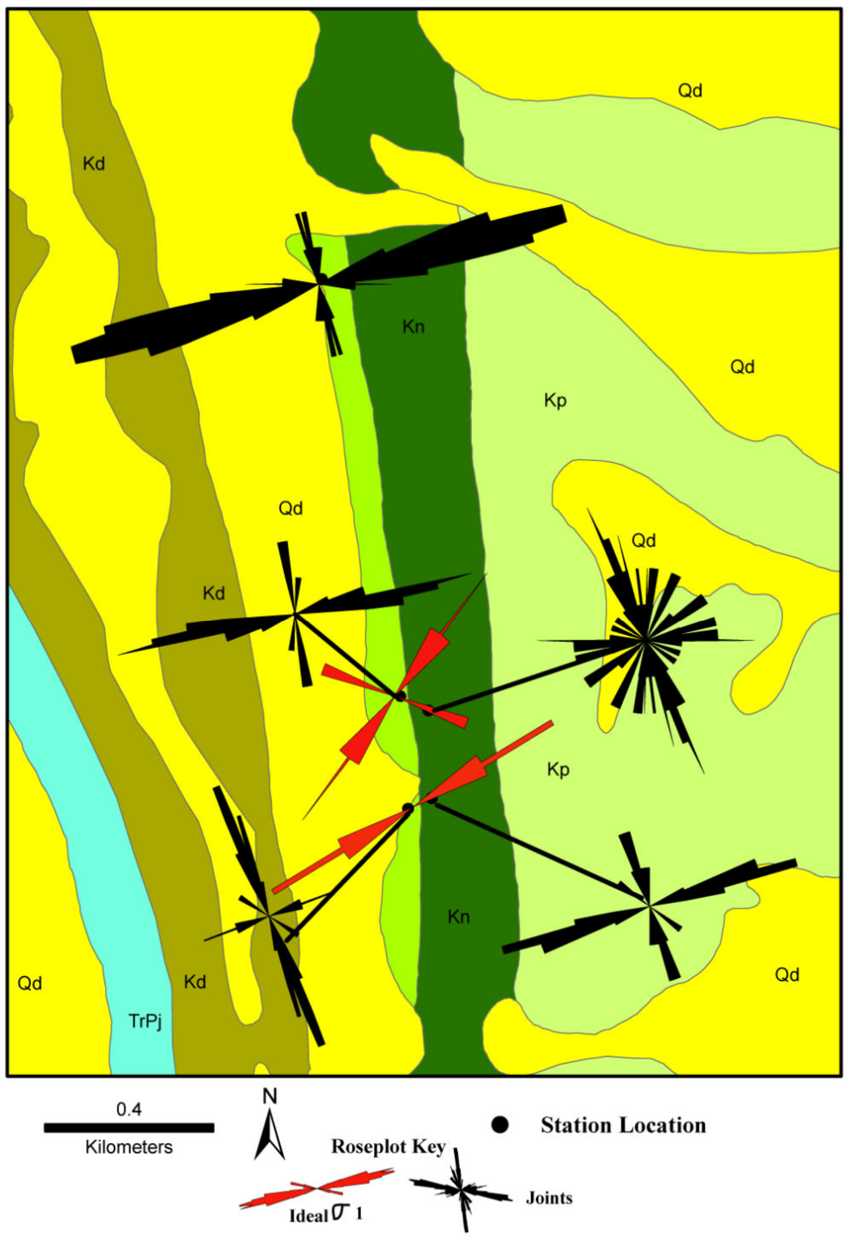

Figure 4.14b. Roseplots of fracture strikes and ideal σ_1 trends measured in the eastern Masonville quadrangle.

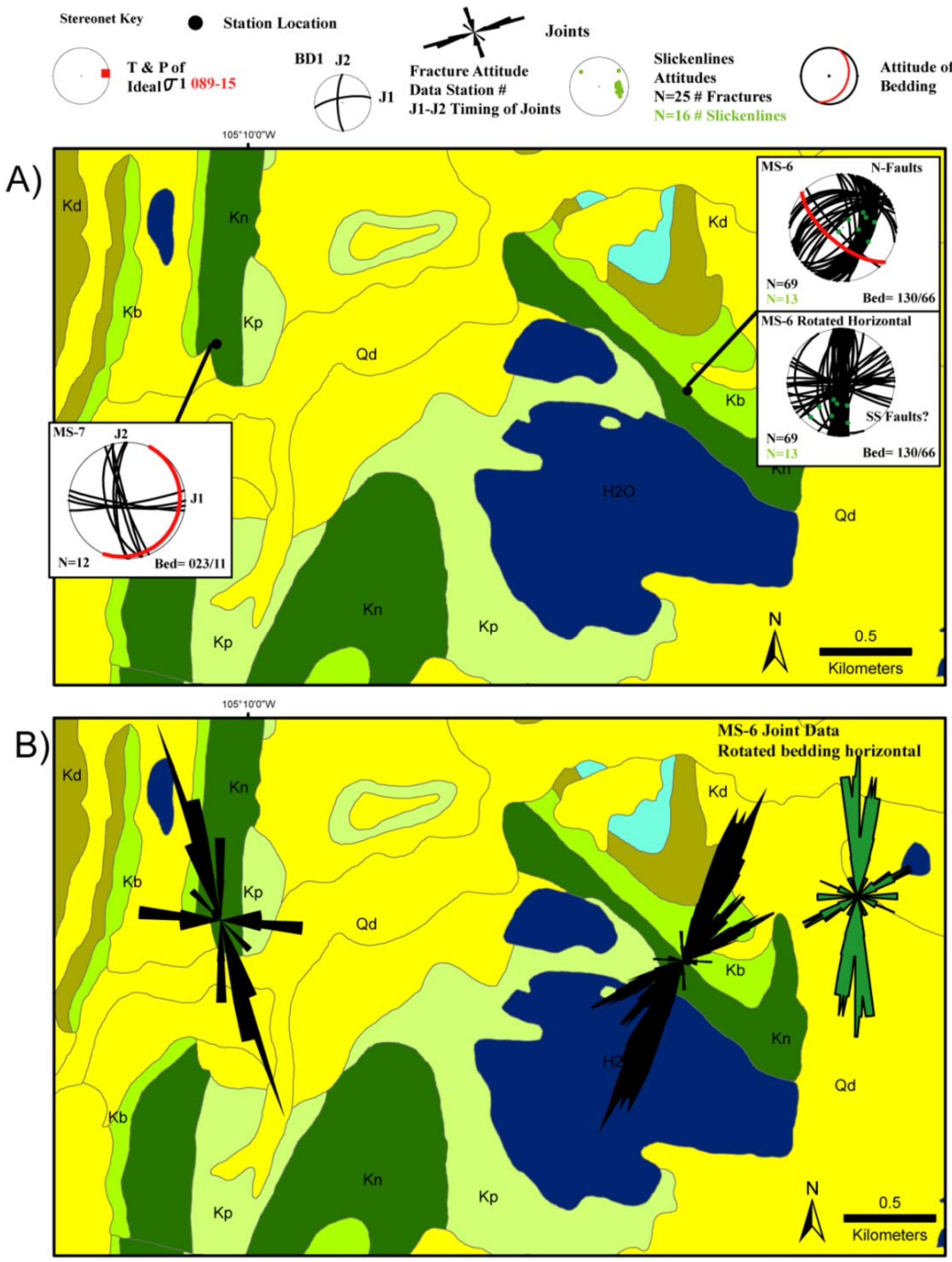

Figure 4.15. A) Stereonets of fracture planes, slickenlines and ideal σ1 axis. B) Roseplots of fracture trends measured in the southern Masonville quadrangle.

Carter Lake Reservoir Quadrangle

Within the Carter Lake Quadrangle a zone of interaction between distinctly different structural trends is described by Erslev et al. (2004). The ridge forming the forelimb of the Carter Lake Anticline is slightly asymmetric and trends north before abruptly trending north-westerly and becoming highly asymmetric. Holdaway (1998) showed ideal σ_1 axis trends around the Carter Lake Reservoir to be dominantly unimodal, with E-W directed compression perpendicular to north trending structures. North of the Carter Lake Quadrangle, Precambrian dikes mapped by Braddock et al. (1970) parallel several northwest trending faults and could be zones of localized pre-existing weakness. This could help explain the obliquity of northwesterly trending structures to east-west Laramide shortening directions (Holdaway, 1998).

Most of the Niobrara Formation is poorly exposed as a low relief hogback east of the more prominent Dakota Group and the Carter Lake Anticline. Road cuts, drainage valleys, and water runoff containment ponds were investigated to determine whether multiple structural trends can be observed within the Niobrara Formation. Braddock et al. (1988) mapped a blind, nearly-vertical NW-trending fault that bounds the forelimb of the Carter Lake Anticline and cuts the Niobrara Formation to the southeast. North of this inferred fault, fracture measurements taken at station CL-8 show J_1 joints strike 87° with J_2 joints striking 170°. J_1 joints at this locality subparallel ideal σ_1 trends (91°) calculated by Holdaway (1998) in the Lyons Formation to the east (Fig. 4.16a).

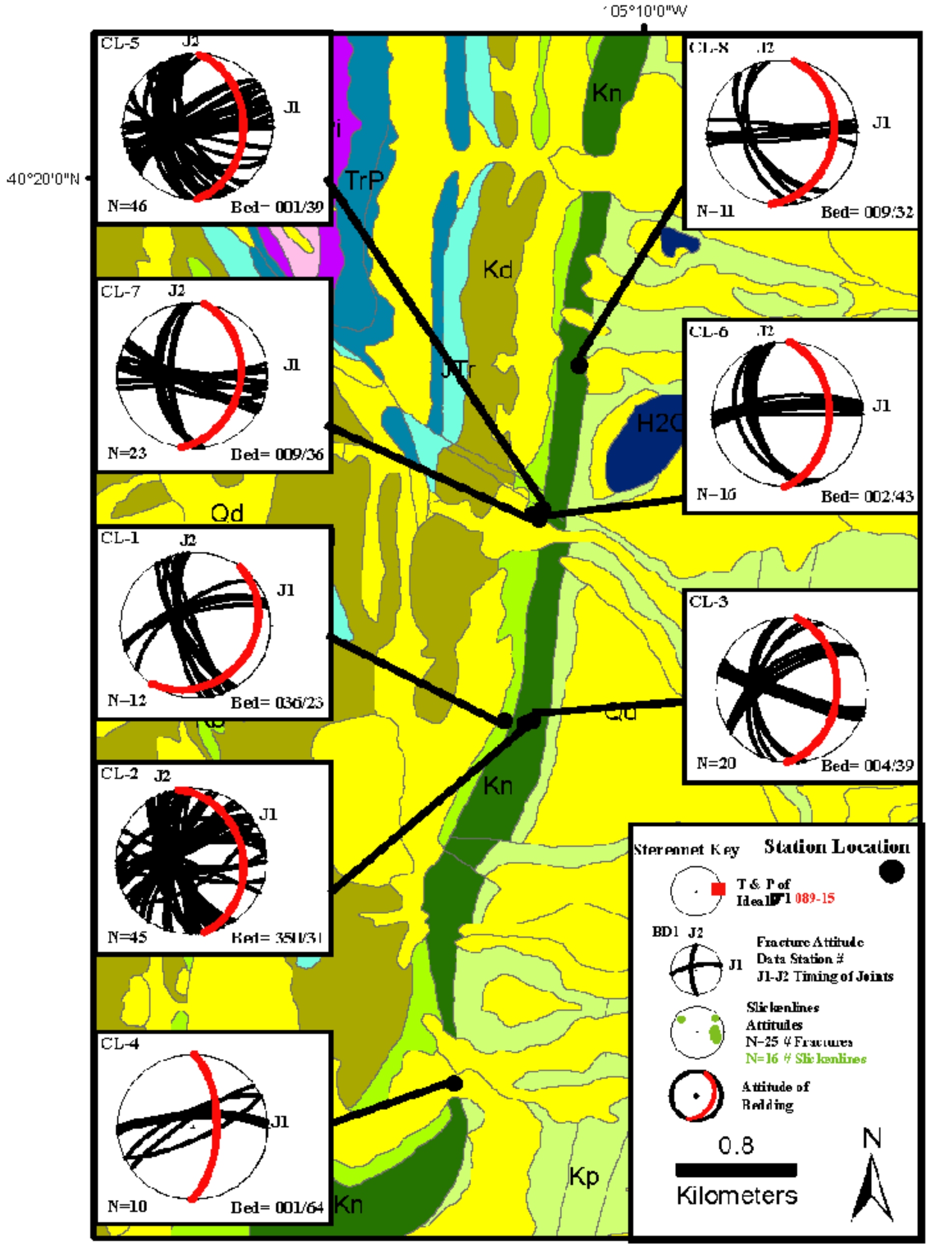

Figure 4.16a. Stereonets of fracture planes trends measured in the Carter Lake Reservoir Quadrangle.

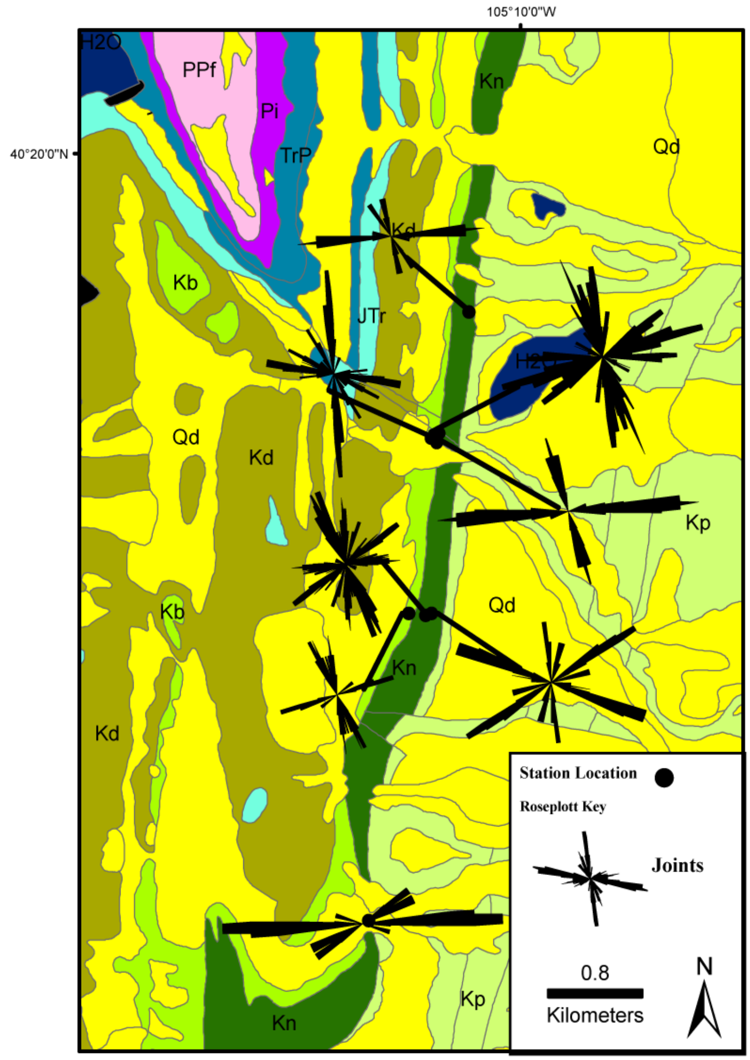

Figure 4.16b. Roseplots of non-slickenlined fracture strikes measured in the Carter Lake Reservoir Quadrangle.

South of this blind fault, the Fort Hays Limestone shows variable fracture strikes from NE to E-W to SE. Lower Niobrara sedimentary strata show dominantly east-west J_1 joints with NNW striking J_2 joints at station CL-6 (Fig. 4.16a). Increased fracture complexity is observed to the south where J_1 joints strike NE-SW (256^o). Data station CL-4 shows two separate fracture orientations of E-W and ENE (Fig. 4.16b). No definitive cross-cutting relationships were observed at CL-4, and no NW to NNW-striking fractures were observed at this station. Fracture variability adjacent to a possible large blind master thrust could be consistent with multiple shortening and compression axes or with pre-existing weaknesses (Fig.4.16b) Joints striking 87º cross-cut conjugate shear fractures. Joints that parallel NE-trending shear fractures (67º) in adjacent areas are probably strike-slip faults. No slickensided minor faults were observed in the Crater Lake quadrangle for upper Cretaceous strata.

Hygiene Quadrangle

The Hygiene Quadrangle's largest structural feature is the south-plunging, slightly-asymmetric Rabbit Mountain Anticline. To the north, Rabbit Mountain is a monocline that is cross-cut by the NW-trending Blue Mountain Fault. Dome Pass Anticline trends NNW and is abruptly redirected NW by the Blue Mountain Fault. The western forelimb of the Rabbit Mountain Anticline dips steeply westward before tightly folding and inverting dip directions shallowly to the east in Dome Flats. At this location, Cemex Inc. actively operates a cement facility called Rock Ridge Quarry. Here the Fort Hays limestone gradually increases in dip magnitude from west to east 10-20º. The active dig face exposes the Niobrara Formation from the Fort Hays contact through the upper Niobrara A member. Here one can directly observe the complicated stratigraphy of the Niobrara Formation and see the finely-laminated shale interfingered with chalks and marl sequences.

Due to mining activity, the Rock Ridge Quarry exposes large ESE-dipping panels of the Niobrara Formation which show multiple orientations for faults, extensional joints, shear joints with no kinematic indicators, and stylolites. At station HY-1 only two slickenside measurements were recorded but a number of conjugate shear fractures were indicated by shear of calcite fill indicating slip-sense (Fig. 4.17a). ENE-striking faults indicate right-lateral slip with ESE-striking faults indicating left-lateral slip. Fractures that parallel right-lateral strike slip faults have aperture but lack any kinematic indicators and strike 078° (Fig. 4.17). These fractures are interpreted to be Mode II shear fractures later reactivated. Cross-cutting relationships were unclear due to multiple stages of calcite fill within these two oblique fracture sets. Also present at this station were E-W oriented fractures with pervasive calcite fill that abutted into various shear fracture orientations. These fractures bisect conjugate shears and could be J_1 joints. Field observations of fractures with no apparent slip were identified as joints, though they may have been reactivated shear fractures. Examination of poles to stylolite planes indicate that conjugate shear fractures and stylolites probably formed under similar principal horizontal shortening axes trending 85°. Ideal σ_1 axes trend on average 87° for this study subarea (Figs 4.18a, 4.18b).

Younger J_2 joints identified from clear abutting relationships strike N-S and NNW in the Fort Hays Limestone, with an average attitude of 173°-77°. J_2 joints appear to be consistent with other study areas in that they are parallel to bedding strike, dip steeply to the west and consistently abut both interpreted J_1 joint sets and shear fractures. No pervasive calcite fill was documented in the J_2 joint sets. No normal faults were identified at this study location.

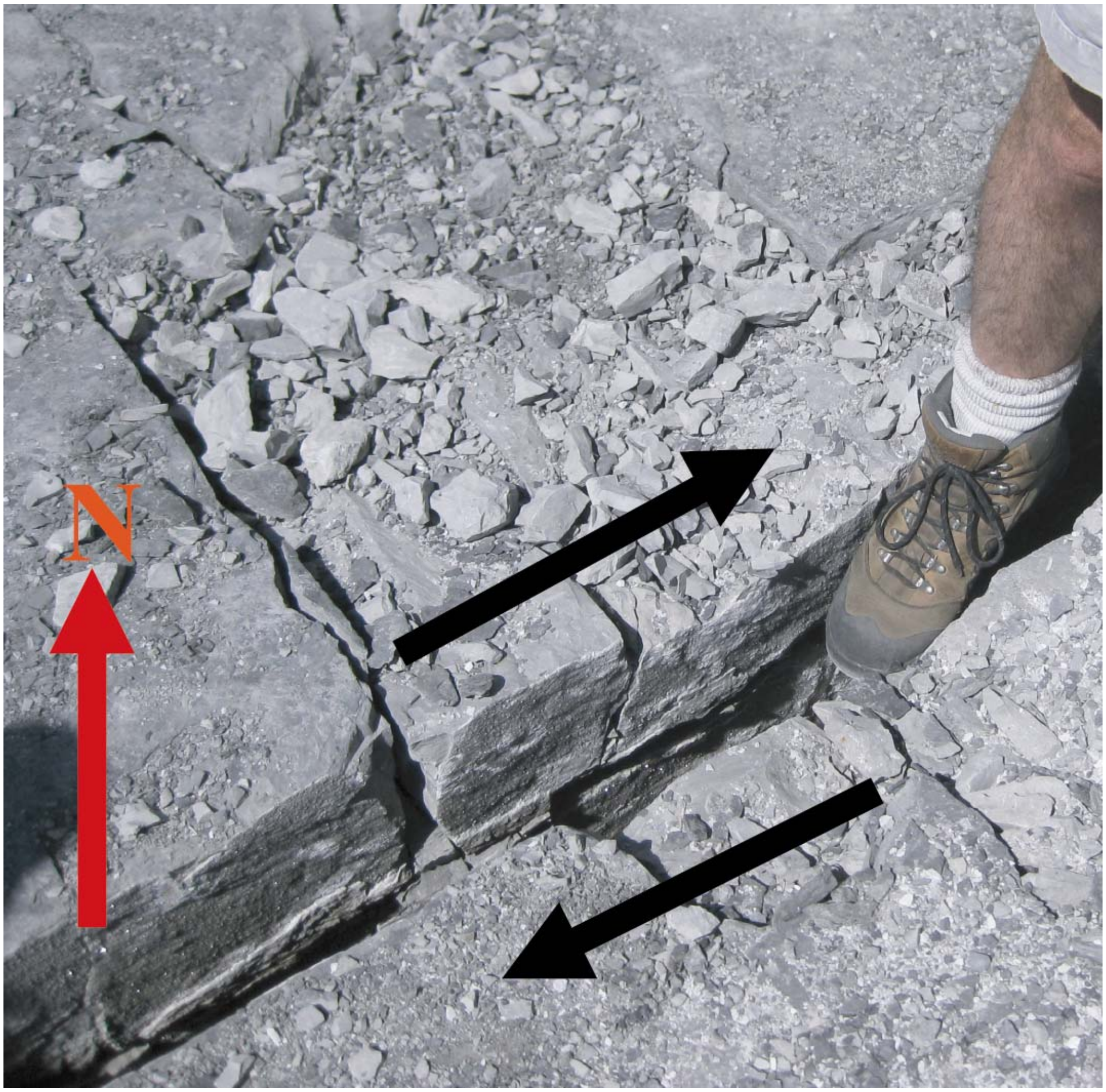

Figure 4.17. Reactivated shear fracture as a joint in the Fort Hays Limestone at station HY-1. Fracture strikes N78E and arrows indicate right-lateral slip identified from slickensurfaces. Picture taken in the Rock Ridge Cement Quarry.

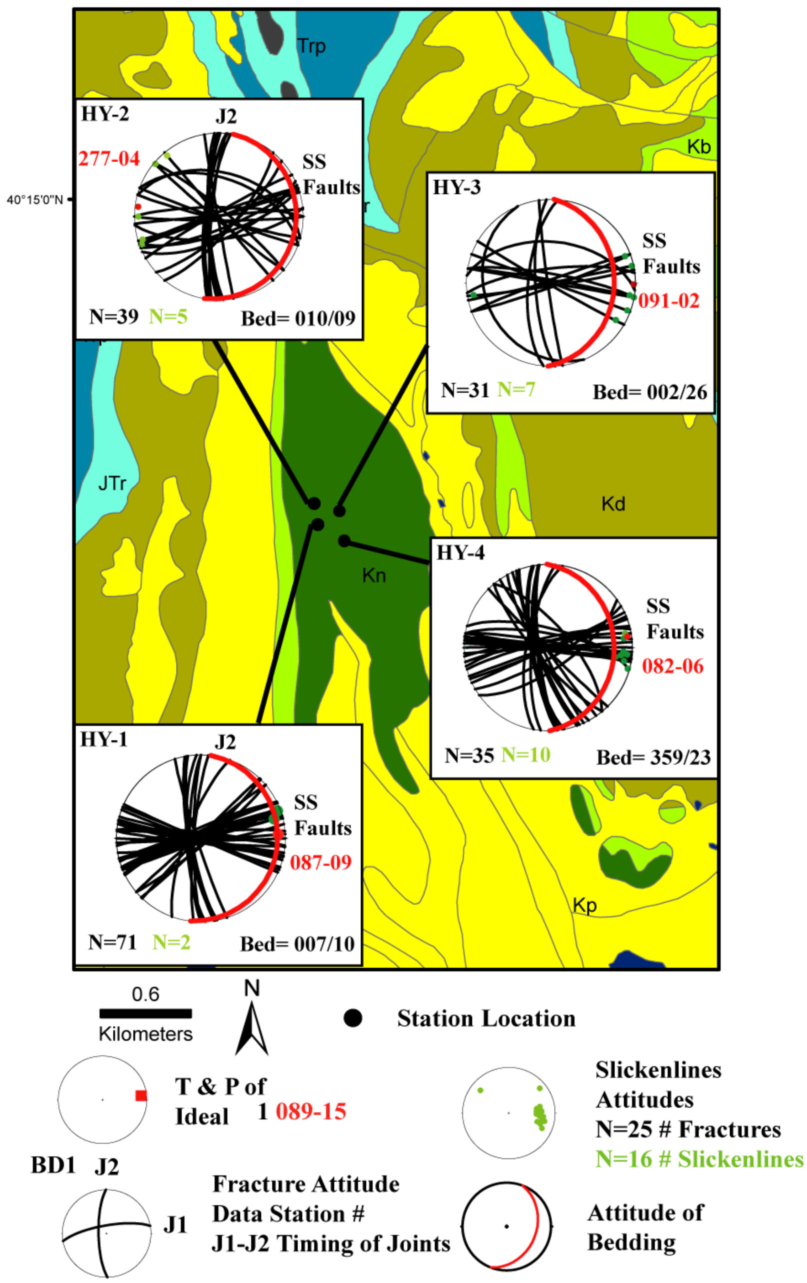

Figure 4.18a. Stereonets of fracture planes, slickenlines and the best fit ideal σ_1 axis measured in the Hygiene Quadrangle.

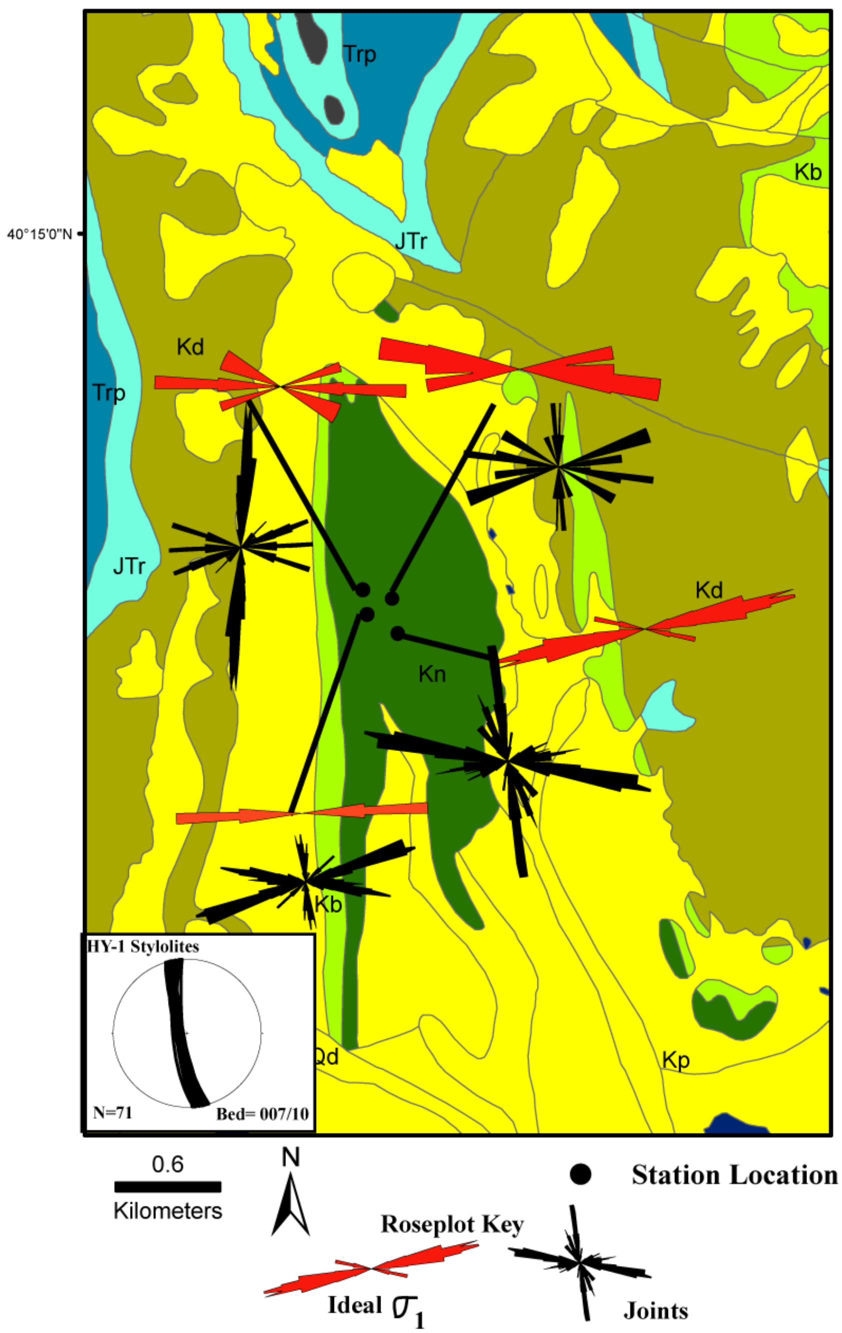

Figure 4.18b. Roseplots of fracture trends, stereonet of stylolites at HY-1, and ideal σ_1 trends measured in the Hygiene Quadrangle.

Boulder Quadrangle

The Boulder quadrangle, specifically the Six Mile Fold exposures, was the locus for this detailed investigation to test hypotheses of fracture mechanism(s) and the timing of extensional fracturing, or jointing, relative to the Laramide Orogeny. Six Mile Fold is a fault-propagation fold north of Boulder, CO exposing the Codell Sandstone, Fort Hays Limestone, and the Niobrara Formation. West of the study area, Wrucke and Wilson (1967) identified major faults cutting Precambrian basement in the Boulder Quadrangle which strike dominantly NW to NNW. The Maxwell Fault bifurcates north of the NW-trending Poorman Fault into two segments. One segment continues SSE and abuts into the Poorman Fault whereas the other trends more northwesterly, sub-paralleling the Poorman Fault before tipping out prior to cutting the Fountain Formation. In the southwestern portion of the Boulder Quadrangle, the Hoosier Fault is oblique to the Maxwell Fault trending NW.

Six Mile Fold is divided into two subareas due to the proximity of fracture data stations. The northern subarea consists of 11 data stations that transect the fold. The fold consists of: 1) an east-dipping backlimb of an asymmetric anticline exposing the Fort Hays Limestone as a low relief hogback, 2) a SE-plunging nose of the anticline with a fold axis trending 176^{o} and 3) the forelimb of the anticline which steeply dips 50-78^{o} WSW before transitioning into a SSE plunging asymmetric syncline with a moderately-east-dipping forelimb with a fold axis trending 175^{o}. Station BD-1 is located on the northeastern backlimb of the Six Mile Fold Anticline and exposes the Codell Sandstone and Fort Hays Limestone (Fig. 4.18). Minor faults are strike slip, dominated by left-lateral slip with a few accompanying right-lateral conjugates. J_1 joints strike E-W bisecting conjugate

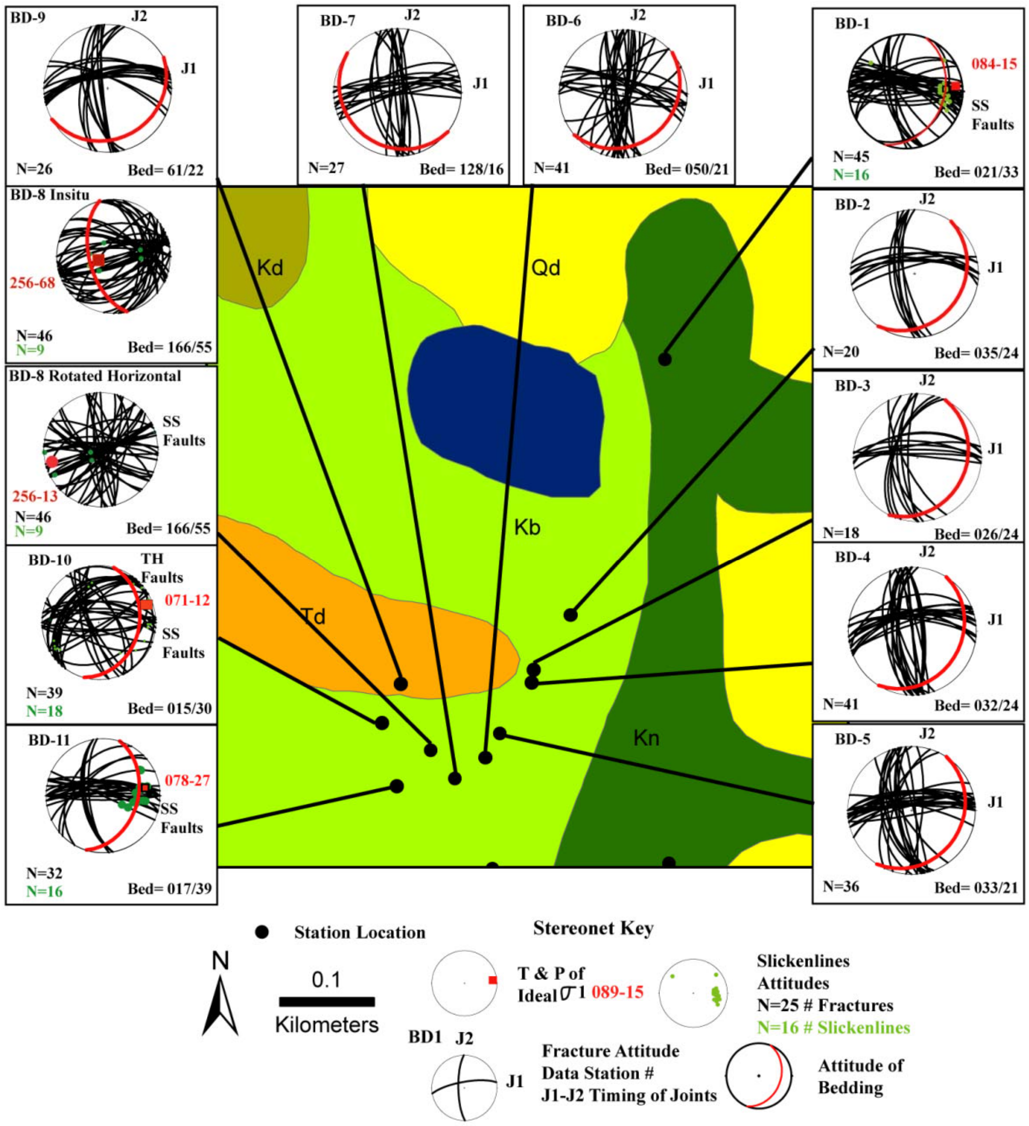

Figure 4.18. Stereonets of fracture planes, slickenlines and the best fit ideal σ_1 axis measured in the north Six Mile Fold subarea of the Boulder Quadrangle.

shear fractures. Ideal σ_1 axes calculated at BD-1 trend 84°, but could be slightly deviated by more NE-striking right-lateral faults. Examinations of poles to stylolite planes show shortening directions (82°) are subparallel with ENE-horizontal shortening axes. J_1 joint attitudes are consistent along the eastern backlimb before approaching the SSE-plunging fold axis. J_2 joints strike nearly N-S and are slightly oblique to bedding strike (Fig. 4.19).

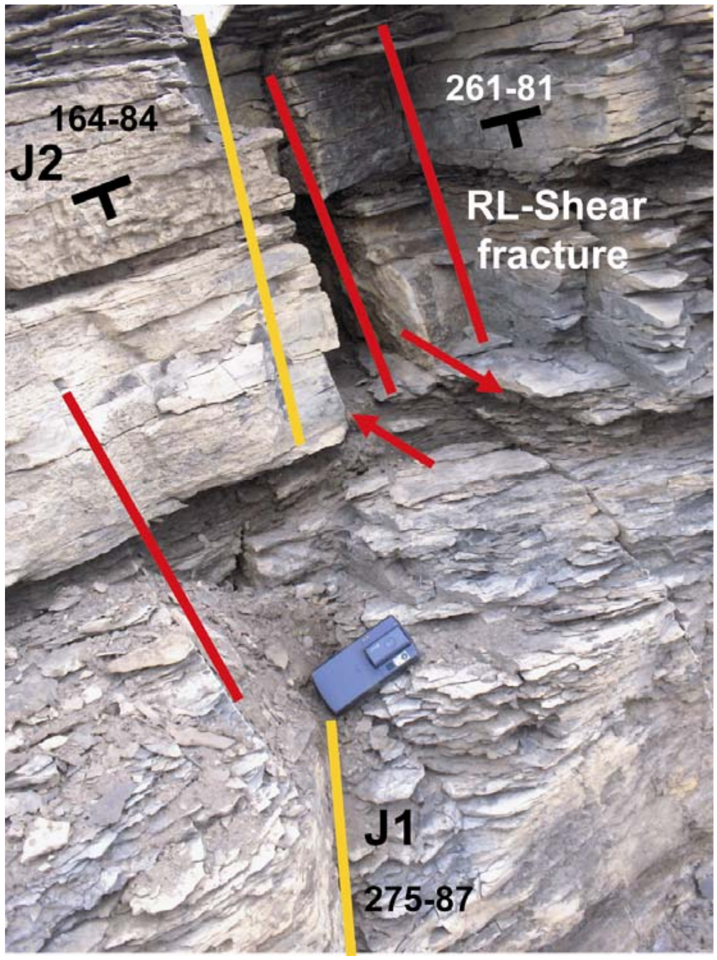

Figure 4.19. Shear fracture and jointing relationships observed in the Six Mile Fold study area

Beginning at the SSE-plunging anticlinal fold hinge, fracture orientations show higher variability. Station BD-6 shows fractures striking ESE that may be faults as well as J_2 joints striking more NNW. Ideal σ_1 axes show multiple shortening directions across the northern subarea, striking either ENE or ESE.

The southern subarea (Fig. 4.20) is south and east of the SE-plunging fold. Bedding-parallel thrust faults were observed in the Fort Hays Limestone and strike N to

NNE. Adjacent to the bedding-parallel thrust faults are unique “pencil cleavage” fractures observed in the Lower Niobrara Formation. The axial plane cleavage strikes SSW (167º) with pencil cleavage lines trending 171º. J_1 joints show variable NE to E-W strikes through the southern subarea. Station BD-17 exposes multiple 80º striking right-lateral faults that contain a second slickenline direction that is interpreted as a reactivated fault surface (Fig. 4.21). Observations show normal displacement dipping to the NE, but it is unclear what the faults do below the exposed sediments.

Engelder and Geiser (1979) explain pencil cleavage as a result of lateral shortening in association with layer parallel slip as observed in Devonian strata in the Appalachian Plateau. The axial plane parallels local stylolite trends, and its proximity to bedding parallel thrust surfaces indicates layer-parallel slip as a likely deformation mechanism in the Niobrara Formation. It is unclear whether cleavage, folding or stylolites formed first. Ideal σ_1 trends observed near stylolites indicate ENE-directed shortening, whereas, south of the fold, ideal σ_1 trends appear to rotate clockwise 5-20°. Multiple shortening directions could be explained by multiple events redirecting maximum principal stresses around the fold. It is also clear that later extensional forces are acting within the Niobrara Formation reactivating older fault systems (Fig. 4.21), and the presence of N-S trending J_2 jointing (Fig. 4.22).

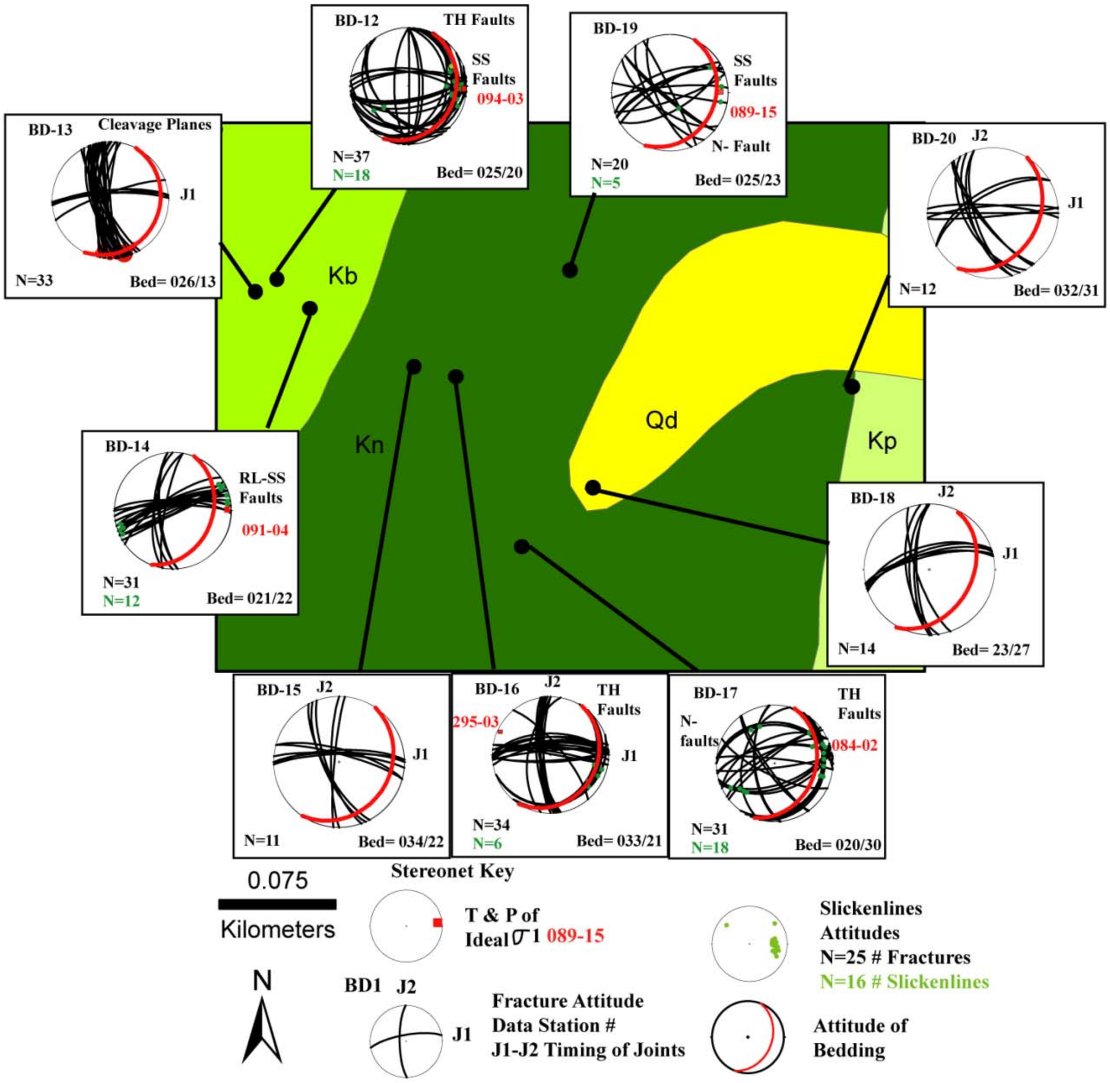

Figure 4.20. Stereonets of fracture planes, slickenlines and the best fit ideal σ_1 axis measured in the south Six Mile Fold subarea of the Boulder quadrangle.

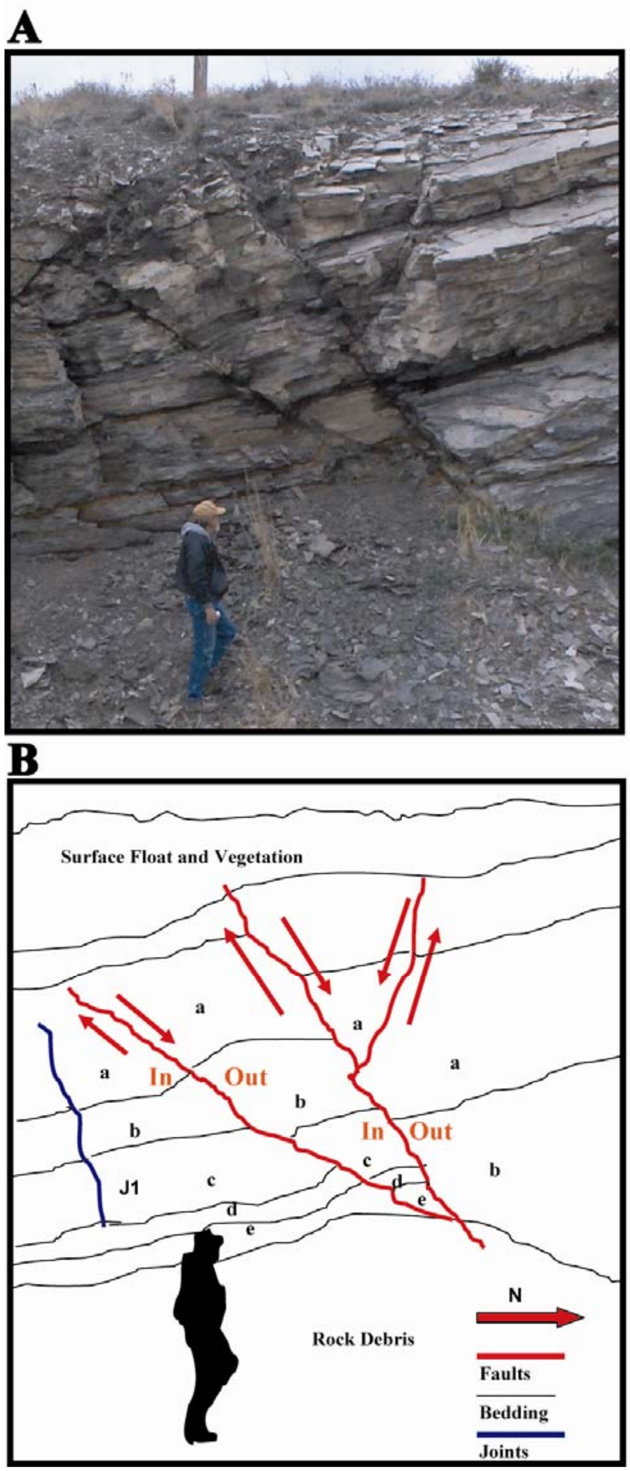

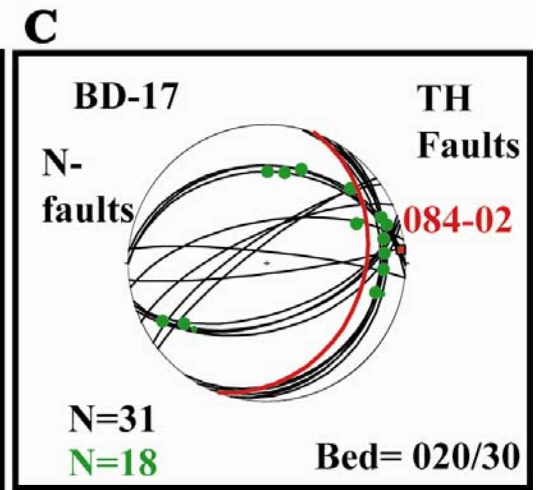

Figure 4.21. Reactivation of right-lateral faults with normal displacement at station BD-17 in the Six Mile Fold southern subarea. A) Outcrop photo of a road cut exposure of the Niobrara "B" Chalk. Beds dip to the southeast and faults strike NE. Man is used for an approximate scale. B) Outcrop sketch shows field observations of normal displacement of faults identified from slickenlines and bedding relationships, and right-lateral strike-slip movement identified by slickenlines on singular fault planes. C) Stereonet of fault planes identified at station BD-17, showing multiple slickenline trends on one fault plane.

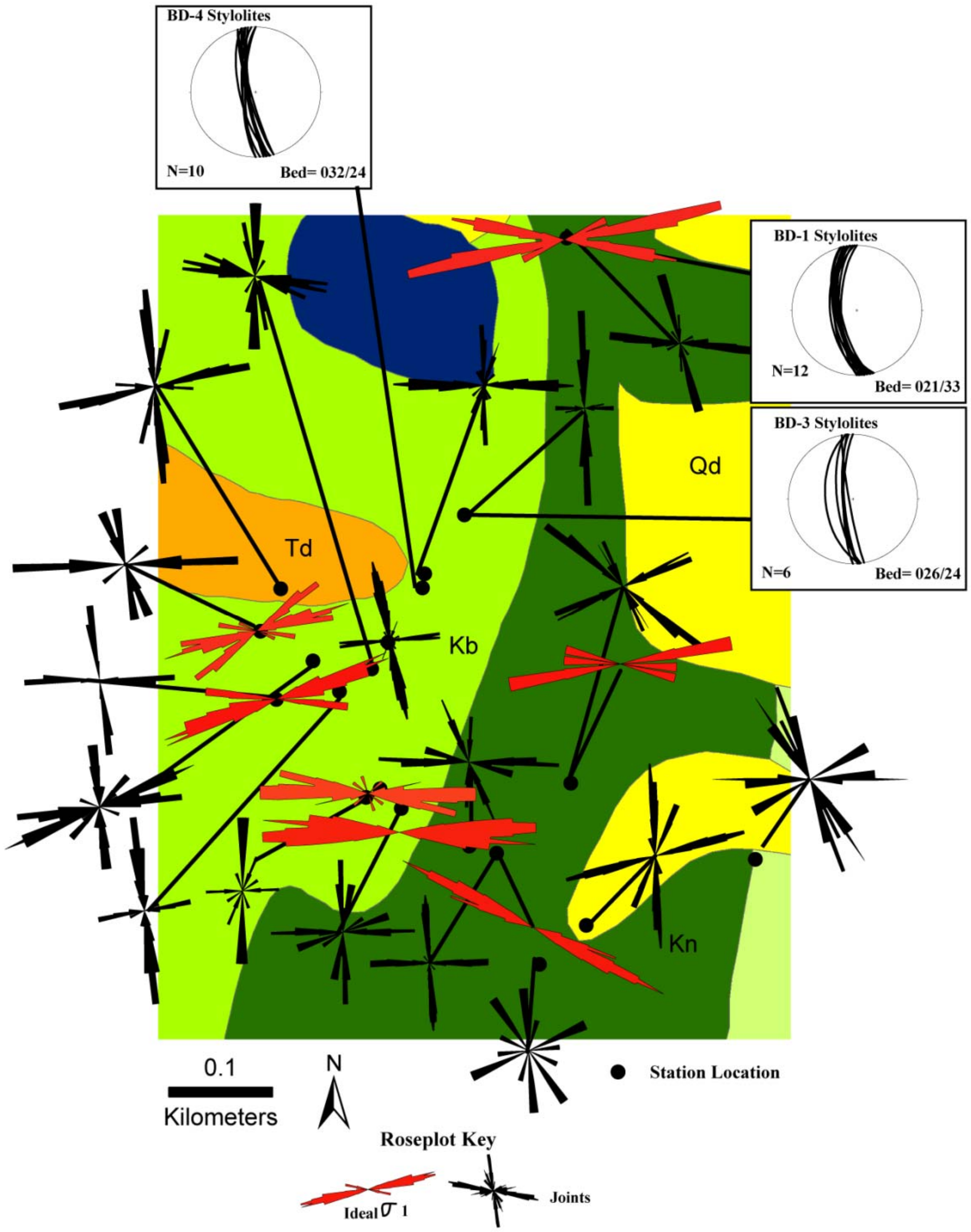

Figure 4.22. Roseplots of fracture trends and ideal σ_1 trends measured in the Six Mile Fold subarea of the Boulder quadrangle.

Observations Summary:

Fracture data collected in the Niobrara Formation along the northeastern Front Range reveals interesting correlations to past fracture studies conducted in Permian to lower Cretaceous rocks (Holdaway, 1998; Erslev et al., 2004; Erslev and Larson, 2006; Tetreault et al., 2008; and Larson, 2009). Thrust and strike-slip minor faults observed in the Niobrara Formation show average ENE to E-W σ_1 trends that are locally subparallel to 80° Laramide shortening directions observed in adjacent study areas (Holdaway, 1998; Erslev et al., 2004; Erslev and Larson, 2006). Slickensides were difficult to identify through much of the study area, but conjugate fractures observed in the Niobrara Formation were nearly identical to Laramide strike-slip faults identified by Erslev and Larson (2004) in the Dakota Group. Ideal σ_1 axes calculated from slickensides and poles to stylolite planes observed in the Niobrara Formation along the Front Range are relatively consistent with Laramide shortening axes calculated by previous studies (Holdaway, 1998; Erslev et al., 2004; Erslev and Larson, 2006; Tetreault et al., 2008; Larson, 2009). Normal faults which cross-cut or reactivate strike-slip faults in the Niobrara Formation remain perplexing. Possible analogs described by Holdaway (1998) include normal faults in the Ingleside Formation which showed N-S extension on the east limb of Milner Mountain Anticline. However no stress inversion or observations of reactivated fault planes were discussed by previous workers.

Larson (2009) identified areas with significant faulting which lacked consistent jointing, and hypothesized that faulting and jointing occurred under slightly different Laramide stress axes. Areas with abundant conjugate fractures lacked consistent ENE-jointing in the Niobrara Formation, however J_1 joint trends observed in the Niobrara

Formation consistently sub-paralleled local ideal σ_1 compression axes calculated in the Dakota Group by Erslev and Larson (2006) and Holdaway (1998), and by adjacent ideal σ_1 analyses in the Niobrara Formation. These fracture trends are Mode I extension fractures in the Niobrara caused by regional Laramide stresses which were also responsible for strike slip and thrust minor faults. It is possible that some fractures could have been misidentified as J_1 joints, and are really shear fractures reactivated in tension by regional uplift and will be addressed by subsequent regional summary plots.

Cross-cutting and abutting relationships identified a NNW-joint set (J_2) that is consistent throughout the entire study area, and is incompatible with Laramide ENE to E-W shortening axes identified in Permian to Lower Cretaceous Rocks (Holdaway, 1998; Erslev et al., 2004; Erslev and Larson, 2006; Tetreault et al., 2008; Larson, 2009). The consistent J_2 joint orientation observed in the Niobrara Formation across the northeastern Front Range generates questions in regards to post-Laramide fracture mechanisms. The presence of normal faults reactivating Laramide strike-slip fault planes and NNW-striking joints suggest post-Laramide extension as a reasonable hypothesis.

Chapter 5

Detailed Fracture Analyses

Fracture data were analyzed to test the possibility of multi-directional shortening trends in the northeastern Front Range, estimate regional Laramide stresses and strain, identify regional jointing patterns, and document calcite-healed fractures and their preferred orientations. Summary stereoplots and roseplots of all minor faults, stylolites, joints, and calcite-filled fracture orientations aid in understanding fracture mechanisms affecting the Niobrara Formation at the surface, and are a useful resource with compare to subsurface fracture data sets.

Minor Fault Slickenline and Ideal σ_1 Axes

The bulk of minor faults observed with slickenlines occurred within and south of the Masonville Quadrangle. Shear fractures observed in the Laporte Quadrangle showed visible lateral offset but no slickenline data was collected. Minor fault data collected between various stations often showed only one fault type where conjugate relationships could not be observed. Areas where conjugate faulting was observed were used to calculate best fit α angles (+/- 1°) using Orient (Vollmer, 1992) and SELECT (Erslev, 1998) between 10° and 40°, which provided the highest first eigenvalue. Further data sorting shows the Fort Hays Limestone consistently has lower best fit α angles than the overlying Niobrara Formation. The best fit α angle average determined for the Fort Hays

Limestone is 15°, and the best fit α angle average determined for the Niobrara Formation is 20°. These values were used in the Compton (1966) ideal compression analysis available by station in Appendix A. The best fit α angle used for the entire minor fault dataset was 17.5°.

Slickenlines and ideal σ_1 axes were plotted on equal area stereonets and 2% contoured stereonets for 213 minor faults measured in upper Cretaceous strata between Owl Canyon, CO and Boulder, CO (Fig. 5.1). All fault types were separated by slip sense to determine whether multiple shortening directions and/or mechanisms are present (Fig. 5.1). Thrust slickenlines have an average orientation of 098°-16°, slickenlines from left-lateral faults show an average slip direction of 101°-18° and slickenlines of right-lateral faults show an average slip direction of 069°-09° (Figs. 5.1, 5.4). Normal fault slickenlines have an average slip direction of 183°-73°, with highly variable distributions (Figs. 5.1, 5.2).

Of the 213 measured faults, strike-slip minor faults consisted of 69% of the fault data set followed by normal faults (19%), and thrust faults (12%). Left-lateral and right-lateral faults occurred at a nearly 1:1 ratio, with right-lateral faults consisting of 51% of the strike slip minor fault data set. Roseplots of minor fault slickenline and ideal σ_1 trends show multimodal distributions, with thrust and strike-slip faults showing lower variability than normal faults (Fig. 5.2). Normal faults were examined separately due to field observations indicating fault plane reactivation, and observations of cross-cutting relationships identifying a separate and younger extensional faulting system.

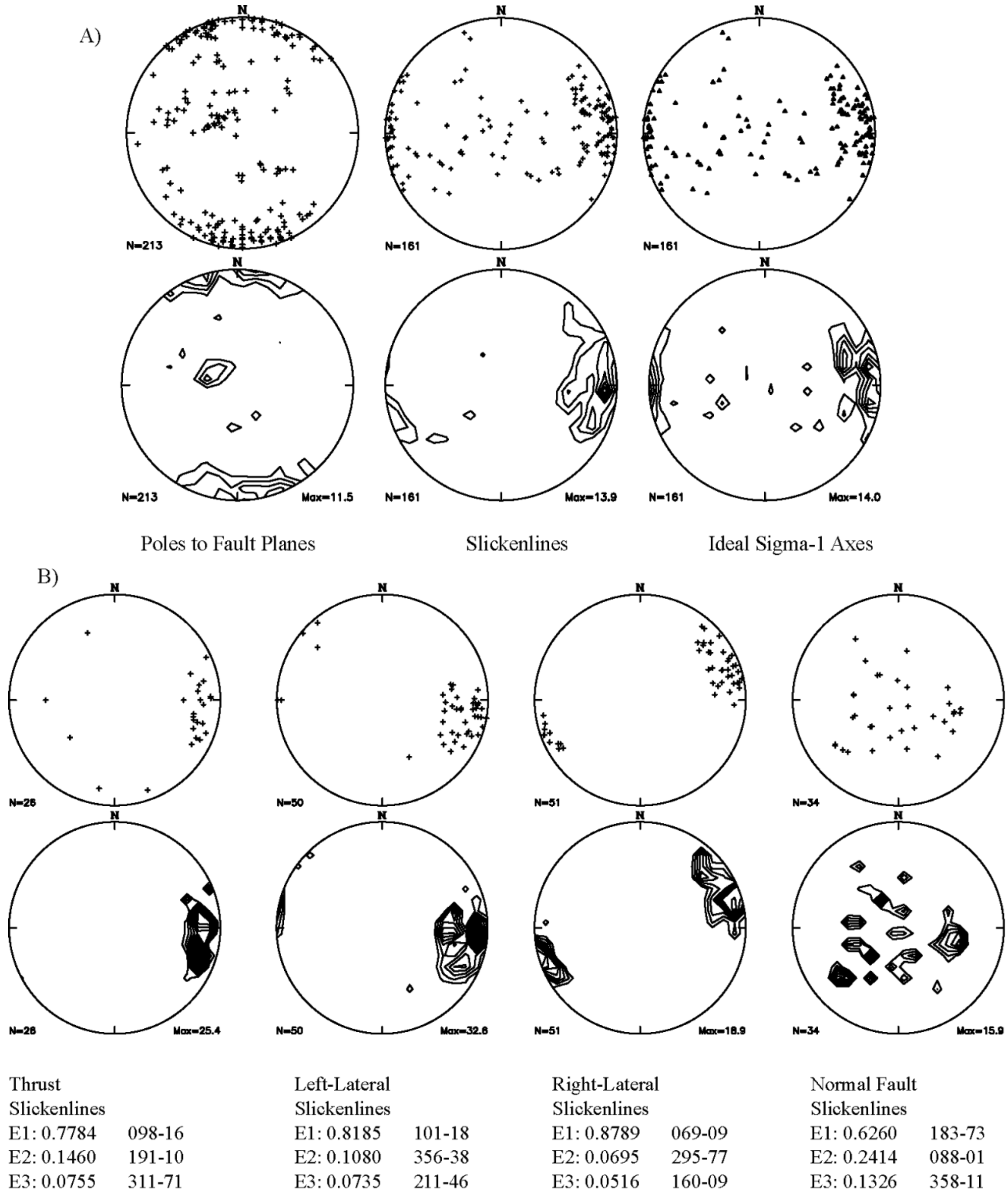

Figure 5.1. Stereoplots and contoured stereoplots (2% CI) of poles to fault planes, slickenlines, and ideal σ_1 axes (α=18°). A) Poles to fault planes, slickenlines, and ideal σ_1 axes calculated from all fault data. B) Stereoplots of slickenlines broken down by fault slip sense with eigenvalue and eigenvector data.

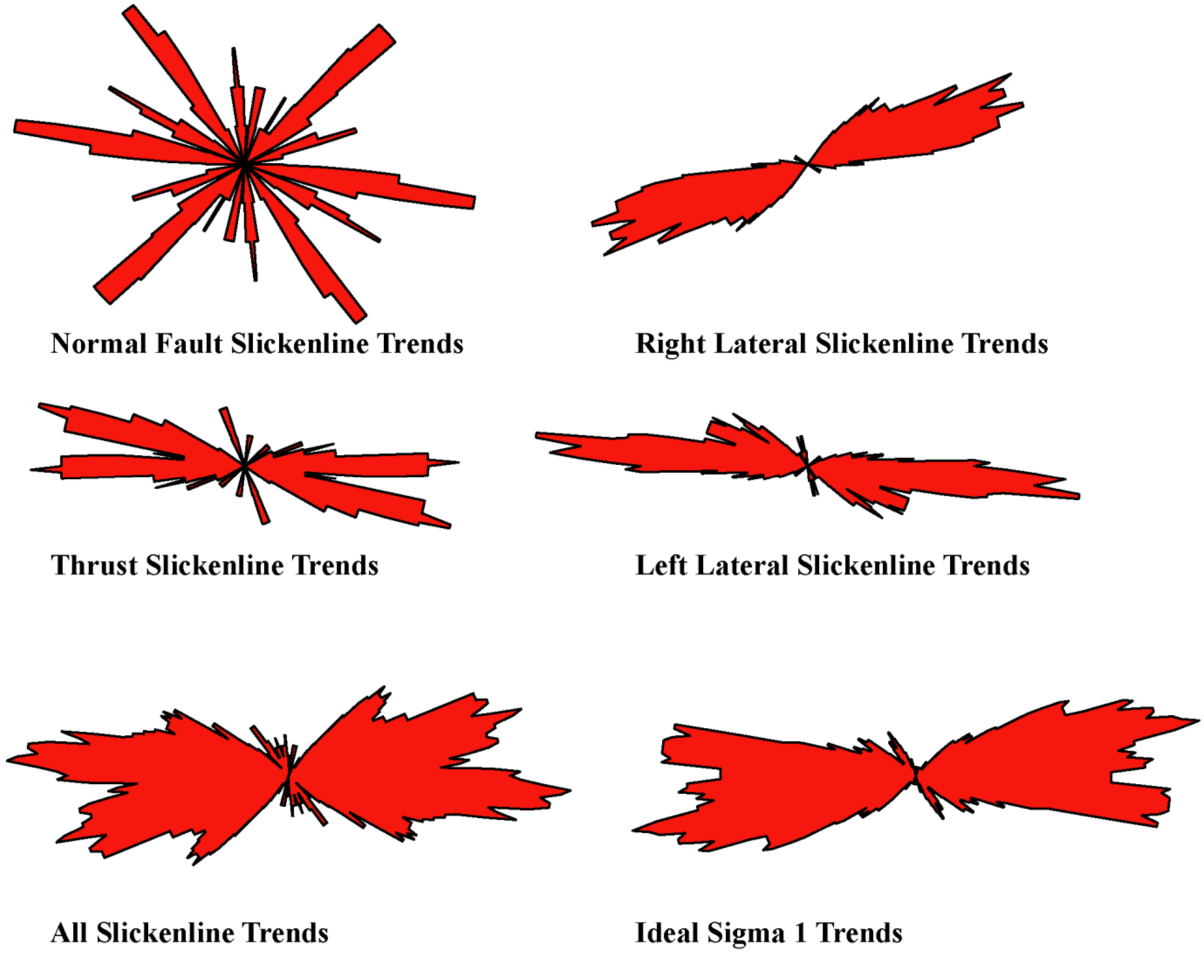

Figure 5.2. Roseplots of ideal σ_1 trends and slickenline trends separated by fault type.

The orientation of regional Laramide stress and strain axes and best fit α angles (+/-1°) were calculated from strike-slip and thrust faults using Orient (Vollmer, 1992) and SELECT (Erslev, 1998) to determine the α angle which provided the highest first eigenvalues (Fig 5.3). The average orientation of Laramide fault slip direction is 086°-14°, whereas Compton's (1966) ideal σ_1 analysis calculated an average regional Laramide σ_1 of 086°-08° using an α angle of 17.5° (Figs. 5.3). These trend and plunge values are comparable to other northeastern Front Range regional Laramide σ_1 studies

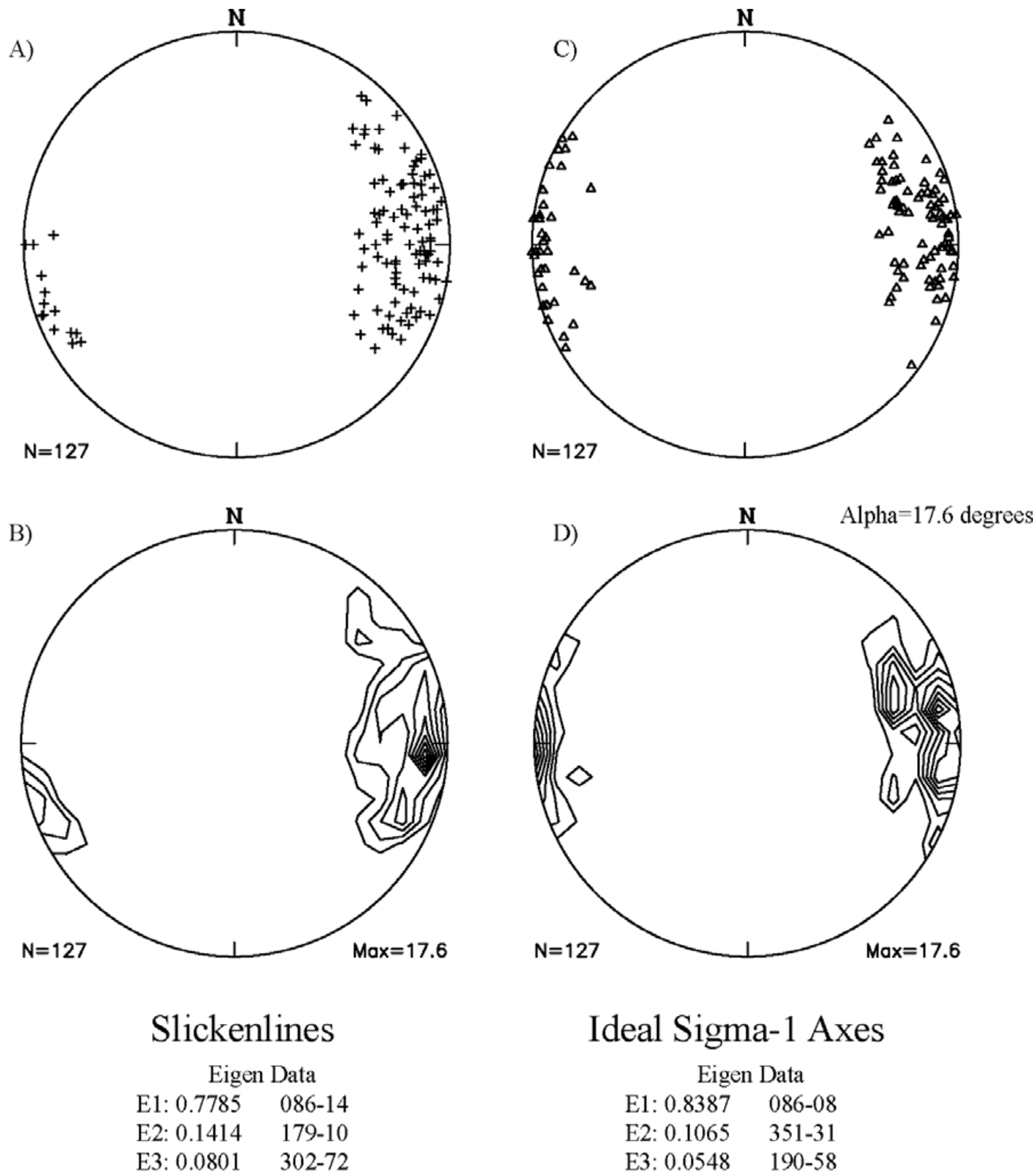

Figure 5.3. Stereoplots and contoured stereoplots (2% CI) from strike-slip and thrust slickenlines, and ideal σ_1 axes (α=17.5°) with eigenvalue and eigenvector data for regional Laramide σ_1 analysis. A) Strike-slip and thrust minor fault slickenlines. B) 2% contours of slickenlines. C) Ideal σ_1 axes. D) 2% contours of ideal σ_1 axes.

such as Holdaway's (1998) of 079-11, and Erslev and Larson (2006) of 93-06°, along the northeastern Front Range from Lyons, CO to northern Fort Collins, CO.

Average conjugate shear fracture orientations predicted by Laramide σ_1 analysis (86°-08°), using a best fit α angle of 17.5°, for the Niobrara Formation and Fort Hays Limestone include right-lateral shears trending 68.5° and left-lateral shears trending 103.5°. The average trend of all right-lateral slickenlines collected through the study area is 69°, with left-lateral slickenlines trending 101°. Average thrust slickenlines trends (98°) are deviated clockwise 12° from the average Laramide compression axes calculated in the Niobrara Formation (86°), however low first eigenvalues show higher variability than strike slip faults. 2% interval contour plots of thrust slickenline show at least two contour maxima, one trending E-W, the other trending ESE.

Previous studies by Holdaway (1998), and Erslev and Larson (2006) have documented consistent ENE- to E-slip directions on thrust conjugates for the lower Cretaceous sandstones. E-W trending thrust slickenlines were taken from the Fort Hays Limestone, whereas ESE- trending slickenlines were collected from the lower Niobrara 'C" sequence, in a much shalier interval. Possible explanations for this variation include slightly different stress orientations which caused two stages of Laramide thrust faulting in the Niobrara Formation, low-angle normal faults have been misidentified as thrusts, or slip on bedding-parallel detachments. The later hypothesis is attractive for two reasons, one being that ESE- trending slickenlines are isolated to one station (BD-16), are bedding parallel, and located adjacent to observed normal fault reactivations of right-lateral fault planes at BD-17. Secondly, these minor fault slip directions are perpendicular to local bedding strikes where dips exceed 20° in shale sequences of the lower Niobrara Formation.

Normal faults (n=40) were analyzed separately from strike-slip and thrust minor faults due to field observations of fault reactivation, and cross-cutting relationships. Observations of normal dip slip and right lateral shearing occurring on a common fault plane were identified at station BD-17 in the Six Mile Fold subarea, and surface relationships indicated normal fault planes offset calcite-filled J_1 orientations in the Masonville Quadrangle. Normal faults slickenlines are highly variable, with low first eigenvalues for the study area, and yielded an average 183°-73° slip direction (Figs. 5.1, 5.2, 5.4). Normal faults have been identified in adjacent minor fault studies along the northeastern Front Range, and from 3D seismic interpretations within Denver Basin (Haberman, 1983; Davis, 1985; Pritchett, 1993; Birmingham, 1998; Holdaway, 1998), however no fault reactivations or estimates of timing have been clearly identified. Average slip directions are nearly perpendicular to average strike-slip and thrust fault slip directions (86°). Normal faults identified at station MV-6 in the Masonville Quadrangle appear to be the result of outer arc extension close to the fold axis on Milner Mountain anticline, but the rest of the data set appears to be a separate extensional event that occurred after Laramide ENE compression (Fig. 5.4).

Minor faults observed in the Fort Hays Limestone and Niobrara Formation appears to be controlled by at least two separate stress fields. One stress field is consistent with Laramide compression observed by previous researchers (Holdaway, 1998; Erslev and Holdaway, 1999; Erslev et al. 2004; Erslev and Larson 2004; Larson 2009), whereas

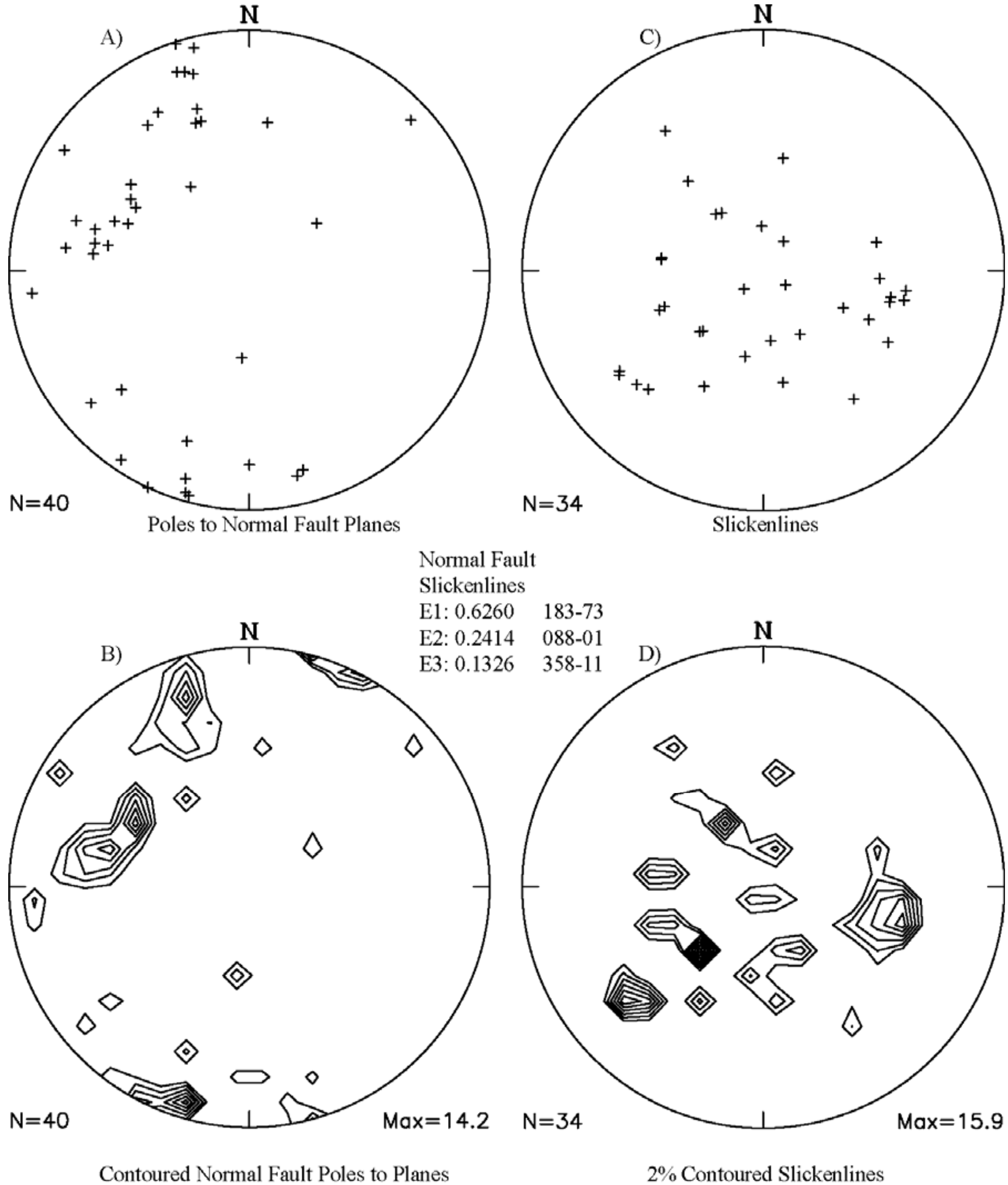

Figure 5.4. Stereoplots and contoured stereoplots (2% CI) of normal fault poles to planes and slickenlines. A) Poles to normal fault planes. B) 2% contours of poles to planes. C) Normal fault slickenlines. D) 2% contours of slickenlines

the other appears to be related to post-Laramide extension indicated by normal fault reactivation and J_2 jointing.

Stylolite Data Analysis

Pressure dissolution stylolites (n=97) were collected over three separate data stations in the Fort Hays Limestone. These were highly serrate and perpendicular to bedding stylolites. They are consistently strike N-S, with steep westward dips and an average attitude of 174°-74° (Fig. 5.5). Cross-cutting relationships showed J_1 master joints consistently cross-cut stylolites. Cross-cutting relationships with strike-slip minor faults were unclear.

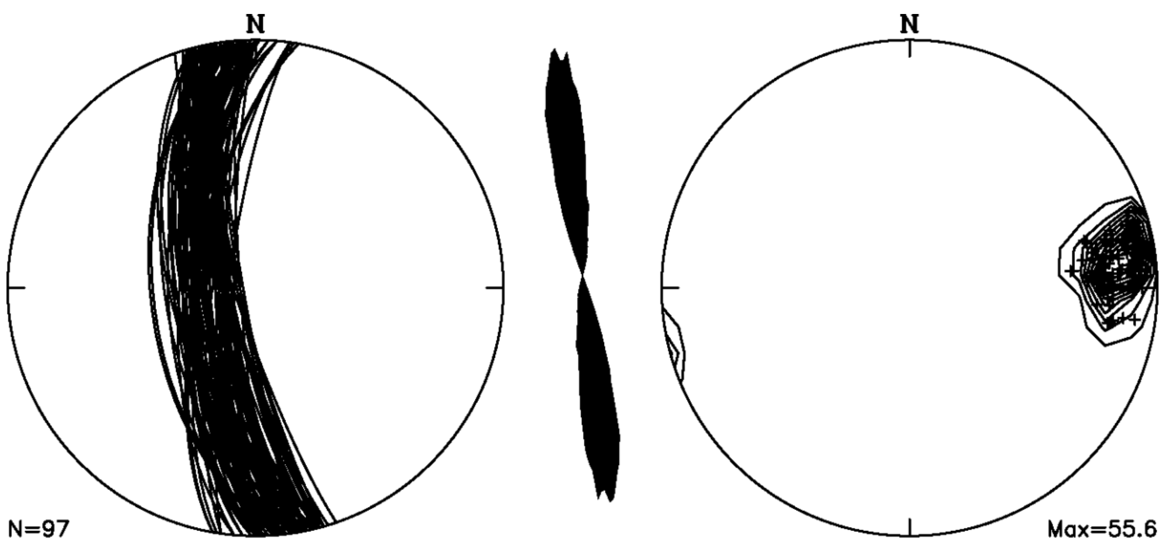

Stylolite Eigenvalues
E1: 0.9740 084-16
E2: 0.0168 197-54
E3: 0.0092 343-31

Figure 5.5. Stereoplots and roseplot of stylolite planes and contoured (CI 2%) poles to planes.

Bedding-oblique solution stylolites can be used as kinematic indicators of horizontal shortening axes normal to the plane of stylolite formation (Twiss and Moore, 1993). The average pole to stylolitic planes is 084°-16°, with a first eigenvalue of 0.9740 showing excellent clustering. The trend-plunge of pole to planes observed in stylolites is nearly identical to Laramide slip directions from slickenline attitudes (this study: 086°-14°) and calculated Laramide compression axes (this study: 086°-09°) (Figs. 5.3, 5.5).

<u>Joint Data Analysis</u>

1168 joint attitudes were collected in upper Cretaceous strata between Owl Canyon, CO and Boulder, CO (Fig. 5.6). Cross-cutting relationships identified the presence of an ENE to E-W J_1 joint set and a later NNW to N-S J_2 joint set that are consistently present at most data stations. J_1 joints cross-cut minor thrust fault surfaces, paralleled local right-lateral and left-lateral shear fractures, and bisect conjugate shear fracture orientations at various different localities across the study area. Initial observations were unclear as to whether some J_1 joints were strike-slip faults with no identifiable slicken-surfaces. Shear fractures with no identifiable slip sense could be easily misidentified if they have been reactivated by regional extension.

J_2 joints consistently abut J_1 joints and shear fractures through much of the study area, except in areas where pervasive calcite fill completely healed the fractures. J_2 joints commonly parallel bedding strike and dip 65° to 85° WSW (Fig. 5.6).

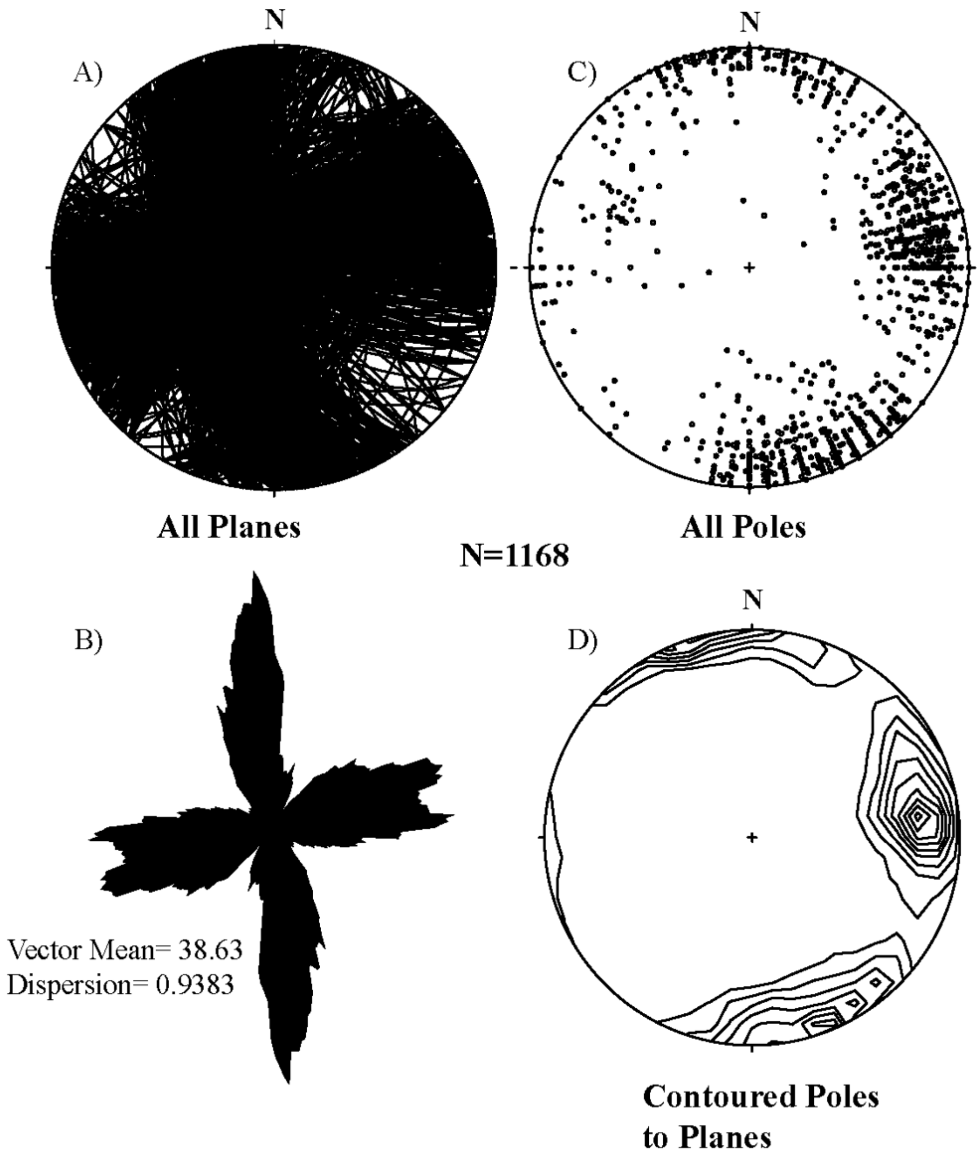

Figure 5.6. Joint data collected from Boulder, CO to north of Fort Collins, CO. A) Joint Planes, B) roseplot of joint planes, C) poles to joint planes D) 2% interval contours of poles to joint planes. J_1 joints strike ENE and J_2 joints strike NNW.

The average plane of J_1 and J_2 joints from each station were plotted on equal area stereonets as summary plots to quantify clustering, and to determine relative timing of jointing, whether some J_1 joints are actually strike-slip faults, and if J_2 joints have a tectonic origin or were the result of regional uplift (Fig. 5.7).

The average attitude of *in situ* J_1 planes is 078°-84° for all data stations with a first eigenvalue of 0.9269 (Fig. 5.7). Hypotheses of pre-Laramide jointing (Hennings et al., 2000; Berbauer and Pollard, 2004), were tested by rotating joint data bedding horizontal. The average attitude of rotated J_1 planes is 076°-89° with a first eigenvalue of 0.9446 (Fig. 5.7). If jointing preceded folding, rotating bedding dips out of the data should cause the first eigenvalue to substantially increase (Berbauer and Pollard, 2004). But past hypothesis of pre-Laramide jointing as the only way to get bedding perpendicular joints is invalid since J_1 joints abut Laramide shear fractures and still develop perpendicular to bedding. The minor increase between *in situ* J_1 first eigenvalues with rotated bedding horizontal J_1 eigenvalues is too little to be definitive as evidence for pre-Laramide timing of J_1 joints.

Comparing J_1 joint strikes to strike-slip fault plane attitudes shows NE- and ESE-orientations parallel average right-lateral and left- lateral faults respectively. Contours of poles to joint planes show three maxima, one which bisects the other two (Fig. 5.7). These styles include mode I extensional joints which parallel Laramide σ_1 trends for this study, and mode II shear fractures later reactivated by uplift or regional extension. Isolated abutting relationships between these fractures show shear fractures are older than E-W trending joints in the Niobrara Formation. Fractures that parallel average Laramide stress axes calculated from strike-slip and thrust fault data support Laramide jointing hypotheses, but may have occurred under slightly different tectonic conditions.

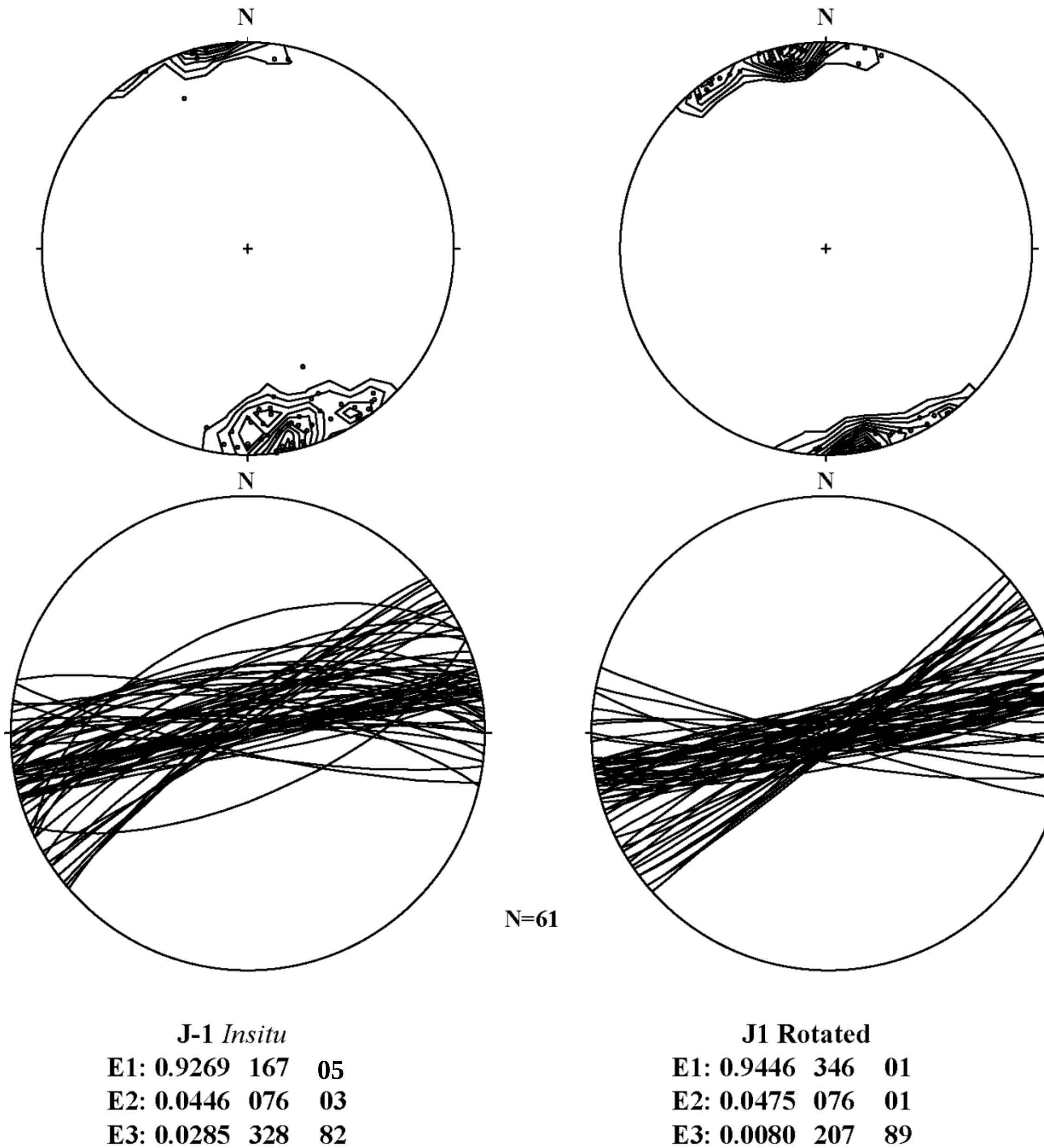

Figure 5.7. Stereonets of average J_1 attitudes for each station, contoured poles to planes (2% CI), and eigendata for *in situ* and bedding rotated horizontal J_1 planes.

The average attitude for *in situ* J2 planes is 170°-171° for 60 data stations and with a first eigenvalue of 0.9316. The average attitude of J_2 data rotated to bedding horizontal is 351°-89° with a first eigenvalue of 0.9650(Fig. 5.8).

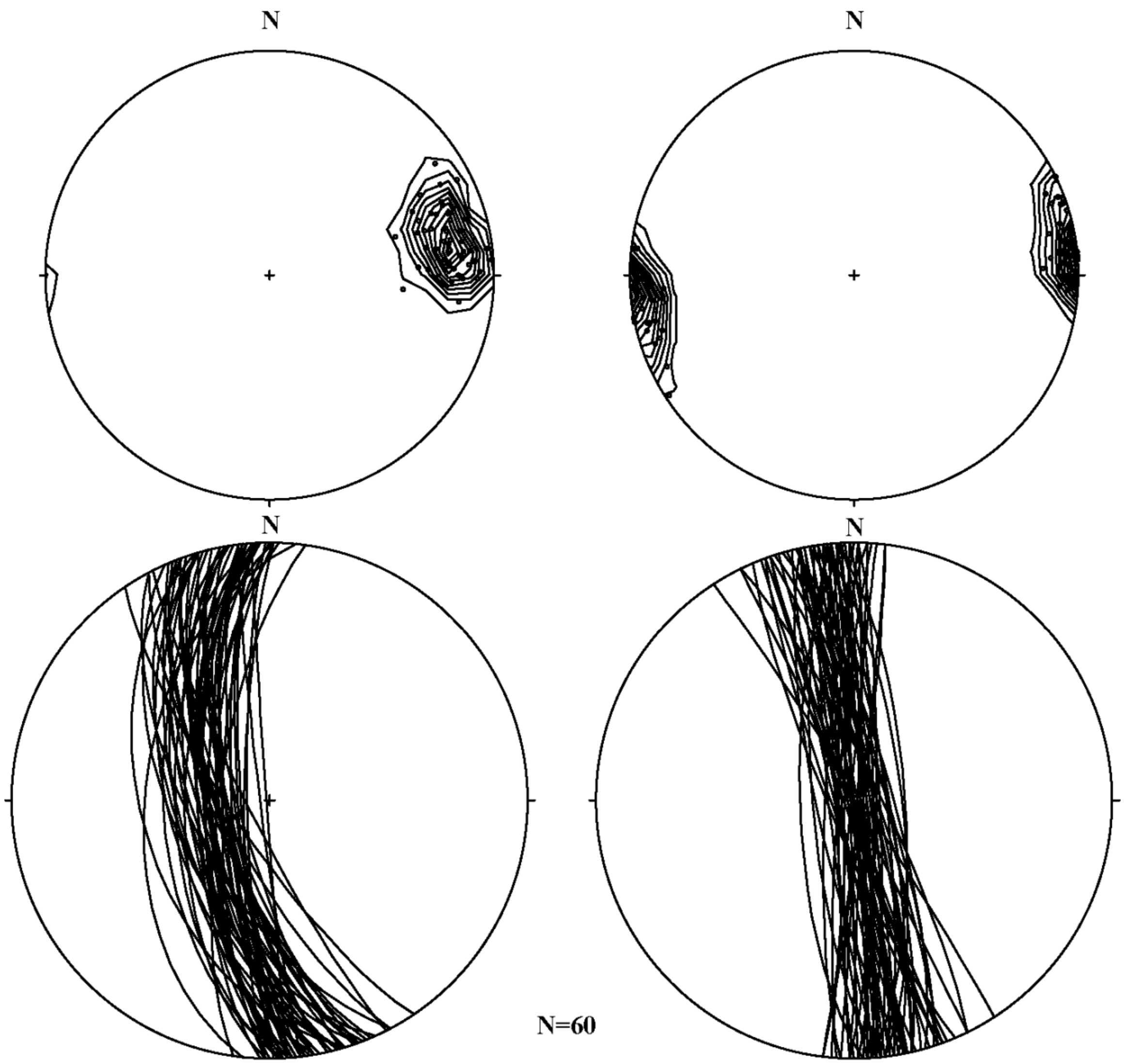

J-2 *Insitu*

E1:	**0.9316**	**080**	**19**
E2:	**0.0463**	**312**	**61**
E3:	**0.0221**	**177**	**21**

J2 Rotated

E1:	**0.9650**	**261**	**01**
E2:	**0.0220**	**171**	**07**
E3:	**0.0130**	**358**	**83**

Figure 5.8. Stereonets of average J_2 attitudes for each station, contoured poles to planes (2% CI), and eigendata for *in situ* and rotated J_2 planes.

Both J_1 and J_2 joint sets show comparable clustering values, where J_2 sets show a higher first eigenvalue (Figs. 5.7, 5.8). Higher first eigenvalues recorded in J_2 jointing suggests these fractures are not a cross-joint set to J_1 joints. Cross joints are typically associated with unloading and would predict a much higher variability in fracture orientations due to variable local surface stress. The presence of a secondary joint set that is nearly perpendicular to Laramide stress axes calculated for this study and the existence of compatible post-Laramide normal faulting supports hypotheses of post-Laramide regional extension in the direction of Laramide compression. Though minor fault analysis is unclear, J_2 jointing suggests some sort of E-W extensional processes have occurred in the Niobrara Formation along the northeastern Front Range after Laramide compression.

Calcite-Filled Fracture Analysis

Calcite-filled fractures (n=209) were measured in upper Cretaceous strata throughout the study area to determine preferred healed fracture orientations which may inhibit fluid movement along fracture planes, and identify whether these fractures are mode I opening fractures or mode II shear fractures.

The average orientation of calcite-filled fractures is 260°-81°, subparallel to J_1 joint trends, but showing a bimodal fracture distribution comparable to observed J_1 and J_2 joint sets in the Six Mile Fold subarea of Boulder, CO (Fig. 5.9). Roseplots of calcite-fracture fill (Fig. 5.9) show 4 fracture nodes. The north-trending nodes are calcite-filled fractures observed at Six Mile Fold approximately parallel to the local fold axes but nowhere else. ENE- and ESE- trending nodes are subparallel to common shear fractures throughout this study, and E-W nodes sub parallel J_1 joint trends.

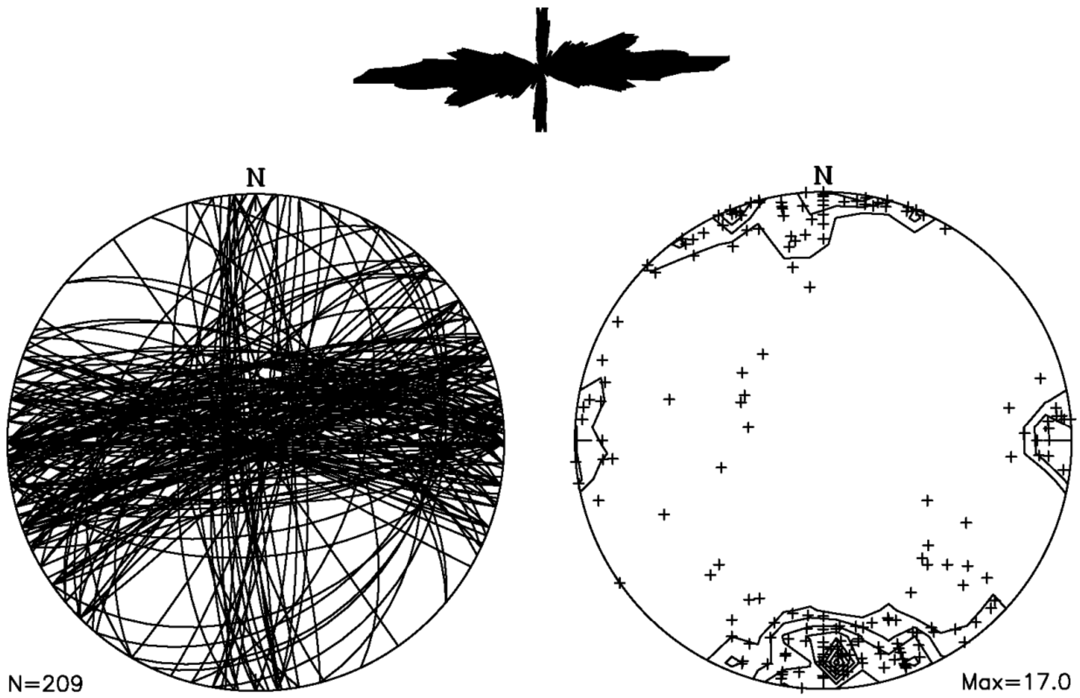

Calcite-filled Fracture Eigenvalues
E1: 0.6832 170-08
E2: 0.2395 260-03
E3: 0.0773 010-81

Figure 5.9. Stereonets of calcite fracture fill attitudes and contoured poles to planes (2% CI) including eigendata.

<u>Conclusions from Fracture Analyses</u>

Regional analyses of upper Cretaceous strain and stress axes using slickenlines and Compton's (1966) ideal σ_1 method from minor strike–slip and thrust fault data document a slightly bimodal subhorizontal Laramide stress with an average attitude of 086°-08° (Figs. 5.1, 5.2). Poles to bedding-oblique stylolite planes collected in the Fort Hays Limestone document shortening directions identical to average strike-slip and thrust slickenline trends of 86°-14°. Normal fault data was highly variable and yielded an average slip direction of 183°-73°. However, observations of normal dip-slip reactivation of right-lateral shear planes and cross-cutting relationships show that normal faults are younger than Laramide thrust and strike slip faults.

Joints observed throughout the study area document at least two separate joint systems. Abutting relationships show older J_1 joints have an average orientation of 78°-84° whereas younger J_2 joints have an average orientation of 170°-71°. J_1 joint strikes are often deviated from average σ_1 trends and some joints may be reactivated strike-slip faults. Jointing appears to have post dated faulting, with E-W-striking joints abutting right-lateral shear fractures. J_2 joints show remarkably consistent orientations with excellent clustering throughout the study area. The presence of NNW-striking J_2 joints is incompatible with Laramide shortening directions and indicates post-Laramide tectonic development. Average J_2 joint strikes are consistent with “frac into” orientations and borehole breakouts observed on the west side of the Denver Basin by Birmingham (2001) and Richter (B. Richter, personal communication, 2009). Conjugate shear fractures and ENE-trending joints are consistently calcite-filled and NNW-striking fractures show calcite mineralization only near fold hinges.

Chapter 6

3D Seismic Fault Analysis

The purpose of this chapter is to investigate subsurface fault geometries in the upper Cretaceous strata using two 3D seismic surveys adjacent to Wattenberg Field. These surveys include the publicly available Sooner Field (T8N R58W) 3D seismic survey collected in 1992 and the proprietary Dana Point (T3S, R64W) 3D seismic survey licensed by Echo Geo Inc. to Noble Energy Inc. in 2006 (Fig. 6.1). These two volumes will be used to test previous hypotheses concerning subsurface fracture mechanisms and quantify fault geometries occurring in the Denver Basin.

Previous subsurface studies and hypotheses

Faults occurring in upper Cretaceous Formations have been identified with subsurface 2D and 3D seismic data, and geophysical well log data. Multiple hypotheses have been proposed for their fault genesis, geometry, and their effects on both aquifers and hydrocarbon-bearing formations in the Denver Basin. Though already discussed in previous chapters, it is important to review past hypotheses derived from seismic and well log data sets to further understand subsurface fracture development in the Denver Basin and to review past structural models used to interpret complex faulting relationships observed in upper Cretaceous strata.

Haberman (1983) and Davis (1985) used 2D seismic lines and well control from Weld County to explain observed subsurface listric faults occurring in upper Cretaceous strata. Haberman (1983) studied seven seismic lines provided by Amoco in the Hambert

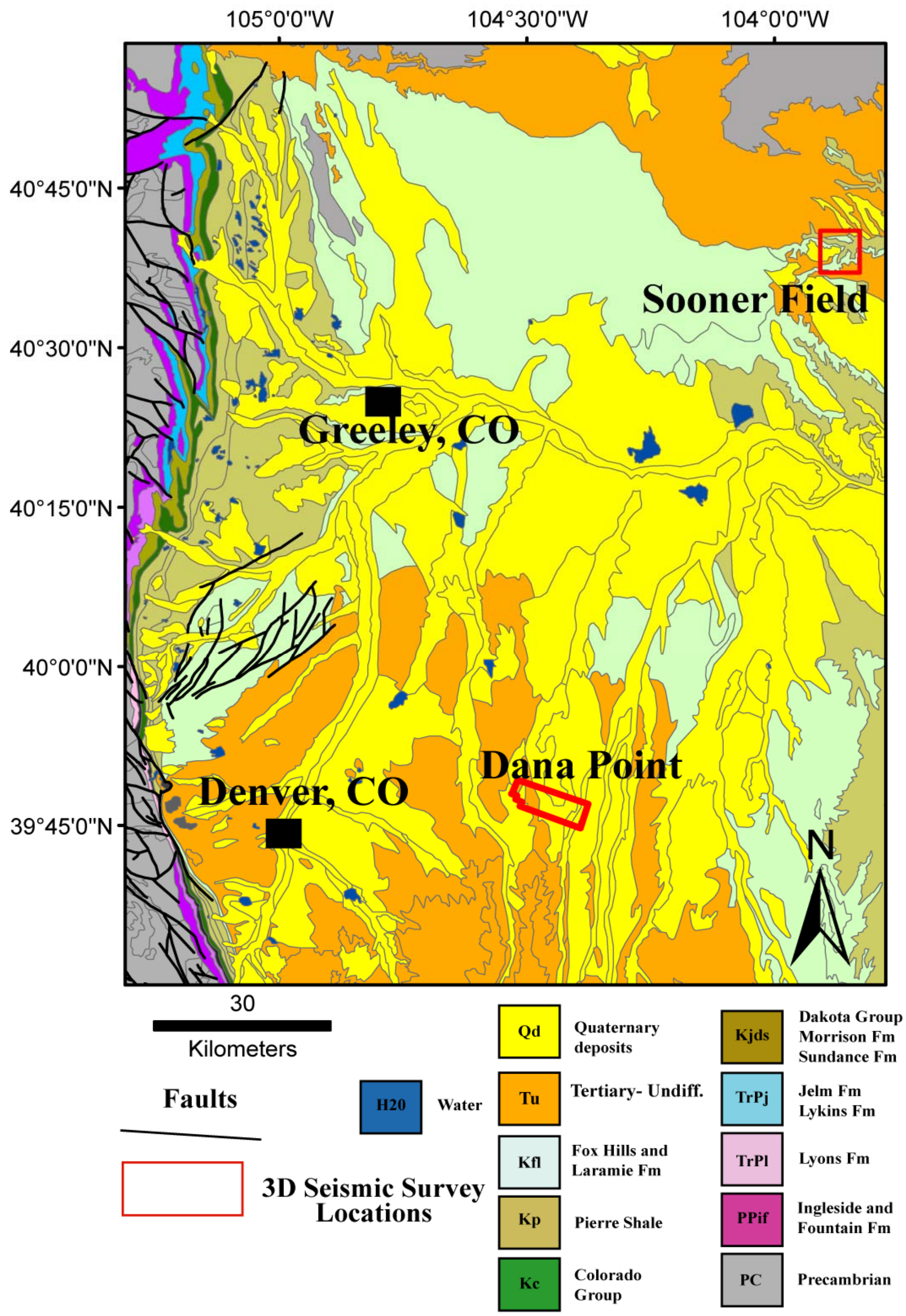

Figure 6.1. Simplified bedrock geologic map of the northeastern Front Range and central Denver Basin with 3D seismic study locations. Figure adapted from Brandt et al. (2003).

Field of Weld County (T4N, R65W) northwest of Denver, CO. Seismic lines show the Niobrara Formation is nearly horizontal, with multiple separations in the identified reflector. Lateral offset of these separations is observed in the immediately underlying Carlile reflectors and into lower portions of the Pierre Formation. Haberman (1983) interpreted concave-up faults that cross-cut the Niobrara Formation and Codell Sandstone of the Carlile Formation and sole horizontally into formations no deeper than the Graneros Shale. He showed near vertical faults in basement rocks below these listric interpretations though the top of basement is poorly constrained due to acoustic impedance problems (Haberman, 1983; Davis, 1985). Haberman (1983) also used electric log cross sections to identify missing section in both the Niobrara and Carlile formations.

Davis (1985) indentified listric fault geometries from reflector relationships observed in the Niobrara Formation. Davis (1985) hypothesized that seismic data could be useful in identifying basement structure from indirect evidence provided by the position of these listric faults. Davis (1985) states “Basement controlled faults may be invisible seismically except for indirect evidence such as the positioning of listric normal faults above the corners of deeper basement blocks or drape folding.” Davis (1985) showed three seismic lines, two of which transect the southern portion of Hambert Field E-W and one seismic line that was oriented N-S southwest of Hambert Field. Davis (1985) showed the same seismic lines with his interpretations showing concave up faults affecting the Niobrara, Hygiene zone, and Upper Pierre levels (0.25 to 0.75 seconds), and vertical fault interpretations that cut into basement (1.75 to 2.0 seconds). Haberman (1983) and Davis (1985) hypothesized that listric normal faults identified in seismic data and stratigraphic thins and thicks identified from well control were supportive of episodic movement of basement-controlled fault systems. They also hypothesized that listric normal fault interpretations supported the existence of the paleostructural “Wattenberg High” (Weimer and Sonnenberg, 1981).

Pritchett (1993) used detailed fault mapping of the Sooner Field 3D seismic volume to show normal listric faults, normal growth faults, planar normal faults, and reverse faults in basement rocks. Illustrations of amplitude anomalies in the Sooner Field by Pritchett (1993) were shown as evidence for the various fault types. Listric normal faults cutting the Niobrara Formation were shown to sole into the Graneros Shale. Subvertical normal and growth faults were shown to cut the Niobrara Formation with shallowing fault dips extending into Permian intervals. Basement faults were interpreted to have both normal and reverse motions. Pritchett (1993) hypothesized that potential fault mechanisms included regional basement wrench faulting, and regional uplift coincident with sedimentation. He linked them in strike-slip flower structures.

Kittleson (1988; 2004) used well control to examine the hydrogeology of the Laramie-Fox Hills Aquifer in Weld County, Colorado. He identified repeated sections of the Upper Pierre and Fox Hill Sandstone from electric logs. Isopachs of the Laramie-Fox Hill Sandstones showed considerable folding, whereas underlying sediments were planar and undeformed. Kittleson hypothesized that layer-parallel detachment surfaces explained thickening sections in the Laramie-Fox Hills sandstones and showed well-log cross-sections with a previously unrecognized *decollement* fault where upper sedimentary packages migrated basinward on bedding-parallel detachment surfaces. This discovery contradicted hypotheses of growth faulting in the area since the deformation involved overlying strata and thus must be post deposition. Thickening of strata previously thought to be due to growth faulting was shown to be caused by down-dip thrust faulting for this area.

Using well logs, seismic and Formation Micro-Imaging (FMI) logs, Birmingham (1998) quantified vertical offset of proposed faults from well control, but did not quantify heave or lateral offset in seismic data. True scale structural cross-sections, shown by Birmingham (1998), show listric normal faults cross cutting the Niobrara Formation and Codell Sandstone. These faults sole into the lower Niobrara Formation and below the Codell sands (Birmingham, 1998). Faults were also shown to cut into the lower Pierre Formation. High-angle normal faults were shown with minimum observed offset. Birmingham (1998) hypothesized that the Denver Basin was effectively compartmentalized by listric, reverse, and wrench faulting mechanisms though no data was provided to support reverse or wrench style motions.

Methods of 3D Seismic Fault Analysis

Initial analysis of both 3D seismic volumes involved using local well control to identify the Niobrara Formation's seismic stratigraphy and map it through both volumes. Separations occurring within the horizon were identified as faults based on observable offset or missing section.

Observations of subsurface faulting relationships in the Niobrara Formation were quantified by measuring fault dip direction, throw, heave, dip, and length at 1032 data stations in the two surveys. Fault attributes were collected 15 to 45 meters apart along fault strike from 16 faults in the Sooner Field survey and from 22 faults in the Dana Point survey. An adjacent proprietary 3D seismic survey's two-way interval velocity calculation of 3,327 m/s for the Niobrara Formation to J sand of the Dakota Group provided an approximate time to depth conversion. Fault lengths were calculated by summing the distance between fault stations from tip to tip. Fault throw values were calculated by subtracting the time of marker horizons in the footwall from the hanging wall values and then depth converted using the 3,327 m/s two-way interval velocity. Fault heave was measured as the horizontal distance between separated reflectors. Fault azimuth was calculated by taking the arctangent of (Dx / Dy), where Dx equals the difference between adjacent stations Easting coordinates, and Dy equals the difference between adjacent stations Northing coordinates. 180˚ was either added or subtracted to get the appropriate strike using the right hand rule which states that the dip direction is clockwise from the strike direction. Dip was calculated by taking the inverse tangent of throw divided by heave.

Subsurface fault data were compared between the two sites and to adjacent data sources to identify regional patterns and local variability, and to test previous hypotheses and interpretations of adjacent studies. Previous hypotheses to be tested include: reactivation of basement high angle faults with differing dip-slip shear (Haberman, 1983; Davis, 1985; Pritchett, 1993), flower structure strike-slip or wrench faulting with faults steeping at depth (Pritchett, 1993, Birmingham, 1998), and local or regional detachment faulting with the possibility of multiple episodes of slip (Kittleson, 1988, 2004). Subsurface fault findings were also compared to surface fracture data from this study to help constrain fracture timing and mechanisms occurring in the subsurface.

Sooner Field 3D Seismic Observations and Fault Analysis

Sooner Field is approximately 153 km northeast of Denver, CO along the eastern flank of the Denver Basin in northeastern Weld County, Colorado. Located in T8N, R58W, 3D seismic data were collected in 1992 over a 20 km^2 area in Sooner Field (Pritchett, 1993).

Using well log tops and synthetic seismograms derived from a sonic log in Sooner Field, the Niobrara Formation was interpreted through the seismic volume along with any identifiable faults (Fig. 6.2). Initial observations of faults showed concave-up fault geometries with low relative dips that cross-cut horizontal reflectors of the Niobrara Formation and lower portions of the Pierre Formation (Figs. 6.2, 6.3). This is consistent with observations by Haberman (1983), Davis (1985), Pritchett (1993) and Birmingham (1998) (Figs. 6.2, 6.3). Fault geometries showed faults eventually became horizontal as underlying reflectors were unaffected. No supportive evidence of faults steeping at depth was observed through the entire seismic volume as no conclusive faulting was observed below 1.45 seconds. No identifiable faults or anomalies were observed in basement rocks due to poor seismic resolution below Permian horizons. All faults identified in seismic data appear to have normal displacement with no evidence of thrust faulting or thickening of section in the Niobrara Formation.

Horizon maps of the Niobrara Formation show multiple normal faults with varying orientations throughout the study area (Fig. 6.4). Identified faults are not linear features but show gradual changes in fault strike from tip to tip (Fig. 6.4). The maximum fault length recorded for this study area was 2052 m, with an average strike of N-S. The second longest fault recorded a length of 1807 m and strikes N45E.

A)

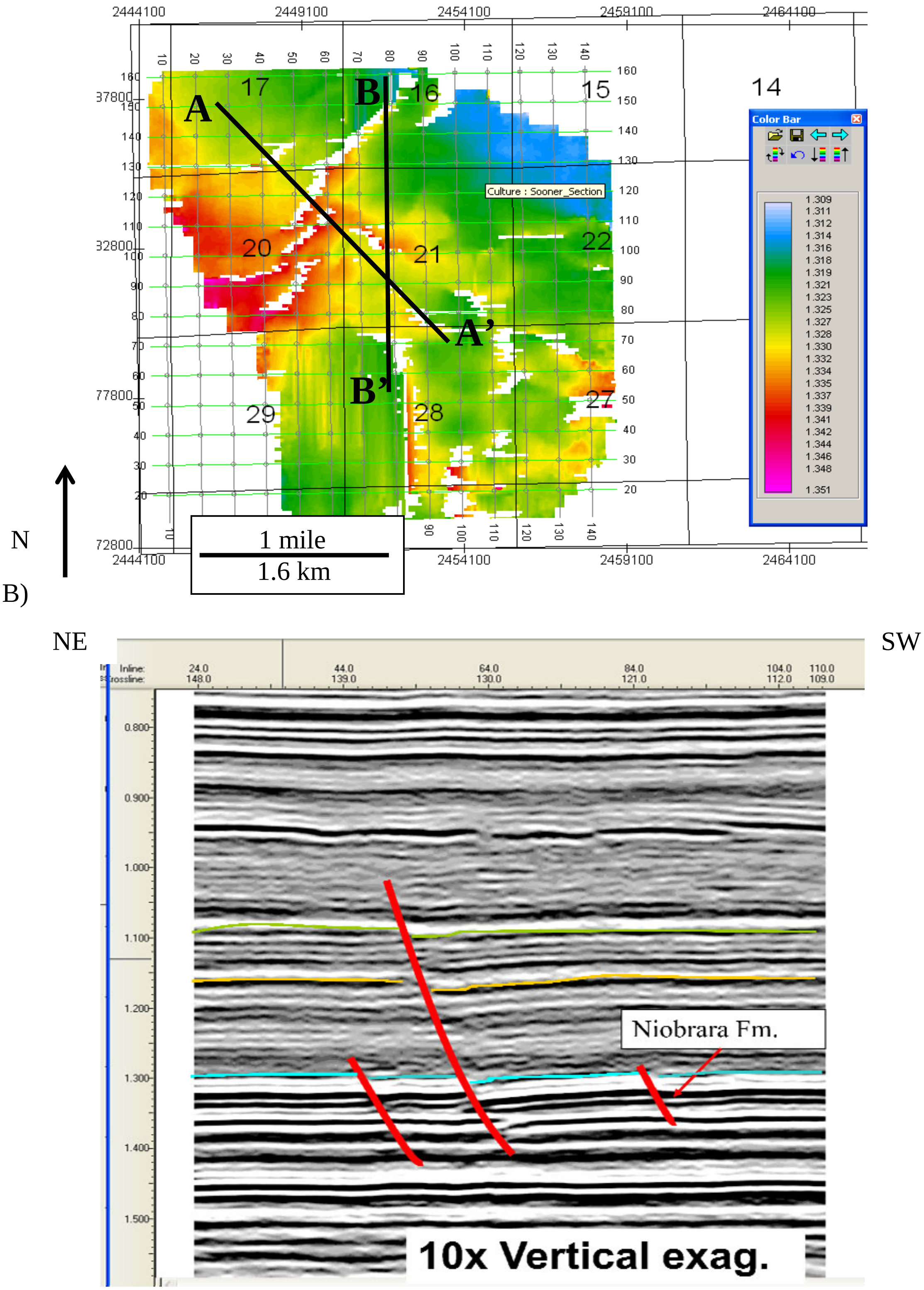

Figure 6.2. A) Amplitude horizon map of the Niobrara Formation. B) A-A' Interpreted seismic line from the Sooner Field data set with 10:1 vertical exaggeration. Faults are not clearly identified below the Graneros horizon, but show clear offset in to the lower Pierre Formation.

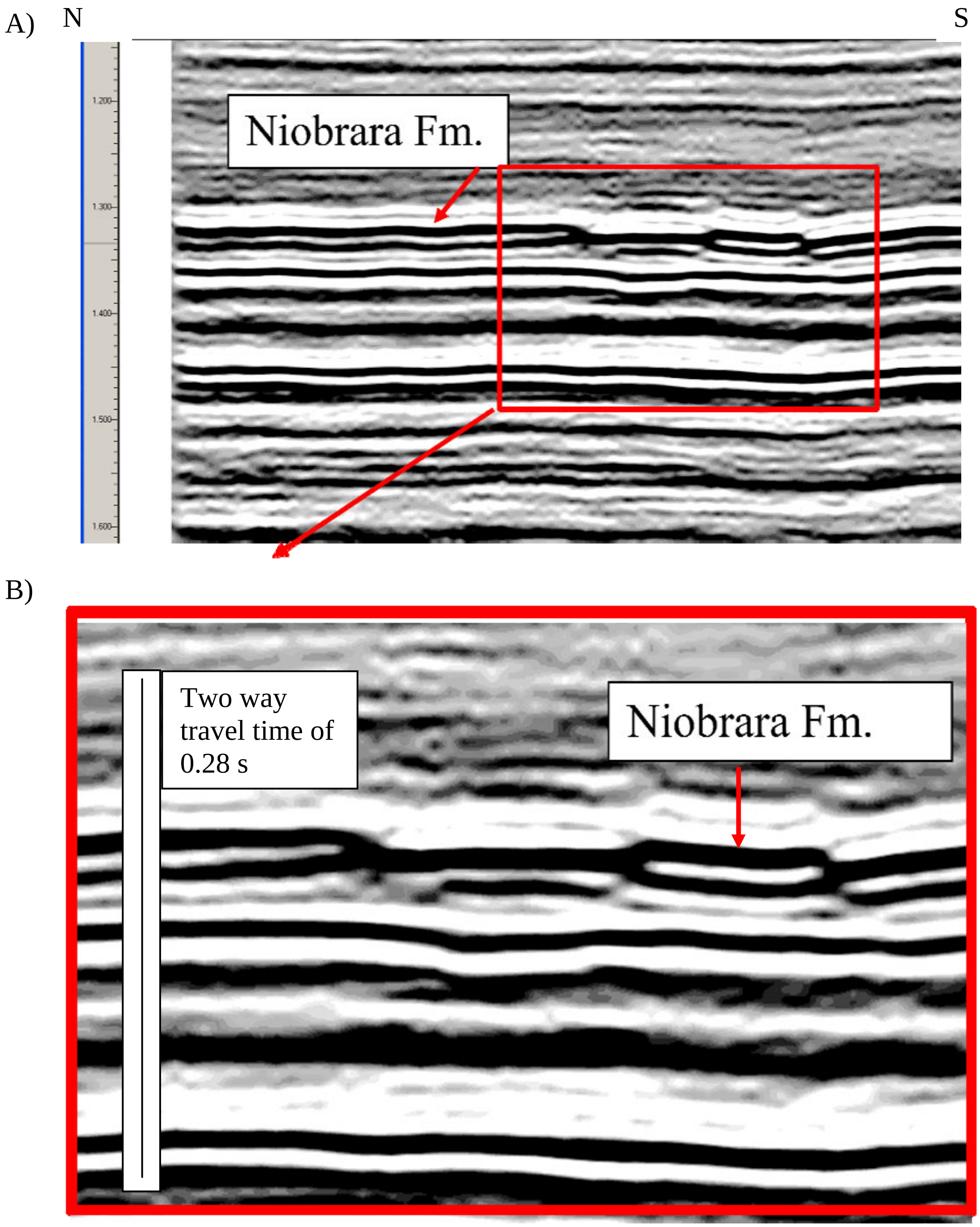

Figure 6.3. N-S seismic line through Sooner Field. A) B-B' Uninterpreted seismic line from the Sooner Field data set with 10:1 vertical exaggeration. Faults show concave up fault curvature. B) Red box shows 200% amplification. Location of seismic line available in Fig. 6.2

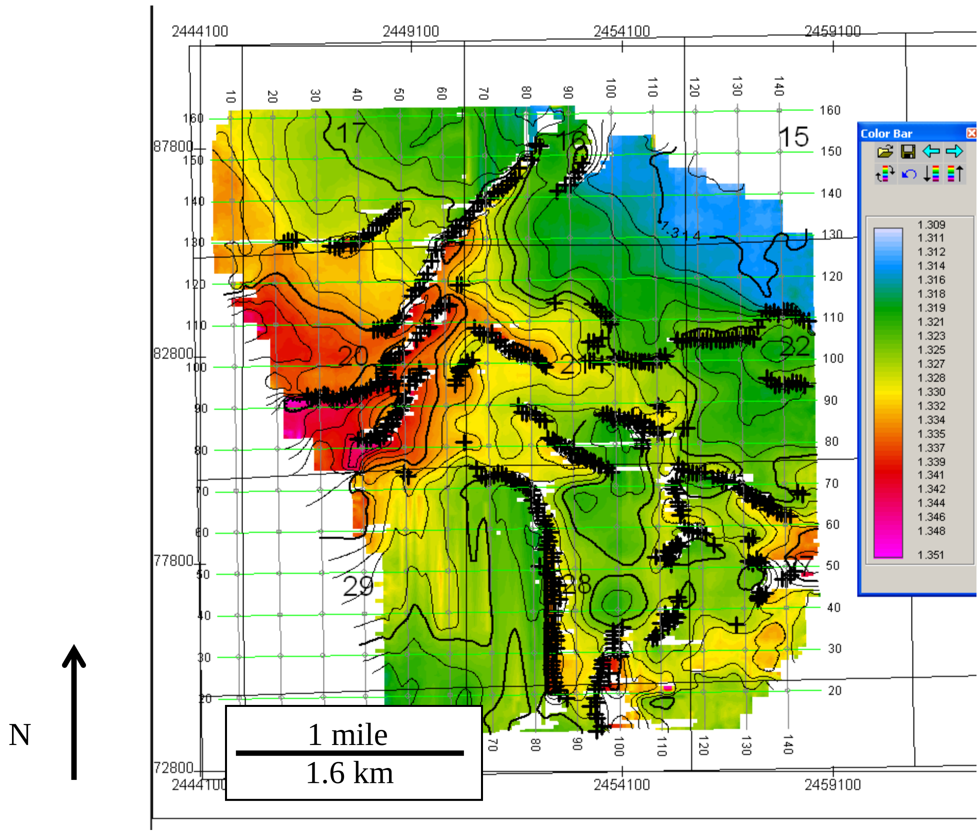

Figure 6.4. Amplitude time horizon map of the Niobrara Formation at Sooner Field (T8N, R58W). Black crosses indicate location of interpreted faults from cross line and inline seismic profiles. Scale bar shows down thrown amplitudes as warm colors with 0.01s contour interval.

Faults throw and heave values were measured perpendicular to fault strikes to identify fault geometries and to calculate dip values at data stations. Measured faults in the Sooner Field survey average 11 +/- 4 m (+/- 1 STD) of vertical offset with a maximum throw of 22 m (Fig. 6.5). Fault heave on these faults average 76 +/- 26 m (+/- 1 STD) of horizontal offset, with a maximum heave of 204 m (Fig. 6.6). Average heave values exceed average throw values by nearly 4:1, indicating low fault dips.

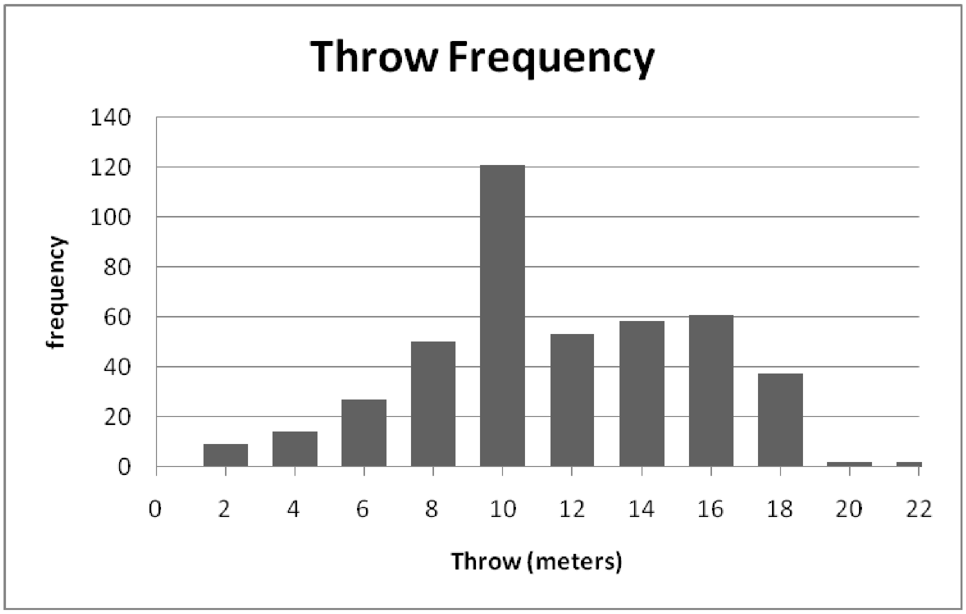

Figure 6.5. Fault throw histogram from 434 stations measured in the Sooner Field seismic volume. Throw averages 11 +/- 4 m (+/- 1 STD).

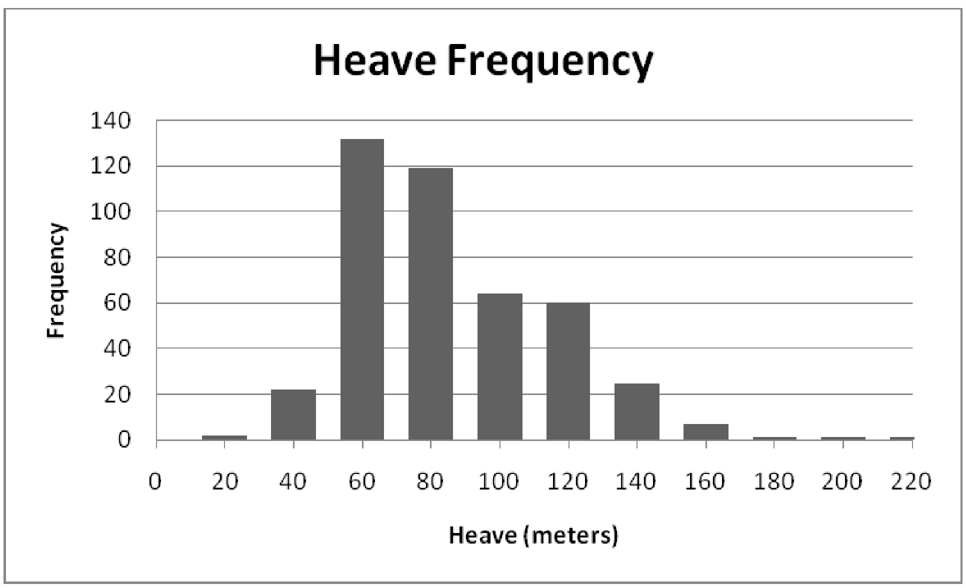

Figure 6.6. Fault heave histogram from 434 stations measured in the Sooner Field seismic volume. Heave averages 76 +/- 26 m (+/- 1 STD).

Calculations of fault dips confirm low-angle faulting estimates and show fault dips average 8° +/- 4° (+/- 1 STD) with maximum fault dips never exceeding 24° (Fig. 6.7). 96% of the data stations through this study area had fault dips less than 15° and occurred at nearly all dip directions (Figs. 6.8 and 6.9). Fault dips greater than 15° occurred at only 26 stations with dip directions of 013° to 030°, 82° to 139°, 208°, and 321° to 360°. 27% of fault dips were greater than 15° (n=8), occurring along dip directions parallel to 208° (Fig. 6.9).

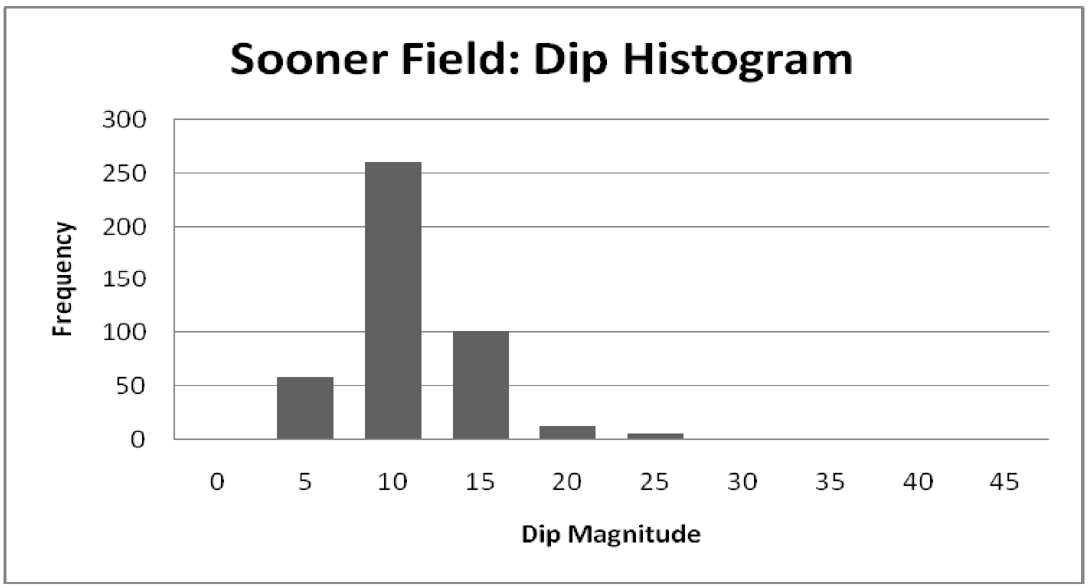

Figure 6.7. Fault dip histogram from 434 stations measured in the Sooner Field seismic volume. Dips average 8° +/- 4° (+/- 1 STD).

Dip directions from all 434 data stations were measured to identify preferred fault plane dip directions and make estimates on a direction of preferred slip. Multiple dip directions observed are expected due to the arrangement of faults occurring in this study area. No dip directions occur between azimuths of 222° to 268° and 270° to 305°. Dip directions with the highest observed frequency trend between 120° to 150° and 180° to 230° (Fig. 6.8). Plotting dip directions and dip together confirm multiple orientations of low-angle faults with a mean vector strike of N75E with a dispersion of 0.7076 (Figs. 6.9 and 6.10).

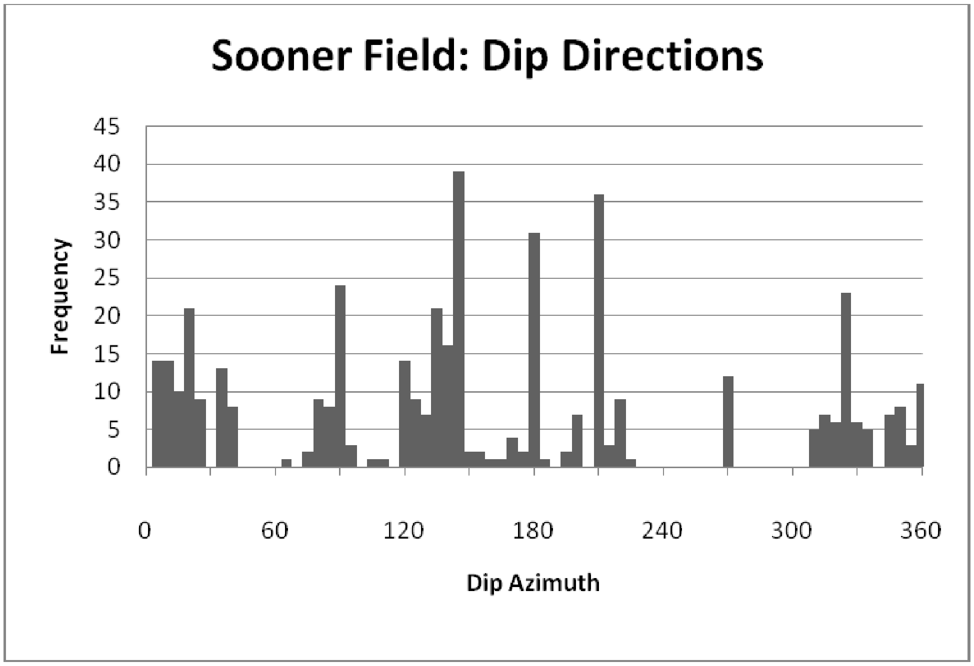

Figure 6.8. Dip directions observed from 434 stations in the Sooner Field seismic volume.

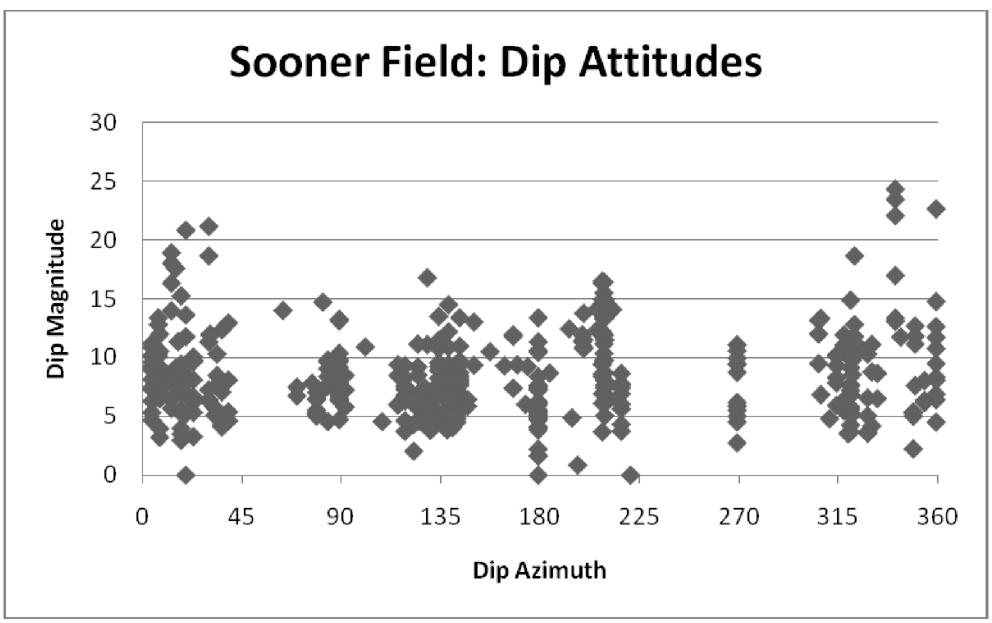

Figure 6.9. Dip directions with dips observed from 434 stations in the Sooner Field seismic volume.

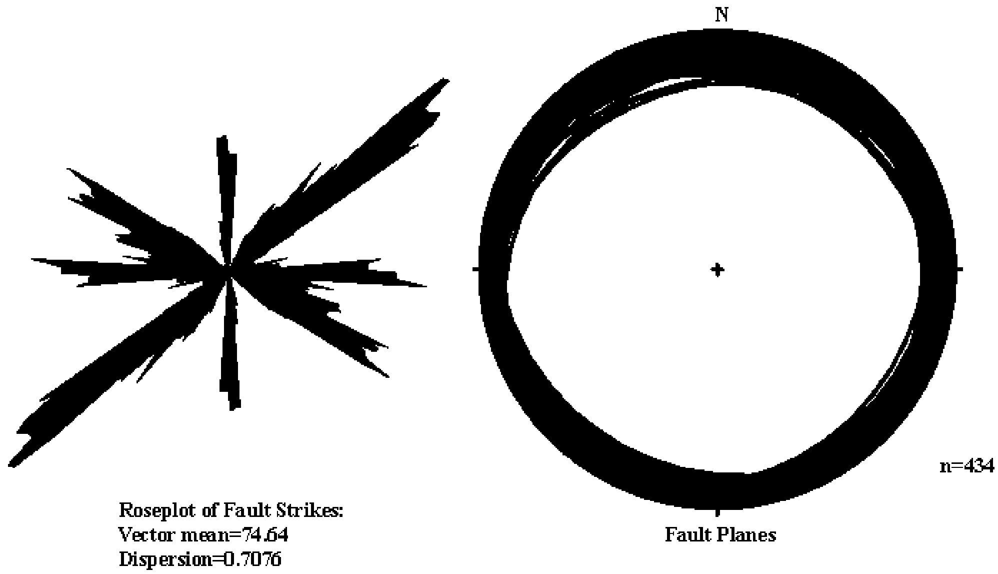

Figure 6.10. 10° smoothed roseplot and equal area stereonet of all fault planes in the Sooner Field study area.

Dana Point 3D Seismic Observations and Fault Analysis

Dana Point is approximately 56 km west of Denver, CO (T3S, R63W), along the eastern flank of the Denver Basin in Adams County, Colorado. The Dana Point 3D seismic survey covers five small operational fields including the Manila, Sonar, Giudon, Bennett and Zenith fields. Echo Geophysical Inc. licensed the Dana Point survey to Noble Energy Inc. in 2006 where multiple proprietary interpretations have occurred.

Using geophysical well log tops from the Dana Point area, the Niobrara Formation was mapped through the seismic volume along with any identifiable faults. Initial observations of faults showed planar fault geometries with higher apparent dips than Sooner Field. They cross-cut gently NW-dipping horizons of the Niobrara Formation and planar normal fault geometries differ from observations of listric fault geometries at Sooner Field in this study and by previous workers (Haberman, 1983; Davis, 1985; Pritchett,1993; and Birmingham,1998) (Figs. 6.11, 6.12).

A)

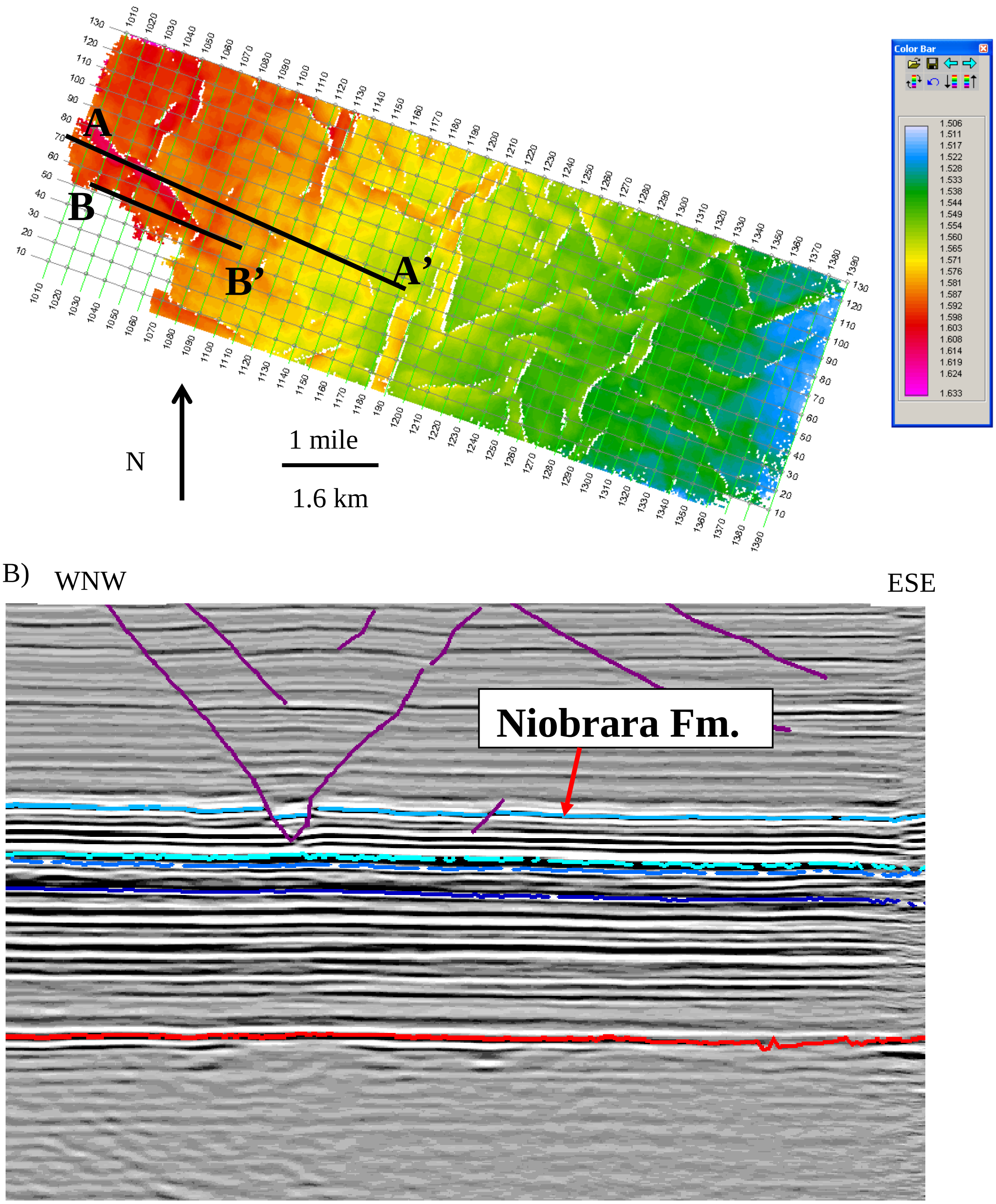

B)

Figure 6.11. A) Amplitude horizon map of the Niobrara horizon. B) A to A' WNW-ESE seismic line through Dana Point. The interpreted seismic line from the Dana Point data set with 10:1 vertical exaggeration shows faults are not clearly identified below Graneros horizon but show clear offset into the lower Pierre Formation.

A)

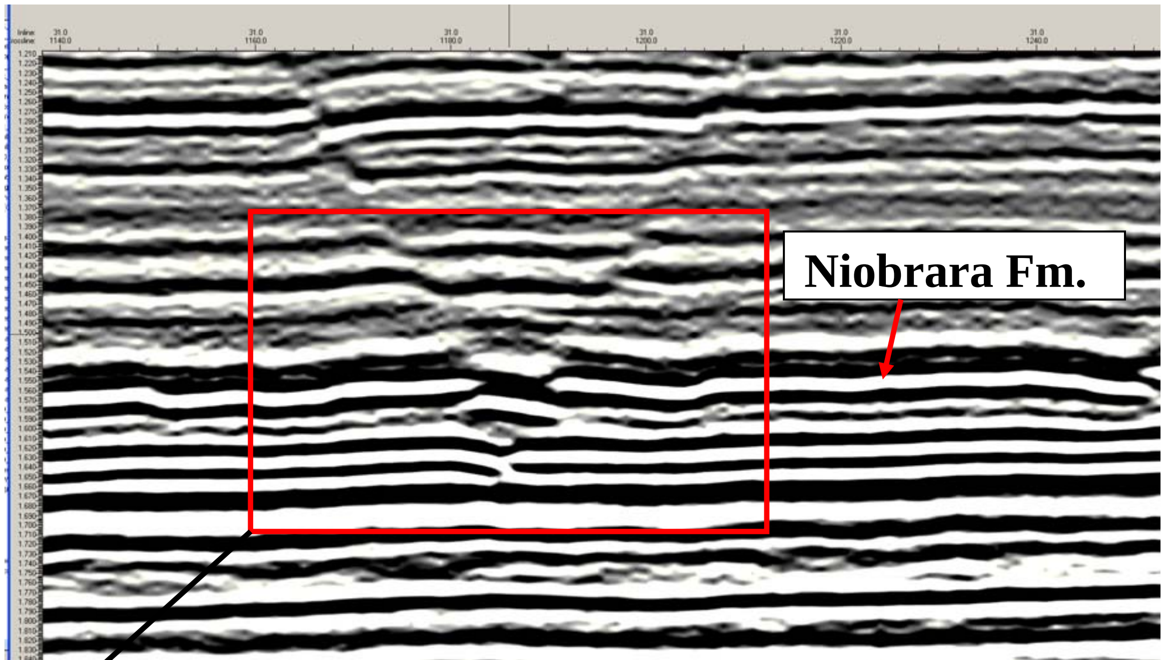

B)

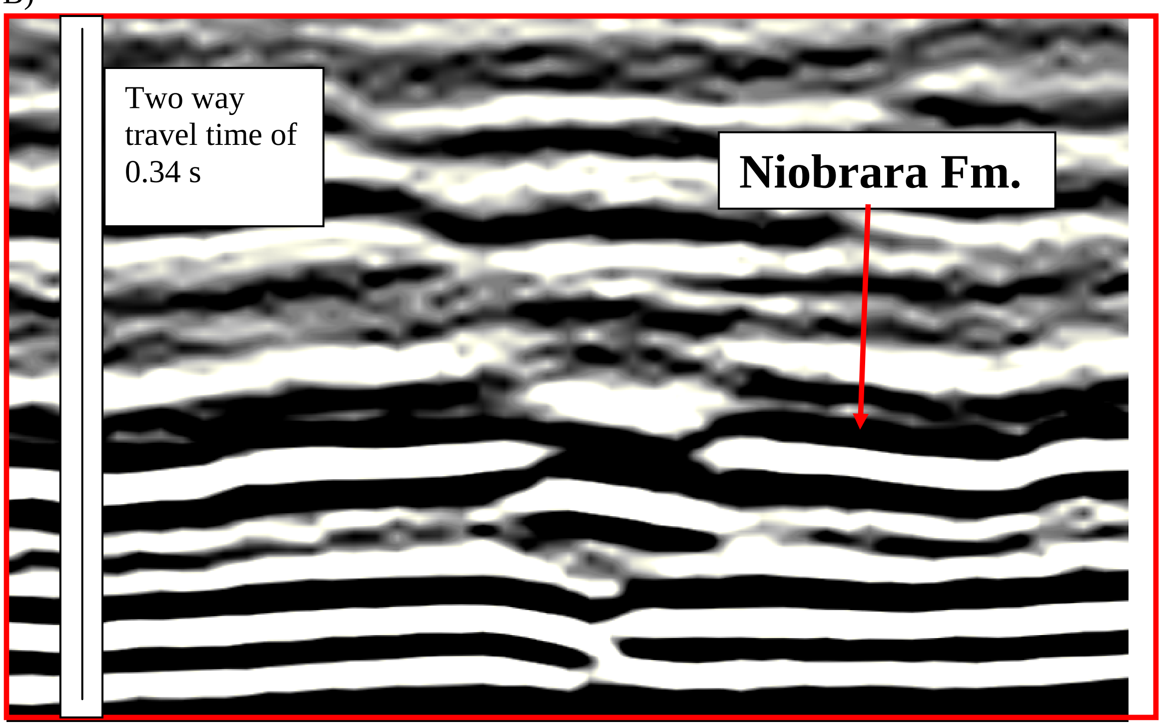

Figure 6.12. A) B-B’ uninterpreted seismic line from the Dana Point data set with 10:1 vertical exaggeration. Faults show planar fault curvature. B) Red box shows 200% amplification. Location of seismic line available in Fig. 6.14.

Fault geometries show that faults abruptly terminate into underlying reflectors probably associated with the Graneros Shale. Concave-up fault curvature is not as clear in the Dana Point survey as the Sooner Field survey. No supportive evidence of faults steeping at depth was observed through the entire seismic volume as no conclusive faulting was observed below 1.65 seconds. Horizon maps of the Niobrara Formation

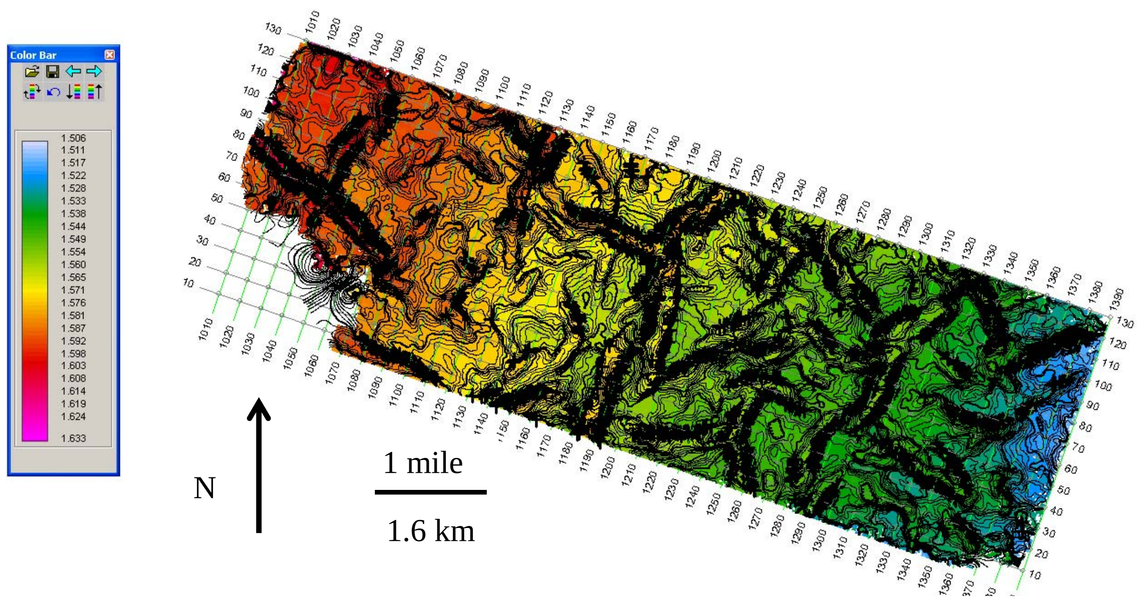

Figure 6.13. Amplitude horizon map of the Niobrara Formation at Dana Point (T3S, R63W). Black crosses indicate location of interpreted faults from cross-line and inline seismic profiles. Scale bar shows down thrown amplitudes as warm colors with 0.01 s contour interval. B to B' is Fig. 6.11 and 6.12. Seismic data courtesy of Echo Geophysical Inc.

show multiple normal faults with varying orientations throughout the study area (Fig. 6.13). Identified faults are not linear features but show changes in fault strike from tip to tip .The maximum fault length recorded for this study area is 1837 m with an average strike 030°. The second longest fault strikes 126°. These faults do not cut through to basement.

Faults throw and heave values measured perpendicular to fault strikes were used to identify fault geometries and to calculate dip values at data stations. Measured faults in the Dana Point 3D seismic survey average 23.5 +/- 9 m (+/- 1 STD) of throw with a maximum offset of 50 m (Fig. 6.14). Observations of fault heave show faults in this study area average 49 +/- 11.5 m (+/- 1 STD) of horizontal offset with a maximum heave of 123 m (Fig. 6.15). Average heave values exceed average throw values by nearly 2.5:1. This contrasts with heave to throw ratios (4:1) observed at Sooner Field.

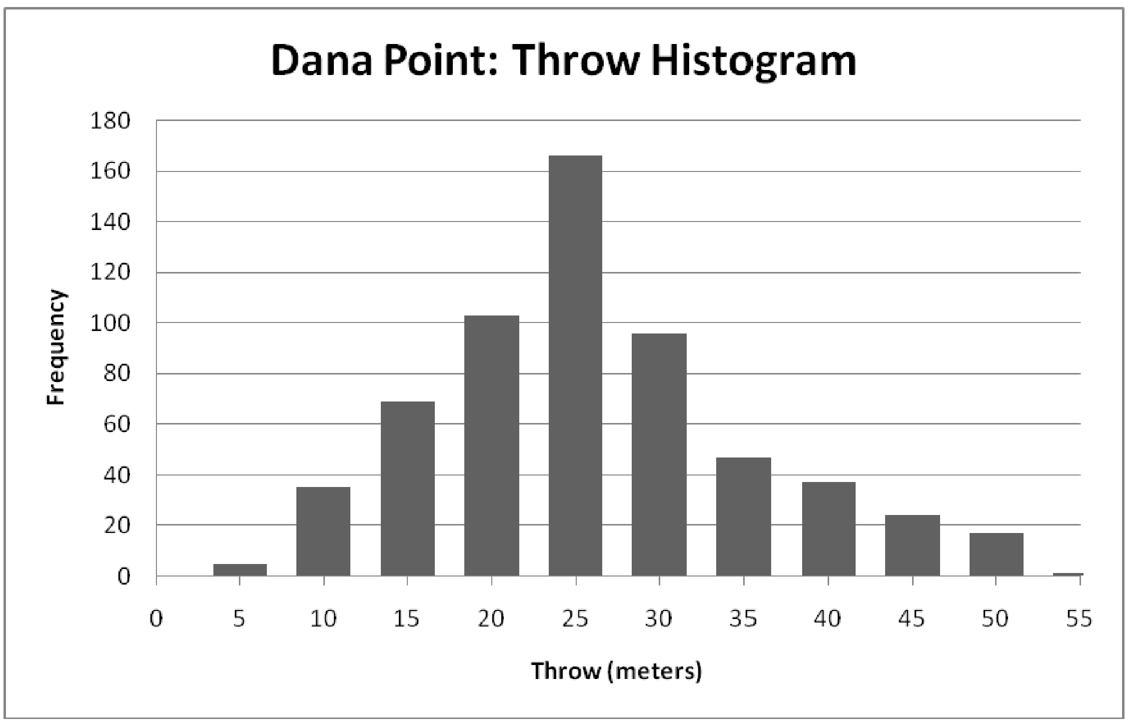

Figure 6.14. Fault throw histogram from 600 stations measured in the Dana Point seismic volume. Throw values average 23 +/- 9 m (+/- 1 STD).

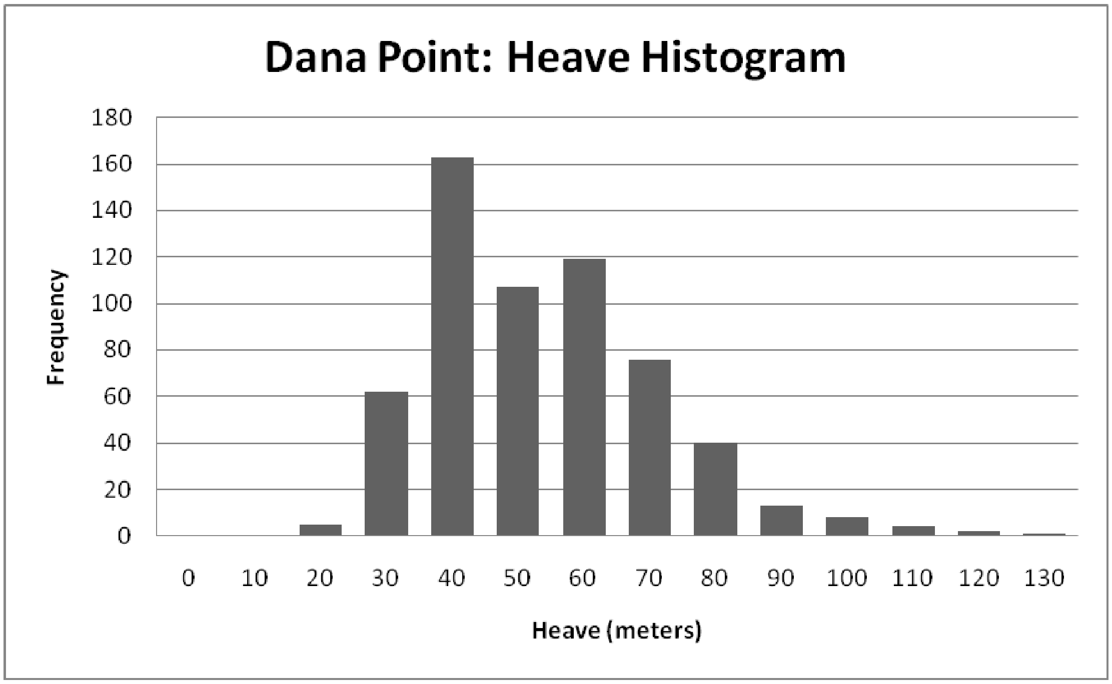

Figure 6.15. Fault heave histogram from 600 stations measured in the Dana Point seismic volume. Heave values average 49 +/- 11.5 m (+/- 1 STD).

Calculated fault dips confirm higher fault plane dips, with average dips of 27° +/- 12° (+/- 1 STD) and a maximum fault dip of 61° (Fig. 6.16). 10.5% of the data stations through this study area (n=63) recorded dips greater than 45°, and occurred at dip directions of 109° to 117°, 132° to 154°, 199° to 233°, 282° to 296°, 316°, and 345°. 52 of the 63 fault data stations have dips exceeding 45° and strike between 19° and 53° (Fig. 6.17). Fault dips of less than 15° occurred at 102 stations, with dip directions of 005° to 046° and 109° to 345° (Fig. 6.17). Average fault dips of Dana Point exceed average fault dips of Sooner Field by nearly 20°. The entire seismic fault study shows an average fault plane dip of 19° (1043 stations along 37 faults) in the Niobrara Formation. No evidence of fault steepening at depth has been observed at either locality.

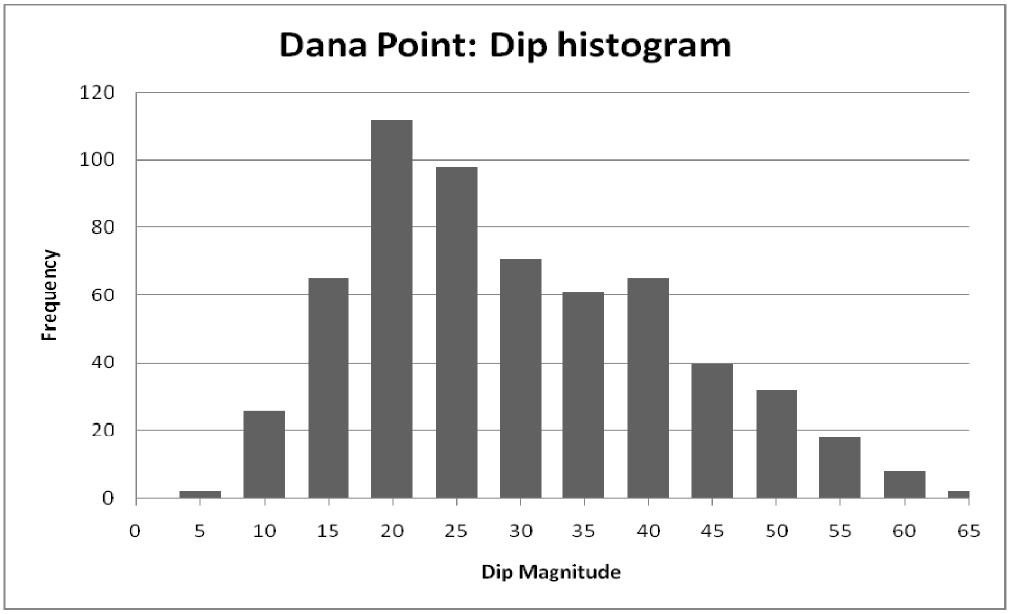

Figure 6.16. Dip magnitudes observed at 600 stations in the Dana Point seismic volume. Dana Point's average dip through the study area is 27° +/- 12° (+/- 1 STD) with a maximum fault dip recorded of 61°.

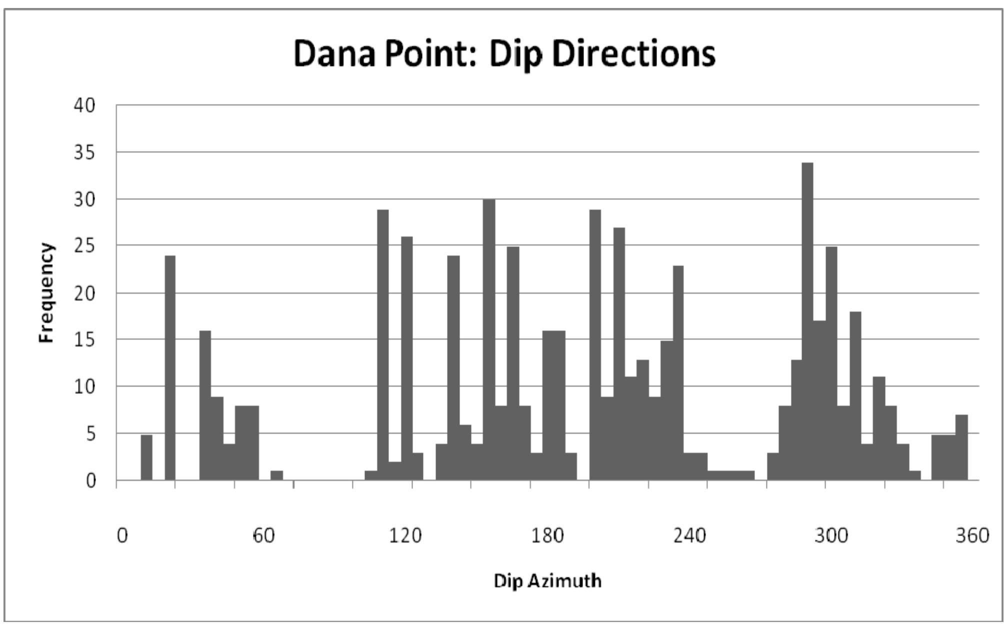

Figure 6.17. Dip directions observed at 600 stations in the Dana Point seismic volume.

Dip directions from all 600 data stations were measured to identify preferred fault plane dip directions and make estimates on direction of preferred slip. Multiple dip directions observed are expected due to the arrangement of faults occurring in this study area. No dip directions occur between azimuths of 075° to 100°. Dip directions with the highest observed frequency trend between 075° to 250°, 180° to 230°, and 275° to 340° (Fig. 6.17). Plotting dip directions and dip together show higher dip angles on fault planes dipping in the SW-quadrant (Fig. 6.18). A 10% smoothed roseplot shows a mean vector for fault strikes of N66E with a dispersion of 0.8493 (Fig. 6.19).

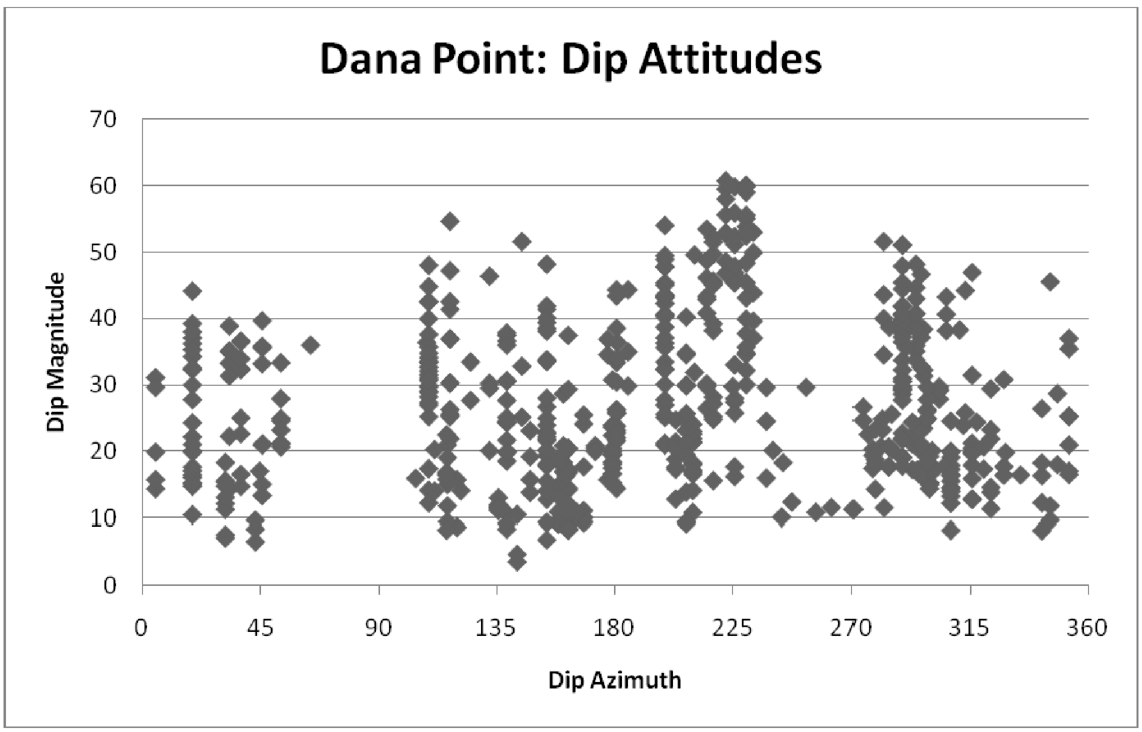

Figure 6.18. Dip directions with dips observed from 600 stations in the Dana Point seismic survey. Highest dip magnitudes recorded in SW- quadrant.

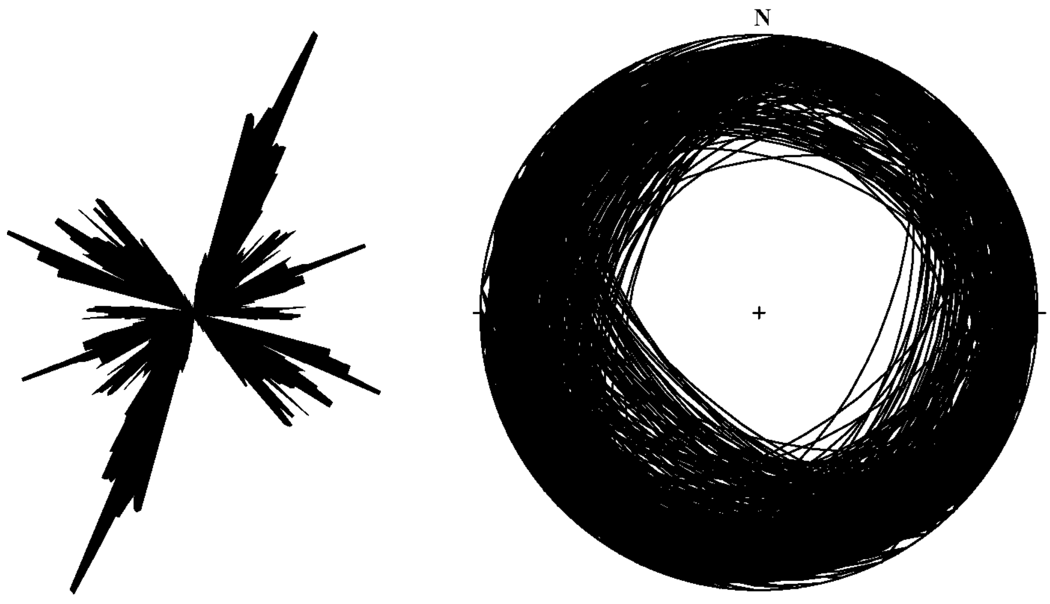

Figure 6.19. 10° smoothed roseplot and stereonet of fault planes. Seismic data courtesy of Echo Geophysical Inc.

Conclusions

Observations between the two seismic surveys show comparable faulting relationships. At both localities, evidence of faulting was indistinguishable much lower than the Niobrara Formation horizon marker. No faulting was observed below 1.45 seconds at Sooner Field (approximately 2400 meters) and 1.65 seconds at Dana Point (approximately 2740 meters) which approximately related to the Graneros Formation. No evidence of fault steepening or concave downward geometries was observed at either study locality. All faults examined appear to have normal dip-slip geometries, either as listric normal faults or planar normal faults. Fault strikes are variable along the fault length at both locations showing multimodal orientations, however both volumes show the longest faults have a NE-strike (Sooner Field= 045°, Dana Point= 030°). No vertical basement faults were observed in either volume.

Several observations are not consistent between the two seismic volumes. Sooner Field's average fault dip recorded is 8º while Dana Point's average fault dip is 27º. 83% of the fault dips recorded at Dana Point exceed dips of 15º, but only 4% do so at Sooner Field. Sooner Field showed no fault dips exceeding 24º, whereas 52% of the fault dip data collected at Dana Point exceed 24º with a maximum dip recorded of 61º. Investigations of fault geometries from cross-sections show fault types may also be different between the two volumes. Sooner Field is dominated by concave up listric fault interpretations, were as Dana Point shows more planar normal fault expressions. Increased dip magnitudes observed at Dana Point confirm these fault style differences. No clear basement faulting was identified at either survey.

Comparing subsurface fault data to surface fracture data from this study shows some comparable normal fault geometries, however clear strike-slip evidence is absent in subsurface data sets. Surface minor fault data predicts right-lateral slip trending 069º and left-lateral slip trending 101º. The largest normal faults in subsurface data sets subparallel Laramide right-lateral strike-slip faults observed at the surface in this study, but their low angle contrasts with the near vertical Laramide right–lateral faults observed at the surface. Dip data generated from this study contradicts hypotheses of both fault steepening at depth and basement reactivation.

Interpretations by Haberman (1980), and Davis (1985) of vertical basement faults and basement reactivation in Hambert Field were inferred by the position of listric faults identified in upper Cretaceous strata. Velocity anomalies below interpreted listric faults and acoustic impedance problems near basement contacts documented by Davis (1985) make basement faults highly interpretive and should be regarded with low confidence.

No continuous basements-to-Cretaceous faults were observed in this study which further questions hypotheses invoking basement block movement. Wrench faulting mechanisms and sub-vertical normal fault hypotheses presented by Pritchett (1993) are also not supported by this study. Very-low-dip angles observed at both localities, the lack of clear fault steepening at depth, and no clear basement offsets are inconsistent with Pritchett's (1993) strike-slip flower structure model.

Hypotheses invoking detachment and layer parallel slip are attractive due to low observed fault angles and listric normal fault geometries. However preferred slip directions are inconclusive from dip direction data. Low dip angles (<15°) observed at Sooner Field are prevalent in nearly all dip directions, whereas low dip angles (15°) observed at Dana Point occur along dip directions between 005° and 046°, and 109° to 345°. No thrust faults were identified at either locality, and balancing arguments have not been addressed by this study.

Dominant normal listric fault geometries and the incompatibility of subsurface fault dip directions with Laramide σ_1 axes suggest post-Laramide extensional mechanisms as a reasonable solution. However two major problems persist in explaining subsurface faulting and fracturing mechanisms in upper Cretaceous strata. Why do normal fault geometries dominate upper Cretaceous sections and not substratigraphic intervals, and where does this layer extension balance?

Recent hypotheses regarding polygonal faulting generated by either density inversion (Watterson at al., 2000) or differential compaction (Davies et al., 2005; 2009) may help address these issues. Watterson's (2000) 3D seismic investigation of the Lake Hope area in southern Australia shows comparable fault geometries and low fault dips with seismic data sets of the Denver Basin. Watterson et al. (2000) hypotheses that polygonal fault systems are generated by density inversions caused by burial of a low-density layers by a normally pressured sequence. Davies et al. (2009) also shows comparable fault geometries with variable orientations and shallow dips from 3D seismic data acquired offshore of Norway. Davies et al. (2009) hypothesizes that polygonal faulting is a result of "cells" were silica diagenesis has occurred at varying burial depths and chemical alterations lead to mechanical compaction and porosity reductions. Circular depressions then form above "cells" and normal fault networks form at the margins of folds generated by differential compaction (Davies et al., 2009).

Other potential hypotheses that do not involve basement reactivation or wrench fault mechanisms include post-Laramide removal of overburden and uplift causing rock volume expansion in multiple orientations; post-Laramide thermal contraction variations in various reservoir rocks during hydrocarbon maturation; slippery bedding-parallel surfaces and reduced internal frictional coefficients; and/ or simple local extensional forces which shatter brittle limestone rocks and accommodate normal fault geometries in shale layers. These hypotheses require further investigation into reservoir geomechanics, mechanical rock properties, and burial/and uplift reconstruction models.

Chapter 7

Conclusions

Low permeability reservoirs like the Niobrara Formation can be economically significant if natural fracture systems are present. Both shear and extensional fractures identified from outcrop in the Niobrara Formation and subsurface studies from the Denver Basin indicate reservoir anisotropy and provided critical tests to tectonic hypotheses. By identifying the mechanisms and timing of naturally-occurring fractures, a better understanding of hydrocarbon transport and storage in open fracture networks of foreland basins is possible. This thesis addressed the complex fracture systems in the Rocky Mountain Foreland, a topic of intense debate regarding fracture genesis, timing, and economic significance to hydrocarbon production.

Previous hypotheses for the origin of fractures within the Denver Basin include: a) propagation of reactivated Precambrian faults into Cretaceous sedimentary rocks during Laramide vertical block motion, Laramide subhorizontal compression, multidirectional slip and post-Laramide extension as well as, b) regional and/or local detachment either in front of basement-cored arches or basin-ward by gravitational sliding. The primary objective of this research is to constrain mechanisms responsible for shear and extensional fractures occurring within the upper Cretaceous Niobrara

Formation of the Denver Basin. This was done by the determination of strain and stress axes across the study area through fracture analysis.

Fault and fracture measurements were collected at 61 outcrop locations in upper Cretaceous strata along the western margin of the Denver Basin. Kinematic analyses of faults using slickenlines and Compton's (1966) ideal σ_1 method from minor strike–slip faults (n=146) and thrust faults (n=26) yield subhorizontal maximum compressive stress axes with an average trend of 086°. This average stress axis is consistent with calculated Laramide compressional axes determined by Erslev and Gregson, (1996; 080°); Holdaway, (1998; 79°); Erslev and Larson, (2006; 090°) and Larson, (2009; 093°). Poles to bedding-oblique stylolite planes (n=97) collected in the Fort Hays Limestone average 086°-14°, paralleling shortening directions of average strike-slip and thrust slickenline trends and providing further support for subhorizontal Laramide compression. Normal fault slickenlines (n=40) collected at the surface yielded an average slip direction of 183°-73°, but are highly variable. Observations of normal dip-slip reactivation of right-lateral shear planes and cross-cutting relationships show that normal faults are younger than Laramide thrust and strike-slip faulting.

Joints observed throughout the study area document at least two separate joint systems. Cross-cutting relationships identified an older J_1 joint set (n=640), with an average attitude of 078°, and a younger J_2 joint set (n=528), with an average attitude of 171°. Fractures identified as J_1 joints (078°) are slightly oblique to average σ_1 trends (this study: 86°) and in some localities may actually be strike-slip faults. E-W striking joints at five localities abut right-lateral shear fractures, indicating jointing post-dated faulting. J_2

joints show consistent orientations with excellent clustering throughout the foothills area. The presence of N-S-striking J_2 joints is incompatible with Laramide shortening directions and indicates post-Laramide tectonic development. Average J_2 joint strikes are consistent with “frac into” orientations and borehole breakouts observed on the west side of the Denver Basin. Calcite-filled fractures (n=244) observed at the surface showed pervasive calcite-fill in all fracture strikes between 65° and 120°. Calcite-fill was also identified in N-S to NNW-striking fractures that parallel hinge lines of adjacent folds, but nowhere else.

Current technical studies by Noble Energy Inc. have focused on *in situ* states of stress and strain in the Wattenberg Field and Denver Basin. 26 wells were logged across the Wattenberg Field from 2008 to 2009 by Noble Energy Inc. but only 13 wells showed statistically significant breakout data. Breakout data revealed a complicated arrangement of varied S_{Hmax} directions with an overall vector mean of N32E. The lack of wellbore failure in 13 wells is probably due to an isotropic horizontal stress state for many portions of the field. The minimal horizontal stress influence and the presence of N-S borehole breakouts and N-S “frac into” directions adjacent to the Front Range suggest NE-trending Laramide horizontal compression ended and was replaced by stresses due to regional uplift, subsequent erosion of overburden, and/or by post-Laramide extension.

Subsurface fracture investigations by Noble Energy Inc. used Formation Micro-Image Logging (FMI) north of Wattenberg Field to identify fracture heterogeneity in Permian through upper Cretaceous rocks. These images revealed fracture that orientations in upper Cretaceous strata differed from lower stratigraphic intervals. Upper Cretaceous fracture strikes averaged N33E, whereas fracture in the Lyons and Lykins formations strike N80E. Faults through the well bore were highly variable, with a mean vector orientation of N67E. “Frac into” orientations, which record a fracture connection of one well to another during hydraulic wellbore treatment methods, give. N-S “frac into” orientations in the Codell Sandstone in the western Denver Basin and E-W orientations east of the synclinal hinge of the Denver Basin.

Surface fracture data collected in the Niobrara Formation show multiple fracture orientations with cross-cutting and abutting relationships indicating multiple fracture episodes. Diverse fracture strikes and relative timing relationships suggest multiple mechanisms are present at outcrop and in the subsurface. N-S “frac into” orientations and N-S borehole breakout data on the west side of the Denver Basin parallel J_2 joint strikes observed at the surface, and may be related. Other potential correlations include N67E fault strikes observed from FMI logs which subparallel average right-lateral fault strikes at the surface (N70E).

3D seismic investigations in the Denver Basin show complex, low angle listric and planar normal fault sets cutting upper Cretaceous strata. The Sooner Field (T8N R58W) and Dana Point (T3S, R64W) 3D seismic surveys showed low average fault dips (Sooner Field; 08^{o}, Dana Point; 27^{o}), with highly variable fault strikes, apparent normal displacement and no identifiable basement-to-Cretaceous faulting. This questions hypotheses invoking basement block motion and wrench faulting mechanisms. Laramide σ_1 trends calculated in this study (086^{o}) are subperpendicular to many observed subsurface fault strikes, suggesting normal faulting in Cretaceous reservoirs post-dates Laramide compression. Hypotheses invoking detachment and layer-parallel slip are attractive due to the low fault angles and normal fault geometries, but the lack of consistent fault strikes indicates multi-directional slip or other mechanisms may be present.

Surface and subsurface fracture data collected in the Niobrara Formation show compelling evidence for at least four different fracture mechanisms at various times. Initial strike-slip and thrust faulting of the Niobrara Formation was generated by Laramide subhorizontal compression trending 086°. Abutting relationships show that post-faulting but still syn-Laramide fracturing produced ENE-to-E-W-striking J_1 joints. Post-Laramide extension in the direction of prior compression is suggested by N-S-striking J_2 joints and N-S “frac into” industry data sets on the western side of the Denver Basin. Lastly, low-angle listric and planar normal faults identified in 3D seismic data and normal fault reactivation of right-lateral shear fractures in outcrop are interpreted to be post-Laramide.

Recent exploration success by EOG Resources Inc. in the Niobrara Formation illustrates the importance of predicting fracture orientations for petroleum companies. The EOG Jake 2-01H, in 1-11n-63w, Weld County, CO, produced 50,000 barrels of oil in its first 90 days on production in the third quarter of 2009 (Petzet, 2010). Its maximum initial rate was 1,558 barrels a day of oil and 350,000 cubic feet of gas per day from a stimulated, NW-SE directed lateral in the Niobrara Formation (Petzet, 2010; COGCC, 2010). Recent permit requests by EOG Resources Inc. show multiple lateral wells are planned in a NW-SE direction (COGCC, 2010).

Certain fracture types may be optimally intercepted as indicated from surface studies. On average, right-lateral shear fractures strike 70° and left-lateral shear fractures strike 108°. Laramide mode 1 splitting fractures in the Niobrara Formation optimally would strike between 074°-086°, whereas post-Laramide joints sets strike N-S. J_2 joints likely have less calcite mineralization than Laramide fractures, but their extent into the eastern Denver Basin is unknown. From this study it appears that EOG Resources Inc. is targeting right-lateral shear fractures and/or Laramide J_1 splitting fractures in northern Weld County, CO. However, targeting fracture anisotropy in the subsurface is difficult without the aid of 3D seismic data sets. The diverse fault orientations observed between the two 3D seismic volumes observed in this study show complex fault strikes from one locality to the next. It is unknown whether normal fault margins identified in seismic data contribute to enhanced fracture density and production rates. Further investigation of fractures associated with subsurface normal faulting is required.

Questions for Future Research

Unanswered questions remain and problems requiring further work have arisen from this investigation. The consistent N-S to NNW strikes of J_2 joints are clearly younger than shear fractures and J_1 joints observed along the Front Range. Their uniform orientations suggest they are not cross-joints related to uplift but are tectonic in origin. Their exact mechanism and eastern extent is poorly constrained. If N-S oriented joints are identified to cut Miocene formations, then it is possible that the deformation is related to the Rio Grande Rift. The reactivation of basement-cored Laramide thrust faults with normal displacement may also be reasonable mechanisms, but this requires further field investigations.

The apparent random strikes of faults observed in 3D seismic volumes are also problematic. Recent studies of polygonal faulting networks suggest density inversion and differential compaction can form variably-striking normal fault systems. In general, the mechanical variability of diverse sediment types can contribute to interval-isolated fault systems. However observations of faults cross-cutting younger strata in the two examined 3D seismic surveys suggest that interval-isolated faulting is not a primary mechanism. Detachment on bedding-parallel slip surfaces and/or uplift with associated unroofing may also generate diverse fault strikes. Their mechanisms remain uncertain.

Isotropic borehole stresses indicated by caliper well logging east of Greeley, CO suggests other explanations, including erosional unroofing and elastic rebound, crustal uplift associated with regional extension, and localized variable extension. Diverse fracture styles and varying fracture orientations are observed in the eastern Denver Basin from the western Denver Basin and outcrop. The reason and mechanism for these contrasting domains remain open questions.

References Cited

Aldrich, M.J., Jr., Chapin, C.E., and Lauglin, A.W., 1986 Stress history and tectonic development of the Rio Grande rift, New Mexico: Journal of Geophysical Research, v. 91, p. 6199-6211, doi: 10.1029/JB091iB06p06199.

Allen, P.A., and Allen, J.R., 1990, Basin Analysis, Blackwell Publications, Oxford, UK, 451 p.

Allmendinger, R., 2002, STEREOWIN v. 1.2.0 for windows program user manual: Cornell University, Department of Earth & Atmospheric Sciences, Ithaca, New York 42 p.

Angelier, J., 1984, Tectonic analysis of fault slip data sets, Journal of Geophysical Research, v. 89, p. 5835-5848.

Angelier, J., 1990, Inversion of field data in fault tectonics to obtain the regional stress-III, a new rapid direct inversion method by analytical means, Geophysical Journal International, v. 103, p. 363-376.

Bauer, P.W., and Ralser, S. 1995, The Picuris-Pecos fault- repeatedly reactivated, from Proterozoic (?) to Neogene: New Mexico Geological Society Guidebook, 46th Annual Field Conference, p. 111-115.

Beaumont, C., 1981. Foreland Basins; Geophysical Journal of the Royal Astronomical Society v. 65, p. 291–329.

Bergbauer, S.B., and Pollard, D.D., A new conceptual fold-fracture model including prefolding joints, based on the Emigrant Gap anticline, Wyoming, Geological Society of America Bulletin, v. 116, p. 294–307.

Bird, P., 1988, Formation of the Rocky Mountains, Western United States; a continuum computer model, Science, v. 239, p. 1501-1507.

Bird, P., 1998, Kinematic history of the Laramide Orogeny in latitudes 35 degrees - 49 degrees N, western United States, Tectonics, v. 17, p. 780-801.

Birmingham, T.J., 1998, Compartmentalization of the Codell and Terry (Sussex) Formations using clay smear technology, Wattenberg Field area, Denver Basin, Colorado; in R.M. Slatt, ed., Compartmentalized reservoirs in Rocky Mountain Basins, 1998 RMAG Symposium, p. 47-69.

Birmingham, T.J., Lytle, D.M., and Sencenbaugh, R.N., 2001, Enhanced recovery from a tight gas sand through hydraulic refracturing: Codell Formation, Wattenberg Field, Colorado; in D. Anderson, eds., Gas in the Rockies; Denver, Colorado, Rocky Mountain Association of Geologist, p. 101-116.

Blackstone, D.L., 1986, Foreland compressional tectonics, southeastern Wyoming; Contribution to Geology, University of Wyoming, v. 22(1), p.1-38.

Boos, C.M., and Boos, M.F., 1957, Tectonics of eastern flank and foothills of Front Range, Colorado, American Association of Petroleum Geologists Bulletin, v. 41, p. 2603-2676.

Braddock, W.A., Calvert, R.H., Gawarecki, S.J., and Nutalaya, P., 1970, Geologic map of the Masonville quadrangle, Larimer County, Colorado: U.S. Geological Survey Geologic Quadrangle Map GQ-832, scale 1:24,000.

Braddock, W.A., and Connor, J.J., 1988a, Geologic map of the Livermore Mountain quadrangle, Larimer County, Colorado: U.S. Geological Survey Geologic Quadrangle Map GQ-1617, scale 1:24,000.

Braddock, W. A., Wohlford, D. D., and Connor, J. J., 1988b, Geologic map of the Livermore quadrangle, Larimer County, Colorado: U.S. Geological Survey Geologic Quadrangle Map GQ-1618, scale 1:24,000.

Braddock, W.A., Connor, J.J., Swann, G.A, and Wohlford, D.D., 1988c, Geologic map of the Laporte quadrangle, Larimer County, Colorado: U.S. Geological Survey Geologic Quadrangle Map GQ-1621, scale 1:24,000.

Braddock, W.A., Nutalaya, P., and Colton, R.B., 1988d, Geologic map of the Carter Lake Reservoir quadrangle, Boulder and Larimer Counties, Colorado: U.S. Geological Survey Geologic Quadrangle Map GQ-1628, scale 1:24,000.

Braddock, W.A., Houston, R.G., Colton, R.B., and Cole, J. C., 1988e, Geologic map of the Lyons quadrangle, Boulder County, Colorado: U.S. Geological Survey Geologic Quadrangle Map GQ-1629, scale 1:24,000.

Braddock, W.A., Calvert, R.H., O’Connor, J.T., and Swann, G.A, 1989, Geologic map of the Horsetooth Reservoir quadrangle, Larimer County, Colorado: U.S. Geological Survey Geologic Quadrangle Map GQ-1625, scale 1:24,000.

Brandt, T.R., Moore, D.W., Murray, K.E., and Colton, R.B., 2003a, A spatial database of of bedding attitudes to accompany geologic map of Boulder- Fort Collins, Greeley area, Colorado: U.S. Geological Survey, Open-File Report OF-2003 -24, scale 1:100000.

Brandt, T.R., Moore, D.W., Murray, K.E., and Machette, M.N. 2003b, A spatial database of bedding attitudes to accompany geologic map of the greater Denver area, Front range urban corridor, Colorado: U.S. Geological Survey Open-File Report OF-2003-25, scale 1:100000.

Breitsprecher, K., Thorkelson, D.J., Groome, W.G., and J. Dostal, 2003, Geochemical confirmation of the Kula-Farallon slab window beneath the Pacific Northwest in Eocene time, Geology, v. 31, p. 351-354.

Bump, A.P., 2003, Reactivation, trishear modeling, and folded basement in Laramide uplifts: Implications for the origins of intracontinental faults, GSA Today, v. 13, p. 4-10.

Byerlee, J., 1978, Friction of rocks, Pure and Applied Geophysics, v. 116, p. 615-626.

Courtwright, T.R., and Braddock, W.A., 1989, Geologic map of the Table Mountain quadrangle and adjacent parts of the Round Butte and Buckeye Quadrangles, Larimer County, Colorado and Laramie County, Wyoming: U.S. Geological Survey Miscellaneous Investigations Series Map I-1805, scale 1:24,000.

Cather, S.M., and Harrison, R.W., 2002, Lower Paleozoic isopach maps of southern New Mexico and there implications for Laramide and ancestral rocky Mountain tectonism: Socorro, New Mexico Geological society, 53rd Annual Field conference Guidebook, p. 85-101.

Cather, S.M., Karlstrom, K. E., Timmons, J.M. and Heizler, M.T., 2006, Palinspastic reconstruction of Proterozoic basement-related aeromagnetic features in northcentral New Mexico: Implications for Mesoproterozoic to late Cenozoic tectonism, Geosphere, v. 2, p. 299-323.

Catuneanu, O., 2004. Retroarc foreland systems evolution through time. Journal of African Earth Sciences no. 38, p. 225–242.

Chapin, C.E., and Cather, S.M., 1981, Eocene tectonism and sedimentation in the Colorado Plateau-Rocky Mountain area, Arizona Geological Digest, v. 14, p. 175-198.

COGCC, 2010, Colorado Oil and Gas Conservation Commission website, http://oil-gas.state.co.us/.

Compton, R.R, 1966, Analyses of Pliocene-Pleistocene deformation and stresses in northern Santa Lucia range, California, Geological Society of America Bulletin, v. 77, n.12, p.1361-1380.

Covington, G., 1966, Stratigraphy and sedimentary structures in the Fox Hills Sandstone (Upper Cretaceous), Golden area, Colorado: the Mountain Geologist, v. 3, no. 4, p. 161-169.

Courtwright, T.R., and Braddock, W.A., 1989, Geologic map of the Table Mountain quadrangle and adjacent parts of the Round Butte and Buckeye Quadrangles, Larimer County, Colorado and Laramie County, Wyoming: U.S. Geological Survey Miscellaneous Investigations Series Map I-1805, scale 1:24,000.

Daggett, P.H., Keller, G.R., Morgan, P. and Wen, C.L., 1986, Structure of the southern Rio Grande rift from gravity interpretation; Journal of geophysical research, v. 91, no. B6, p. 6157-6167.

Davies, R.J., 2005, Differential compaction and subsidence in sedimentary basins due to silica diagenesis: A case study; GSA Bulletin, vol. 117, p. 1146-1155, doi: 10.1130/B25769.1

Davies, R.J., Ireland, M.T., and Cartwright, J.A., 2009, Differential compaction due to the irregular topology of a diagenetic reaction boundary: anew mechanism for the formation of polygonal faults: Basin Research, vol. 21, p. 354-359 doi: 10.1111/j.1365-217.2008.00389x.

Davis, T.L., 1974, Seismic investigations of Late Cretaceous faulting along the east flank of the Central Colorado Front range, Colorado: Professional Contributions of the Colorado School of Mines, , no. 8, p. 280-300.

Davis, T.L., 1985, Seismic evidence of tectonic influence on development of Cretaceous listric normal faults, Boulder-Wattenberg-Greeley area, Denver basin, Colorado: The Mountain Geologist, v. 22, no. 2, p. 47-54.

Davis, T.L., and Weimer, R.J., 1976, Late Cretaceous growth faulting, Denver basin, Colorado, *in* Epis, R.C., and Weimer, R.J., eds: Studies in Colorado field geology: Colorado School of Mines Prof. Contributions, no. 8, p. 280-300.

DeCelles, P.G., and Giles, K.A., 1996, Foreland basin systems; Basin Research, v.8, p. 105-123.

DePaolo, D.J., 1981, Neodymium isotopes in the Colorado Front Range and crust-mantle evolution in the Proterozoic, Nature, v.291, p.136-196.

Eardley, A.G., 1963, Relation of uplift to thrusts in the Rocky Mountains, Backbone of America: American Association of Petroleum Geologists, mem. 2, p. 203-219.

Engelder, T., and Geiser, P., 1979, The relationship between pencil cleavage and lateral shortening within the Devonian section of the Appalachian Plateau, New York; Geology, v.7, p. 460-474.

Ehrlich, T.K., 1999, Fault analysis and regional balancing of Cenozoic Deformation in Northwest Colorado and South-Central Wyoming {M.S. thesis}: Fort Collins, Colorado State University, 116 p.

Erslev, E.A., 1986, Basement balancing of Rocky Mountain foreland uplifts, Geology, v. 14, p. 259-262.

Erslev, E.A., 1993, Thrusts, backthrusts and detachment of Laramide foreland arches, *in* C.J. Schmidt, R. Chase, and E.A. Erslev, eds., Laramide basement deformation in the Rocky Mountain foreland of the western United States, Geological Society of America Special Paper 280, p. 125-146.

Erslev, E.A., 1998a, LDIS 2: Dept. of Geosciences, Colorado State University, Fort Collins, Colorado.

Erslev, E.A., 1998b, SELECT 1.2: Dept. of Geosciences, Colorado State University, Fort Collins, Colorado.

Erslev, E.A., 2001, Multi-stage, multi-directional Tertiary shortening and compression in north-central New Mexico, Geological Society of America Bulletin, v.113, p. 63–74.

Erslev, E.A., 2005, 2D Laramide geometries and kinematics of the Rocky Mountains, Western U.S.A., *in* K.E. Karlstrom and G.R. Keller, eds., 2005, The Rocky Mountain Region — An Evolving Lithosphere: Tectonics, Geochemistry, and Geophysics: American Geophysical Union Geophysical Monograph 154, p. 7-20.

Erslev, E.A., and Gregson, J.D., 1996, Oblique Laramide convergence in the northeastern Front Range; regional implications from the analysis of minor faults, *in* Thompson, R. A., Hudson, M. R., and Pillmore, C. L., eds., Geologic excursions to the Rocky Mountains and beyond, Special Publication - Colorado Geological Survey, Open-File Report 96-4, 11 p.

Erslev, E.A., Holdaway, S.M., O'Meara, S.A., Jurista, B., and Selvig, B.W, 2004, Laramide minor faulting in the Colorado Front Range, *in* Cather, S.M., McIntosh,W.C.,and Kelley,S.A.,eds.,Tectonics,geochronology,and volcanism in the southern Rocky Mountains and Rio Grande Rift, New Mexico Bureau of Geology and Mineral Resources Bulletin 160, p.181-04.

Erslev, E.A., and Koenig, N.V., 2009, Three-dimensional kinematics of Laramide, basement-involved Rocky Mountain deformation, USA: Insight from minor faults and GIS-enhanced structure maps, *in* Kay, S.M., Ramos,V.A and Dickinson, W.R., eds., Backbone of the Americas: Shallow Subduction, Plateau Uplift, and Ridge and terrain Collision: geological Society of America Memoir 204, p. 125-150.

Erslev, E.A., and Larson, S.M., 2006, Testing Laramide hypothesis for the Colorado front Range arch using minor faults, *in* Raynolds, R., and Stern, E., eds., Special Issue on the Colorado Front Range: The Mountain Geologist, v. 43, p. 45-64.

Erslev, E.A., and Rogers, J.L., 1993, Basement-cover kinematics of Laramide fault propagation folds: *in* C.J. Schmidt, R. Chase, and E.A. Erslev, eds., Laramide basement deformation in the Rocky Mountain foreland of the western United States: Geological Society of America Special Paper 280, p. 339-358.

Erslev, E.A., and Wiechelman, D., 1997, Fault and fold orientations in the central Rocky Mountains of Colorado and Utah, Fractured Reservoirs: Characterization and Modeling Guidebook: Rocky Mountain Association of Geologists, p. 131-136.

Fankhauser, S.D., and Erslev, E.A., 2004, Unconformable and cross-cutting relationships indicate major Precambrian faulting on the Picuris-Pecos fault system, southern Sangre de Cristo Mountains, New Mexico: Socorro, New Mexico Geological Society, 55th Annual Field Conference Guidebook, p. 121–133.

Fisher, A.B., 2003, Geometry and Kinematics of Laramide basement-involved anticlines: Southeastern Bighorn Mountains, Wyoming {M.S thesis}: Fort Collins, Colorado State University, 208 p.

Fryer, S.L., 1996 Laramide faulting associated with the Isle Fault System, Northern Wet Mountains, Colorado {M.S. thesis}: Fort Collins, Colorado State University, 120p.

Graham, J.P., 2000, Revised stratigraphy, depositional systems, and hydrocarbon exploration potential for the Lower Cretaceous Muddy Sandstone, northern Denver basin: AAPG Bulletin, vol. 84, no. 1, p. 183-209.

Gregson, J.D., and Erslev, E.A., 1997, Heterogeneous Laramide Deformation in the Uinta Mountains, Colorado and Utah, *in* Fractured Reservoirs: Characterization and Modeling, Hoak, T.E., Klawitter, A.L., Blomquist, P.K., eds., Rocky Mountain Association of Geologist Guidebook, Denver, Colorado, p. 137-154.

Gries, R.R., 1983a, Oil and gas prospecting beneath the Precambrian of foreland thrust plates in Rocky Mountains, American Association of Petroleum Geologists Bulletin, v. 67, p. 1-28.

Gries, R.R., 1983b, North-south compression of the Rocky Mountain foreland structures, *in* Rocky Mountain foreland basins and uplifts Lowell, J.D., and Gries, R.R., eds., Rocky Mountain Association of Geologists, Denver, Colorado, p. 9-32.

Gustason, G., and Deacon, M., 2008, Shale gas resource of the Niobrara Formation, northern Colorado Front range and adjacent DJ Basin, RMAG-AAPG core workshop and fieldtrip, field guide, July, p. 23-49.

Hager, D.H., Jr., 2001 Geometry and kinematics of Fault-Propagation folds in the Northwest Flank of the Bighorn Mountains, Wyoming [M.S. thesis]: Fort Collins, Colorado state university 126 p.

Haberman, S.A., 1983, An integrated geophysical case-study of the Cretaceous Codell Sandstone in the vicinity of Hambert Field, Weld County, Colorado: Master's thesis T-2772, Colorado School of Mines, 111 p.

Hamilton, W., 1981, Plate-tectonic mechanism of Laramide deformation, *in* Rocky Mountain Foreland Basement Tectonics, edited by D. W. Boyd and J. A. Lillegraven, Contrib. Geol., p. 1987-92.

Hayden, F.V., 1874, Annual Report of the United States Geological and Geographical Survey of the Territories Embracing Colorado: 7th Annual Report (1873).

Hayden, F.V., 1877, Annual Report of the United States Geological and Geographical Survey of the Territories, Embracing Colorado and Parts of Adjacent Territories: 9th Annual Report (1875).

Hennings, P.H., Olson, J.E., and Thompson, L.B., 2000, Combining outcrop data and three-dimensional models to characterize fractured reservoirs: An example from Wyoming, American Association of Petroleum Geologists Bulletin, v. 84, no. 6, p. 830-849.

Hoblitt, R.P., and Larson, E., E., 1975, Paelomagnetic and geochronologic data bearing on the structural evolution of the northeastern margin of the Front Range, Colorado: Geological Society of America Bulletin, v. 86, no.2, p. 237- 242.

Holdaway, S.M., 1998, Laramide deformation for the Northeastern Front Range, Colorado: Evidence for deep crustal wedging during horizontal compression: Master's Thesis, Colorado State University, Fort Collins, CO, 146p.

Hoy, R.G., and Ridgeway, K. D., 2002, Syndepositional thrust-related deformation and sedimentation in an Ancestral Rocky Mountains basin, central Colorado trough, Colorado, USA: GSA Bulletin, v. 114, no. 7, p. 804-828.

Jordan, T., 1981. Thrust loads and foreland basin evolution, Cretaceous, western United States. American Association of Petroleum Geologists Bulletin 65, p. 2506–2520.

Jordan, T.E., Flemings, P.B., 1991. Large-scale stratigraphic architecture, eustatic variation, and unsteady tectonism: a theoretical evaluation. Journal of Geophysical Research 96,p. 6681–6699.

Jordan, T.E., 1995, Retroarc foreland and related basins: Tectonic Sedimentary Basins, *eds* C.J. Busby and R.V. Ingersoll, Blackwell Science, Boston, p. 331-362.

Jurista, B.K., 1996 East-Northeast Laramide compression and Shortening of the Canon City Embayement, South-Central Colorado [M.S. thesis]: Fort Collins, Colorado State University, 147 p.

Karlstrom, K.E., and Daniel, C.G., 1993, Restoration of Laramide right-lateral strike slip in northern New Mexico by using Proterozoic piercing points: Tectonic implications from the Proterozoic to the Cenozoic, Geology, v. 21, p. 1139-1142.

Kellog, K.S., 1999, Neogene basins of the northern Rio Grande rift- Partioning and asymmetry inherited from Laramide and older uplifts: Tectonophysics, v. 305, p 141-152.

Kellog, K.S., Schmidt, C.J., Young, S.W., 1995, Basement and cover rock deformation during the Laramide contraction in the northern Madison Range (Montana) and its influence on Cenozoic basin formation: American Association of Petroleum Geologist, v. 79, p. 1117-1137.

Kittleson, K.L, 1988, The hydrogeology of the Laramie-Fox Hills aquifer southwest Weld County, CO; Master of Science Thesis: Colorado State University, 84 p.

Kittleson, K.L., 2004, The effect of reverse faulting on the thickness, depth, and water quality of the Laramie Fox Hills aquifer in the western Denver Basin: The Mountain Geologist, vol. 41, no. 4, pg 185-194.

Kluth, C.F., 1997, Comparison of the location and structure of the Late Paleozoic and Late Cretaceous-Early Tertiary Front Range Uplift, *in* Bolyard, D.W., and Sonnenberg, S.A., eds., Geologic History of the Colorado Front Range: Denver, Colorado, Rocky Mountain Association of Geologists, p. 31-42.

Larson, S. M., 2009, Laramide transpression and oblique thrusting in the northeastern Front Range, Colorado: {Master's Thesis} Colorado State University, Fort Collins, CO, 210 p.

Leeder, M. 1999, Sedimentology and sedimentary basins: Blackwell Publishing, Maden, MA. 524 p.

LeMasurier, W.E., 1970, Structural study of a Laramide fold involving shallow-seated basement rock, Front range, Colorado: geological society of America Bulletin, v. 81, p. 421-434.

Longman, M.W., Luneau, B.A., and S.M. Landon, 1998, Nature and distribution of Niobrara lithologies in the cretaceous western interior seaway of the Rocky Mountain region: The Mountain Geologist, vol.35, no.4, p. 137-170.

MacKenzie, D., 1971, Post-Lytle Dakota Group on west flank of Denver Basin, Colorado: The Mountain geologist, v. 8, p. 91-131.

Madole, R.F, Braddock, W.A., and Colton, R.B., 1998, Geologic map of the Hygiene quadrangle, Boulder County, Colorado: US Geological Survey Geologic Quadrangle Map GQ-1772, scale 1:24,000.

Magnani, M.B., Levander, A., Erslev, E.A., Bolay-Koenig, N., and Karlstrom, K., 2005, Listric thrust faulting in the Laramide front of north-central New Mexico guided by Precambrian basement anisotropics, *in* Karlstrom, K.E., and Keller, G.R., eds., The rocky Mountain Region-An evolving Lithosphere: Tectonics, geochemistry, and Geophysics: American Geophysical Union Geophysical Monograph 154, p. 239-252.

Matthews, V., III and Sherman, G.D., 1976, Origin of monoclinal folding near Livermore, CO, Mountain Geologist, v.13, p.61-66.

Matthews, V., III and Work, D.F., 1978, Laramide folding associated with basement block faulting along the northeastern Front Range, Colorado, *in* Matthews, V., III, ed., Laramide folding associated with basement block faulting in the western United States, Geological Society of America Memoir 151, p. 101-124.

McCallum, M.E., and Mabarak, C.D, 1976, Diamond in state-line kimberlite diatremes, Albany County, Wyoming; Larimer County, Colorado, Report of Investigations Issue 12; Geological Survey of Wyoming: Laramie, WY. p. 467-469.

McMillan, M.E., Angevine, C.L., and Heller, P.L., 2002, Postdepositional tilt of the Miocene Pliocene Ogallala Group on the western Great Plains: Evidence of late Cenozoic uplift of the Rocky Mountains, Geology, v. 30, no. 1, p. 63-66.

McMillan, M.E., Heller, P.L., and Wing, S.L., 2006, History and causes of post-Laramide relief in the Rocky Mountain orogenic plateau: GSA Bulletin, vol. 118, no.3/4 p. 393-405.

Molzer, P. and Erslev, E.A., 1995, Oblique convergence on east-west Laramide arches, Wind River Basin, Wyoming, American Association of Petroleum Geologists Bulletin, v. 19, p. 1377-1394.

Neeley, T.G., 2006, Three-Dimensional Strain at Foreland Arch Transitions: Structural Modeling of the Southern Beartooth Arch Transition Zone, Northwest Wyoming {M.S. thesis}: Fort Collins, Colorado State University, 107 p.

Nibbelink, K.A., 1983, Depositional environments of the Fox Hills Sandstone (Upper Cretaceous), Cheyenne Basin, Colorado: {M.S thesis}: Colorado State University, Fort Collins, CO, 245 p.

Oldham, D.W, 1996, Permian salt in the northern Denver Basin: Control on occurrence and relationship to oil and gas production from cretaceous reservoirs: in M.W. Longman and M.D. Sonnefield, eds.,1996, Paleozoic systems of the Rocky Mountain regions, Rocky Mountain section, Society of Sedimentary Geology, p. 335-354.

Peterman, Z.E., Hedge, C.E., and Braddock, W.A, 1968, Age of Precambrian events in the northeastern Front Range, Colorado: Journal of Geophysical Research, v. 73, no. 6, p. 2277-2296.

Petit, J.P., 1987, Criteria for the sense of movement on fault surfaces in brittle rocks: Journal of Structural Geology, v. 9, p. 597-608.

Petzet, A., 2010, EOG pursues Denver basin fractured reservoir: Oil and Gas Journal website, http//www.ogj.com.

Prezzi, C.B., Uba, C.E., Gotze, H.J., 2009, Flexural isostasy in the Bolivian Andes: Chaco foreland basin development: Tectonophysics, v. 474, p.526-543.

Pritchett, R.W., 1993, Sooner Unit Weld County, Colorado, 3-D seismic and well control, a summary of Public Domain Data; DOE Cooperative Agreement DE-FC22-93BC14954, p. 1-35.

Prucha, J.J., Graham, J.A., and Nickleson, R.P., 1965, Basement controlled deformation in Wyoming province of Rocky Mountain foreland: AAPG Bulletin, 49, p. 966-992.

Ramos, V.A, Cristallinni, E.O., and Pérez, D.J., 2002, The Pampean flat-slab of the Central Andes, Journal of South American Earth Sciences, v. 15, p. 59-78.

Raynolds, R.G., 1997, Synorogenic and post-orogenic strata in the central Front Range, Colorado, *in* Bolyard, D.W., and Sonnenberg, S.A., eds., Geologic History of the Colorado Front Range: Denver, Colorado, Rocky Mountain Association of Geologists, p. 43-47.

Rhoads, H., 1987, Facies relationships of the Ingleside Formation in northern Colorado and southeastern Wyoming: {M.S. thesis}: Colorado School of Mines, Golden, CO, 98 p.

Richter, B. R., 2009, Personal communication, Noble Energy Inc., Denver, Colorado.

Ruf, J.C., and Erslev, E.A., 2005, Origin of Cretaceous to Holocene fractures in the northern San Juan Basin, Colorado and New Mexico, Rocky Mountain Geology, v. 40, no. 1, p. 91–114.

Russell, L.R., and Snelson, S., 1994, Structure and tectonics of the Albuquerque Basin segment of the Rio Grande rift- insights from the reflection seismic data. *In*: Keller, G.R., Cather, S.M. (Eds.), Basins of the Rio Grande rift- Structure, Stratigraphy, and Tectonic Setting. Geological Society of America Special Paper, 291, 83-112.

Saleeby, J., 2003, Segmentation of the Laramide slab-evidence from the southern Sierra Nevada region, Geological Society of America Bulletin, v.115, p. 655-668.

Sales, J.K., 1968, Cordilleran foreland deformation: American Association of Petroleum Geologists Bulletin, v. 52, p. 2000-2015.

Scott, G. R., and Cobban, W. A., 1965, Geologic and biostratigraphic map of the Pierre Shale between Jarre Creek and Loveland, Colorado: U.S. Geological Survey Miscellaneous Geologic Investigation Map i-439, scale 1:48,000.

Scott, G.R., and Cobban, W.A., 1986, Geologic, biostratigraphic, and structure map of the Pierre Shale between Loveland and Round Butte, Colorado: U.S. Geological Survey Miscellaneous Investigations Series Map I-1700, scale 1:50,000.

Selvig, B.J., 1994 Kinematics and structural models of faulting adjacent to the rocky flats plant, central Colorado:{M.S. thesis}: Colorado State University, Fort Collins, CO, 134 p.

Selverstone, J., Hodgins, M., Shaw, C., Aleinikoff, J.N., and Fanning, C.M., 1997 Proterozoic Tectonics of the northern Front Range, *in* Bolyard, D.W., and Sonnenberg, S.A., eds., Geologic History of the Colorado Front Range: Denver, Colorado, Rocky Mountain Association of Geologists, p. 9-18.

Selverstone, J., Hodgins, M., Alehikoffz, J.N, and Fanning, C.M., 2000, Mesoproterozoic reactivation of a Paleoproterozoic transcurrent boundary in the northern Colorado Front Range: Implications for ~ 1.7- and 1.4-Ga tectonism, Rocky Mountain Geology, v. 35, no. 2, p.139-162.

Sharry, C.J., Langden, R.T., Jovanovich, D.B., Jones, G.M., Hill, N.R., Guidish, T.M., 1986, Enhanced imaging of the COCORP seismic line, Wind River Mountains *in:*Barazingi, M., Brown, L. (Eds.) Reflection Seismology- A Global Perspective: American geophysical Union of geodynamics, Ser. 13, p. 223-236.

Smith, C.B., 1977, Kimberlite and mantle derived xenoliths at Iron Mountain, Wyoming: Master's Thesis, Colorado State University, Fort Collins, CO, 218p.

Smithson, S. B., J.A. Brewer, S. Kaufman, J.E. Oliver, and Hurich, C.A., 1979, Structure of the Laramide Wind River uplift, Wyoming, from COCORP deep reflection data and from gravity data, Journal of Geophysical Research, v. 84, p. 5955-5972.

Sonnenberg, S.A., and Bolyard, D.W., 1997, Tectonic history of the Front Range in Colorado: Rocky Mountain Association of Geologists, Colorado Front Range Guidebook-1997.

Sonnenberg, S.A., and Weimer, R.J., 1981, Tectonics, sedimentation and petroleum potential, northern Denver basin, Colorado, Wyoming and Nebraska: Colorado School of Mines Quarterly, v. 76, no. 2, 45 p.

Stearns, D. W., 1971, Mechanisms of drape folding in the Wyoming Province, *in* Renfro, A. R., ed., Symposium on Wyoming Tectonics and their Economic Significance. Wyoming Geological Association, Annual Field Conference, 23rd Guidebook, p. 125-143.

Stearns, D. W., 1978, Faulting and forced folding in the Rocky Mountain foreland, in Mathews, V., III, ed., Laramide folding associated with block faulting in the western United States, Geological Society of America Memoir 151, p. 1-37.

Stone, D.S., 1969, Wrench faulting and Rocky Mountain tectonics: the Mountain Geologist, v. 6, p. 67-79.

Stone, D.S., 1984, The Rattlesnake Mountain, Wyoming, debate: A review and critique of models: the Mountain Geologist, v. 21, p. 37-42.

Stone, D.S., 2005, On illogical interpretation of geological structures in the central Rocky Mountain foreland province: The Mountain Geologist, v. 42, p. 159-186.

Tetreault, J., Jones, C.H., Erslev, E.A., Larson, S.M., Hudson, M., and Holdaway, S.M., 2008, Paleomagnetic and structural evidence for oblique slip in a fault-related fold, Grayback Monocline, Colorado, Geological Society of America Bulletin, v.120, p. 877-892.

Tweto, O, 1979, Geologic Map of Colorado, United States Geological Survey Map, scale 1:500,000.

Tweto, O., 1980, Summary of the Laramide orogeny in Colorado, *in* Kent, H.C., and Porter, K.W., eds., Colorado geology: Rocky Mountain Association of Geologists Symposium, p. 129-134.

Twiss, Robert J. and Moores, Eldridge M.; Structural Geology W. H. Freeman and Company, 1993, p. 193-199.

Varga, R.J., 1993, Rocky Mountain foreland uplifts: Products of a rotating stress field or strain partitioning?, Geology, v. 21, p. 1115-1118.

Vollmer, F.W., 1992, ORIENT v. 1.62 orientation data analysis program user’s manual: State University of New York-New Paltz, New Paltz, New York, 26p.

Watterson, J., Walsh, J., Nicol, A., Nell, P.A., and Bretan, P.G., 2000, Geometry and origin of polygonal fault system; Journal of the Geological Society, London, vol. 157, pp. 152-162.

Weimer, R.J., 1980, Recurrent movement on basement faults, a tectonic style for Colorado and Adjacent areas, in Kent, H.C., and K.W Porter, eds., Colorado Geology: RMAG, p. 23-35.

Weimer, R. J., 1996, Guide to the petroleum geology and Laramide Orogeny, Denver Basin and Front Range, Colorado: Colorado Geological Survey Department of Natural Resources Bulletin 51, 127 p.

Weimer, R.J., and Davis, T.L., 1978, Growth faults in Cretaceous foreland basin, Rocky Mountain Region- new exploration targets: Geophysics, v. 42, no. 1, p. 190-191.

Weimer, R. J., J. Dolson, F. G. Ethridge, and J. Warme, 1990,2-Day geology field trip: sequence stratigraphy—Lower K:Rocky Mountain Section, AAPG, 130 p.

Weimer, R.J., and Land, C., B., 1972, Field guide to Dakota Group (Cretaceous) stratigraphy Golden-Morrison area, Colorado: The Mountain Geologist, vol. 9, nos 2-3, p.241-267.

Weimer, R.J., and Sonnenberg, S.A., 1982, Wattenberg Field, paleostructure-stratigraphic trap, Denver basin, Colorado: Oil and Gas journal, v. 80, no. 12, p. 204-210.

Weimer, R. J., and Sonnenberg S. A., 1989, Sequence stratigraphic analysis of Muddy (J) Sandstone reservoir, Wattenberg field, 208 Muddy Sandstone: Revised Denver basin, Colorado, *in* E. B. Coalson, S. S. Kaplan, C. Wm.Keighin, C. A. Oglesby, and J. W. Robinson, eds., Petrogenesis and petrophysics of selected sandstone reservoirs of the Rocky Mountain regions: Rocky Mountain Association of Geologists, p. 197–220.

Weimer, R.J., Sonnenberg, S.A, Davis, T.L., and Berryman, W.M., 1998, Stratigraphic and structural compartmentalization in the J and D sandstones, central Denver Basin, Colorado: in R.M. Slatt, 1998, Compartmentalized reservoirs in the Rocky Basins 1998 RMAG Symposium, pp 1-27.

Wise, D.U., 1963, An outrageous hypothesis for the tectonic pattern of the North American Cordillera: geological Society of America Bulletin, v. 74, p. 357-362.

Wrucke, C.T., and Wilson, R.F., 1957, Geologic map of the Boulder quadrangle, Boulder County, Colorado: US Geological Survey Geologic Quadrangle Map OF 67-281, scale 1:24,000.

Vollmer, F.W., 1992, ORIENT v. 1.62 orientation data analysis program user's manual: State University of New York-New Paltz, New Paltz, New York, 26p.

Ziegler, V., 1917, Foothills structure in northern Colorado, Journal of Geology, v. 25, p. 715-743.

Zoback, M.D., 2007, Reservoir Geomechanics; Cambridge University Press, New York, New York, p. 167-206.

Zielinski, R.A., Peterman, Z.E., Stuckless, J.S., Rosholt, J.N., and Nkomo, I.T., 1981, The chemical and isotopic record of rock-water interaction of the Sherman Granite, Wyoming and Colorado, Contributions to Mineralogy and Petrology, v.78, p. 209-219.

APPENDICES

Appendix 1: Shear Fractures (Minor Faults) Data Tables.

Station #	N-Total	Lat. ^{0}N	Long. ^{0}W	Fm.*	S/D Beds	Ideal σ1 Stress Analysis (SS, TH Faults)(Compton 1966)		Strain Analysis Average Slickenline (SS and TH)		Insitu Normal Fault Slickenline eigenvectors	
						**Best Fit Alpha for m	T-P	Eigenvalues	T-P	Eigenvalues	T-P
MS-3	**9**	**40.478617**	**-105.1276**	**Kns-C**	**000/33**	E1: 0.4918 E2: 0.3352 E3: 0.1730 α= 20	**082-48** 224-36 329-20 `	E1: 0.7338 E2: 0.1484 E3: 0.1178	187-69 318-14 052-15	E1: 0.7882 E2: 0.1699 E3: 0.0489	258-82 356-01 086-09
MS-5	**2**	**40.476544**	**-105.1282**	**Knf**	**354/31**	E1: 0.9968 E2: 0.0032 E3: 0.0000 α= 15	**058-28** 157-16 273-57 `	E1: 0.9972 E2: 0.0028 E3: 0.0000	048-26 159-37 291-42	E1: NA E2: NA E3: NA	NA NA NA
MS-6	**13**	**40.390919**	**-105.138**	**Knf**	**130/66**	E1: **Insitu Normal Faults** E2: E3: α= 15	` ` ` `	E1: NA E2: NA E3: NA	NA NA NA	E1: 0.7451 E2: 0.1691 E3: 0.0858	124-73 336-14 244-09
CL-1	**1**	**40.298817**	**-105.1777**	**Knf**	**036/23**	E1: **Insitu Normal Faults** E2: E3: α= 15	` ` ` `	E1: NA E2: NA E3: NA	NA NA NA	E1: 1.0000 E2: 0.0000 E3: 0.0000	145-64 298-24 033-10
HY-1 (only 2 slicks observed)	**10**	**40.230299**	**-105.2298**	**Knf**	**007/10**	E1: 0.9951 E2: 0.0040 E3: 0.0009 α= 15	**087-09** 192-59 352-29 `	E1: 0.9944 E2: 0.0056 E3: 0.0000	073-08 173-54 337-35	E1: NA E2: NA E3: NA	NA NA NA
HY-2	**5**	**40.231569**	**-105.23**	**Kns-C**	**010/9**	E1: 0.9154 E2: 0.0825 E3: 0.0020 α= 20	**277-04** 187-05 050-84 `	E1: 0.7713 E2: 0.2281 E3: 0.0006	278-05 188-01 095-85	E1: NA E2: NA E3: NA	NA NA NA
HY-3	**7**	**40.231095**	**-105.2281**	**Kns-A**	**002/26**	E1: 0.9687 E2: 0.0211 E3: 0.0102 α= 20	**091-02** 001-00 264-88 `	E1: 0.9081 E2: 0.0837 E3: 0.0082	094-03 185-10 346-79	E1: NA E2: NA E3: NA	NA NA NA
HY-4	**10**	**40.22933**	**-105.2277**	**Kns-C**	**359/23**	E1: 0.956 E2: 0.0321 E3: 0.0118 α= 20	**082-06** 173-14 330-75 `	E1: 0.9666 E2: 0.0253 E3: 0.0081	096-18 189-18 340-70	E1: NA E2: NA E3: NA	NA NA NA
BD-1	**16**	**40.109807**	**-105.282**	**Knf**	**021/33**	E1: 0.8975 E2: 0.0731 E3: 0.0294 α= 15	**084-15** 333-54 184-32 `	E1: 0.8678 E2: 0.0956 E3: 0.0366	101-31 359-19 242-52	E1: NA E2: NA E3: NA	NA NA NA
BD-8	**9**	**40.106052**	**-105.2849**	**Knf**	**166/55**	E1: **Insitu Normal Faults** E2: E3: α= 15	` ` ` `	E1: NA E2: NA E3: NA	NA NA NA	E1: 0.7602 E2: 0.1966 E3: 0.0432	256-68 080-22 350-01

Appendix 1: Shear Fractures (Minor Faults) Data Tables (continued).

Station #	N-Total	Lat. ^{0}N	Long. ^{0}W	Fm.*	S/D Beds	Ideal σ1 Stress Analysis (SS, TH Faults)(Compton 1966)		Strain Analysis Average Slickenline (SS and TH)		Insitu Normal Fault Slickenline eigenvectors	
						**Best Fit Alpha for m	T-P	Eigenvalues	T-P	Eigenvalues	T-P
BD-10	**18**	**40.106312**	**-105.2856**	**Knf**	**015/30**	E1: 0.8833	**071-12**	E1: 0.6751	072-05	E1: 1.0000	145-35
						E2: 0.0908	162-01	E2: 0.2503	342-02	E2: 0.0000	300-52
						E3: 0.0259	256-78	E3: 0.0746	235-84	E3: 0.0000	046-12
						α= 15	`				
BD-11	**16**	**40.105709**	**-105.2854**	**Knf**	**017/39**	E1: 0.9595	**078-27**	E1: 0.9430	079-28	E1: 0.9756	106-47
						E2: 0.1095	186-15	E2: 0.0426	173-08	E2: 0.0221	248-36
						E3: 0.0084	265-63	E3: 0.0144	277-61	E3: 0.0015	353-19
						α= 15	`				
BD-12	**18**	**40.104919**	**-105.2842**	**Knf**	**025/20**	E1: 0.8492	**094-03**	E1: 0.7571	091-12	E1: NA	NA
						E2: 0.1095	186-15	E2: 0.1807	193-44	E2: NA	NA
						E3: 0.0413	346-75	E3: 0.0622	349-44	E3: NA	NA
						α= 15	`				
BD-14	**12**	**40.104748**	**-105.2839**	**Kns-C**	**021/22**	E1: 0.9738	**091-04**	E1: 0.9710	071-02	E1: NA	NA
						E2: 0.0149	185-41	E2: 0.0159	340-33	E2: NA	NA
						E3: 0.0113	356-49	E3: 0.0130	164-57	E3: NA	NA
						α= 20	`				
BD-16	**6**	**40.104355**	**-105.2828**	**Kns-B**	**033/21**	E1: 0.9861	**295-03**	E1: 0.9848	112-17	E1: NA	NA
						E2: 0.0112	028-42	E2: 0.0108	002-49	E2: NA	NA
						E3: 0.0026	201-47	E3: 0.0044	215-36	E3: NA	NA
						α= 20	`				
BD-17	**18**	**40.103374**	**-105.2823**	**Kns-B**	**020/30**	E1: 0.7739	**084-02**	E1: 0.8052	073-15	E1: 0.7563	234-32
						E2: 0.1275	352-32	E2: 0.1341	339-17	E2: 0.2409	338-22
						E3: 0.0986	177-58	E3: 0.0607	203-68	E3: 0.0028	097-50
						α= 20	`				
BD-19	**5**	**40.104978**	**-105.282**	**Kns-B**	**025/23**	E1: 0.9524	**089-15**	E1: 0.9566	080-14	E1: 1.0000	150-65
						E2: 0.0369	350-30	E2: 0.0412	348-07	E2: 0.0000	282-17
						E3: 0.0107	203-56	E3: 0.0023	232-74	E3: 0.0000	018-17
						α= 20	`				

Appendix 1: Shear Fractures (Minor Faults) Data Tables (continued).

Station #	N-Total	Lat. ^{0}N	Long. ^{0}W	Fm.*	S/D Beds	Rotated Slickenline (SS,TH Faults) eigenvectors** Eigenvalues	T-P	Rotated Slickenline (Normal Faults) eigenvectors** Eigenvalues	T-P
MS-3	**9**	**40.478617**	**-105.1276**	**Kns-C**	**000/33**	E1: 0.7338 E2: 0.1484 E3: 0.1178	127-54 331-34 233-12	E1: 0.7882 E2: 0.1699 E3: 0.0489	094-65 357-03 266-25
MS-5	**2**	**40.476544**	**-105.1282**	**Knf**	**354/31**	E1: 0.9972 E2: 0.0028 E3: 0.0000	052-00 142-24 321-66	E1: NA E2: NA E3: NA	N A N A N A
MS-6	**13**	**40.390919**	**-105.138**	**Knf**	**130/66**	E1: NA E2: NA E3: NA	NA NA NA	E1: 0.7451 E2: 0.1691 E3: 0.0858	202-25 307-30 079-50
CL-1	**1**	**40.298817**	**-105.1777**	**Knf**	**036/23**	E1: NA E2: NA E3: NA	NA NA NA	E1: 1.0000 E2: 0.0000 E3: 0.0000	137-42 261-32 013-32
HY-1 (only 2 slicks observed)	**10**	**40.230299**	**-105.2298**	**Knf**	**007/10**	E1: 0.9944 E2: 0.0056 E3: 0.0000	252-02 161-51 344-39	E1: NA E2: NA E3: NA	NA NA NA
HY-2	**5**	**40.231569**	**-105.23**	**Kns-C**	**010/9**	E1: 0.7713 E2: 0.2281 E3: 0.0006	278-14 188-00 98-76	E1: NA E2: NA E3: NA	NA NA NA
HY-3	**7**	**40.231095**	**-105.2281**	**Kns-A**	**002/26**	E1: 0.9081 E2: 0.0837 E3: 0.0082	274-23 180-10 067-65	E1: NA E2: NA E3: NA	NA NA NA
HY-4	**10**	**40.22933**	**-105.2277**	**Kns-C**	**359/23**	E1: 0.9666 E2: 0.0253 E3: 0.0081	275-14 181-20 038-65	E1: NA E2: NA E3: NA	NA NA NA
BD-1	**16**	**40.109807**	**-105.282**	**Knf**	**021/33**	E1: 0.8678 E2: 0.0956 E3: 0.0366	283-02 013-28 190-62	E1: NA E2: NA E3: NA	NA NA NA

Appendix 1: Shear Fractures (Minor Faults) Data Tables (continued).

Station #	N-Total	Lat. ^{0}N	Long. ^{0}W	Fm.*	S/D Beds	Rotated Slickenline (SS,TH Faults) eigenvectors** Eigenvalues	T-P	Rotated Slickenline (Normal Faults) eigenvectors** Eigenvalues	T-P
BD-8	**9**	**40.106052**	**-105.2849**	**Knf**	**166/55**	E1: NA E2: NA E3: NA	NA NA NA	E1: 0.7602 E2: 0.1966 E3: 0.0432	256-13 094-76 347-04
BD-10	**18**	**40.106312**	**-105.2856**	**Knf**	**015/30**	E1: 0.6751 E2: 0.2503 E3: 0.0746	250-20 346-17 115-63	E1: 1.0000 E2: 0.0000 E3: 0.0000	137-11 236-37 034-51
BD-11	**16**	**40.105709**	**-105.2854**	**Knf**	**017/39**	E1: 0.9430 E2: 0.0426 E3: 0.0144	263-07 354-08 132-79	E1: 0.9756 E2: 0.0221 E3: 0.0015	106-08 210-59 011-30
BD-12	**18**	**40.104919**	**-105.2842**	**Knf**	**025/20**	E1: 0.7571 E2: 0.1807 E3: 0.0622	272-06 177-37 010-52	E1: NA E2: NA E3: NA	NA NA NA
BD-14	**12**	**40.104748**	**-105.2839**	**Kns-C**	**021/22**	E1: 0.9710 E2: 0.0159 E3: 0.0130	250-15 355-45 146-41	E1: NA E2: NA E3: NA	NA NA NA
BD-16	**6**	**40.104355**	**-105.2828**	**Kns-B**	**033/21**	E1: 0.9848 E2: 0.0108 E3: 0.0044	292-04 029-56 200-34	E1: NA E2: NA E3: NA	NA NA NA
BD-17	**18**	**40.103374**	**-105.2823**	**Kns-B**	**020/30**	E1: 0.8052 E2: 0.1341 E3: 0.0607	254-10 351-34 150-54	E1: 0.7563 E2: 0.2409 E3: 0.0028	211-44 353-40 101-20
BD-19	**5**	**40.104978**	**-105.282**	**Kns-B**	**025/23**	E1: 0.9566 E2: 0.0412 E3: 0.0023	261-05 353-20 158-69	E1: 1.0000 E2: 0.0000 E3: 0.0000	135-44 260-31 010-30

Total Faults 216****

Appendix 1: Shear Fractures (Minor Faults) Data Tables (continued).

*** Formation abbreviations in Appendix 1:**
Kns-A : Upper chalk-marl sequence of the Smokey Hill member of the Niobrara Formation
Kns-B: Intermediate chalk-marl sequence of the Smokey Hill member of the Niobrara Formation
Kns-C: Lower chalk-marl sequence of the Smokey Hill member of the Niobrara Formation
Knf: Fort Hays limestone member of the Niobrara Formation
**** Best Fit alphas averaged for the Fort Hays Member α = 15+/- 1 and Smokey hill member α= 20+/- 1**
***** Insitu data rotated about bedding strike until bedding is horizontal**
******Station LP-1 (n=38) shows clear offset in fractures but no slickenlines were observed**
Fault types: SS= Strike Slip, TH = Thrust, N= Normal
Normal faults analyzed separately from SS and TH faults since they are interpreted as later events from reactivated surfaces and cross-cutting relationships.

Appendix 2: Extensional Fractures (Joints) Data Tables.

Station #	N	Lat. °N	Long. °W	Fm.*	S/D Beds	Insitu J1 eigenvectors Eigenvalues	T-P	Insitu J2 eigenvectors Eigenvalues	T-P	Rotated J1 eigenvectors** Eigenvalues	T/P	Rotated J2 eigenvectors** Eigenvalues	T/P
LV-1	**20**	**40.7726**	**-105.12595**	**Kns-A**	**005/10**	E1: 0.9448	172-01	E1: 0.8181	083-11	E1: 0.9448	352-02	E1: 0.8181	83-02
						E2: 0.0490	082-11	E2: 0.1754	352-03	E2: 0.0490	082-01	E2: 0.1754	353-05
						E3: 0.0062	264-79	E3: 0.0065	249-78	E3: 0.0062	202-88	E3: 0.0065	192-85
						N=10 Avg. J1 S/D	**262-90**	**N=10 Avg. J2 S/D**	**173-79**	**N=10 Avg. J1 S/D**	**83-87**	**N=10 Avg. J2 S/D**	**173-89**
LP-1	**21**	**40.644761**	**-106.18018**	**Knf**	**000 /20**	E1: 0.7799	352-01	E1: 0.9510	083-14	E1: 0.7799	353-04	E1: 0.9510	264-06
						E2: 0.2140	083-21	E2: 0.0389	237-78	E2: 0.2140	83-02	E2: 0.0389	140-79
						E3: 0.0061	260-69	E3: 0.0101	352-07	E3: 0.0061	191-86	E3: 0.0101	354-09
						N=15 Avg. J1 S/D	**082-89**	**N=6 Avg. J2 S/D**	**173-76**	**N=15 Avg. J1 S/D**	**83-86**	**N=6 Avg. J2 S/D**	**354-84**
LP-2	**16**	**40.6499**	**-105.138412**	**Kns-A**	**355/22**	E1: 0.9514	169-01	E1: 0.9979	085-23	E1: 0.9514	349-01	E1: 0.9979	85-01
						E2: 0.0425	079-10	E2: 0.0017	309-59	E2: 0.0425	259-12	E2: 0.0017	352-69
						E3: 0.0061	265-80	E3: 0.0004	183-20	E3: 0.0061	85-78	E3: 0.0004	175-21
						N=12 Avg. J1 S/D	**259-89**	**N=4 Avg. J2 S/D**	**175-67**	**N=12 Avg. J1 S/D**	**079-78**	**N=4 Avg. J2 S/D**	**175-90**
LP-3	**14**	**40.650269**	**-105.138495**	**Kns-B**	**000/12**	E1: 0.9890	344-02	E1: 0.9964	091-15	E1: 0.9890	344-05	E1: 0.9964	091-03
						E2: 0.0090	250-60	E2: 0.0029	311-70	E2: 0.0090	238-71	E2: 0.0029	347-77
						E3: 0.0020	075-30	E3: 0.0006	184-12	E3: 0.0020	76-18	E3: 0.0006	182-13
						N=7 Avg. J1 S/D	**074-88**	**N=7 Avg. J2 S/D**	**181-75**	**N=7 Avg. J1 S/D**	**074-85**	**N=7 Avg. J2 S/D**	**181-87**
LP-4	**9**	**40.65062**	**-105.138803**	**Kns-B**	**358/13**	E1: 0.9917	167-01	E1: 0.9981	088-30	E1: 0.9917	347-02	E1: 0.9981	88-17
						E2; 0.0066	258-34	E2: 0.0014	308-54	E2; 0.0066	255-47	E2: 0.0014	323-62
						E3: 0.0017	075-56	E3: 0.0005	190-19	E3: 0.0017	78-43	E3: 0.0005	185-21
						N=6 Avg. J1 S/D	**257-89**	**N=3 Avg. J2 S/D**	**178-60**	**N=6 Avg. J1 S/D**	**77-89**	**N=3 Avg. J2 S/D**	**178-73**
LP-5	**14**	**40.651043**	**-105.138946**	**Kns-B**	**000/20**	E1: 0.9611	170-01	E1: 0.9200	087-12	E1: 0.9611	350-02	E1: 0.9200	267-08
						E2: 0.0327	080-06	E2: 0.0770	357-03	E2: 0.0327	260-14	E2: 0.0770	358-04
						E3: 0.0062	272-84	E3: 0.0030	253-78	E3: 0.0062	89-76	E3: 0.0030	113-81
						N=9 Avg. J1 S/D	**260-89**	**N=5 Avg. J2 S/D**	**177-78**	**N=9 Avg. J1 S/D**	**80-88**	**N=5 Avg. J2 S/D**	**357-82**
LP-6	**18**	**40.651259**	**-105.139124**	**Kns-C**	**000/21**	E1: 0.9353	172-01	E1: 0.9127	079-19	E1: 0.9353	352-02	E1: 0.9127	260-02
						E2: 0.0621	082-03	E2: 0.0703	336-33	E2: 0.0621	262-18	E2: 0.0703	351-39
						E3: 0.0026	271-87	E3: 0.0170	195-51	E3: 0.0026	90-72	E3: 0.0170	168-51
						N=10 Avg. J1 S/D	**262-89**	**N=8 Avg. J2 S/D**	**169-71**	**N=10 Avg. J1 S/D**	**082-88**	**N=8 Avg. J2 S/D**	**350-89**
LP-7	**12**	**40.6726**	**-105.146871**	**Kns-A**	**340/15**	E1: 0.8943	330-01	E1: 0.9905	056-12	E1: 0.8943	331-04	E1: 0.9905	236-02
						E2: 0.0939	060-12	E2: 0.0095	285-72	E2: 0.0939	241-03	E2: 0.0095	339-80
						E3: 0.0118	233-78	E3: 0.0001	149-14	E3: 0.0118	115-85	E3: 0.0001	146-10
						N=9 Avg. J1 S/D	**060-89**	**N=3 Avg. J2 S/D**	**146-78**	**N=9 Avg. J1 S/D**	**61-86**	**N=3 Avg. J2 S/D**	**327-88**
LP-8	**43**	**40.672219**	**-105.149142**	**Kcgm**	**349/15**	E1: 0.9165	147-02	E1: 0.9058	071-17	E1: 0.9165	328-04	E1: 0.9058	71-02
						E2: 0.0689	057-12	E2: 0.0829	161-02	E2: 0.0689	238-02	E2: 0.0829	341-01
						E3; 0.0146	247-78	E3: 0.0114	256-73	E3; 0.0146	114-86	E3: 0.0114	236-88
						N=24 Avg. J1 S/D	**237-88**	**N=19 Avg. J2 S/D**	**161-73**	**N=24 Avg. J1 S/D**	**58-87**	**N=19 Avg. J2 S/D**	**161-88**
LP-9	**18**	**40.672383**	**-105.147995**	**Kns-B**	**355/15**	E1: 0.8280	164-01	E1: 0.9330	068-18	E1: 0.8280	344-02	E1: 0.9330	069-03
						E2: 0.1688	073-24	E2: 0.0489	159-04	E2: 0.1688	074-09	E2: 0.0489	159-00
						E3: 0.0032	256-66	E3: 0.0180	263-72	E3: 0.0032	242-81	E3: 0.0180	253-87
						N=10 Avg. J1 S/D	**254-89**	**N=8 Avg. J2 S/D**	**158-72**	**N=10 Avg. J1 S/D**	**74-88**	**N=8 Avg. J2 S/D**	**159-87**

Appendix 2: Extensional Fractures (Joints) Data Tables (continued).

Station	N	Lat.	Long.	Fm.*	S/D	Insitu J1 eigenvectors		Insitu J2 eigenvectors		Rotated J1 eigenvectors**		Rotated J2 eigenvectors**	
#		^{0}N	^{0}W		Beds	Eigenvalues	T-P	Eigenvalues	T-P	Eigenvalues	T/P	Eigenvalues	T/P
LP-10	**19**	**40.683431**	**-105.152398**	**Kcgm**	**355/15**	E1: 0.9434	162-08	E1: 0.9671	067-18	E1: 0.9434	161-05	E1: 0.9671	068-08
						E2: 0.0494	063-49	E2: 0.0223	326-30	E2: 0.0494	066-40	E2: 0.0223	332-34
						E3: 0.0072	258-40	E3: 0.0106	184-55	E3: 0.0072	257-50	E3: 0.0106	169-55
						N=9 Avg. J1 S/D	**252-82**	**N=10 Avg. J2 S/D**	**157-72**	**N=9 Avg. J1 S/D**	**251-85**	**N=10 Avg. J2 S/D**	**157-82**
LP-11	**16**	**40.683613**	**-105.150481**	**Kns-B**	**000/15**	E1: 0.9723	160-10	E1: 0.9529	080-20	E1: 0.9723	158-05	E1: 0.9529	081-05
						E2: 0.0274	063-33	E2: 0.0364	171-01	E2: 0.0274	066-20	E2: 0.0364	351-01
						E3: 0.0004	265-55	E3: 0.0107	264-70	E3: 0.0004	261-70	E3: 0.0107	245-85
						N=5 Avg. J1 S/D	**250-80**	**N=11 Avg. J2 S/D**	**170-70**	**N=5 Avg. J1 S/D**	**248-85**	**N=11 Avg. J2 S/D**	**171-85**
LP-12	**19**	**40.685498**	**-105.149089**	**Kns-A**	**355/16**	E1: 0.9895	139-08	E1: 0.9589	078-17	E1: 0.9895	318-02	E1: 0.9589	079-02
						E2: 0.0093	046-17	E2: 0.0251	345-11	E2: 0.0093	048-04	E2: 0.0251	348-14
						E3: 0.0013	253-71	E3: 0.0160	223-69	E3: 0.0013	208-85	E3: 0.0160	174-76
						N=9 Avg. J1 S/D	**229-82**	**N=10 Avg. J2 S/D**	**163-73**	**N=9 Avg. J1 S/D**	**048-89**	**N=10 Avg. J2 S/D**	**169-88**
LP-13	**28**	**40.716243**	**-105.150306**	**Kcgm**	**359/17**	E1: 0.7391	149-13	E1: 0.8373	063-07	E1: 0.7391	147-04	E1: 0.8373	243-09
						E2: 0.1962	56-11	E2: 0.1472	156-18	E2: 0.1962	237-03	E2: 0.1472	152-11
						E3: 0.0647	287-73	E3: 0.0155	314-71	E3: 0.0647	008-85	E3: 0.0155	012-76
						N=17 Avg. J1 S/D	**239-77**	**N=11 Avg. J2 S/D**	**153-83**	**N=17 Avg. J1 S/D**	**237-86**	**N=11 Avg. J2 S/D**	**334-82**
LP-14	**23**	**40.716264**	**-105.148447**	**Kns-B**	**010/16**	E1: 0.8877	167-04	E1: 0.9641	087-21	E1: 0.8877	347-03	E1: 0.9641	087-05
						E2: 0.1059	076-18	E2: 0.0254	350-16	E2: 0.1059	077-03	E2: 0.0254	355-21
						E3: 0.0064	268-72	E3: 0.0105	225-63	E3: 0.0064	213-86	E3: 0.0105	191-68
						N=9 Avg. J1 S/D	**257-86**	**N=14 Avg. J2 S/D**	**177-69**	**N=9 Avg. J1 S/D**	**077-87**	**N=14 Avg. J2 S/D**	**177-84**
LP-15	**15**	**40.694029**	**-105.149664**	**Kns-A**	**355/13**	E1: 0.9910	143-03	E1: 0.9123	089-07	E1: 0.9910	323-04	E1: 0.9123	269-06
						E2: 0.0080	233-08	E2: 0.0795	356-24	E2: 0.0080	232-19	E2: 0.0795	002-23
						E3: 0.0010	035-82	E3: 0.0082	194-66	E3: 0.0010	065-71	E3: 0.0082	164-66
						N=5 Avg. J1 S/D	**233-87**	**N=10 Avg. J2 S/D**	**179-83**	**N=5 Avg. J1 S/D**	**053-86**	**N=10 Avg. J2 S/D**	**359-84**
LP-16	**14**	**40.694486**	**-105.150825**	**Kns-B**	**005/12**	E1: 0.8918	350-07	E1: 0.9877	090-17	E1: 0.8918	352-10	E1: 0.9877	091-05
						E2: 0.1054	083-24	E2: 0.0121	228-68	E2: 0.1054	084-12	E2: 0.0121	198-74
						E3: 0.0028	245-65	E3: 0.0002	356-14	E3: 0.0028	223-74	E3: 0.0002	359-16
						N=9 Avg. J1 S/D	**080-83**	**N=5 Avg. J2 S/D**	**180-73**	**N=9 Avg. J1 S/D**	**082-81**	**N=5 Avg. J2 S/D**	**180-85**
HT-1	**25**	**40.605175**	**-105.15638**	**Knf**	**357/16**	E1: 0.7243	170-03	E1: 0.9491	084-17	E1: 0.7243	170-01	E1: 0.9491	084-01
						E2: 0.2669	079-24	E2: 0.0413	183-27	E2: 0.2669	80-08	E2: 0.0413	175-28
						E3: 0.0087	267-66	E3: 0.0097	327-57	E3: 0.0087	267-82	E3: 0.0097	353-62
						N=18 Avg. J1 S/D	**260-87**	**N=7 Avg. J2 S/D**	**174-74**	**N=18 Avg. J1 S/D**	**260-88**	**N=7 Avg. J2 S/D**	**174-90**
HT-2	**33**	**40.554764**	**-105.139845**	**Knf**	**001/19**	E1: 0.8258	146-08	E1: 0.9422	080-14	E1: 0.8258	326-03	E1: 0.9422	261-05
						E2: 0.1671	054-17	E2: 0.0463	174-13	E2: 0.1671	056-01	E2: 0.0463	170-10
						E3: 0.0071	260-71	E3: 0.0115	304-71	E3: 0.0071	169-86	E3: 0.0115	017-79
						N=19 Avg. J1 S/D	**236-82**	**N=14 Avg. J2 S/D**	**170-76**	**N=19 Avg. J1 S/D**	**055-87**	**N=14 Avg. J2 S/D**	**351-85**
HT-3	**11**	**40.544516**	**-105.136671**	**Knf**	**338/21**	E1: 0.9649	146-03	E1: 0.9930	070-22	E1: 0.9649	326-02	E1: 0.9930	070-01
						E2: 0.0336	056-00	E2: 0.0049	313-49	E2: 0.0336	235-20	E2: 0.0049	339-54
						E3: 0.0016	317-87	E3: 0.0021	175-33	E3: 0.0016	61-70	E3: 0.0021	161-36
						N=6 Avg. J1 S/D	**236-87**	**N=5 Avg. J2 S/D**	**160-68**	**N=6 Avg. J1 S/D**	**056-89**	**N=5 Avg. J2 S/D**	**160-89**
HT-4	**9**	**40.537989**	**-105.133292**	**Knf**	**352/19**	E1: 0.8160	140-05	E1: 0.9918	078-30	E1: 0.8160	320-05	E1: 0.9918	079-11
						E2: 0.1808	044-50	E2: 0.0042	318-41	E2: 0.1808	054-34	E2: 0.0042	335-49
						E3: 0.0032	235-40	E3: 0.0040	192-34	E3: 0.0032	223-56	E3: 0.0040	178-39
						N=6 Avg. J1 S/D	**230-85**	**N=3 Avg. J2 S/D**	**160-60**	**N=6 Avg. J1 S/D**	**050-85**	**N=3 Avg. J2 S/D**	**168-78**

Appendix 2: Extensional Fractures (Joints) Data Tables (continued).

Station	N	Lat.	Long.	Fm.*	S/D	Insitu J1 eigenvectors		Insitu J2 eigenvectors		Rotated J1 eigenvectors**		Rotated J2 eigenvectors**	
#		^{0}N	^{0}W		Beds	Eigenvalues	T-P	Eigenvalues	T-P	Eigenvalues	T/P	Eigenvalues	T/P
HT-5	**17**	**40.534639**	**-105.131857**	**Knf**	**358/15**	E1: 0.7111	141-05	E1: 0.9475	076-20	E1: 0.7111	321-05	E1: 0.9475	076-06
						E2: 0.2664	048-28	E2: 0.0497	345-1	E2: 0.2664	052-16	E2: 0.0497	346-04
						E3: 0.0225	239-62	E3: 0.0028	253-70	E3: 0.0225	215-74	E3: 0.0028	220-83
						N=11 Avg. J1 S/D	**231-85**	**N=6 Avg. J2 S/D**	**165-70**	**N=11 Avg. J1 S/D**	**050-86**	**N=6 Avg. J2 S/D**	**166-84**
HT-6	**13**	**40.53647**	**-105.13003**	**Kns-A**	**347/21**	E1: 0.9843	168-01	E1: 0.9689	098-16	E1: 0.9843	168-02	E1: 0.9689	277-04
						E2: 0.0140	078-04	E2: 0.0248	253-42	E2: 0.0140	258-17	E2: 0.0248	010-37
						E3: 0.0016	275-86	E3: 0.0063	204-43	E3: 0.0016	073-73	E3: 0.0063	182-53
						N=10 Avg. J1 S/D	**258-89**	**N=3 Avg. J2 S/D**	**188-74**	**N=10 Avg. J1 S/D**	**258-88**	**N=3 Avg. J2 S/D**	**007-87**
MS-1	**19**	**40.479364**	**-105.119609**	**Kb**	**350/35**	E1: 0.9582	345-01	E1: 0.9181	082-20	E1: 0.9582	346-03	E1: 0.9181	262-15
						E2: 0.0279	254-66	E2: 0.0799	322-54	E2: 0.0279	092-79	E2: 0.0799	015-55
						E3: 0.0139	076-24	E3: 0.0020	183-29	E3: 0.0139	256-11	E3: 0.0020	163-31
						N=14 Avg. J1 S/D	**075-90**	**N=5 Avg. J2 S/D**	**172-70**	**N=14 Avg. J1 S/D**	**077-87**	**N=5 Avg. J2 S/D**	**353-75**
MS-2	**9**	**40.550994**	**-105.128535**	**Knf**	**001/36**	E1: 0.8488	164-12	E1: 0.9859	087-34	E1: 0.8488	341-00	E1: 0.9859	268-02
						E2: 0.1454	068-26	E2: 0.0141	184-11	E2: 0.1454	251-08	E2: 0.0141	177-10
						E3: 0.0058	276-61	E3: 0.0001	289-54	E3: 0.0058	072-83	E3: 0.0001	009-80
						N=7 Avg. J1 S/D	**254-78**	**N=2 Avg. J2 S/D**	**177-56**	**N=7 Avg. J1 S/D**	**071-90**	**N=2 Avg. J2 S/D**	**358-87**
MS-3	**22**	**40.478617**	**-105.127618**	**Kns-C**	**000/33**	E1: 0.7847	345-01	E1: 0.8921	079-22	E1: 0.7847	348-09	E1: 0.8921	260-11
						E2: 0.1971	075-28	E2: 0.0963	338-25	E2: 0.1971	258-05	E2: 0.0963	357-33
						E3: 0.0182	253-63	E3: 0.0116	204-56	E3: 0.0182	140-80	E3: 0.0116	154-55
						N=12 Avg. J1 S/D	**075-89**	**N=10 Avg. J2 S/D**	**169-68**	**N=12 Avg. J1 S/D**	**078-82**	**N=10 Avg. J2 S/D**	**350-79**
MS-4	**10**	**40.47677**	**-105.12752**	**Kns-C**	**356/35**	E1: 0.8614	166-14	E1: 0.9591	074-29	E1: 0.8614	159-06	E1: 0.9591	255-06
						E2: 0.1381	066-33	E2: 0.0275	277-59	E2: 0.1381	249-00	E2: 0.0275	034-83
						E3: 0.0005	275-53	E3: 0.0134	170-10	E3: 0.0005	341-84	E3: 0.0134	165-05
						N=6 Avg. J1 S/D	**256-76**	**N=4 Avg. J2 S/D**	**164-61**	**N=6 Avg. J1 S/D**	**250-84**	**N=4 Avg. J2 S/D**	**345-85**
MS-5	**10**	**40.476544**	**-105.128192**	**Knf**	**354/31**	E1: 0.8705	346-05	E1: 0.9436	069-24	E1: 0.8705	349-09	E1: 0.9436	250-06
						E2: 0.1280	078-30	E2: 0.0555	282-62	E2: 0.1280	259-01	E2: 0.0555	022-81
						E3: 0.0016	247-60	E3: 0.0009	165-13	E3: 0.0016	162-81	E3: 0.0009	160-07
						N=5 Avg. J1 S/D	**075-85**	**N=5 Avg. J2 S/D**	**159-66**	**N=5 Avg. J1 S/D**	**079-82**	**N=5 Avg. J2 S/D**	**341-83**
MS-6	**43**	**40.390919**	**-105.137998**	**Knf**	**130/66**	E1: 0.8261	155-37	E1: 0.9290	297-31	E1: 0.8261	354-04	E1: 0.9290	276-02
						E2: 0.1526	277-34	E2: 0.0541	173-43	E2: 0.1526	085-11	E2: 0.0541	007-11
						E3: 0.0213	034-34	E3: 0.0169	049-32	E3: 0.0213	245-79	E3: 0.0169	175-79
						N=15 Avg. J1 S/D	**245-53**	**N=28 Avg. J2 S/D**	**027-59**	**N=15 Avg. J1 S/D**	**084-86**	**N=28 Avg. J2 S/D**	**007-88**
MS-7	**12**	**40.393194**	**-105.168721**	**Kns-A**	**023/11**	E1: 0.9041	008-08	E1: 0.9574	077-13	E1: 0.9041	010-11	E1: 0.9574	078-04
						E2: 0.0945	099-05	E2: 0.0291	184-51	E2: 0.0945	279-06	E2: 0.0291	173-46
						E3: 0.0014	220-80	E3: 0.0135	337-36	E3: 0.0014	163-78	E3: 0.0135	344-44
						N=5 Avg. J1 S/D	**098-82**	**N=7 Avg. J2 S/D**	**167-77**	**N=5 Avg. J1 S/D**	**100-80**	**N=7 Avg. J2 S/D**	**168-85**
CL-1	**12**	**40.298817**	**-105.177722**	**Knf**	**036/23**	E1: 0.9742	157-22	E1: 0.9610	070-15	E1: 0.9742	155-02	E1: 0.9610	073-01
						E2: 0.0238	057-24	E2: 0.0244	168-29	E2: 0.0238	65-14	E2: 0.0244	163-11
						E3: 0.0019	284-57	E3: 317-57	317-57	E3: 0.0019	252-76	E3: 317-57	338-79
						N=4 Avg. J1 S/D	**247-68**	**N=8 Avg. J2 S/D**	**160-76**	**N=4 Avg. J1 S/D**	**245-87**	**N=8 Avg. J2 S/D**	**163-89**
CL-2	**45**	**40.298666**	**-105.176051**	**Kns-B**	**350/31**	E1: 0.8139	156-15	E1: 0.9099	076-20	E1: 0.8139	151-06	E1: 0.9099	257-11
						E2: 0.1362	058-29	E2: 0.0763	168-04	E2: 0.1362	061-00	E2: 0.0763	166-02
						E3: 0.0499	270-56	E3: 0.0138	267-70	E3: 0.0499	328-84	E3: 0.0138	067-79
						N=21 Avg. J1 S/D	**246-75**	**N=24 Avg. J2 S/D**	**166-70**	**N=21 Avg. J1 S/D**	**241-83**	**N=24 Avg. J2 S/D**	**347-80**

Appendix 2: Extensional Fractures (Joints) Data Tables (continued).

Station	N	Lat.	Long.	Fm.*	S/D	Insitu J1 eigenvectors		Insitu J2 eigenvectors		Rotated J1 eigenvectors**		Rotated J2 eigenvectors**	
#		^{0}N	^{0}W		Beds	Eigenvalues	T-P	Eigenvalues	T-P	Eigenvalues	T/P	Eigenvalues	T/P
CL-3	**20**	**40.298812**	**-105.175404**	**Kns-A**	**004/39**	E1: 0.7703	176-08	E1: 0.9603	096-40	E1: 0.7703	173-01	E1: 0.9603	095-01
						E2: 0.2180	080-37	E2: 0.0314	346-22	E2: 0.2180	263-01	E2: 0.0314	005-29
						E3: 0.0116	277-52	E3: 0.0083	234-42	E3: 0.0116	031-88	E3: 0.0083	187-61
						N=14 Avg. J1 S/D	**266-82**	**N=6 Avg. J2 S/D**	**186-50**	**N=14 Avg. J1 S/D**	**263-88**	**N=6 Avg. J2 S/D**	**185-89**
CL-4	**10**	**40.275752**	**-105.178685**	**Knf**	**001/64**	E1: 0.8059	166-14	NA	NA	E1: 0.8059	342-07	NA	NA
						E2: 0.1511	028-72			E2: 0.1511	074-17		
						E3: 0.0430	258-12			E3: 0.0430	230-72		
						N=10 Avg. J1 S/D	**256-76**			**N=10 Avg. J1 S/D**	**073-84**		
CL-5	**46**	**40.3123**	**-105.17471**	**Kns-B**	**001/39**	E1: 0.8706	165-03	E1: 0.9218	074-32	E1: 0.8706	346-08	E1: 0.9218	257-06
						E2: 0.1181	072-34	E2: 0.0554	198-41	E2: 0.1181	256-03	E2: 0.0554	162-40
						E3: 0.0113	259-56	E3: 0.0228	321-32	E3: 0.0113	142-82	E3: 0.0228	353-49
						N=27 Avg. J1 S/D	**254-87**	**N=19 Avg. J2 S/D**	**164-58**	**N=27 Avg. J1 S/D**	**076-82**	**N=19 Avg. J2 S/D**	**347-84**
CL-6	**16**	**40.31166**	**-105.174943**	**Kns-C**	**002/43**	E1: 0.9822	174-11	E1: 0.9822	073-41	E1: 0.9822	169-03	E1: 0.9822	258-00
						E2: 0.0107	079-26	E2: 0.0167	290-42	E2: 0.0107	260-16	E2: 0.0167	348-77
						E3: 0.0071	284-62	E3: 0.0011	181-19	E3: 0.0071	071-74	E3: 0.0011	168-13
						N=10 Avg. J1 S/D	**264-80**	**N=6 Avg. J2 S/D**	**163-49**	**N=10 Avg. J1 S/D**	**260-87**	**N=6 Avg. J2 S/D**	**348-90**
CL-7	**23**	**40.311956**	**-105.175521**	**Knf**	**009/36**	E1: 0.9276	012-06	E1: 0.9269	080-30	E1: 0.9276	015-04	E1: 0.9269	262-04
						E2: 0.0630	105-21	E2: 0.0596	172-04	E2: 0.0630	284-15	E2: 0.0596	353-06
						E3: 0.0094	265-68	E3: 0.0135	270-59	E3: 0.0094	118-74	E3: 0.0135	139-83
						N=13 Avg. J1 S/D	**102-83**	**N=10 Avg. J2 S/D**	**170-60**	**N=13 Avg. J1 S/D**	**106-87**	**N=10 Avg. J2 S/D**	**352-86**
CL-8	**11**	**40.321448**	**-105.171755**	**Kns-A**	**009/32**	E1: 0.9793	357-00	E1: 0.9244	066-31	E1: 0.9793	359-06	E1: 0.9244	071-03
						E2: 0.0149	267-37	E2: 0.5073	283-53	E2: 0.0149	254-68	E2: 0.5073	307-84
						E3: 0.0058	87-53	E3: 0.0183	158-18	E3: 0.0058	092-21	E3: 0.0183	162-05
						N=6 Avg. J1 S/D	**087-90**	**N=5 Avg. J2 S/D**	**156-59**	**N=6 Avg. J1 S/D**	**089-84**	**N=5 Avg. J2 S/D**	**161-87**
HY-1	**47**	**40.230299**	**-105.229793**	**Knf**	**007/10**	E1: 0.8948	171-01	E1: 0.9680	086-10	E1: 0.8948	352-02	E1: 0.9680	086-00
						E2: 0.1007	081-03	E2: 0.0299	178-10	E2: 0.1007	261-06	E2: 0.0299	176-08
						E3: 0.0045	272-87	E3: 0.0021	311-76	E3: 0.0045	100-83	E3: 0.0021	356-82
						N=37 Avg. J1 S/D	**261-89**	**N=10 Avg. J2 S/D**	**176-80**	**N=37 Avg. J1 S/D**	**81-89**	**N=10 Avg. J2 S/D**	**176-90**
HY-2	**30**	**40.231569**	**-105.230044**	**Kns-C**	**010/9**	E1: 0.8172	348-03	E1: 0.8866	083-08	E1: 0.8172	348-06	E1: 0.8866	083-08
						E2: 0.1398	256-40	E2: 0.1115	176-15	E2: 0.1398	252-48	E2: 0.1115	176-15
						E3: 0.0430	081-50	E3: 0.0019	327-73	E3: 0.0430	084-41	E3: 0.0019	327-73
						N=17 Avg. J1 S/D	**078-87**	**N=13 Avg. J2 S/D**	**176-81**	**N=17 Avg. J1 S/D**	**079-85**	**N=13 Avg. J2 S/D**	**174-82**
HY-3	**18**	**40.231095**	**-105.228068**	**Kns-A**	**002/26**	E1: 0.8779	183-04	E1: 0.8280	086-24	E1: 0.8779	182-04	E1: 0.8280	267-02
						E2: 0.0873	273-01	E2: 0.1636	282-66	E2: 0.0873	274-27	E2: 0.1636	030-86
						E3: 0.0348	017-86	E3: 0.0084	179-06	E3: 0.0348	84-63	E3: 0.0084	177-04
						N=14 Avg. J1 S/D	**273-86**	**N=4 Avg. J2 S/D**	**176-67**	**N=14 Avg. J1 S/D**	**272-86**	**N=4 Avg. J2 S/D**	**357-88**
HY-4	**45**	**40.22933**	**-105.227674**	**Kns-C**	**359/23**	E1: 0.8984	180-04	E1: 0.9203	074-10	E1: 0.8984	178-04	E1: 0.9203	254-12
						E2: 0.0819	271-15	E2: 0.0723	170-28	E2: 0.0819	271-38	E2: 0.0723	159-22
						E3: 0.0197	075-75	E3: 0.0074	326-60	E3: 0.0197	083-52	E3: 0.0074	011-64
						N=27 Avg. J1 S/D	**270-86**	**N=18 Avg. J2 S/D**	**164-80**	**N=27 Avg. J1 S/D**	**268-86**	**N=18 Avg. J2 S/D**	**344-78**
BD-1	**17**	**40.109807**	**-105.282025**	**Knf**	**021/33**	E1: 0.9529	180-19	E1: 0.9636	075-20	E1: 0.9529	173-05	E1: 0.9636	257-07
						E2: 0.0372	073-40	E2: 0.0272	172-19	E2: 0.0372	082-12	E2: 0.0272	167-01
						E3: 0.0099	289-44	E3: 0.0092	301-62	E3: 0.0099	285-77	E3: 0.0092	070-83
						N=9 Avg. J1 S/D	**270-71**	**N=8 Avg. J2 S/D**	**165-70**	**N=9 Avg. J1 S/D**	**263-85**	**N=8 Avg. J2 S/D**	**347-83**

Appendix 2: Extensional Fractures (Joints) Data Tables (continued).

Station	N	Lat.	Long.	Fm.*	S/D	Insitu J1 eigenvectors		Insitu J2 eigenvectors		Rotated J1 eigenvectors**		Rotated J2 eigenvectors**	
#		^{0}N	^{0}W		Beds	Eigenvalues	T-P	Eigenvalues	T-P	Eigenvalues	T/P	Eigenvalues	T/P
BD-2	**18**	**40.107354**	**-105.2832**	**Knf**	**035/24**	E1: 0.9680	177-21	E1: 0.9875	086-21	E1: 0.9680	173-06	E1: 0.9875	089-02
						E2: 0.0269	287-41	E2: 0.0074	203-50	E2: 0.0269	274-63	E2: 0.0074	180-40
						E3: 0.0051	067-41	E3: 0.0051	342-33	E3: 0.0051	080-26	E3: 0.0051	357-50
						N=6 Avg. J1 S/D	**267-69**	**N=12 Avg. J2 S/D**	**176-69**	**N=6 Avg. J1 S/D**	**263-84**	**N=12 Avg. J2 S/D**	**179-89**
BD-3	**18**	**40.10683**	**-105.283656**	**Knf**	**026/24**	E1: 0.9154	175-16	E1: 0.9276	091-27	E1: 0.9154	172-03	E1: 0.9276	094-05
						E2: 0.0550	267-08	E2: 0.0596	190-16	E2: 0.0550	263-28	E2: 0.0596	185-08
						E3: 0.0296	022-72	E3: 0.0128	307-58	E3: 0.0296	076-62	E3: 0.0128	333-80
						N=9 Avg. J1 S/D	**265-74**	**N=9 Avg. J2 S/D**	**181-63**	**N=9 Avg. J1 S/D**	**262-87**	**N=9 Avg. J2 S/D**	**184-85**
BD-4	**25**	**40.106704**	**-105.283679**	**Knf**	**032/24**	E1: 0.9568	176-23	E1: 0.9083	085-15	E1: 0.9568	171-08	E1: 0.9083	266-05
						E2: 0.0283	055-51	E2: 0.0610	220-70	E2: 0.0283	078-37	E2: 0.0610	168-61
						E3: 0.0149	280-30	E3: 0.0307	351-14	E3: 0.0149	271-52	E3: 0.0307	359-28
						N=8 Avg. J1 S/D	**266-67**	**N=17 Avg. J2 S/D**	**175-75**	**N=8 Avg. J1 S/D**	**261-81**	**N=17 Avg. J2 S/D**	**356-86**
BD-5	**23**	**40.106217**	**-105.284075**	**Knf**	**033/21**	E1: 0.9781	172-20	E1: 0.8965	082-20	E1: 0.9781	168-05	E1: 0.8965	085-04
						E2: 0.0147	078-11	E2: 0.0564	214-61	E2: 0.0147	259-04	E2: 0.0564	181-55
						E3: 0.0072	320-67	E3: 0.0470	345-20	E3: 0.0072	026-84	E3: 0.0470	352-35
						N=7 Avg. J1 S/D	**262-70**	**N=16 Avg. J2 S/D**	**172-70**	**N=7 Avg. J1 S/D**	**258-84**	**N=16 Avg. J2 S/D**	**175-86**
BD-6	**19**	**40.105982**	**-105.284262**	**Knf**	**050/21**	E1: 0.9389	193-12	E1: 0.9169	091-08	E1: 0.9389	011-01	E1: 0.9169	271-06
						E2: 0.0403	013-78	E2: 0.0435	182-09	E2: 0.0403	105-73	E2: 0.0435	002-07
						E3: 0.0208	283-00	E3: 0.0396	321-78	E3: 0.0208	281-17	E3: 0.0396	138-81
						N=9 Avg. J1 S/D	**283-78**	**N=10 Avg. J2 S/D**	**181-82**	**N=9 Avg. J1 S/D**	**101-89**	**N=10 Avg. J2 S/D**	**001-83**
BD-7	**16**	**40.105783**	**-105.284637**	**Knf**	**128/16**	E1: 0.8872	163-17	E1: 0.8951	083-03	E1: 0.8872	165-07	E1: 0.8951	085-14
						E2: 0.1035	257-13	E2: 0.0877	219-86	E2: 0.1035	255-01	E2: 0.0877	218-70
						E3: 0.0093	024-69	E3: 0.0172	353-03	E3: 0.0093	351-83	E3: 0.0172	351-14
						N=6 Avg. J1 S/D	**253-74**	**N=10 Avg. J2 S/D**	**173-87**	**N=6 Avg. J1 S/D**	**255-82**	**N=10 Avg. J2 S/D**	**175-77**
BD-8	**21**	**40.106052**	**-105.284943**	**Knf**	**166/55**	E1: 0.7460	337-22	E1: 0.9468	266-54	E1: 0.7460	323-06	E1: 0.9468	082-00
						E2: 0.2121	201-61	E2: 0.0478	090-36	E2: 0.2121	232-16	E2: 0.0478	173-79
						E3: 0.0419	075-18	E3: 0.0055	359-02	E3: 0.0419	072-73	E3: 0.0055	352-11
						N=15 Avg. J1 S/D	**067-68**	**N=6 Avg. J2 S/D**	**356-36**	**N=15 Avg. J1 S/D**	**053-85**	**N=6 Avg. J2 S/D**	**172-89**
BD-9	**16**	**40.106691**	**-105.285321**	**Knf**	**061/22**	E1: 0.9752	170-28	E1: 0.9479	088-20	E1: 0.9752	168-07	E1: 0.9479	093-08
						E2: 0.0244	287-40	E2: 0.0372	201-48	E2: 0.0244	268-53	E2: 0.0372	188-31
						E3: 0.0004	057-37	E3: 0.0149	344-36	E3: 0.0004	073-36	E3: 0.0149	350-57
						N=7 Avg. J1 S/D	**260-62**	**N=9 Avg. J2 S/D**	**178-71**	**N=7 Avg. J1 S/D**	**258-83**	**N=9 Avg. J2 S/D**	**183-81**
BD-10	**10**	**40.106312**	**-105.285554**	**Knf**	**015/30**	E1: 0.9062	173-23	E1: 0.9742	071-16	E1: 0.9062	165-09	E1: 0.9742	252-10
						E2: 0.0848	056-47	E2: 0.0226	170-29	E2: 0.0848	071-24	E2: 0.0226	159-13
						E3: 0.0090	279-35	E3: 0.0032	316-57	E3: 0.0090	274-64	E3: 0.0032	017-74
						N=5 Avg. J1 S/D	**262-67**	**N=5 Avg. J2 S/D**	**161-74**	**N=5 Avg. J1 S/D**	**255-80**	**N=5 Avg. J2 S/D**	**342-80**
BD-11	**8**	**40.105709**	**-105.285364**	**Knf**	**017/39**	E1: 0.9846	179-17	E1: 0.9949	081-26	E1: 0.9846	172-02	E1: 0.9949	263-10
						E2: 0.0153	312-66	E2: 0.0049	303-57	E2: 0.0153	077-70	E2: 0.0049	056-79
						E3: 0.0001	084-17	E3: 0.0002	181-19	E3: 0.0001	263-19	E3: 0.0002	173-05
						N=4 Avg. J1 S/D	**269-73**	**N=4 Avg. J2 S/D**	**171-64**	**N=4 Avg. J1 S/D**	**262-87**	**N=4 Avg. J2 S/D**	**353-80**
BD-12	**10**	**40.104919**	**-105.284164**	**Knf**	**025/20**	E1: 0.6142	154-09	E1: 0.8885	087-02	E1: 0.6142	333-06	E1: 0.8885	265-16
						E2: 0.3425	254-47	E2: 0.1027	352-74	E2: 0.3425	233-60	E2: 0.1027	063-73
						E3: 0.0433	055-42	E3: 0.0088	177-16	E3: 0.0433	067-30	E3: 0.0088	174-06
						N=5 Avg. J1 S/D	**244-81**	**N=5 Avg. J2 S/D**	**176-89**	**N=5 Avg. J1 S/D**	**064-85**	**N=5 Avg. J2 S/D**	**356-74**

Appendix 2: Extensional Fractures (Joints) Data Tables (continued).

Station	N	Lat.	Long.	Fm.*	S/D	Insitu J1 eigenvectors		Insitu J2 eigenvectors		Rotated J1 eigenvectors**		Rotated J2 eigenvectors**	
#		**^{0}N**	**^{0}W**		**Beds**	**Eigenvalues**	**T-P**	**Eigenvalues**	**T-P**	**Eigenvalues**	**T/P**	**Eigenvalues**	**T/P**
BD-13	**0**	**40.104847**	**-105.284328**	**Kns-C**	**026/16**	Pencil Cleavage		Pencil Cleavage		Pencil Cleavage		Pencil Cleavage	
BD-14	**11**	**40.104748**	**-105.283917**	**Kns-C**	**021/22**	E1: 0.9486	167-14	E1: 0.9783	092-20	E1: 0.9486	165-01	E1: 0.9783	273-01
						E2: 0.0487	075-09	E2: 0.0130	354-21	E2: 0.0487	255-09	E2: 0.0130	004-29
						E3: 0.0026	313-74	E3: 0.0088	223-60	E3: 0.0026	070-81	E3: 0.0088	182-61
						N=6 Avg. J1 S/D	**257-77**	**N=5 Avg. J2 S/D**	**182-70**	**N=6 Avg. J1 S/D**	**255-88**	**N=5 Avg. J2 S/D**	**003-89**
BD-15	**11**	**40.104417**	**-105.283129**	**Kns-C**	**034/22**	E1: 0.9827	185-12	E1: 0.9422	077-14	E1: 0.9827	183-01	E1: 0.9422	259-01
						E2: 0.0155	276-03	E2: 0.0574	341-20	E2: 0.0155	273-22	E2: 0.0574	349-37
						E3: 0.0019	019-77	E3: 0.0004	200-65	E3: 0.0019	090-68	E3: 0.0004	168-53
						N=6 Avg. J1 S/D	**275-78**	**N=5 Avg. J2 S/D**	**167-76**	**N=6 Avg. J1 S/D**	**273-87**	**N=5 Avg. J2 S/D**	**349-90**
BD-16	**21**	**40.104355**	**-105.282812**	**Kns-B**	**033/21**	E1: 0.9714	180-06	E1: 0.9367	084-14	E1: 0.9714	359-05	E1: 0.9367	266-03
						E2: 0.0487	036-83	E2: 0.0597	187-41	E2: 0.0487	103-67	E2: 0.0597	174-29
						E3: 0.0075	270-05	E3: 0.0036	339-46	E3: 0.0075	267-22	E3: 0.0036	000-61
						N=10 Avg. J1 S/D	**270-84**	**N=11 Avg. J2 S/D**	**174-76**	**N=10 Avg. J1 S/D**	**90-84**	**N=11 Avg. J2 S/D**	**355-87**
BD-17	**9**	**40.103374**	**-105.282315**	**Kns-B**	**020/30**	E1: 0.7833	171-09	E1: 0.8715	074-26	E1: 0.7833	350-06	E1: 0.8715	079-01
						E2: 0.2017	071-46	E2: 0.1250	184-34	E2: 0.2017	083-21	E2: 0.1250	169-21
						E3: 0.0150	269-42	E3: 0.0035	315-45	E3: 0.0150	244-68	E3: 0.0035	345-69
						N=4 Avg. J1 S/D	**261-81**	**N=5 Avg. J2 S/D**	**164-64**	**N=4 Avg. J1 S/D**	**080-84**	**N=5 Avg. J2 S/D**	**168-88**
BD-18	**14**	**40.103718**	**-105.281777**	**Kns-B**	**023/27**	E1: 0.8394	154-23	E1: 0.9499	088-23	E1: 0.8394	150-02	E1: 0.9499	270-02
						E2: 0.1215	247-09	E2: 0.0348	352-15	E2: 0.1215	241-27	E2: 0.0348	001-27
						E3: 0.0391	357-66	E3: 0.0153	231-62	E3: 0.0391	057-64	E3: 0.0153	176-63
						N=7 Avg. J1 S/D	**244-67**	**N=7 Avg. J2 S/D**	**178-67**	**N=7 Avg. J1 S/D**	**240-88**	**N=7 Avg. J2 S/D**	**001-88**
BD-19	**11**	**40.104978**	**-105.281958**	**Kns-B**	**025/23**	E1: 0.6531	187-05	E1: 0.9433	062-15	E1: 0.6531	006-02	E1: 0.9433	064-00
						E2: 0.3293	095-28	E2: 0.0498	280-72	E2: 0.3293	097-06	E2: 0.0498	157-83
						E3: 0.0176	287-61	E3: 0.0069	155-11	E3: 0.0176	260-83	E3: 0.0069	334-07
						N=8 Avg. J1 S/D	**277-85**	**N=3 Avg. J2 S/D**	**152-75**	**N=8 Avg. J1 S/D**	**096-88**	**N=3 Avg. J2 S/D**	**154-90**
BD-20	**12**	**40.104308**	**-105.27982**	**Kns-A**	**032/31**	E1: 0.9065	170-11	E1: 0.9635	063-25	E1: 0.9065	350-10	E1: 0.9635	070-07
						E2: 0.0859	070-43	E2: 0.0286	172-36	E2: 0.0859	084-21	E2: 0.0286	162-13
						E3: 0.0076	272-45	E3: 0.0079	306-44	E3: 0.0076	237-67	E3: 0.0079	313-75
						N=6 Avg. J1 S/D	**260-79**	**N=6 Avg. J2 S/D**	**152-65**	**N=6 Avg. J1 S/D**	**080-82**	**N=6 Avg. J2 S/D**	**160-83**
Total:	**1165**					**Total N J1= 637**		**Total N J2= 528**					

*** Formation abbreviations in Appendix 2:**
Kns-A : Upper chalk-marl sequence of the Smokey Hill member of the Niobrara Formation
Kns-B: Intermediate chalk-marl sequence of the Smokey Hill member of the Niobrara Formation
Kns-C: Lower chalk-marl sequence of the Smokey Hill member of the Niobrara Formation
Knf: Fort Hays limestone member of the Niobrara Formation
Kcgm: Codell Sandstone
Kb: Carlile Shale
**** Insitu data rotated about bedding strike until bedding is horizontal**

Appendix 3: Calcite-Filled Fracture Data Tables.

Station #	N	Lat. ^{0}N	Long. ^{0}W	Fm.*	S/D Beds	**Insitu Healed Fracture eigenvectors Eigenvalues	T-P	***Rotated Healed Fracture eigenvectors Eigenvalues	T-P
LP-1	**6**	**40.644761**	**-106.1802**	**Knf**	**000 /20**	E1: 0.8909	335-01	E1: 0.8909	337-09
						E2: 0.1081	245-09	E2: 0.1081	242-27
						E3: 0.0010	070-81	E3: 0.0010	084-62
						AVG. S/D	**065-90**	**AVG. S/D**	**067-81**
LP-6	**2**	**40.651259**	**-105.1391**	**Kns-C**	**000/21**	E1: 0.9990	340-01	E1: 0.9990	341-08
						E2: 0.0009	070-34	E2: 0.0009	073-14
						E3: 0.0001	248-56	E3: 0.0001	221-74
						AVG. S/D	**070-89**	**AVG. S/D**	**072-83**
LP-14	**7**	**40.716264**	**-105.1484**	**Kns-B**	**010/16**	E1: 0.9751	148-08	E1: 0.9751	327-03
						E2: 0.0219	238-05	E2: 0.0219	236-17
						E3: 0.0030	358-81	E3: 0.0030	066-73
						AVG. S/D	**238-81**	**AVG. S/D**	**057-88**
LP-15	**3**	**40.694029**	**-105.1497**	**Kns-A**	**355/13**	E1: 0.9905	090-13	E1: 0.9905	090-00
						E2: 0.0073	327-66	E2: 0.0073	359-69
						E3: 0.0022	184-19	E3: 0.0022	180-21
						AVG. S/D	**180-77**	**AVG. S/D**	**179-90**
HT-4	**2**	**40.537989**	**-105.1333**	**Knf**	**352/19**	E1: 0.9978	138-06	E1: 0.9978	317-05
						E2: 0.0022	230-22	E2: 0.0022	224-37
						E3: 0.0000	033-67	E3: 0.0000	054-52
						AVG. S/D	**227-83**	**AVG. S/D**	**048-85**
HT-6	**2**	**40.53647**	**-105.13**	**Kns-A**	**347/21**	E1: 0.9985	354-08	E1: 0.9985	356-05
						E2: 0.0015	248-63	E2: 0.0015	224-83
						E3: 0.0000	088-26	E3: 0.0000	087-05
						AVG. S/D	**084-83**	**AVG. S/D**	**086-85**
MS-3	**9**	**40.478617**	**-105.1276**	**Kns-C**	**000/33**	E1: 0.5981	223-05	E1: 0.5981	216-27
						E2: 0.3212	318-38	E2: 0.3212	349-54
						E3: 0.0807	126-52	E3: 0.0807	114-23
						AVG. S/D	**314-84**	**AVG. S/D**	**306-63**
MS-5	**2**	**40.476544**	**-105.1282**	**Knf**	**354/31**	E1: 0.9970	138-12	E1: 0.9970	316-07
						E2: 0.0030	040-38	E2: 0.0030	048-15
						E3: 0.000	241-49	E3: 0.000	202-74
						AVG. S/D	**227-78**	**AVG. S/D**	**047-84**

Appendix 3: Calcite-Filled Fracture Data Tables (continued).

Station #	N	Lat. ^{0}N	Long. ^{0}W	Fm.*	S/D Beds	**Insitu Healed Fracture eigenvectors Eigenvalues	T-P	***Rotated Healed Fracture eigenvectors Eigenvalues	T-P
MS-6	**13**	**40.390919**	**-105.138**	**Knf**	**130/66**	E1: 0.8827	284-35	E1: 0.8827	088-06
						E2: 0.1100	035-28	E2: 0.1100	272-84
						E3: 0.0073	154-43	E3: 0.0073	178-00
						AVG. S/D	**014-56**	**AVG. S/D**	**178-84**
HY-1	**15**	**40.230299**	**-105.2298**	**Knf**	**007/10**	E1: 0.9215	003-02	E1: 0.9215	004-02
						E2: 0.0755	093-04	E2: 0.0755	273-06
						E3: 0.0030	252-86	E3: 0.0030	112-83
						AVG. S/D	**094-89**	**AVG. S/D**	**094-89**
HY-2	**4**	**40.231569**	**-105.23**	**Kns-C**	**010/9**	E1: 0.9382	005-02	E1: 0.9382	005-03
						E2: 0.0614	095-03	E2: 0.0614	275-06
						E3: 0.0004	236-86	E3: 0.0004	123-83
						AVG. S/D	**095-88**	**AVG. S/D**	**095-88**
HY-3	**6**	**40.231095**	**-105.2281**	**Kns-A**	**002/26**	E1: 0.8838	182-03	E1: 0.8838	181-02
						E2: 0.1607	092-04	E2: 0.1607	272-22
						E3: 0.0094	306-85	E3: 0.0094	085-68
						AVG. S/D	**272-87**	**AVG. S/D**	**271-87**
HY-4	**7**	**40.22933**	**-105.2277**	**Kns-C**	**359/23**	E1: 0.9411	182-06	E1: 0.9411	179-07
						E2: 0.0494	275-27	E2: 0.0494	277-50
						E3: 0.0095	080-63	E3: 0.0095	084-40
						AVG. S/D	**272-83**	**AVG. S/D**	**269-83**
BD-1	**12**	**40.109807**	**-105.282**	**Knf**	**021/33**	E1: 0.8214	180-01	E1: 0.8214	003-10
						E2: 0.1397	273-68	E2: 0.1397	140-77
						E3: 0.0389	090-22	E3: 0.0389	271-09
						AVG. S/D	**271-88**	**AVG. S/D**	**093-80**
BD-2	**2**	**40.107354**	**-105.2832**	**Knf**	**035/24**	E1: 0.9848	178-20	E1: 0.9848	174-04
						E2: 0.0152	269-04	E2: 0.0152	265-23
						E3: 0.0000	009-70	E3: 0.0000	074-67
						AVG. S/D	**268-69**	**AVG. S/D**	**264-85**
BD-4	**16**	**40.106704**	**-105.2837**	**Knf**	**032/24**	E1: 0.5215	124-10	E1: 0.5215	304-14
						E2: 0.4150	218-22	E2: 0.4150	208-22
						E3: 0.0636	011-66	E3: 0.0636	064-63
						AVG. S/D	**213-80**	**AVG. S/D**	**034-76**

Appendix 3: Calcite-Filled Fracture Data Tables (continued).

Station #	N	Lat. ^{0}N	Long. ^{0}W	Fm.*	S/D Beds	**Insitu Healed Fracture eigenvectors Eigenvalues	T-P	***Rotated Healed Fracture eigenvectors Eigenvalues	T-P
BD-5	**13**	**40.106217**	**-105.2841**	**Knf**	**033/21**	E1: 0.7441	174-08	E1: 0.7441	354-05
						E2: 0.2100	274-50	E2: 0.2100	252-66
						E3: 0.0460	078-39	E3: 0.0460	086-23
						AVG. S/D	**264-81**	**AVG. S/D**	**084-85**
BD-6	**22**	**40.105982**	**-105.2843**	**Knf**	**050/21**	E1: 0.8201	099-02	E1: 0.8201	277-13
						E2: 0.1518	008-07	E2: 0.1518	012-20
						E3: 0.0281	208-83	E3: 0.0281	156-65
						AVG. S/D	**189-88**	**AVG. S/D**	**008-77**
BD-7	**11**	**40.105783**	**-105.2846**	**Knf**	**128/16**	E1: 0.6948	158-03	E1: 0.6948	338-05
						E2: 0.2928	248-02	E2: 0.2928	069-12
						E3: 0.0124	010-87	E3: 0.0124	225-77
						AVG. S/D	**248-86**	**AVG. S/D**	**069-86**
BD-8	**16**	**40.106052**	**-105.2849**	**Knf**	**166/55**	E1: 0.6589	186-22	E1: 0.6589	016-02
						E2: 0.2881	298-42	E2: 0.2881	106-04
						E3: 0.0551	076-40	E3: 0.0551	253-86
						AVG. S/D	**276-68**	**AVG. S/D**	**105-89**
BD-9	**10**	**40.106691**	**-105.2853**	**Knf**	**061/22**	E1: 0.8534	179-19	E1: 0.8534	357-01
						E2: 0.1419	081-21	E2: 0.1419	087-12
						E3: 0.0046	307-62	E3: 0.0046	262-78
						AVG. S/D	**269-71**	**AVG. S/D**	**087-89**
BD-10	**11**	**40.106312**	**-105.2856**	**Knf**	**015/30**	E1: 0.7627	160-13	E1: 0.7627	338-04
						E2: 0.1594	047-58	E2: 0.1594	071-37
						E3: 0.0779	257-28	E3: 0.0779	242-53
						AVG. S/D	**250-77**	**AVG. S/D**	**069-86**
BD-11	**8**	**40.105709**	**-105.2854**	**Knf**	**017/39**	E1: 0.7997	167-22	E1: 0.7997	341-00
						E2: 0.1808	058-40	E2: 0.1808	071-10
						E3; 0.0195	279-43	E3; 0.0195	250-80
						AVG. S/D	**257-68**	**AVG. S/D**	**257-68**
BD-12	**9**	**40.104919**	**-105.2842**	**Knf**	**025/20**	E1: 0.8177	359-05	E1: 0.8177	002-14
						E2: 0.1791	253-71	E2: 0.1791	180-76
						E3: 0.0032	091-18	E3: 0.0032	272-01
						AVG. S/D	**089-86**	**AVG. S/D**	**092-77**

Appendix 3: Calcite-Filled Fracture Data Tables (continued).

Station #	N	Lat. ^{0}N	Long. ^{0}W	Fm.*	S/D Beds	**Insitu Healed Fracture eigenvectors		***Rotated Healed Fracture eigenvectors	
						Eigenvalues	**T-P**	**Eigenvalues**	**T-P**
BD-13	**13**	**40.104847**	**-105.2843**	**Kns-C**	**026/16**	E1: 0.6105	173-12	E1: 0.6105	171-03
						E2: 0.3867	082-03	E2: 0.3867	262-10
						E3: 0.0027	339-78	E3: 0.0027	067-79
						AVG. S/D	**263-79**	**AVG. S/D**	**262-87**
BD-14	**8**	**40.104748**	**-105.2839**	**Kns-C**	**021/22**	E1: 0.9721	159-08	E1: 0.9721	339-07
						E2: 0.0223	262-58	E2: 0.0223	224-74
						E3: 0.0055	065-31	E3: 0.0055	071-15
						AVG. S/D	**249-83**	**AVG. S/D**	**070-83**
BD-16	**7**	**40.104355**	**-105.2828**	**Kns-B**	**033/21**	E1: 0.9773	179-20	E1: 0.9773	175-08
						E2: 0.0195	055-57	E2: 0.0195	077-45
						E3: 0.0032	279-25	E3: 0.0032	273-44
						AVG. S/D	**269-69**	**AVG. S/D**	**266-82**
BD-17	**4**	**40.103374**	**-105.2823**	**Kns-B**	**020/30**	E1: 0.6288	181-39	E1: 0.6288	164-25
						E2: 0.3587	348-50	E2: 0.3587	030-57
						E3: 0.0125	086-06	E3: 0.0125	264-21
						AVG. S/D	**271-51**	**AVG. S/D**	**254-65**
BD-19	**4**	**40.104978**	**-105.282**	**Kns-B**	**025/23**	E1: 0.8917	172-07	E1: 0.8917	352-06
						E2: 0.0724	067-66	E2: 0.0724	089-47
						E3: 0.0358	265-23	E3: 0.0358	257-42
						AVG. S/D	**262-83**	**AVG. S/D**	**082-85**
TOTAL:	**244**								

[*] Formation abbreviations in Appendix 3:
Kns-A : Upper chalk-marl sequence of the Smokey Hill member of the Niobrara Formation
Kns-B: Intermediate chalk-marl sequence of the Smokey Hill member of the Niobrara Formation
Kns-C: Lower chalk-marl sequence of the Smokey Hill member of the Niobrara Formation
Knf: Fort Hays limestone member of the Niobrara Formation
**** Insitu data rotated about bedding strike until bedding is horizontal**

Appendix 4: Stylolite Data Tables.

Station #	N	Lat. ^{0}N	Long. ^{0}W	Fm.*	S/D Beds	Insitu Styolite eigenvectors Eigenvalues	T-P	*Rotated Styolite eigenvectors Eigenvalues	T-P
LP-1	**48**	**40.7726**	**-105.12595**	**Kns-A**	**005/10**	E1: 0.9772	086-18	E1: 0.9772	266-02
						E2: 0.0155	184-22	E2: 0.0155	175-22
						E3: 0.0074	321-61	E3: 0.0074	002-68
						AVG. S/D	**176-73**	**AVG. S/D**	**357-88**
HY-1	**21**	**40.230299**	**-105.229793**	**Knf**	**007/10**	E1: 0.9928	080-10	E1: 0.9928	080-00
						E2: 0.0046	171-07	E2: 0.0046	170-04
						E3: 0.0027	295-78	E3: 0.0027	347-86
						AVG. S/D	**170-80**	**AVG. S/D**	**170-89**
BD-1	**12**	**40.109807**	**-105.282025**	**Knf**	**021/33**	E1: 0.9901	082-26	E1: 0.9901	265-04
						E2: 0.0056	325-43	E2: 0.0056	003-64
						E3: 0.0042	193-36	E3: 0.0042	173-26
						AVG. S/D	**171-65**	**AVG. S/D**	**355-87**
BD-3	**6**	**40.10683**	**-105.283656**	**Knf**	**026/24**	E1: 0.9703	085-16	E1: 0.9703	266-05
						E2: 0.0270	261-74	E2: 0.0270	156-76
						E3: 0.0027	354-01	E3: 0.0027	357-13
						AVG. S/D	175-74	AVG. S/D	356-85
BD-4	**10**	**40.106704**	**-105.283679**	**Knf**	**032/24**	E1: 0.9856	081-12	E1: 0.9856	262-06
						E2: 0.0106	178-28	E2: 0.0106	171-13
						E3: 0.0038	330-59	E3: 0.0038	017-75
						AVG. S/D	**171-78**	**AVG. S/D**	**352-84**
TOTAL:	**97**								

*** Formation abbreviations in Appendix 4:**
Knf: Fort Hays limestone member of the Niobrara Formation
**** Insitu data rotated about bedding strike until bedding is horizontal**

Appendix 5: Pencil Cleavage Data Table.

Station #	N	Lat. ^{0}N	Long. ^{0}W	Fm.*	S/D Beds	Insitu Axial Plane Cleavage eigenvectors		Insitu Pencil Cleavage eigenvectors	
						Eigenvalues	T-P	Eigenvalues	T-P
BD-13	**20**	**40.104847**	**-105.2843**	**Kns-C**	**026/16**	E1: 0.9630	078-18	E1: 0.9642	171-11
						E2: 0.0289	171-10	E2: 0.0312	261-02
						E3: 0.0081	288-69	E3: 0.0046	001-79
						AVG. S/D	**167-73**		

**Rotated Axial Plane Cleavage eigenvectors		**Rotated Pencil Cleavage eigenvectors	
Eigenvalues	T-P	Eigenvalues	T-P
E1: 0.9630	080-05	E1: 0.9642	169-01
E2: 0.0289	170-01	E2: 0.0312	260-15
E3: 0.0081	265-85	E3: 0.0046	075-75
AVG. S/D	**169-85**		

TOTAL: 20

*** Formation abbreviations in Appendix 5:**
Kns-C: Lower chalk-marl sequence of the Smokey Hill member of the Niobrara Formation
**** Insitu data rotated about bedding strike until bedding is horizontal**

Appendix 6: Borehole Breakout Data Table.

Well Number: UWI#	No. of breakouts	Fm.*	**Shmax Vector Mean	Dispersion	Azimuth
5123302600000	15	Kp	70.27	0.127	070
5123296690000	62	Kp	-33.6	0.738	326
5123298330000	200	Kp	57.62	0.122	057
5123261550000	412	Kp	37.31	0.339	037
5123294150000	14	Kp	-58.28	0.891	301
5123252760000	422	Kp	-30.93	0.225	329
5123261070000	19	Kp	6.27	0.506	006
5123281950000	31	Kp	88.29	0.116	088
5123294900000	8	Kp	48.92	0.426	049
512329670000	6	Kp	-64.63	1.432	295
5123298920000	71	Kp	71.29	0.247	071
5123303500000	33	Kp	-61.28	0.415	299
5123391430000	23	Kp	1.23	0.245	001
ALL	**1316**		**32.44**	**0.858**	**032**

*** Formation abbreviations in Appendix 6:**
Kp: Pierre Shale
****The SHmax vector direction is 90^0 to the borehole breakout direction or SHmin vector direction**

Appendix 7: Formation Micro-Image Log Fracture Tables.

Well Name	Fm.*	N	S/D Beds	Fracture Type	Insitu Eigenvalues	Fracture eigenvectors T-P	Vector Mean	Dispersion
Shable USX AB11-06	**Kp**	1	063-03	Fault Plane	E1: 1.0000	085-20	-5.00	0.0000
					E2: 0.0000	265-70		
					E3: 0.0000	175-0		
					AVG. S/D	**175-70**		
	Kp	4	063-03	Natural	E1: 0.9982	297-11	27.25	0.0019
					E2: 0.0012	037-40		
					E3: 0.0005	194-48		
					AVG. S/D	**028-79**		
	Kns	13	080-02	Healed	E1: 0.9936	307-10	36.92	0.0089
					E2: 0.0048	041-23		
					E3: 0.0018	195-65		
					AVG. S/D	**038-80**		
	Knf	10	047-05	Healed	E1: 0.9923	308-09	37.71	0.0120
					E2: 0.0060	216-11		
					E3: 0.0016	076-75		
					AVG. S/D	**038-81**		
	Kcgm	1	045-03	Fault plane	E1: 1.0000	011-36	-79.00	0.0000
					E2: 0.0000	244-39		
					E3: 0.0000	126-30		
					AVG. S/D	**101-54**		
	Kcgm	133	045-03	Healed	E1: 0.9520	307-10	36.85	0.0800
					E2: 0.0364	217-00		
					E3: 0.0116	126-80		
					AVG. S/D	**037-80**		

Appendix 7: Formation Micro-Image Log Fracture Tables (continued).

Well Name	Fm.*	N	S/D Beds	Fracture Type	Insitu Eigenvalues	Fracture eigenvectors T-P	Vector Mean	Dispersion
Shable USX AB11-06	**TrP**	12	296-07	Fault Plane	E1: 0.5106	193-31	80.76	0.7826
					E2: 0.3413	302-28		
					E3: 0.1481	065-45		
					AVG. S/D	**284-59**		
	TrP	21	296-07	Healed	E1: 0.7349	357-38	87.58	0.4460
					E2: 0.1738	108-24		
					E3: 0.0913	222-42		
					AVG. S/D	**087-52**		
	TrP	3	296-07	Natural	E1: 0.8899	004-46	-83.78	0.3455
					E2: 0.1100	112-17		
					E3: 0.0002	216-39		
					AVG. S/D	**094-45**		
	Plo	3	283-05	Fault Plane	E1: 0.5147	278-63	12.15	0.4160
					E2: 0.3544	131-24		
					E3: 0.1309	035-13		
					AVG. S/D	**009-28**		
	Plo	11	283-05	Induced	E1: 0.9372	356-04	83.60	0.0871
					E2: 0.0620	266-02		
					E3: 0.0008	146-86		
					AVG. S/D	**086-88**		
	Plo	13	283-05	Healed	E1: 0.8819	336-19	65.96	0.2313
					E2: 0.1017	244-05		
					E3: 0.0163	140-70		
					AVG. S/D	**066-72**		

Appendix 7: Formation Micro-Image Log Fracture Tables (continued).

Well Name	Fm.*	N	S/D Beds	Fracture Type	Insitu Eigenvalues	Fracture eigenvectors T-P	Vector Mean	Dispersion
Shable USX AB11-06	**Plo**	17	283-05	Natural	E1: 0.8231	346-19	76.62	0.3159
					E2: 0.1301	080-13		
					E3: 0.0468	203-67		
					AVG. S/D	**076-71**		
Total	**All**	242	356-02		E1: 0.8004	314-13	44.75	0.3428
					E2: 0.1413	048-14		
					E3: 0.0583	184-71		
					AVG S/D	**044-78**		

* **Formation abbreviations in Appendix 7:**

Kp: Pierre Shale
Kns : Smokey Hill member of the Niobrara Formation
Knf: Fort Hays limestone member of the Niobrara Formation
Kcgm: Codell Sandstone
TrP: Lykins Formation
Plo: Lyons Formation

Appendix 8: Sooner Field 3D Seismic Fault Data Tables.

Seismic Fault Analysis
Data Set: Sooner Field T8N R58W **UTM NAD 83**

Fault Name	Total Fault Length (m)	Station #	Distance from last station (m)	Hangingwall Orientation Easting 1 x	Northing 1 y	Hangingwall (s)	Footwall Orientation Easting 2 x2	Northing 2 y2	Footwall (s)	dx Easting	dy Northing	Fault Type	Throw (meters)	Heave (meters)	RH Rule Fault Strike	dip degrees
1	1807.80	1	0.00	2448367.37	483491.6	1.330	2448435.2	483414.7	1.335	-67.78	76.86	**Normal**	8.09	31.24	49	15
1		2	44.19	2448495.45	483559.5	1.331	2448604.9	483435.4	1.337	-109.49	124.16	**Normal**	9.71	50.46	49	11
1		3	47.71	2448646.17	483601.8	1.332	2448772.9	483458.0	1.338	-126.76	143.75	**Normal**	9.71	58.42	49	9
1		4	43.74	2448734.32	483715	1.333	2448847.2	483587.0	1.338	-112.92	128.04	**Normal**	8.09	52.04	49	9
1		5	23.52	2448782.17	483775.5	1.331	2448931.6	483606.1	1.338	-149.41	169.43	**Normal**	11.33	68.85	49	9
1		6	47.81	2448842.46	483920.4	1.331	2448988.5	483754.8	1.34	-145.99	165.55	**Normal**	14.57	67.28	49	12
1		7	21.35	2448874.13	483982.8	1.331	2449442.6	483791.8	1.34	-568.48	191.04	**Normal**	14.57	182.80	19	5
1		8	33.18	2448964.02	484044.3	1.331	2449140.8	483921.7	1.339	-176.81	122.57	**Normal**	12.95	65.57	35	11
1		9	25.49	2448994.49	484122.2	1.332	2449182.6	483991.8	1.339	-188.07	130.37	**Normal**	11.33	69.75	35	9
1		10	23.82	2449001.83	484200	1.331	2449161.7	484044.6	1.339	-159.83	155.4	**Normal**	12.95	67.95	44	11
1		11	23.42	2449029.58	484271.6	1.331	2449199.3	484106.6	1.338	-169.71	165	**Normal**	11.33	72.15	44	9
1		12	21.70	2449072.98	484328	1.331	2449240.7	484165.0	1.337	-167.7	163.04	**Normal**	9.71	71.29	44	8
1		13	43.14	2449175.58	484425.5	1.330	2449333.4	484272.1	1.337	-157.83	153.44	**Normal**	11.33	67.09	44	10
1		14	26.23	2449189.72	484510.4	1.328	2449332.0	484372.1	1.337	-142.28	138.33	**Normal**	14.57	60.48	44	14
1		15	24.08	2449264.29	484536.5	1.328	2449418.5	484386.6	1.336	-154.17	149.88	**Normal**	12.95	65.54	44	11
1		16	21.94	2449303.93	484596.6	1.328	2449454.1	484450.6	1.336	-150.14	145.98	**Normal**	12.95	63.83	44	11
1		17	21.57	2449355.19	484645.4	1.328	2449489.8	484514.5	1.335	-134.6	130.86	**Normal**	11.33	57.22	44	11
1		18	18.94	2449394.31	484693.7	1.328	2449598.3	484552.3	1.335	-204.02	141.42	**Normal**	11.33	75.66	35	9
1		19	25.03	2449431.58	484766.9	1.327	2449683.0	484592.6	1.334	-251.41	174.28	**Normal**	11.33	93.24	35	7
1		20	25.18	2449466.3	484841.8	1.327	2449724.7	484662.7	1.333	-258.42	179.14	**Normal**	9.71	95.84	35	6
1		21	16.18	2449467.87	484894.9	1.326	2449694.0	484769.9	1.334	-226.09	125	**Normal**	12.95	78.74	29	9
1		22	15.51	2449481.96	484943.8	1.326	2449737.5	484802.5	1.334	-255.57	141.3	**Normal**	12.95	89.01	29	8
1		23	27.25	2449505.37	485030	1.325	2449817.6	484857.4	1.333	-312.19	172.61	**Normal**	12.95	108.73	29	7
1		24	15.12	2449528.58	485073.9	1.326	2449863.3	484888.8	1.334	-334.68	185.04	**Normal**	12.95	116.56	29	6
1		25	26.59	2449563.23	485153.9	1.325	2449889.0	484973.8	1.334	-325.77	180.11	**Normal**	14.57	113.46	29	7
1		26	26.91	2449591.3	485237.6	1.326	2449898.8	484967.6	1.335	-307.53	270.03	**Normal**	14.57	124.74	41	7
1		27	26.78	2449621.5	485320.1	1.326	2449935.8	485146.4	1.335	-314.31	173.78	**Normal**	14.57	109.47	29	8
1		28	17.60	2449619.68	485377.8	1.326	2449977.1	485180.3	1.335	-357.37	197.59	**Normal**	14.57	124.47	29	7
1		29	44.14	2449687.37	485505.9	1.326	2450016.9	485185.5	1.334	-329.55	320.39	**Normal**	12.95	140.09	44	5
1		30	28.12	2449770.93	485545	1.325	2450025.8	485198.6	1.334	-254.85	346.37	**Normal**	14.57	131.07	54	6
1		31	43.11	2449869.51	485646.4	1.325	2450088.3	485349.0	1.335	-218.83	297.42	**Normal**	16.18	112.55	54	8
1		32	42.63	2449987.71	485721.1	1.323	2450221.3	485403.7	1.334	-233.54	317.42	**Normal**	17.80	120.11	54	8
1		33	27.79	2450028.85	485802.5	1.324	2450254.3	485496.1	1.335	-225.42	306.37	**Normal**	17.80	115.93	54	9
1		34	17.72	2450074.79	485838.1	1.324	2450308.5	485520.5	1.334	-233.7	317.63	**Normal**	16.18	120.20	54	8
1		35	31.40	2450102.91	485937.2	1.323	2450352.9	485597.5	1.334	-249.95	339.71	**Normal**	17.80	128.55	54	8
1		36	22.15	2450175.06	485928.5	1.322	2450405.4	485624.2	1.333	-230.33	304.3	**Normal**	17.80	116.32	53	9
1		37	26.39	2450245.63	485978.6	1.320	2450484.1	485654.6	1.333	-238.45	324.08	**Normal**	21.04	122.64	54	10
1		38	18.10	2450299.69	486003.2	1.321	2450494.2	485738.9	1.333	-194.47	264.3	**Normal**	19.42	100.02	54	11
1		39	43.99	2450390.15	486115.7	1.320	2450561.6	485882.6	1.333	-171.49	233.06	**Normal**	21.04	88.20	54	13
1		40	47.58	2450461	486254.8	1.321	2450681.5	485955.1	1.331	-220.52	299.71	**Normal**	16.18	113.41	54	8

Appendix 8: Sooner Field 3D Seismic Fault Data Tables (continued).

Fault Name	Total Fault Length (m)	Station #	Distance from last station (m)	Hangingwall Orientation Easting 1 x	Northing 1 y	Hangingwall (s)	Footwall Orientation Easting 2 x2	Northing 2 y2	Footwall (s)	dx Easting	dy Northing	Fault Type	Throw (meters)	Heave (meters)	RH Rule Fault Strike	dip degrees
1		41	53.78	2450547.57	486408.5	1.320	2450796.8	486117.8	1.329	-249.25	290.68	**Normal**	14.57	116.71	49	7
1		42	17.23	2450562.44	486463.1	1.320	2450941.8	486155.9	1.327	-379.32	307.15	**Normal**	11.33	148.77	39	4
1		43	15.11	2450601.97	486493	1.321	2450936.7	486307.9	1.329	-334.68	185.04	**Normal**	12.95	116.56	29	6
1		44	15.53	2450615.85	486542	1.321	2451016.3	486320.6	1.328	-400.43	221.39	**Normal**	11.33	139.46	29	5
1		45	27.58	2450680.19	486605.6	1.321	2451107.6	486369.4	1.327	-427.36	236.28	**Normal**	9.71	148.84	29	4
1		46	35.05	2450794.62	486594.3	1.320	2451121.0	486368.1	1.326	-326.42	226.28	**Normal**	9.71	121.06	35	5
1		47	17.95	2450820.02	486647.5	1.320	2451125.8	486435.5	1.327	-305.8	211.99	**Normal**	11.33	113.41	35	6
1		48	33.04	2450837.7	486754.4	1.321	2451114.9	486484.9	1.327	-277.19	269.49	**Normal**	9.71	117.84	44	5
1		49	20.97	2450875.73	486811.7	1.320	2451108.5	486529.0	1.328	-232.79	282.73	**Normal**	12.95	111.63	51	7
1		50	48.05	2451009.9	486894.5	1.320	2451274.8	486572.8	1.327	-264.87	321.69	**Normal**	11.33	127.01	51	5
1		51	19.05	2451056.68	486936	1.319	2451303.9	486635.7	1.327	-247.25	300.29	**Normal**	12.95	118.56	51	6
1		52	26.53	2451092.52	487015.3	1.320	2451335.0	486720.8	1.327	-242.43	294.43	**Normal**	11.33	116.25	51	6
1		53	24.20	2451161.95	487053.8	1.320	2451407.5	486755.5	1.327	-245.59	298.28	**Normal**	11.33	117.77	51	5
1		54	25.45	2451241.01	487080.6	1.319	2451478.6	486792.0	1.326	-237.61	288.58	**Normal**	11.33	113.94	51	6
1		55	23.84	2451304.11	487126.8	1.319	2451541.7	486838.3	1.326	-237.61	288.59	**Normal**	11.33	113.94	51	6
1		56	31.68	2451299.54	487230.7	1.319	2451572.4	486899.3	1.325	-272.84	331.38	**Normal**	9.71	130.83	51	4
1		57	20.56	2451363.93	487250.7	1.320	2451601.5	486962.2	1.325	-237.61	288.58	**Normal**	8.09	113.94	51	4
1		58	27.67	2451394.81	487336.1	1.319	2451653.3	487022.1	1.325	-258.53	314	**Normal**	9.71	123.97	51	4
1		59	25.05	2451476.97	487334.6	1.319	2451680.9	487087.0	1.325	-203.88	247.62	**Normal**	9.71	97.77	51	6
1		60	42.84	2451585.19	487424.3	1.319	2451779.4	487188.4	1.325	-194.24	235.92	**Normal**	9.71	93.14	51	6
1		61	43.86	2451674.13	487537.4	1.318	2451878.0	487289.8	1.324	-203.88	247.62	**Normal**	9.71	97.77	51	6
1		62	42.84	2451784	487625.1	1.317	2451992.7	487371.6	1.323	-208.7	253.47	**Normal**	9.71	100.08	51	6
1		63	42.87	2451895.39	487710.9	1.316	2452038.3	487537.4	1.322	-142.89	173.56	**Normal**	9.71	68.52	51	8
2	1054.52	1	0.00	2445974.48	485651.8	1.330	2445976.8	485460.1	1.333	-2.32	191.65	**Normal**	4.86	58.42	89	5
2		2	34.27	2446074.82	485601	1.329	2446076.6	485478.1	1.332	-1.73	122.89	**Normal**	4.86	37.46	89	7
2		3	31.28	2446174.49	485625.5	1.329	2446176.6	485475.4	1.332	-2.11	150.04	**Normal**	4.86	45.74	89	6
2		4	30.90	2446274.25	485643.5	1.329	2446276.6	485478.8	1.332	-2.32	164.7	**Normal**	4.86	50.21	89	6
2		5	30.50	2446374.18	485649	1.329	2446376.3	485498.9	1.331	-2.11	150.05	**Normal**	3.24	45.74	89	4
2		6	30.72	2446473.99	485662.9	1.329	2446476.6	485477.5	1.33	-2.61	185.41	**Normal**	1.62	56.52	89	2
2		7	30.64	2446573.84	485674.7	1.328	2446575.2	485576.8	1.33	-1.37	97.88	**Normal**	3.24	29.84	89	6
2		8	30.80	2446673.62	485690.7	1.328	2446674.2	485651.1	1.329	-0.56	39.66	**Normal**	1.62	12.09	89	8
2		9	31.27	2446773.93	485669.3	1.328	2446775.8	485535.8	1.328	-1.88	133.43	**Normal**	0.00	40.67	89	0
2		10	34.08	2446874.63	485620.7	1.327	2446875.7	485541.5	1.329	-1.11	79.13	**Normal**	3.24	24.12	89	8
2		11	30.48	2446974.62	485622.1	1.327	2446976.6	485484.5	1.328	-1.93	137.55	**Normal**	1.62	41.93	89	2
2		12	70.90	2447176.27	485506.1	1.329	2447179.4	485285.3	1.332	-3.11	220.77	**Normal**	4.86	67.30	89	4
2		13	30.50	2447276.2	485511.6	1.328	2447279.3	485290.9	1.332	-3.11	220.77	**Normal**	6.47	67.30	89	5
2		14	30.72	2447376.37	485500.5	1.328	2447379.1	485306.9	1.332	-2.72	193.61	**Normal**	6.47	59.02	89	6
2		15	35.30	2447475.54	485560.4	1.328	2447477.9	485393.7	1.332	-2.34	166.66	**Normal**	6.47	50.80	89	7
2		16	31.14	2447575.82	485540.9	1.328	2447577.8	485397.3	1.333	-2.02	143.6	**Normal**	8.09	43.77	89	10
2		17	13.98	2447620.3	485552	1.328	2447636.1	485389.7	1.333	-15.83	162.36	**Normal**	8.09	49.72	84	9
2		18	16.36	2447658.15	485590.1	1.328	2447692.4	485400.8	1.334	-34.29	189.26	**Normal**	9.71	58.63	80	9
2		19	15.62	2447708.61	485599	1.328	2447753.4	485443.5	1.333	-44.78	155.5	**Normal**	8.09	49.32	74	9

Appendix 8: Sooner Field 3D Seismic Fault Data Tables (continued).

Fault Name	Total Fault Length (m)	Station #	Distance from last station (m)	Hangingwall Orientation Easting 1 x	Northing 1 y	Hangingwall (s)	Footwall Orientation Easting 2 x2	Northing 2 y2	Footwall (s)	dx Easting	dy Northing	Fault Type	Throw (meters)	Heave (meters)	RH Rule Fault Strike	dip degrees
2		20	24.03	2447741.48	485670.7	1.328	2447796.4	485538.7	1.333	-54.94	131.93	Normal	8.09	43.56	67	11
2		21	26.96	2447824.55	485640.3	1.327	2447920.7	485472.8	1.333	-96.16	167.48	Normal	9.71	58.86	60	9
2		22	27.89	2447913.83	485660.4	1.327	2447982.2	485541.2	1.333	-68.41	119.16	Normal	9.71	41.88	60	13
2		23	21.95	2447950.93	485722.1	1.327	2448029.9	485619.9	1.331	-78.94	102.22	Normal	6.47	39.37	52	9
2		24	42.68	2448063.48	485805.4	1.327	2448166.7	485671.8	1.331	-103.19	133.61	Normal	6.47	51.46	52	7
2		25	42.94	2448164.69	485903.4	1.327	2448250.0	485793.0	1.33	-85.27	110.42	Normal	4.86	42.52	52	7
2		26	42.88	2448267.09	485999.9	1.326	2448390.6	485840.0	1.329	-123.49	159.91	Normal	4.86	61.58	52	5
2		27	45.67	2448345.25	486127.7	1.324	2448485.3	485946.3	1.329	-140.09	181.4	Normal	8.09	69.86	52	7
2		28	42.73	2448451.48	486219.2	1.324	2448589.1	486041.1	1.329	-137.58	178.15	Normal	8.09	68.61	52	7
2		29	24.77	2448523.52	486256.8	1.324	2448624.1	486126.6	1.329	-100.56	130.22	Normal	8.09	50.15	52	9
2		30	20.18	2448553.88	486315.7	1.324	2448663.4	486173.9	1.329	-109.52	141.81	Normal	8.09	54.61	52	8
2		31	25.52	2448632.26	486345.1	1.324	2448735.3	486211.6	1.328	-103.06	133.46	Normal	6.47	51.40	52	7
2		32	26.60	2448641	486431.9	1.324	2448795.1	486232.4	1.328	-154.06	199.49	Normal	6.47	76.83	52	5
2		33	33.35	2448749.95	486421.7	1.325	2448841.6	486303.1	1.329	-91.6	118.61	Normal	6.47	45.68	52	8
2		34	46.89	2448821.78	486557.8	1.325	2448893.1	486465.4	1.327	-71.29	92.32	Normal	3.24	35.55	52	5
3	341.62	1	0.00	2452686.68	486651.6	1.319	2452551.0	486816.4	1.322	135.68	-164.78	Normal	4.86	65.06	231	4
3		2	43.59	2452778.38	486761.4	1.318	2452645.4	486922.8	1.322	132.96	-161.47	Normal	6.47	63.75	231	6
3		3	24.16	2452829.94	486821.6	1.318	2452705.3	486973.0	1.323	124.64	-151.38	Normal	8.09	59.77	231	8
3		4	27.54	2452831.65	486911.9	1.318	2452751.6	487066.5	1.323	80.03	-154.58	Normal	8.09	53.06	243	9
3		5	1.79	2452828.95	486917.1	1.318	2452743.5	487082.1	1.322	85.42	-165	Normal	6.47	56.63	243	7
3		6	20.93	2452886.67	486880	1.317	2452765.5	487075.6	1.322	121.15	-195.62	Normal	8.09	70.13	238	7
3		7	54.52	2453015.87	487003.6	1.316	2452888.4	487127.6	1.322	127.48	-123.93	Normal	9.71	54.19	224	10
3		8	22.22	2453077.82	487042	1.316	2452930.5	487185.3	1.323	147.35	-143.25	Normal	11.33	62.64	224	10
3		9	25.12	2453096.76	487122.2	1.315	2452888.1	487325.1	1.323	208.68	-202.88	Normal	12.95	88.71	224	8
3		10	28.33	2453061.25	487208.1	1.315	2452896.3	487328.3	1.324	164.94	-120.11	Normal	14.57	62.19	216	13
3		11	26.47	2453135.65	487252.9	1.315	2452904.8	487421.0	1.324	230.85	-168.11	Normal	14.57	87.04	216	10
3		12	18.92	2453158.13	487310.8	1.314	2452956.8	487457.4	1.324	201.3	-146.58	Normal	16.18	75.90	216	12
3		13	17.09	2453213.81	487304.3	1.315	2452965.4	487545.8	1.324	248.43	-241.52	Normal	14.57	105.61	224	8
3		14	30.95	2453315.35	487304.2	1.314	2453060.4	487552.1	1.325	254.94	-247.86	Normal	17.80	108.38	224	9
4	647.00	1	0.00	2450536.59	483368.3	1.329	2450637.2	483506.5	1.333	-100.61	-138.15	Normal	6.47	52.09	306	7
4		2	19.44	2450572.35	483315.5	1.329	2450739.1	483544.5	1.333	-166.78	-229.02	Normal	6.47	86.35	306	4
4		3	25.29	2450624.11	483250.7	1.328	2450841.6	483549.3	1.333	-217.47	-298.63	Normal	8.09	112.60	306	4
4		4	30.24	2450717.92	483283	1.328	2450930.4	483545.4	1.334	-212.48	-262.4	Normal	9.71	102.91	309	5
4		5	24.61	2450723.3	483202.4	1.328	2450916.7	483501.5	1.334	-193.36	-299.07	Normal	9.71	108.55	303	5
4		6	30.96	2450824.82	483206.2	1.328	2451025.2	483516.2	1.335	-200.42	-310.01	Normal	11.33	112.52	303	6
4		7	22.84	2450899.74	483205.7	1.328	2450990.6	483491.6	1.335	-90.86	-285.92	Normal	11.33	91.44	288	7
4		8	16.47	2450952.48	483193.9	1.328	2450997.8	483491.7	1.335	-45.33	-297.79	Normal	11.33	91.81	279	7
4		9	32.59	2451043.78	483138.3	1.328	2451088.9	483434.8	1.337	-45.13	-296.49	Normal	14.57	91.41	279	9
4		10	30.30	2451143.14	483135.5	1.328	2451180.8	483383.2	1.335	-37.7	-247.66	Normal	11.33	76.36	279	8
4		11	36.80	2451172.45	483018.4	1.328	2451314.7	483213.7	1.338	-142.25	-195.33	Normal	16.18	73.65	306	12
4		12	20.02	2451237.47	483009.1	1.328	2451443.9	483264.1	1.333	-206.47	-254.99	Normal	8.09	100.00	309	5
4		13	23.42	2451296.48	482959.9	1.328	2451437.3	483133.7	1.334	-140.77	-173.84	Normal	9.71	68.18	309	8

Appendix 8: Sooner Field 3D Seismic Fault Data Tables (continued).

Fault Name	Total Fault Length (m)	Station #	Distance from last station (m)	Hangingwall Orientation Easting 1 x	Northing 1 y	Hangingwall (s)	Footwall Orientation Easting 2 x2	Northing 2 y2	Footwall (s)	dx Easting	dy Northing	Fault Type	Throw (meters)	Heave (meters)	RH Rule Fault Strike	dip degrees
4		14	42.93	2451405.56	482870.8	1.328	2451521.6	483014.1	1.336	-116.04	-143.31	Normal	12.95	56.20	309	13
4		15	13.07	2451444.21	482852.2	1.328	2451470.7	483058.1	1.335	-26.47	-205.94	Normal	11.33	63.29	277	10
4		16	35.11	2451534.89	482781.2	1.328	2451564.4	483010.9	1.336	-29.52	-229.7	Normal	12.95	70.59	277	10
4		17	30.77	2451635.6	482788.2	1.328	2451658.3	482964.9	1.336	-22.71	-176.71	Normal	12.95	54.30	277	13
4		18	30.93	2451730.95	482753.4	1.328	2451754.7	482938.5	1.336	-23.78	-185.06	Normal	12.95	56.87	277	13
4		19	5.96	2451749.78	482748.1	1.328	2451791.0	482877.8	1.335	-41.21	-129.68	Normal	11.33	41.47	288	15
4		20	7.22	2451768.46	482733.6	1.328	2451831.6	482842.2	1.336	-63.09	-108.58	Normal	12.95	38.28	300	19
4		21	33.56	2451877.29	482750.2	1.328	2451925.4	482833.1	1.335	-48.14	-82.86	Normal	11.33	29.21	300	21
4		22	33.71	2451872.6	482639.7	1.328	2452015.0	482884.8	1.334	-142.39	-245.08	Normal	9.71	86.39	300	6
4		23	44.72	2452017.37	482615.8	1.328	2452161.8	482864.4	1.334	-144.42	-248.58	Normal	9.71	87.63	300	6
4		24	21.70	2452086.57	482632.5	1.328	2452212.0	482848.4	1.334	-125.47	-215.96	Normal	9.71	76.13	300	7
4		25	34.34	2452197.43	482652.6	1.329	2452263.9	482767.0	1.334	-66.46	-114.38	Normal	8.09	40.32	300	11
5	841.27	1	0.00	2448317.34	482557.8	1.334	2448376.7	482488.6	1.336	-59.34	69.19	Normal	3.24	27.78	229	7
5		2	33.07	2448308.91	482666	1.334	2448420.4	482535.9	1.336	-111.52	130.05	Normal	3.24	52.22	229	4
5		3	41.01	2448443.26	482658.8	1.334	2448522.4	482543.6	1.339	-79.16	115.2	Normal	8.09	42.60	236	11
5		4	12.57	2448484.03	482665	1.334	2448566.9	482564.4	1.339	-82.84	100.62	Normal	8.09	39.73	231	12
5		5	40.34	2448496.96	482796.7	1.330	2448685.4	482567.8	1.339	-188.46	228.88	Normal	14.57	90.37	231	9
5		6	26.36	2448580.87	482817.6	1.333	2448731.1	482635.2	1.337	-150.21	182.43	Normal	6.47	72.03	231	5
5		7	26.08	2448663.38	482840.3	1.332	2448756.6	482727.1	1.337	-93.17	113.16	Normal	8.09	44.68	231	10
5		8	24.62	2448710.51	482905.9	1.332	2448862.2	482721.7	1.338	-151.64	184.17	Normal	9.71	72.71	231	8
5		9	25.45	2448752.04	482978.3	1.333	2448921.8	482772.1	1.339	-169.78	206.21	Normal	9.71	81.42	231	7
5		10	24.82	2448826.97	483010.1	1.333	2448941.0	482871.6	1.342	-114.06	138.53	Normal	14.57	54.69	231	15
5		11	42.85	2448936.65	483098.1	1.332	2449107.9	482890.1	1.337	-171.21	207.94	Normal	8.09	82.10	231	6
5		12	42.98	2449037.97	483196.1	1.332	2449198.1	483001.7	1.338	-160.12	194.47	Normal	9.71	76.78	231	7
5		13	26.19	2449075.45	483273.5	1.334	2449210.4	483109.6	1.341	-134.94	163.88	Normal	11.33	64.70	231	10
5		14	42.88	2449187.87	483358.1	1.334	2449378.5	483192.4	1.338	-190.62	165.63	Normal	6.47	76.97	221	5
5		15	22.39	2449211.51	483427.6	1.333	2449352.1	483256.9	1.338	-140.55	170.7	Normal	8.09	67.40	231	7
5		16	24.99	2449255.91	483496.5	1.335	2449413.0	483305.7	1.338	-157.12	190.82	Normal	4.86	75.34	231	4
5		17	6.44	2449273.62	483508.1	1.334	2449460.2	483304.0	1.339	-186.57	204.03	Normal	8.09	84.27	228	5
5		18	24.58	2449353.5	483519.2	1.334	2449513.0	483344.8	1.339	-159.48	174.4	Normal	8.09	72.03	228	6
5		19	20.32	2449406.29	483559.9	1.334	2449516.1	483439.8	1.34	-109.8	120.08	Normal	9.71	49.59	228	11
5		20	23.45	2449449.12	483623.8	1.333	2449584.5	483475.8	1.341	-135.34	148.01	Normal	12.95	61.13	228	12
5		21	29.49	2449521.43	483688.1	1.334	2449646.4	483593.7	1.341	-124.97	94.41	Normal	11.33	47.74	217	13
5		22	28.09	2449531.05	483779.7	1.334	2449742.4	483620.1	1.34	-211.33	159.63	Normal	9.71	80.72	217	7
5		23	24.00	2449602.18	483813.5	1.333	2449821.7	483600.2	1.339	-219.47	213.37	Normal	9.71	93.30	224	6
5		24	23.71	2449635.31	483883.9	1.335	2449750.5	483740.1	1.341	-115.17	143.84	Normal	9.71	56.16	231	10
5		25	24.09	2449699.39	483930.2	1.334	2449831.8	483764.7	1.34	-132.45	165.43	Normal	9.71	64.59	231	9
5		26	24.13	2449764.82	483974.7	1.333	2449871.3	483841.7	1.339	-106.52	133.05	Normal	9.71	51.95	231	11
5		27	30.32	2449809.75	484063.5	1.333	2449901.9	483914.7	1.339	-92.14	148.78	Normal	9.71	53.34	238	10
5		28	44.73	2449819.95	484209.9	1.334	2449995.1	483927.1	1.338	-175.1	282.74	Normal	6.47	101.37	238	4
5		29	31.34	2449910.57	484161.3	1.334	2450036.8	483957.4	1.338	-126.27	203.88	Normal	6.47	73.10	238	5
5		30	21.55	2449918.78	484231.5	1.331	2450139.0	483956.5	1.337	-220.2	275.04	Normal	9.71	107.39	231	5

Appendix 8: Sooner Field 3D Seismic Fault Data Tables (continued).

Fault Name	Total Fault Length (m)	Station #	Distance from last station (m)	Hangingwall Orientation Easting 1 x	Northing 1 y	Hangingwall (s)	Footwall Orientation Easting 2 x2	Northing 2 y2	Footwall (s)	dx Easting	dy Northing	Fault Type	Throw (meters)	Heave (meters)	RH Rule Fault Strike	dip degrees
5		31	28.43	2449996.68	484282.8	1.333	2450130.8	484066.2	1.336	-134.15	216.62	Normal	4.86	77.66	238	4
6	800.34	1	0.00	2446328.58	481786.1	1.337	2446332.1	481535.5	1.346	-3.53	250.67	Normal	14.57	76.41	269	11
6		2	31.99	2446428.12	481819.4	1.336	2446431.1	481606.7	1.345	-3	212.71	Normal	14.57	64.84	269	13
6		3	32.62	2446528.65	481782.7	1.336	2446531.2	481601.7	1.345	-2.55	181	Normal	14.57	55.17	269	15
6		4	50.02	2446626.8	481914.2	1.336	2446630.8	481628.6	1.345	-4.03	285.65	Normal	14.57	87.07	269	9
6		5	34.41	2446727.53	481863.2	1.335	2446730.8	481633.1	1.344	-3.24	230.13	Normal	14.57	70.15	269	12
6		6	30.72	2446827.7	481852	1.334	2446829.5	481725.0	1.344	-1.79	126.98	Normal	16.18	38.71	269	23
6		7	30.67	2446927.53	481864.6	1.336	2446930.1	481683.5	1.341	-2.55	181.01	Normal	8.09	55.18	269	8
6		8	30.02	2446996.01	481935.3	1.335	2447047.4	481764.6	1.342	-51.41	170.79	Normal	11.33	54.36	253	12
6		9	40.94	2447126.98	481905.5	1.337	2447130.1	481686.4	1.342	-3.08	219.11	Normal	8.09	66.79	269	7
6		10	35.62	2447240.68	481878.5	1.337	2447188.9	481687.2	1.343	51.76	191.3	Normal	9.71	60.40	285	9
6		11	32.83	2447320.81	481806.5	1.336	2447285.9	481677.4	1.344	34.93	129.13	Normal	12.95	40.77	285	18
6		12	9.81	2447352.8	481810.1	1.336	2447398.6	481679.0	1.344	-45.77	131.11	Normal	12.95	42.33	251	17
6		13	29.47	2447436.24	481858.9	1.335	2447476.5	481743.7	1.345	-40.24	115.26	Normal	16.18	37.21	251	24
6		14	29.57	2447519.12	481909.4	1.335	2447579.2	481737.2	1.343	-60.09	172.16	Normal	12.95	55.58	251	13
6		15	29.55	2447615.28	481921.7	1.333	2447662.7	481786.0	1.344	-47.37	135.71	Normal	17.80	43.81	251	22
6		16	31.64	2447690.96	481992.8	1.335	2447729.6	481882.1	1.345	-38.64	110.67	Normal	16.18	35.73	251	24
6		17	29.37	2447774.97	482040	1.334	2447841.2	481850.3	1.343	-66.2	189.64	Normal	14.57	61.22	251	13
6		18	24.01	2447852.64	482026.8	1.334	2447886.2	481841.4	1.342	-33.57	185.33	Normal	12.95	57.41	260	13
6		19	30.19	2447948.05	482053.4	1.333	2447984.2	481854.0	1.341	-36.14	199.45	Normal	12.95	61.78	260	12
6		20	30.38	2448042.58	482085	1.333	2448076.1	481899.8	1.34	-33.55	185.18	Normal	11.33	57.36	260	11
6		21	30.19	2448141.25	482093.7	1.334	2448176.6	481898.8	1.339	-35.3	194.84	Normal	8.09	60.35	260	8
6		22	14.61	2448173.1	482129.5	1.333	2448259.4	482017.7	1.342	-86.34	111.81	Normal	14.57	43.06	232	19
6		23	27.50	2448210.94	482211.4	1.333	2448339.1	482045.5	1.342	-128.11	165.9	Normal	14.57	63.89	232	13
6		24	26.03	2448292.55	482236.6	1.333	2448401.2	482095.9	1.34	-108.64	140.68	Normal	11.33	54.18	232	12
6		25	18.85	2448330.9	482285.1	1.334	2448456.0	482123.1	1.341	-125.11	162.01	Normal	11.33	62.39	232	10
6		26	28.45	2448420.97	482260.6	1.335	2448501.6	482120.2	1.341	-80.59	140.37	Normal	9.71	49.33	240	11
6		27	30.86	2448471.35	482348.4	1.336	2448573.9	482169.8	1.342	-102.57	178.65	Normal	9.71	62.79	240	9
6		28	30.02	2448569.74	482352.6	1.337	2448678.0	482164.1	1.34	-108.22	188.49	Normal	4.86	66.25	240	4
7	729.99	1	0.00	2447906.41	480921.3	1.336	2447845.9	480747.2	1.343	60.56	174.15	Normal	11.33	56.20	109	11
7		2	30.26	2448005.67	480920.6	1.336	2447931.6	480707.7	1.345	74.06	212.94	Normal	14.57	68.72	109	12
7		3	10.63	2448034.18	480900.5	1.336	2447972.1	480659.5	1.34	62.09	241	Normal	6.47	75.86	104	5
7		4	21.91	2448105.87	480905.9	1.335	2448082.0	480594.6	1.344	23.89	311.32	Normal	14.57	95.17	94	9
7		5	12.06	2448140.9	480924.3	1.335	2448144.6	480659.9	1.345	-3.72	264.45	Normal	16.18	80.61	89	11
7		6	34.85	2448240.1	480981.2	1.334	2448245.2	480621.3	1.343	-5.07	359.9	Normal	14.57	109.71	89	8
7		7	34.55	2448339.34	481035.9	1.332	2448345.8	480580.4	1.34	-6.42	455.55	Normal	12.95	138.87	89	5
7		8	14.63	2448354.91	481081.3	1.333	2448582.7	480859.9	1.341	-227.77	221.45	Normal	12.95	96.83	44	8
7		9	21.72	2448410.63	481125.8	1.332	2448648.2	480894.8	1.34	-237.61	231.01	Normal	12.95	101.01	44	7
7		10	11.10	2448431.97	481155.3	1.333	2448647.2	480911.2	1.341	-215.21	244.04	Normal	12.95	99.18	49	7
7		11	23.46	2448497.22	481196.1	1.332	2448726.1	480936.5	1.338	-228.91	259.57	Normal	9.71	105.49	49	5
7		12	24.03	2448556.85	481247.6	1.331	2448752.5	480944.1	1.338	-195.69	303.51	Normal	11.33	110.07	57	6
7		13	27.40	2448644.29	481268.5	1.331	2448822.2	480992.5	1.338	-177.94	275.97	Normal	11.33	100.08	57	6

Appendix 8: Sooner Field 3D Seismic Fault Data Tables (continued).

Fault Name	Total Fault Length (m)	Station #	Distance from last station (m)	Hangingwall Orientation Easting 1 x	Northing 1 y	Hangingwall (s)	Footwall Orientation Easting 2 x2	Northing 2 y2	Footwall (s)	dx Easting	dy Northing	Fault Type	Throw (meters)	Heave (meters)	RH Rule Fault Strike	dip degrees
7		14	31.53	2448667.29	481369.3	1.332	2448956.4	481088.3	1.338	-289.1	281.07	Normal	9.71	122.90	44	5
7		15	10.99	2448670.22	481405.3	1.332	2448806.7	481294.8	1.342	-136.47	110.51	Normal	16.18	53.52	39	17
7		16	24.62	2448699.17	481480.7	1.331	2448888.0	481327.8	1.34	-188.81	152.88	Normal	14.57	74.05	39	11
7		17	43.94	2448763.91	481609.5	1.334	2448973.1	481440.1	1.339	-209.21	169.4	Normal	8.09	82.05	39	6
7		18	21.01	2448798.25	481669.3	1.334	2449012.4	481487.4	1.34	-214.18	181.88	Normal	9.71	85.64	40	6
7		19	26.40	2448814.74	481754.3	1.335	2449034.3	481567.6	1.34	-219.57	186.73	Normal	8.09	87.85	40	5
7		20	23.46	2448851.13	481822.1	1.334	2449079.7	481627.8	1.34	-228.52	194.34	Normal	9.71	91.43	40	6
7		21	45.13	2448908.36	481958.7	1.335	2449151.2	481752.2	1.339	-242.87	206.54	Normal	6.47	97.18	40	4
7		22	11.14	2448943.75	481967.8	1.335	2449159.4	481810.8	1.339	-215.66	157.04	Normal	6.47	81.31	36	5
7		23	28.67	2448974.81	482056.6	1.335	2449115.2	481920.1	1.341	-140.39	136.49	Normal	9.71	59.68	44	9
7		24	34.88	2449030.3	482156.7	1.334	2449212.2	481954.6	1.339	-181.88	202.04	Normal	8.09	82.86	48	6
7		25	49.12	2449083.08	482308.9	1.334	2449293.3	482075.4	1.338	-210.19	233.49	Normal	6.47	95.76	48	4
7		26	20.96	2449118.73	482367.8	1.334	2449279.9	482188.8	1.339	-161.12	178.98	Normal	8.09	73.40	48	6
7		27	44.36	2449247.4	482435.7	1.333	2449380.1	482288.4	1.338	-132.67	147.38	Normal	8.09	60.44	48	8
7		28	47.19	2449394.9	482482.8	1.335	2449467.7	482401.9	1.337	-72.78	80.85	Normal	3.24	33.16	48	6
8	2061.77	1	0.00	2450747.41	479820.7	1.324	2450799.5	480194.1	1.328	-52.06	-373.33	Normal	6.47	114.89	278	3
8		2	30.61	2450847.76	479824.7	1.324	2450879.5	480052.6	1.327	-31.78	-227.9	Normal	4.86	70.14	278	4
8		3	30.21	2450946.7	479818.6	1.323	2450978.8	480049.1	1.328	-32.14	-230.49	Normal	8.09	70.93	278	7
8		4	30.75	2451047.38	479824.9	1.323	2451076.1	480030.5	1.328	-28.67	-205.58	Normal	8.09	63.27	278	7
8		5	31.31	2451149.14	479839	1.322	2451176.4	480034.3	1.328	-27.23	-195.24	Normal	9.71	60.09	278	9
8		6	31.29	2451250.86	479852.9	1.322	2451275.0	480025.8	1.329	-24.12	-172.92	Normal	11.33	53.22	278	12
8		7	31.76	2451344.2	479806.6	1.321	2451375.7	480032.2	1.329	-31.46	-225.55	Normal	12.95	69.41	278	11
8		8	26.98	2451432.56	479811.7	1.321	2451491.8	480014.3	1.329	-59.25	-202.68	Normal	12.95	64.36	286	11
8		9	48.02	2451535.78	479692.6	1.320	2451663.5	479906.8	1.33	-127.67	-214.17	Normal	16.18	76.00	301	12
8		10	43.75	2451674.93	479657.4	1.321	2451790.9	479851.9	1.33	-115.94	-194.49	Normal	14.57	69.01	301	12
8		11	52.84	2451803.68	479541.3	1.320	2451966.2	479783.3	1.33	-162.52	-241.96	Normal	16.18	88.84	304	10
8		12	24.65	2451818.91	479461.9	1.320	2452017.2	479757.1	1.33	-198.31	-295.24	Normal	16.18	108.40	304	8
8		13	88.06	2452006.59	479242.2	1.319	2452203.6	479535.5	1.328	-197.02	-293.32	Normal	14.57	107.70	304	8
8		14	3.17	2452014.66	479248.8	1.318	2452205.2	479342.8	1.328	-190.51	-94.03	Normal	16.18	64.76	334	14
8		15	19.82	2452030.26	479185.7	1.319	2452273.4	479138.6	1.328	-243.1	47.08	Normal	14.57	75.47	11	11
8		16	61.47	2451988.18	478988.4	1.320	2452317.7	479034.4	1.328	-329.51	-45.91	Normal	12.95	101.40	352	7
8		17	19.26	2452051.25	478984.7	1.320	2452352.3	479054.6	1.328	-301.04	-69.9	Normal	12.95	94.20	347	8
8		18	59.13	2451986.86	478801.7	1.319	2452365.8	478939.6	1.328	-378.96	-137.82	Normal	14.57	122.91	340	7
8		19	31.64	2451978.65	478698.2	1.319	2452357.6	478836.1	1.329	-378.96	-137.83	Normal	16.18	122.91	340	8
8		20	22.03	2452047.56	478676.4	1.319	2452287.2	478711.1	1.331	-239.63	-34.7	Normal	19.42	73.80	352	15
8		21	103.62	2452144.77	478350.6	1.320	2452424.7	478354.6	1.329	-279.93	-3.94	Normal	14.57	85.33	359	10
8		22	35.15	2452203.62	478251.4	1.320	2452498.6	478255.6	1.329	-294.93	-4.16	Normal	14.57	89.90	359	9
8		23	36.34	2452140.09	478150.5	1.320	2452502.5	478155.6	1.33	-362.45	-5.1	Normal	16.18	110.49	359	8
8		24	33.11	2452183.93	478051.2	1.320	2452606.4	478057.1	1.329	-422.47	-5.95	Normal	14.57	128.78	359	6
8		25	31.25	2452207.96	477951.5	1.321	2452577.9	477956.7	1.329	-369.95	-5.21	Normal	12.95	112.77	359	7
8		26	30.52	2452214.29	477851.6	1.321	2452544.4	477856.2	1.33	-330.1	-4.65	Normal	14.57	100.62	359	8
8		27	53.07	2452073.16	477749.6	1.322	2452470.8	477755.2	1.331	-397.62	-5.6	Normal	14.57	121.21	359	7

Appendix 8: Sooner Field 3D Seismic Fault Data Tables (continued).

Fault Name	Total Fault Length (m)	Station #	Distance from last station (m)	Hangingwall Orientation Easting 1 x	Northing 1 y	Hangingwall (s)	Footwall Orientation Easting 2 x2	Northing 2 y2	Footwall (s)	dx Easting	dy Northing	Fault Type	Throw (meters)	Heave (meters)	RH Rule Fault Strike	dip degrees
8		28	40.49	2452162.02	477650.8	1.322	2452527.1	477655.9	1.331	-365.03	-5.14	Normal	14.57	111.27	359	7
8		29	9.99	2452189.81	477633.4	1.322	2452526.6	477699.5	1.33	-336.74	-66.14	Normal	12.95	104.60	349	7
8		30	30.03	2452213.67	477537.8	1.323	2452535.4	477601.0	1.33	-321.77	-63.2	Normal	11.33	99.95	349	6
8		31	32.46	2452192.63	477433.4	1.323	2452584.1	477510.3	1.33	-391.45	-76.88	Normal	11.33	121.59	349	5
8		32	30.03	2452206.67	477335.9	1.323	2452620.6	477417.2	1.33	-413.9	-81.29	Normal	11.33	128.57	349	5
8		33	30.00	2452223.04	477238.9	1.322	2452676.7	477328.0	1.33	-453.66	-89.1	Normal	12.95	140.92	349	5
8		34	32.77	2452199.43	477134	1.322	2452683.0	477228.9	1.331	-483.59	-94.98	Normal	14.57	150.21	349	6
8		35	30.79	2452240.82	477041.8	1.322	2452654.7	477123.1	1.331	-413.91	-81.29	Normal	14.57	128.57	349	6
8		36	32.46	2452219.78	476937.4	1.322	2452735.9	477038.8	1.331	-516.1	-101.36	Normal	14.57	160.31	349	5
8		37	16.63	2452262.7	476903.7	1.322	2452637.8	476892.0	1.331	-375.12	11.76	Normal	14.57	114.39	2	7
8		38	31.55	2452286.63	476803.1	1.321	2452641.8	476791.9	1.331	-355.18	11.14	Normal	16.18	108.31	2	8
8		39	33.78	2452235.49	476704.7	1.322	2452653.3	476691.6	1.33	-417.81	13.1	Normal	12.95	127.41	2	6
8		40	17.56	2452213.61	476651.4	1.322	2452726.1	476658.6	1.33	-512.5	-7.21	Normal	12.95	156.23	359	5
8		41	31.63	2452242.69	476551.8	1.322	2452590.1	476556.7	1.33	-347.44	-4.89	Normal	12.95	105.91	359	7
8		42	30.57	2452236.59	476451.7	1.323	2452551.5	476456.2	1.331	-314.86	-4.44	Normal	12.95	95.98	359	8
8		43	32.55	2452200.49	476351.2	1.323	2452487.9	476355.3	1.331	-287.43	-4.05	Normal	12.95	87.62	359	8
8		44	30.52	2452206.82	476251.3	1.323	2452494.3	476255.3	1.33	-287.43	-4.05	Normal	11.33	87.62	359	7
8		45	31.82	2452238.24	476151.7	1.323	2452595.8	476156.8	1.332	-357.52	-5.04	Normal	14.57	108.98	359	8
8		46	32.89	2452279.74	476052.1	1.323	2452632.1	476057.3	1.332	-352.36	-5.14	Normal	14.57	107.41	359	8
8		47	31.19	2452303.65	475952.6	1.323	2452653.4	475957.6	1.332	-349.79	-4.92	Normal	14.57	106.63	359	8
8		48	30.48	2452305.06	475852.6	1.323	2452594.8	475856.7	1.333	-289.77	-4.09	Normal	16.18	88.33	359	10
8		49	30.56	2452313.97	475752.8	1.323	2452696.4	475758.1	1.331	-382.38	-5.39	Normal	12.95	116.56	359	6
8		50	31.82	2452345.39	475653.2	1.323	2452702.7	475658.2	1.331	-357.29	-5.04	Normal	12.95	108.91	359	7
8		51	30.49	2452349.14	475553.2	1.323	2452574.2	475556.4	1.333	-225.07	-3.17	Normal	16.18	68.61	359	13
8		52	33.73	2452303.19	475452.6	1.323	2452553.1	475456.1	1.334	-249.92	-3.52	Normal	17.80	76.18	359	13
8		53	35.57	2452244.46	475351.7	1.323	2452594.5	475356.7	1.333	-350.03	-4.93	Normal	16.18	106.70	359	9
8		54	37.22	2452315.97	475252.7	1.323	2452660.8	475257.6	1.332	-344.87	-4.86	Normal	14.57	105.13	359	8
8		55	31.08	2452337.31	475153	1.323	2452612.3	475156.9	1.332	-275	-3.87	Normal	14.57	83.83	359	10
8		56	30.14	2452358.6	475056.5	1.323	2452670.7	475089.3	1.331	-312.11	-32.81	Normal	12.95	95.66	354	8
8		57	30.37	2452372.65	474957.8	1.324	2452617.3	474983.5	1.332	-244.68	-25.72	Normal	12.95	74.99	354	10
8		58	30.37	2452386.47	474859.1	1.324	2452651.1	474886.9	1.332	-264.58	-27.82	Normal	12.95	81.09	354	9
8		59	44.40	2452502.61	474771.2	1.324	2452717.3	474793.8	1.33	-214.71	-22.58	Normal	9.71	65.80	354	8
8		60	32.86	2452554.12	474676.5	1.322	2452833.7	474705.9	1.331	-279.57	-29.39	Normal	14.57	85.68	354	10
8		61	33.15	2452607.98	474582	1.323	2453004.9	474623.7	1.329	-396.87	-41.72	Normal	9.71	121.63	354	5
9	599.01	1	0.00	2455434.39	483117.3	1.322	2455408.3	483250.3	1.323	26.11	-132.98	Normal	1.62	41.31	259	2
9		2	31.06	2455536.04	483110.3	1.321	2455503.1	483278.2	1.324	32.98	-167.91	Normal	4.86	52.16	259	5
9		3	30.04	2455633.73	483123.4	1.321	2455598.8	483301.3	1.324	34.94	-177.87	Normal	4.86	55.25	259	5
9		4	30.08	2455731.76	483134.8	1.321	2455699.1	483301.0	1.324	32.64	-166.19	Normal	4.86	51.62	259	5
9		5	15.42	2455774.1	483107.1	1.321	2455753.6	483301.7	1.325	20.46	-194.65	Normal	6.47	59.66	264	6
9		6	11.93	2455810.72	483120.9	1.321	2455808.1	483309.2	1.325	2.65	-188.33	Normal	6.47	57.41	269	6
9		7	12.25	2455849.5	483131.4	1.321	2455865.4	483338.3	1.326	-15.87	-206.89	Normal	8.09	63.25	274	7
9		8	30.35	2455948.85	483124.5	1.320	2455966.9	483359.8	1.327	-18.05	-235.22	Normal	11.33	71.91	274	9

Appendix 8: Sooner Field 3D Seismic Fault Data Tables (continued).

Fault Name	Total Fault Length (m)	Station #	Distance from last station (m)	Hangingwall Orientation Easting 1 x	Northing 1 y	Hangingwall (s)	Footwall Orientation Easting 2 x2	Northing 2 y2	Footwall (s)	dx Easting	dy Northing	Fault Type	Throw (meters)	Heave (meters)	RH Rule Fault Strike	dip degrees
9		9	30.73	2456049.35	483132.5	1.320	2456065.2	483339.4	1.327	-15.87	-206.89	**Normal**	11.33	63.25	274	10
9		10	60.76	2456248.56	483125.3	1.319	2456262.9	483312.3	1.325	-14.35	-187.02	**Normal**	9.71	57.17	274	10
9		11	30.36	2456348.04	483120.2	1.319	2456363.0	483315.3	1.325	-14.98	-195.15	**Normal**	9.71	59.66	274	9
9		12	30.44	2456447.9	483119.9	1.320	2456462.6	483311.7	1.324	-14.72	-191.86	**Normal**	6.47	58.65	274	6
9		13	30.41	2456546.74	483106.2	1.320	2456562.2	483308.1	1.325	-15.49	-201.88	**Normal**	8.09	61.71	274	7
9		14	19.64	2456610.92	483112.1	1.321	2456608.1	483313.8	1.324	2.84	-201.62	**Normal**	4.86	61.46	269	5
9		15	19.85	2456672.62	483133	1.319	2456653.0	483319.4	1.324	19.59	-186.38	**Normal**	8.09	57.12	264	8
9		16	30.37	2456771.38	483146.1	1.320	2456751.4	483335.8	1.324	19.94	-189.66	**Normal**	6.47	58.13	264	6
9		17	17.39	2456809.87	483188.3	1.320	2456807.2	483374.9	1.325	2.63	-186.62	**Normal**	8.09	56.89	269	8
9		18	13.74	2456851.32	483170.6	1.319	2456864.0	483335.8	1.325	-12.68	-165.26	**Normal**	9.71	50.52	274	11
9		19	30.41	2456951.06	483168.7	1.320	2456963.3	483328.8	1.326	-12.28	-160.1	**Normal**	9.71	48.94	274	11
9		20	31.14	2457048.61	483138.3	1.320	2457065.6	483360.2	1.326	-17.03	-221.91	**Normal**	9.71	67.84	274	8
9		21	31.78	2457150.27	483161.5	1.320	2457163.8	483338.3	1.326	-13.57	-176.84	**Normal**	9.71	54.06	274	10
9		22	30.49	2457248.84	483144.4	1.320	2457263.7	483338.0	1.323	-14.86	-193.58	**Normal**	4.86	59.18	274	5
9		23	30.37	2457348.33	483139.3	1.320	2457357.0	483252.7	1.322	-8.7	-113.46	**Normal**	3.24	34.68	274	5
10	1181.33	1	0.00	2455427.09	480092	1.322	2455463.6	480247.5	1.325	-36.54	-155.43	**Normal**	4.86	48.67	283	6
10		2	31.01	2455514.52	480040	1.321	2455548.0	480182.4	1.325	-33.47	-142.37	**Normal**	6.47	44.58	283	8
10		3	45.62	2455612.49	479926.9	1.321	2455655.5	480109.8	1.325	-43	-182.9	**Normal**	6.47	57.27	283	6
10		4	22.92	2455661.29	479984.1	1.321	2455720.8	480149.8	1.325	-59.49	-165.7	**Normal**	6.47	53.66	290	7
10		5	29.61	2455758.17	479976.8	1.322	2455816.6	480139.7	1.326	-58.47	-162.86	**Normal**	6.47	52.74	290	7
10		6	31.00	2455859.72	479982.6	1.321	2455902.7	480102.2	1.326	-42.94	-119.62	**Normal**	8.09	38.74	290	12
10		7	29.61	2455956.6	479975.3	1.320	2456008.3	480119.4	1.327	-51.73	-144.08	**Normal**	11.33	46.66	290	14
10		8	24.88	2456007.53	479911.5	1.319	2456044.8	480070.0	1.328	-37.25	-158.47	**Normal**	14.57	49.62	283	16
10		9	29.96	2456105.59	479904.8	1.318	2456141.0	480055.3	1.328	-35.4	-150.58	**Normal**	16.18	47.15	283	19
10		10	29.82	2456202.94	479894.9	1.319	2456240.2	480053.4	1.329	-37.25	-158.46	**Normal**	16.18	49.62	283	18
10		11	38.43	2456313.08	479833.5	1.319	2456361.8	480040.7	1.329	-48.71	-207.18	**Normal**	16.18	64.87	283	14
10		12	32.74	2456372.96	479922.7	1.318	2456420.0	480053.8	1.328	-47.07	-131.1	**Normal**	16.18	42.46	290	21
10		13	48.28	2456462.96	479792.4	1.321	2456547.3	480027.3	1.328	-84.33	-234.9	**Normal**	11.33	76.07	290	8
10		14	39.69	2456590.75	479767.3	1.322	2456656.5	479950.3	1.328	-65.71	-183	**Normal**	9.71	59.27	290	9
10		15	28.92	2456684.05	479750.1	1.322	2456762.7	479969.0	1.326	-78.61	-218.95	**Normal**	6.47	70.91	290	5
10		16	37.58	2456677.16	479627	1.325	2456768.2	479880.7	1.325	-91.08	-253.69	**Normal**	0.00	82.16	290	0
10		17	59.53	2456823.2	479756.7	1.323	2456776.1	479625.5	1.328	47.07	131.11	**Normal**	8.09	42.46	110	11
10		18	29.27	2456918.53	479745.1	1.322	2456865.7	479598.0	1.328	52.79	147.05	**Normal**	9.71	47.62	110	12
10		19	28.99	2457012.31	479729.2	1.322	2456937.8	479521.7	1.33	74.48	207.47	**Normal**	12.95	67.19	110	11
10		20	39.41	2457020.86	479600.2	1.322	2456939.1	479452.2	1.33	81.8	147.95	**Normal**	12.95	51.53	119	14
10		21	15.22	2457067.04	479581.2	1.322	2456963.3	479393.5	1.329	103.78	187.7	**Normal**	11.33	65.37	119	10
10		22	27.55	2457130.89	479517.2	1.322	2457032.6	479339.4	1.329	98.33	177.83	**Normal**	11.33	61.94	119	10
10		23	15.22	2457171.61	479488.3	1.322	2457074.8	479313.3	1.331	96.77	175.04	**Normal**	14.57	60.96	119	13
10		24	27.42	2457236.2	479425.7	1.322	2457149.7	479269.2	1.331	86.53	156.49	**Normal**	14.57	54.50	119	15
10		25	26.49	2457314.2	479387.4	1.322	2457227.7	479230.9	1.33	86.52	156.49	**Normal**	12.95	54.50	119	13
10		26	20.59	2457364.79	479432.1	1.322	2457315.3	479221.7	1.331	49.46	210.37	**Normal**	14.57	65.87	103	12
10		27	18.68	2457422.71	479452.2	1.324	2457364.2	479289.3	1.332	58.48	162.86	**Normal**	12.95	52.74	110	14

Appendix 8: Sooner Field 3D Seismic Fault Data Tables (continued).

Fault Name	Total Fault Length (m)	Station #	Distance from last station (m)	Hangingwall Orientation Easting 1 x	Northing 1 y	Hangingwall (s)	Footwall Orientation Easting 2 x2	Northing 2 y2	Footwall (s)	dx Easting	dy Northing	Fault Type	Throw (meters)	Heave (meters)	RH Rule Fault Strike	dip degrees
10		28	30.19	2457428	479353.3	1.324	2457354.2	479200.3	1.331	73.82	152.99	Normal	11.33	51.78	116	12
10		29	41.30	2457540.57	479277.8	1.323	2457467.4	479126.2	1.331	73.17	151.64	Normal	12.95	51.32	116	14
10		30	37.66	2457664.08	479281.5	1.324	2457545.7	479070.1	1.331	118.42	211.36	Normal	11.33	73.84	119	9
10		31	22.23	2457726.09	479243	1.324	2457586.8	478994.4	1.331	139.33	248.68	Normal	11.33	86.88	119	7
10		32	32.82	2457770.27	479144.8	1.324	2457681.1	478985.7	1.331	89.14	159.1	Normal	11.33	55.59	119	12
10		33	29.66	2457867.52	479141.3	1.324	2457721.3	478880.3	1.332	146.27	261.04	Normal	12.95	91.20	119	8
10		34	29.66	2457964.76	479137.8	1.325	2457849.1	478931.4	1.331	115.68	206.46	Normal	9.71	72.13	119	8
10		35	28.88	2458059.13	479129.2	1.325	2457912.9	478885.4	1.331	146.26	243.79	Normal	9.71	86.65	121	6
10		36	36.21	2458174.41	479157.9	1.324	2457983.6	478817.3	1.332	190.83	340.6	Normal	12.95	119.00	119	6
10		37	30.08	2458273.1	479157	1.325	2458165.8	478965.5	1.33	107.32	191.53	Normal	8.09	66.92	119	7
10		38	54.18	2458272.7	478979.2	1.329	2458184.9	478822.5	1.332	87.83	156.77	Normal	4.86	54.77	119	5
11	549.97	1	0.00	2452358.78	480847.9	1.328	2452300.3	480747.3	1.331	58.44	100.58	Normal	4.86	35.46	120	8
11		2	28.94	2452436.54	480793.4	1.327	2452375.6	480683.1	1.332	60.96	110.25	Normal	8.09	38.40	119	12
11		3	22.88	2452507.21	480818.7	1.327	2452417.4	480656.2	1.333	89.84	162.49	Normal	9.71	56.59	119	10
11		4	26.74	2452589.27	480787.6	1.324	2452485.3	480599.6	1.332	103.98	188.07	Normal	12.95	65.50	119	11
11		5	27.75	2452652.01	480721.7	1.325	2452567.3	480568.5	1.332	84.67	153.14	Normal	11.33	53.34	119	12
11		6	26.74	2452734.07	480690.7	1.324	2452655.8	480549.1	1.333	78.29	141.59	Normal	14.57	49.31	119	16
11		7	27.51	2452819.99	480663	1.324	2452722.4	480490.1	1.334	97.62	172.94	Normal	16.18	60.53	119	15
11		8	17.33	2452847.02	480613	1.323	2452754.6	480445.8	1.333	92.43	167.17	Normal	16.18	58.22	119	16
11		9	30.08	2452945.69	480612	1.323	2452837.3	480415.9	1.333	108.44	196.12	Normal	16.18	68.31	119	13
11		10	17.00	2452995.54	480587	1.324	2452892.3	480427.3	1.333	103.23	159.68	Normal	14.57	57.96	123	14
11		11	15.37	2453011.24	480539	1.323	2452895.2	480323.0	1.333	116.05	216	Normal	16.18	74.74	118	12
11		12	27.29	2453079.12	480480.7	1.322	2452928.5	480200.3	1.332	150.63	280.35	Normal	16.18	97.00	118	9
11		13	19.23	2453104.94	480423.1	1.322	2452999.8	480230.4	1.332	105.17	192.74	Normal	16.18	66.92	119	14
11		14	26.91	2453190.14	480400	1.323	2453105.5	480242.5	1.332	84.6	157.47	Normal	14.57	54.49	118	15
11		15	41.47	2453312.1	480339.7	1.323	2453235.8	480197.7	1.332	76.3	142.02	Normal	14.57	49.14	118	17
11		16	27.34	2453398.62	480316	1.323	2453330.0	480188.3	1.331	68.6	127.7	Normal	12.95	44.18	118	16
11		17	26.95	2453481.9	480286.3	1.324	2453399.2	480132.4	1.328	82.68	153.89	Normal	6.47	53.25	118	7
11		18	26.86	2453553.69	480235.3	1.323	2453478.0	480094.5	1.328	75.65	140.8	Normal	8.09	48.72	118	9
11		19	27.26	2453639.61	480210.5	1.322	2453556.9	480056.5	1.327	82.74	154.01	Normal	8.09	53.29	118	9
11		20	27.20	2453708.15	480153.3	1.321	2453640.2	480026.9	1.325	67.95	126.47	Normal	6.47	43.76	118	8
11		21	29.79	2453798.82	480116.9	1.320	2453705.2	479942.6	1.324	93.63	174.26	Normal	6.47	60.30	118	6
11		22	29.36	2453894.96	480111.1	1.319	2453739.2	479821.1	1.323	155.8	289.98	Normal	6.47	100.34	118	4
12	296.80	1	0.00	2451646.5	481643.9	1.326	2451609.8	481601.7	1.326	36.68	42.25	Normal	0.00	17.05	131	0
12		2	27.09	2451685.91	481564.3	1.326	2451588.8	481434.3	1.328	97.09	130.011	Normal	3.24	49.46	127	4
12		3	24.93	2451737.4	481500.7	1.326	2451659.0	481395.8	1.329	78.4	104.94	Normal	4.86	39.93	127	7
12		4	53.42	2451894.45	481578.5	1.325	2451726.6	481353.9	1.329	167.82	224.64	Normal	6.47	85.47	127	4
12		5	26.51	2451936.5	481502.4	1.325	2451775.5	481286.8	1.33	161.03	215.55	Normal	8.09	82.01	127	6
12		6	25.84	2451981.99	481430.8	1.326	2451898.5	481319.1	1.33	83.51	111.79	Normal	6.47	42.53	127	9
12		7	27.40	2452070.87	481417.4	1.326	2451950.8	481256.6	1.33	120.11	160.78	Normal	6.47	61.17	127	6
12		8	30.21	2452169.98	481417.6	1.325	2452048.2	481254.6	1.33	121.79	163.03	Normal	8.09	62.03	127	7
12		9	26.16	2452213.79	481343.8	1.326	2452143.1	481249.1	1.329	70.72	94.67	Normal	4.86	36.02	127	8

Appendix 8: Sooner Field 3D Seismic Fault Data Tables (continued).

Fault Name	Total Fault Length (m)	Station #	Distance from last station (m)	Hangingwall Orientation Easting 1 x	Northing 1 y	Hangingwall (s)	Footwall Orientation Easting 2 x2	Northing 2 y2	Footwall (s)	dx Easting	dy Northing	Fault Type	Throw (meters)	Heave (meters)	RH Rule Fault Strike	dip degrees
12		10	19.46	2452273.94	481322.5	1.326	2452204.1	481229.0	1.329	69.85	93.5	Normal	4.86	35.57	127	8
12		11	35.79	2452307.52	481435	1.327	2452203.6	481095.8	1.328	103.97	339.17	Normal	1.62	108.13	107	1
13	294.20	1	0.00	2450002.14	482201.5	1.332	2450251.1	482040.5	1.334	-249	160.98	Normal	3.24	90.37	33	2
13		2	26.92	2450072.21	482255.2	1.331	2450248.2	482141.5	1.334	-175.98	113.77	Normal	4.86	63.87	33	4
13		3	12.26	2450074.69	482295.4	1.330	2450202.7	482233.7	1.334	-127.98	61.75	Normal	6.47	43.31	26	9
13		4	18.26	2450130.02	482318.4	1.330	2450265.4	482253.0	1.333	-135.38	65.32	Normal	4.86	45.82	26	6
13		5	27.33	2450174.67	482396.1	1.330	2450311.6	482330.1	1.333	-136.91	66.06	Normal	4.86	46.33	26	6
13		6	30.25	2450174.8	482495.4	1.328	2450319.1	482425.8	1.333	-144.31	69.63	Normal	8.09	48.84	26	9
13		7	29.98	2450268.77	482524.5	1.328	2450428.6	482400.2	1.333	-159.83	124.21	Normal	8.09	61.70	38	7
13		8	20.96	2450284.42	482591.4	1.328	2450441.4	482469.4	1.332	-156.97	121.99	Normal	6.47	60.59	38	6
13		9	15.43	2450330.53	482612.3	1.328	2450405.5	482539.4	1.332	-74.95	72.88	Normal	6.47	31.86	44	11
13		10	23.05	2450360.6	482681.7	1.327	2450465.5	482579.7	1.331	-104.94	102.02	Normal	6.47	44.61	44	8
13		11	14.25	2450388.33	482719.3	1.327	2450504.6	482583.8	1.331	-116.22	135.54	Normal	6.47	54.42	49	7
13		12	43.06	2450502.33	482802.8	1.327	2450627.2	482657.1	1.331	-124.85	145.61	Normal	6.47	58.46	49	6
13		13	32.45	2450501.95	482909.2	1.326	2450620.3	482763.5	1.329	-118.38	145.72	Normal	4.86	57.22	51	5
14	464.30	1	0.00	2453815.51	482766.4	1.326	2453818.1	482582.4	1.327	-2.6	183.99	Normal	1.62	56.09	89	2
14		2	46.23	2453913.9	482881.8	1.323	2453917.3	482643.8	1.327	-3.35	238	Normal	6.47	72.55	89	5
14		3	31.65	2454014.28	482855.3	1.323	2454016.9	482669.2	1.326	-2.62	186.05	Normal	4.86	56.71	89	5
14		4	31.35	2454114.61	482832.7	1.323	2454118.2	482576.7	1.327	-3.61	256	Normal	6.47	78.04	89	5
14		5	33.29	2454213.98	482878	1.321	2454218.7	482542.1	1.327	-4.73	335.91	Normal	9.71	102.40	89	5
14		6	34.35	2454314.7	482827.4	1.322	2454318.0	482591.5	1.326	-3.33	235.94	Normal	6.47	71.92	89	5
14		7	10.98	2454350.57	482824	1.322	2454379.1	482574.3	1.327	-28.52	249.65	Normal	8.09	76.59	83	6
14		8	10.74	2454385.54	482828.4	1.321	2454436.9	482589.2	1.327	-51.35	239.2	Normal	9.71	74.57	78	7
14		9	39.93	2454514.38	482852.2	1.321	2454517.9	482604.2	1.327	-3.49	247.95	Normal	9.71	75.58	89	7
14		10	36.84	2454615.32	482785.7	1.321	2454617.7	482615.6	1.327	-2.4	170.11	Normal	9.71	51.85	89	11
14		11	24.40	2454695.35	482786.8	1.321	2454732.6	482613.3	1.328	-37.26	173.56	Normal	11.33	54.11	78	12
14		12	30.26	2454794.49	482792.2	1.321	2454831.3	482620.7	1.328	-36.82	171.5	Normal	11.33	53.46	78	12
14		13	36.83	2454915.18	482797.8	1.321	2454917.4	482641.9	1.328	-2.2	155.85	Normal	11.33	47.51	89	13
14		14	32.61	2455014.63	482837.3	1.320	2455017.7	482621.2	1.326	-3.05	216.06	Normal	9.71	65.86	89	8
14		15	34.35	2455113.89	482890.6	1.321	2455116.7	482688.6	1.325	-2.85	202	Normal	6.47	61.58	89	6
14		16	30.49	2455213.85	482894.1	1.321	2455216.1	482736.2	1.323	-2.23	157.92	Normal	3.24	48.14	89	4
15	424.23	1	0.00	2455567.49	478998.9	1.328	2455346.2	478995.8	1.33	221.27	3.12	Normal	3.24	67.45	179	3
15		2	40.44	2455653.28	479100.1	1.327	2455385.3	479096.3	1.331	267.97	3.77	Normal	6.47	81.69	179	5
15		3	45.94	2455539.14	479198.5	1.326	2455332.8	479195.6	1.33	206.31	2.91	Normal	6.47	62.89	179	6
15		4	31.03	2455556.88	479298.8	1.325	2455282.3	479294.9	1.33	274.54	3.87	Normal	8.09	83.69	179	6
15		5	39.18	2455474.69	479397.6	1.324	2455304.5	479395.2	1.33	170.19	2.4	Normal	9.71	51.88	179	11
15		6	31.03	2455454.13	479497.4	1.323	2455247.6	479494.4	1.329	206.51	2.91	Normal	9.71	62.95	179	9
15		7	33.14	2455410.02	479596.7	1.322	2455218.7	479594.0	1.328	191.34	2.7	Normal	9.71	58.33	179	9
15		8	33.93	2455359.73	479696	1.323	2455200.1	479693.8	1.328	159.62	2.25	Normal	8.09	48.66	179	9
15		9	33.39	2455403.02	479796.7	1.321	2455213.7	479794.0	1.328	189.35	2.67	Normal	11.33	57.72	179	11
15		10	31.03	2455382.45	479896.4	1.321	2455080.4	479892.1	1.326	302.08	4.26	Normal	8.09	92.08	179	5
15		11	62.44	2455559.82	479998.9	1.323	2455266.1	479994.8	1.329	293.7	4.14	Normal	9.71	89.53	179	6

Appendix 8: Sooner Field 3D Seismic Fault Data Tables (continued).

Fault Name	Total Fault Length (m)	Station #	Distance from last station (m)	Hangingwall Orientation Easting 1 x	Northing 1 y	Hangingwall (s)	Footwall Orientation Easting 2 x2	Northing 2 y2	Footwall (s)	dx Easting	dy Northing	Fault Type	Throw (meters)	Heave (meters)	RH Rule Fault Strike	dip degrees
15		12	42.67	2455460.44	480097.5	1.323	2455309.4	480095.4	1.328	151.04	2.13	Normal	8.09	46.04	179	10
16	668.20	1	0.00	2453434.84	481523.3	1.325	2453507.5	481693.1	1.327	-72.64	-169.85	Normal	3.24	56.31	293	3
16		2	43.47	2453475.8	481386.7	1.323	2453564.9	481595.0	1.327	-89.08	-208.28	Normal	6.47	69.05	293	5
16		3	33.80	2453535.11	481293	1.322	2453624.2	481501.3	1.327	-89.08	-208.28	Normal	8.09	69.05	293	7
16		4	27.88	2453620.57	481260.4	1.321	2453694.2	481432.6	1.327	-73.65	-172.2	Normal	9.71	57.09	293	10
16		5	30.20	2453719.66	481259.7	1.320	2453801.9	481452.1	1.327	-82.27	-192.36	Normal	11.33	63.77	293	10
16		6	12.72	2453760.75	481252.5	1.320	2453857.5	481478.8	1.328	-96.79	-226.34	Normal	12.95	75.03	293	10
16		7	42.12	2453886.46	481195.1	1.319	2453945.8	481481.1	1.327	-59.34	-285.98	Normal	12.95	89.02	282	8
16		8	7.10	2453907.72	481185.5	1.319	2453994.7	481459.2	1.328	-86.97	-273.71	Normal	14.57	87.54	288	9
16		9	31.62	2454010.85	481196.8	1.319	2454108.2	481503.3	1.327	-97.38	-306.44	Normal	12.95	98.01	288	8
16		10	9.42	2454022.94	481168.4	1.320	2454140.1	481442.3	1.328	-117.14	-273.9	Normal	12.95	90.80	293	8
16		11	31.83	2454126.84	481178.9	1.320	2454256.5	481482.1	1.327	-129.67	-303.19	Normal	11.33	100.51	293	6
16		12	42.35	2454231.14	481087.1	1.319	2454403.4	481489.9	1.328	-172.26	-402.77	Normal	14.57	133.52	293	6
16		13	45.21	2454349.76	481176.2	1.318	2454434.4	481512.6	1.327	-84.66	-336.44	Normal	14.57	105.74	284	8
16		14	39.37	2454422.55	481069.5	1.318	2454508.4	481410.6	1.327	-85.82	-341.08	Normal	14.57	107.20	284	8
16		15	32.50	2454527.26	481089.7	1.318	2454526.7	481484.8	1.327	0.58	-395.12	Normal	14.57	120.43	270	7
16		16	20.27	2454554.83	481029.2	1.318	2454703.0	481495.3	1.327	-148.12	-466.16	Normal	14.57	149.09	288	6
16		17	75.24	2454576.23	480783.3	1.319	2454783.5	481435.6	1.328	-207.28	-652.31	Normal	14.57	208.62	288	4
16		18	80.55	2454741.34	480989.6	1.325	2454810.9	481208.4	1.329	-69.53	-218.83	Normal	6.47	69.99	288	5
16		19	29.29	2454827.08	480946.2	1.326	2454919.9	481238.1	1.329	-92.77	-291.93	Normal	4.86	93.37	288	3
16		20	33.25	2454933.81	480968.8	1.326	2454986.2	481133.7	1.328	-52.42	-164.95	Normal	3.24	52.75	288	4

Appendix 9: Dana Point 3d Seismic Fault Data Tables.

Seismic Fault Analysis
Data Set: Dana Point T3S R63W **UTM NAD 83**

Fault Name	Total Fault Length (m)	Station #	Distance from last station (m)	Hangingwall Orientation Easting 1 x	Northing 1 y	Hangingwall (s)	Footwall Orientation Easting 2 x2	Northing 2 y2	Footwall (s)	dx Easting	dy Northing	Fault Type	Throw (meters)	Heave (meters)	Rule Fault Fault Strike	dip degrees
1	579.49	1	0.00	2271810.57	173023.89	1.59	2271897.7	173109.1	1.605	-87.09	-85.25	Normal	24.28	37.15	316	33
1		2	46.83	2271883.27	172888.53	1.589	2272051.7	173053.4	1.606	-168.44	-164.89	Normal	27.51	71.85	316	21
1		3	34.18	2271990.56	172855.87	1.59	2272070.1	172933.8	1.605	-79.58	-77.91	Normal	24.28	33.95	316	36
1		4	47.52	2272056.00	172714.38	1.589	2272223.4	172877.3	1.606	-167.43	-162.93	Normal	27.51	71.21	316	21
1		5	33.32	2272158.31	172675.89	1.591	2272242.5	172758.3	1.607	-84.21	-82.43	Normal	25.90	35.92	316	36
1		6	41.18	2272284.29	172627.09	1.592	2272346.4	172722.4	1.607	-62.07	-95.29	Normal	24.28	34.66	303	35
1		7	33.58	2272388.63	172591.76	1.592	2272449.8	172685.7	1.609	-61.18	-93.91	Normal	27.51	34.16	303	39
1		8	42.57	2272370.67	172453.24	1.592	2272527.6	172572.7	1.606	-156.95	-119.41	Normal	22.66	60.11	323	21
1		9	29.91	2272397.94	172358.98	1.593	2272552.6	172476.6	1.61	-154.63	-117.64	Normal	27.51	59.22	323	25
1		10	51.07	2272545.46	172279.54	1.594	2272698.8	172396.2	1.608	-153.29	-116.63	Normal	22.66	58.71	323	21
1		11	18.79	2272589.35	172236.27	1.594	2272737.0	172348.8	1.61	-147.65	-112.48	Normal	25.90	56.57	323	25
1		12	30.78	2272610.82	172137.59	1.594	2272768.6	172257.7	1.61	-157.8	-120.06	Normal	25.90	60.44	323	23
1		13	50.99	2272757.85	172057.78	1.596	2272910.2	172173.7	1.61	-152.35	-115.92	Normal	22.66	58.35	323	21
1		14	33.13	2272859.95	172020.46	1.597	2272937.1	172079.2	1.609	-77.16	-58.7	Normal	19.42	29.55	323	33
1		15	47.38	2272928.53	171880.96	1.596	2273008.3	171941.6	1.606	-79.75	-60.68	Normal	16.18	30.54	323	28
1		16	38.26	2273012.88	171787.99	1.598	2273051.2	171899.1	1.606	-38.35	-111.09	Normal	12.95	35.82	289	20
2	735.53	1	0.00	2272256.01	174148.34	1.587	2271995.2	173893.0	1.607	260.81	255.31	Normal	32.37	111.24	136	16
2		2	47.42	2272324.09	174008.46	1.589	2272151.2	173839.2	1.611	172.91	169.26	Normal	35.61	73.75	136	26
2		3	49.57	2272404.12	173866.88	1.589	2272346.9	173769.2	1.614	57.24	97.73	Normal	40.46	34.52	120	50
2		4	33.53	2272508.10	173830.99	1.587	2272395.9	173639.4	1.613	112.2	191.58	Normal	42.08	67.67	120	32
2		5	29.78	2272599.30	173795.98	1.59	2272453.3	173653.1	1.615	146.01	142.93	Normal	40.46	62.28	136	33
2		6	47.11	2272669.74	173658.41	1.589	2272494.0	173486.4	1.613	175.77	172.06	Normal	38.84	74.97	136	27
2		7	47.27	2272738.89	173519.59	1.589	2272488.9	173274.9	1.61	249.95	244.68	Normal	33.99	106.61	136	18
2		8	42.05	2272813.89	173403.80	1.59	2272685.1	173305.8	1.613	128.78	97.98	Normal	37.23	49.32	143	37
2		9	47.35	2272882.83	173264.58	1.587	2272803.1	173203.9	1.612	79.77	60.7	Normal	40.46	30.55	143	53
2		10	34.50	2272977.34	173202.28	1.588	2272805.7	173034.3	1.612	171.65	168.03	Normal	38.84	73.21	136	28
2		11	36.72	2272996.50	173083.35	1.588	2272903.5	172992.4	1.613	92.96	91	Normal	40.46	39.65	136	46
2		12	32.96	2273097.41	173044.46	1.589	2273044.3	172992.5	1.613	53.09	51.98	Normal	38.84	22.65	136	60
2		13	47.28	2273166.55	172905.61	1.589	2273077.6	172818.6	1.614	88.94	87.06	Normal	40.46	37.93	136	47
2		14	50.13	2273323.58	172856.75	1.589	2273166.2	172698.8	1.613	157.37	158	Normal	38.84	67.97	135	30
2		15	43.07	2273399.09	172737.32	1.589	2273289.0	172653.6	1.614	110.1	83.76	Normal	40.46	42.17	143	44
2		16	47.35	2273468.09	172598.14	1.59	2273345.4	172504.8	1.614	122.71	93.35	Normal	38.84	46.99	143	40
2		17	47.34	2273537.18	172459.03	1.588	2273455.3	172396.8	1.611	81.87	62.28	Normal	37.23	31.35	143	50
2		18	18.58	2273578.02	172413.77	1.588	2273508.9	172213.5	1.609	69.14	200.27	Normal	33.99	64.58	109	28
2		19	33.53	2273681.61	172376.75	1.589	2273611.3	172173.2	1.608	70.27	203.56	Normal	30.75	65.64	109	25
2-A	30.09	1	0.00	2273767.44	172290.77	1.59	2273867.0	172011.5	1.607	-99.51	279.24	Normal	27.51	90.36	70	17
2-A		2	30.09	2273832.01	172365.45	1.59	2273910.8	172144.3	1.601	-78.81	221.16	Normal	17.80	71.56	70	14
3	584.04	1	0.00	2275388.09	173825.44	1.592	2275461.2	173742.0	1.599	-73.06	83.43	Normal	11.33	33.80	49	19
3		2	33.88	2275422.48	173931.13	1.592	2275500.1	173842.5	1.6	-77.63	88.64	Normal	12.95	35.91	49	20
3		3	47.42	2275562.36	173999.21	1.591	2275608.0	173947.1	1.601	-45.66	52.14	Normal	16.18	21.12	49	37

Appendix 9: Dana Point 3D Seismic Fault Data table (continued).

Fault Name	Total Fault Length (m)	Station #	Distance from last station (m)	Hangingwall Orientation Easting 1 x	Northing 1 y	Hangingwall (s)	Footwall Orientation Easting 2 x2	Northing 2 y2	Footwall (s)	dx Easting	dy Northing	Fault Type	Throw (meters)	Heave (meters)	Rule Fault Fault Strike	dip degrees
3		4	16.65	2275601.69	174037.13	1.591	2275679.3	173948.6	1.601	-77.56	88.56	**Normal**	16.18	35.88	49	24
3		5	60.76	2275779.09	174128.04	1.591	2275851.2	174026.6	1.602	-72.13	101.42	**Normal**	17.80	37.93	55	25
3		6	29.13	2275871.44	174152.63	1.589	2275905.7	174104.5	1.603	-34.22	48.12	**Normal**	22.66	18.00	55	52
3		7	49.39	2275966.31	174284.00	1.591	2276028.4	174196.7	1.604	-62.08	87.3	**Normal**	21.04	32.65	55	33
3		8	89.01	2276041.16	174566.26	1.588	2276104.9	174508.4	1.605	-63.76	57.91	**Normal**	27.51	26.25	42	46
3		9	55.48	2276221.19	174593.01	1.588	2276291.9	174512.3	1.603	-70.71	80.74	**Normal**	24.28	32.71	49	37
3		10	31.13	2276269.22	174683.14	1.59	2276332.4	174611.0	1.604	-63.14	72.1	**Normal**	22.66	29.21	49	38
3		11	46.07	2276370.28	174795.55	1.588	2276442.6	174713.0	1.603	-72.27	82.53	**Normal**	24.28	33.44	49	36
3		12	32.85	2276409.24	174896.02	1.588	2276498.3	174794.3	1.603	-89.04	101.68	**Normal**	24.28	41.20	49	31
3		13	46.26	2276536.99	174977.96	1.589	2276613.7	174890.3	1.602	-76.74	87.67	**Normal**	21.04	35.51	49	31
3		14	46.03	2276660.88	175064.29	1.591	2276722.5	174994.0	1.598	-61.57	70.31	**Normal**	11.33	28.49	49	22
4	463.10	1	0.00	2275709.42	172193.34	1.582	2275578.7	172260.5	1.594	130.76	-67.12	**Normal**	19.42	44.80	207	23
4		2	52.57	2275771.15	172354.38	1.58	2275642.3	172398.9	1.594	128.9	-44.5	**Normal**	22.66	41.56	199	29
4		3	35.81	2275768.04	172471.83	1.579	2275678.1	172502.9	1.595	89.9	-31.03	**Normal**	25.90	28.99	199	42
4		4	33.79	2275816.94	172571.32	1.581	2275691.3	172614.7	1.595	125.66	-43.38	**Normal**	22.66	40.52	199	29
4		5	36.60	2275807.33	172691.01	1.581	2275730.4	172717.6	1.596	76.9	-26.54	**Normal**	24.28	24.80	199	44
4		6	34.65	2275870.34	172785.62	1.581	2275779.3	172817.0	1.596	91.01	-31.42	**Normal**	24.28	29.35	199	40
4		7	49.34	2275945.23	172929.12	1.582	2275855.7	172975.1	1.597	89.52	-45.96	**Normal**	24.28	30.67	207	38
4		8	33.19	2275993.49	173026.75	1.582	2275888.5	173080.6	1.596	104.97	-53.89	**Normal**	22.66	35.96	207	32
4		9	34.29	2276018.08	173136.53	1.584	2275917.2	173188.3	1.597	100.91	-51.81	**Normal**	21.04	34.57	207	31
4		10	54.66	2276167.50	173235.68	1.586	2276100.8	173341.2	1.6	66.66	-105.48	**Normal**	22.66	38.03	238	31
4		11	48.43	2276317.79	173287.29	1.587	2276229.0	173427.9	1.597	88.84	-140.56	**Normal**	16.18	50.68	238	18
4		12	49.77	2276420.41	173414.31	1.589	2276343.3	173536.3	1.597	77.08	-121.95	**Normal**	12.95	43.97	238	16
5	709.85	1	0.00	2277535.76	174069.79	1.587	2277465.5	174115.5	1.596	70.23	-45.75	**Normal**	14.57	25.55	213	30
5		2	33.31	2277606.03	174153.48	1.588	2277515.8	174210.2	1.599	90.23	-56.68	**Normal**	17.80	32.48	212	29
5		3	32.00	2277665.06	174240.29	1.589	2277572.4	174300.6	1.6	92.62	-60.33	**Normal**	17.80	33.69	213	28
5		4	34.25	2277752.84	174310.46	1.589	2277657.0	174372.9	1.601	95.84	-62.44	**Normal**	19.42	34.86	213	29
5		5	35.39	2277849.39	174374.93	1.586	2277714.5	174462.8	1.603	134.93	-87.9	**Normal**	27.51	49.08	213	29
5		6	31.67	2277851.03	174478.82	1.585	2277770.0	174518.7	1.603	81.08	-39.85	**Normal**	29.13	27.54	206	47
5		7	33.34	2277905.35	174573.75	1.587	2277798.3	174626.4	1.604	107.03	-52.6	**Normal**	27.51	36.35	206	37
5		8	33.35	2277960.46	174668.29	1.589	2277841.7	174726.6	1.605	118.72	-58.33	**Normal**	25.90	40.32	206	33
5		9	57.54	2278077.17	174816.68	1.589	2277934.7	174865.8	1.605	142.43	-49.16	**Normal**	25.90	45.93	199	29
5		10	92.02	2278069.92	175118.49	1.587	2277999.7	175133.3	1.604	70.18	-14.81	**Normal**	27.51	21.86	192	52
5		11	33.36	2278100.35	175223.62	1.589	2278007.3	175243.3	1.604	93.01	-19.63	**Normal**	24.28	28.97	192	40
5		12	33.72	2278105.21	175334.15	1.59	2278023.2	175351.5	1.605	81.98	-17.31	**Normal**	24.28	25.54	192	44
5		13	33.63	2278111.95	175444.28	1.587	2277983.5	175471.4	1.604	128.48	-27.12	**Normal**	27.51	40.02	192	35
5		14	34.59	2278104.08	175557.50	1.589	2278007.5	175581.7	1.604	96.6	-24.24	**Normal**	24.28	30.36	194	39
5		15	52.58	2278138.07	175726.61	1.587	2278035.0	175762.2	1.604	103.1	-35.59	**Normal**	27.51	33.24	199	40
5		16	35.85	2278213.30	175817.01	1.588	2278090.1	175859.6	1.602	123.25	-42.55	**Normal**	22.66	39.74	199	30
5		17	35.76	2278210.68	175934.29	1.588	2278110.2	175969.0	1.6	100.47	-34.68	**Normal**	19.42	32.40	199	31
5		18	33.91	2278230.84	176043.70	1.591	2278100.7	176088.6	1.6	130.14	-44.92	**Normal**	14.57	41.96	199	19
5		19	33.59	2278272.88	176145.56	1.591	2278153.2	176186.9	1.601	119.73	-41.33	**Normal**	16.18	38.61	199	23

Appendix 9: Dana Point 3D Seismic Fault Data table (continued).

Fault Name	Total Fault Length (m)	Station #	Distance from last station (m)	Hangingwall Orientation Easting 1 x	Northing 1 y	Hangingwall (s)	Footwall Orientation Easting 2 x2	Northing 2 y2	Footwall (s)	dx Easting	dy Northing	Fault Type	Throw (meters)	Heave (meters)	Rule Fault Fault Strike	dip degrees
6	1773.16	1	0.00	2274088.15	172351.36	1.59	2274042.3	172262.1	1.603	45.84	89.29	**Normal**	21.04	30.59	117	35
6		2	33.72	2274193.92	172318.97	1.588	2274126.7	172188.0	1.604	67.21	130.93	**Normal**	25.90	44.86	117	30
6		3	33.42	2274285.00	172257.94	1.586	2274218.7	172128.7	1.605	66.34	129.22	**Normal**	30.75	44.27	117	35
6		4	17.42	2274324.59	172216.71	1.587	2274272.6	172066.2	1.606	51.98	150.56	**Normal**	30.75	48.55	109	32
6		5	17.46	2274365.81	172176.91	1.585	2274308.4	172065.1	1.605	57.41	111.82	**Normal**	32.37	38.31	117	40
6		6	35.25	2274480.48	172161.84	1.588	2274404.4	172013.6	1.606	76.11	148.25	**Normal**	29.13	50.79	117	30
6		7	17.44	2274536.17	172148.74	1.589	2274436.6	172006.5	1.608	99.58	142.26	**Normal**	30.75	52.93	125	30
6		8	42.54	2274629.57	172045.03	1.589	2274568.0	171957.1	1.612	61.58	87.98	**Normal**	37.23	32.73	125	49
6		9	46.55	2274701.10	171910.09	1.59	2274636.7	171818.0	1.612	64.44	92.06	**Normal**	35.61	34.25	125	46
6		10	33.45	2274804.54	171873.42	1.591	2274723.4	171757.5	1.614	81.17	115.96	**Normal**	37.23	43.14	125	41
6		11	32.94	2274903.88	171830.89	1.59	2274819.9	171710.8	1.616	84.03	120.05	**Normal**	42.08	44.66	125	43
6		12	46.27	2274976.61	171697.65	1.59	2274915.6	171610.5	1.617	61.04	87.2	**Normal**	43.70	32.44	125	53
6		13	33.21	2275078.27	171658.44	1.592	2275012.6	171564.7	1.612	65.63	93.76	**Normal**	32.37	34.88	125	43
6		14	36.37	2275196.60	171643.06	1.593	2275080.4	171477.1	1.612	116.2	166.01	**Normal**	30.75	61.76	125	26
6		15	41.81	2275318.23	171579.67	1.584	2275174.3	171374.1	1.611	143.89	205.56	**Normal**	43.70	76.48	125	30
6		16	52.83	2275445.58	171462.11	1.582	2275351.7	171358.7	1.61	93.88	103.38	**Normal**	45.32	42.56	132	47
6		17	33.21	2275547.71	171424.17	1.583	2275459.4	171326.9	1.611	88.33	97.25	**Normal**	45.32	40.04	132	49
6		18	14.46	2275566.78	171380.72	1.583	2275505.6	171313.4	1.612	61.16	67.35	**Normal**	46.94	27.73	132	59
6		19	32.68	2275617.65	171286.34	1.584	2275561.5	171224.5	1.612	56.18	61.86	**Normal**	45.32	25.47	132	61
6		20	30.87	2275696.32	171222.58	1.583	2275630.2	171149.8	1.61	66.09	72.77	**Normal**	43.70	29.96	132	56
6		21	14.59	2275714.75	171178.42	1.583	2275641.3	171097.5	1.61	73.5	80.93	**Normal**	43.70	33.32	132	53
6		22	30.86	2275786.00	171106.49	1.582	2275721.1	171035.1	1.611	64.86	71.43	**Normal**	46.94	29.41	132	58
6		23	31.11	2275870.23	171048.85	1.582	2275791.8	170962.5	1.611	78.42	86.35	**Normal**	46.94	35.55	132	53
6		24	39.72	2275938.32	170937.75	1.58	2275846.5	170847.8	1.61	91.84	89.91	**Normal**	48.55	39.17	136	51
6		25	46.53	2276013.72	170805.03	1.581	2275939.1	170731.9	1.61	74.67	73.1	**Normal**	46.94	31.85	136	56
6		26	31.33	2276103.82	170755.55	1.58	2275992.2	170646.2	1.611	111.67	109.32	**Normal**	50.17	47.63	136	46
6		27	15.07	2276134.67	170716.90	1.58	2276034.8	170619.2	1.609	99.84	97.73	**Normal**	46.94	42.58	136	48
6		28	32.80	2276234.68	170677.13	1.582	2276129.6	170574.2	1.61	105.1	102.89	**Normal**	45.32	44.83	136	45
6		29	45.03	2276333.13	170566.98	1.582	2276253.9	170489.4	1.609	79.26	77.59	**Normal**	43.70	33.81	136	52
6		30	45.02	2276465.86	170502.17	1.582	2276334.3	170391.8	1.609	131.52	110.33	**Normal**	43.70	52.32	140	40
6		31	31.46	2276494.38	170402.97	1.58	2276408.9	170331.3	1.61	85.51	71.72	**Normal**	48.55	34.02	140	55
6		32	28.88	2276548.09	170324.91	1.581	2276400.8	170201.4	1.609	147.29	123.55	**Normal**	45.32	58.60	140	38
6		33	17.61	2276593.39	170289.04	1.582	2276435.3	170156.4	1.609	158.07	132.6	**Normal**	43.70	62.89	140	35
6		34	55.12	2276614.04	170109.37	1.579	2276533.6	170041.9	1.606	80.45	67.48	**Normal**	43.70	32.01	140	54
6		35	51.99	2276771.94	170044.84	1.58	2276603.1	169903.2	1.604	168.85	141.64	**Normal**	38.84	67.18	140	30
6		36	34.18	2276786.10	169933.61	1.583	2276717.1	169875.7	1.605	68.99	57.88	**Normal**	35.61	27.45	140	52
6		37	46.00	2276883.63	169818.43	1.583	2276829.7	169773.2	1.605	53.9	45.21	**Normal**	35.61	21.44	140	59
6		38	28.76	2276945.97	169747.61	1.585	2276901.4	169710.2	1.604	44.6	37.42	**Normal**	30.75	17.75	140	60
6		39	31.65	2277039.84	169703.23	1.585	2276992.5	169663.5	1.605	47.36	39.73	**Normal**	32.37	18.84	140	60
6		40	46.01	2277139.53	169589.87	1.585	2277061.2	169524.2	1.603	78.3	65.68	**Normal**	29.13	31.15	140	43
6		41	47.34	2277208.35	169450.62	1.582	2277128.6	169383.8	1.604	79.71	66.87	**Normal**	35.61	31.71	140	48
6		42	48.64	2277265.66	169301.70	1.58	2277198.1	169245.1	1.602	67.52	56.63	**Normal**	35.61	26.86	140	53

Appendix 9: Dana Point 3D Seismic Fault Data table (continued).

Fault Name	Total Fault Length (m)	Station #	Distance from last station (m)	Hangingwall Orientation Easting 1 x	Northing 1 y	Hangingwall (s)	Footwall Orientation Easting 2 x2	Northing 2 y2	Footwall (s)	dx Easting	dy Northing	Fault Type	Throw (meters)	Heave (meters)	Rule Fault Fault Strike	dip degrees
6		43	30.38	2277350.97	169250.15	1.582	2277297.8	169205.6	1.601	53.16	44.6	**Normal**	30.75	21.15	140	55
6		44	31.66	2277444.91	169205.83	1.583	2277322.0	169102.7	1.602	122.9	103.09	**Normal**	30.75	48.89	140	32
6		45	46.22	2277553.22	169099.70	1.582	2277446.9	169010.5	1.6	106.32	89.19	**Normal**	29.13	42.30	140	35
6		46	48.19	2277614.10	168953.78	1.579	2277506.4	168863.4	1.598	107.74	90.38	**Normal**	30.75	42.86	140	36
6		47	46.52	2277693.71	168823.57	1.579	2277625.5	168766.3	1.596	68.26	57.26	**Normal**	27.51	27.16	140	45
6		48	43.88	2277762.29	168696.98	1.583	2277651.7	168627.1	1.597	110.62	69.92	**Normal**	22.66	39.89	148	30
6		49	47.23	2277836.42	168560.92	1.584	2277738.0	168498.8	1.594	98.38	62.17	**Normal**	16.18	35.47	148	25
6		50	47.49	2277902.79	168419.96	1.587	2277840.1	168380.3	1.591	62.7	39.62	**Normal**	6.47	22.61	148	16
7	1383.61	1	0.00	2276596.67	164303.13	1.581	2276560.5	164198.3	1.589	36.2	104.87	**Normal**	12.95	33.82	109	21
7		2	34.09	2276694.04	164248.08	1.579	2276662.6	164156.9	1.591	31.48	91.19	**Normal**	19.42	29.40	109	33
7		3	33.68	2276794.56	164202.17	1.578	2276758.7	164098.2	1.59	35.91	104.01	**Normal**	19.42	33.54	109	30
7		4	37.49	2276880.58	164114.27	1.58	2276845.0	164011.2	1.593	35.58	103.08	**Normal**	21.04	33.24	109	32
7		5	33.78	2276980.16	164065.63	1.581	2276947.1	163969.8	1.595	33.07	95.81	**Normal**	22.66	30.89	109	36
7		6	14.42	2277018.59	164038.05	1.581	2276961.0	163963.0	1.595	57.58	75.09	**Normal**	22.66	28.84	127	38
7		7	42.51	2277123.18	163945.79	1.579	2277050.8	163851.4	1.591	72.38	94.4	**Normal**	19.42	36.26	127	28
7		8	31.82	2277207.37	163884.08	1.58	2277125.1	163776.7	1.592	82.31	107.34	**Normal**	19.42	41.23	127	25
7		9	43.02	2277303.31	163780.54	1.576	2277260.6	163724.8	1.593	42.72	55.71	**Normal**	27.51	21.40	127	52
7		10	32.68	2277401.08	163736.55	1.576	2277357.1	163679.2	1.592	43.94	57.31	**Normal**	25.90	22.01	127	50
7		11	15.50	2277451.26	163744.79	1.577	2277418.8	163650.8	1.593	32.45	94.01	**Normal**	25.90	30.31	109	41
7		12	34.60	2277546.09	163682.37	1.576	2277520.9	163609.4	1.592	25.19	72.96	**Normal**	25.90	23.53	109	48
7		13	33.53	2277650.72	163648.36	1.577	2277623.3	163569.0	1.593	27.41	79.38	**Normal**	25.90	25.60	109	45
7		14	14.40	2277693.55	163628.40	1.577	2277692.4	163515.6	1.591	1.2	112.84	**Normal**	22.66	34.40	91	33
7		15	19.24	2277754.37	163611.52	1.575	2277715.7	163499.4	1.591	38.71	112.14	**Normal**	25.90	36.16	109	36
7		16	33.59	2277860.56	163582.04	1.575	2277832.2	163499.9	1.589	28.34	82.11	**Normal**	22.66	26.48	109	41
7		17	33.68	2277968.00	163556.16	1.576	2277940.3	163475.9	1.591	27.7	80.24	**Normal**	24.28	25.87	109	43
7		18	33.63	2278074.81	163528.47	1.575	2278037.3	163419.9	1.586	37.47	108.55	**Normal**	17.80	35.00	109	27
7		19	34.59	2278169.67	163466.15	1.574	2278142.3	163386.8	1.589	27.41	79.39	**Normal**	24.28	25.60	109	43
7		20	13.98	2278144.72	163504.64	1.575	2278163.2	163433.9	1.589	-18.47	70.72	**Normal**	22.66	22.28	255	45
7		21	29.86	2278242.10	163494.00	1.576	2278623.4	163412.3	1.591	-381.34	81.69	**Normal**	24.28	118.87	192	12
7		22	27.22	2278317.79	163446.61	1.575	2278316.8	163354.1	1.592	0.99	92.53	**Normal**	27.51	28.20	91	44
7		23	22.49	2278388.97	163427.20	1.574	2278361.2	163346.9	1.59	27.73	80.32	**Normal**	25.90	25.90	109	45
7		24	33.61	2278495.46	163398.58	1.574	2278464.9	163310.1	1.59	30.54	88.45	**Normal**	25.90	28.52	109	42
7		25	36.26	2278584.64	163319.83	1.574	2278564.5	163261.4	1.59	20.17	58.43	**Normal**	25.90	18.84	109	54
7		26	34.20	2278695.86	163304.89	1.576	2278669.1	163227.4	1.593	26.76	77.5	**Normal**	27.51	24.99	109	48
7		27	35.94	2278813.69	163309.11	1.577	2278785.0	163226.1	1.591	28.65	82.97	**Normal**	22.66	26.75	109	40
7		28	34.82	2278907.60	163244.05	1.574	2278873.0	163143.7	1.59	34.64	100.34	**Normal**	25.90	32.35	109	39
7		29	33.55	2279012.84	163211.83	1.575	2278983.2	163126.0	1.591	29.61	85.79	**Normal**	25.90	27.66	109	43
7		30	33.59	2279114.61	163169.52	1.574	2279090.4	163099.3	1.59	24.24	70.23	**Normal**	25.90	22.65	109	49
7		31	34.99	2279207.87	163102.58	1.57	2279176.7	163012.3	1.591	31.15	90.25	**Normal**	33.99	29.10	109	49
7		32	18.40	2279262.79	163077.49	1.573	2279205.9	163003.2	1.591	56.94	74.26	**Normal**	29.13	28.52	127	46
7		33	31.88	2279341.40	163008.51	1.572	2279274.0	162920.6	1.589	67.44	87.96	**Normal**	27.51	33.78	127	39
7		34	42.73	2279462.14	162937.30	1.571	2279404.6	162862.2	1.589	57.58	75.09	**Normal**	29.13	28.84	127	45

Appendix 9: Dana Point 3D Seismic Fault Data table (continued).

Fault Name	Total Fault Length (m)	Station #	Distance from last station (m)	Hangingwall Orientation Easting 1 x	Northing 1 y	Hangingwall (s)	Footwall Orientation Easting 2 x2	Northing 2 y2	Footwall (s)	dx Easting	dy Northing	Fault Type	Throw (meters)	Heave (meters)	Rule Fault Fault Strike	dip degrees
7		35	32.75	2279560.54	162894.14	1.572	2279499.3	162814.2	1.591	61.29	79.94	**Normal**	30.75	30.70	127	45
7		36	33.13	2279624.88	162806.54	1.571	2279576.0	162742.8	1.59	48.87	63.74	**Normal**	30.75	24.48	127	51
7		37	25.67	2279661.50	162730.71	1.571	2279632.1	162645.9	1.587	29.44	84.86	**Normal**	25.90	27.38	109	43
7		38	21.31	2279729.47	162714.28	1.572	2279727.2	162584.4	1.59	2.26	129.9	**Normal**	29.13	39.60	91	36
7		39	24.44	2279805.57	162689.06	1.573	2279803.9	162532.4	1.586	1.67	156.62	**Normal**	21.04	47.74	91	24
7		40	22.32	2279864.88	162646.09	1.572	2279832.8	162553.1	1.586	32.1	92.98	**Normal**	22.66	29.98	109	37
7		41	33.71	2279972.64	162621.14	1.574	2279923.5	162478.9	1.585	49.11	142.25	**Normal**	17.80	45.87	109	21
7		42	34.04	2280070.33	162567.03	1.574	2280041.4	162483.1	1.582	28.97	83.92	**Normal**	12.95	27.06	109	26
7		43	60.01	2280218.47	162437.33	1.574	2280180.7	162388.1	1.58	37.79	49.27	**Normal**	9.71	18.93	127	27
7		44	33.73	2280323.67	162403.03	1.573	2280253.7	162311.8	1.583	69.95	91.22	**Normal**	16.18	35.04	127	25
7		45	42.72	2280423.91	162305.09	1.574	2280342.9	162199.4	1.581	81.03	105.67	**Normal**	11.33	40.59	127	16
8	142.53	1	0.00	2279514.88	170216.25	1.582	2279586.3	170143.3	1.586	-71.44	72.98	**Normal**	6.47	31.13	46	12
8		2	31.02	2279603.38	170266.49	1.582	2279715.6	170151.9	1.589	-112.2	114.62	**Normal**	11.33	48.89	46	13
8		3	30.91	2279656.49	170352.88	1.583	2279778.9	170227.8	1.59	-122.43	125.06	**Normal**	11.33	53.34	46	12
8		4	15.57	2279682.04	170397.10	1.583	2279776.2	170300.9	1.588	-94.17	96.2	**Normal**	8.09	41.03	46	11
8		5	31.37	2279731.25	170487.48	1.584	2279803.4	170413.8	1.588	-72.18	73.73	**Normal**	6.47	31.45	46	12
8		6	33.67	2279766.41	170592.21	1.584	2279840.1	170516.9	1.588	-73.72	75.31	**Normal**	6.47	32.12	46	11
10	678.75	1	0.00	2283714.07	161186.36	1.564	2283761.6	161088.7	1.582	-47.55	97.7	**Normal**	29.13	33.12	64	41
10		2	23.85	2283787.80	161212.60	1.564	2283839.7	161106.1	1.584	-51.86	106.53	**Normal**	32.37	36.11	64	42
10		3	23.82	2283854.39	161253.53	1.562	2283900.2	161159.4	1.584	-45.81	94.12	**Normal**	35.61	31.91	64	48
10		4	23.77	2283926.78	161282.52	1.563	2283988.2	161156.4	1.584	-61.39	126.11	**Normal**	33.99	42.75	64	38
10		5	26.43	2284013.49	161282.11	1.566	2284073.1	161159.6	1.583	-59.64	122.53	**Normal**	27.51	41.54	64	34
10		6	47.63	2284146.88	161363.52	1.567	2284235.1	161182.4	1.583	-88.18	181.16	**Normal**	25.90	61.41	64	23
10		7	27.50	2284236.82	161356.47	1.565	2284292.1	161242.9	1.585	-55.3	113.61	**Normal**	32.37	38.51	64	40
10		8	36.13	2284314.45	161446.04	1.565	2284354.8	161320.5	1.584	-40.35	125.5	**Normal**	30.75	40.18	72	37
10		9	26.85	2284401.57	161458.99	1.566	2284392.1	161350.5	1.586	9.5	108.46	**Normal**	32.37	33.19	95	44
10		10	46.73	2284550.56	161422.81	1.563	2284607.3	161306.3	1.583	-56.7	116.51	**Normal**	32.37	39.49	64	39
10		11	24.30	2284628.16	161441.11	1.563	2284697.5	161298.7	1.578	-69.32	142.43	**Normal**	24.28	48.28	64	27
10		12	37.29	2284656.76	161560.06	1.564	2284779.6	161307.8	1.576	-122.81	252.3	**Normal**	19.42	85.53	64	13
10		13	33.54	2284760.77	161524.10	1.563	2284828.9	161384.3	1.576	-68.08	139.85	**Normal**	21.04	47.41	64	24
10		14	23.91	2284826.24	161567.33	1.563	2284874.9	161467.5	1.577	-48.61	99.87	**Normal**	22.66	33.85	64	34
10		15	24.82	2284906.73	161579.69	1.562	2284967.9	161454.0	1.576	-61.19	125.72	**Normal**	22.66	42.62	64	28
10		16	28.04	2284955.16	161657.90	1.563	2285041.1	161481.4	1.576	-85.91	176.47	**Normal**	21.04	59.82	64	19
10		17	35.13	2285057.04	161604.04	1.562	2285045.7	161474.9	1.576	11.32	129.14	**Normal**	22.66	39.51	95	30
10		18	35.55	2285167.46	161641.62	1.562	2285156.9	161520.6	1.578	10.61	121.07	**Normal**	25.90	37.04	95	35
10		19	16.42	2285220.13	161652.98	1.563	2285242.5	161483.6	1.575	-22.36	169.35	**Normal**	19.42	52.07	82	20
10		20	34.08	2285315.06	161712.05	1.563	2285372.0	161535.0	1.576	-56.91	177.02	**Normal**	21.04	56.68	72	20
10		21	28.61	2285388.83	161770.09	1.565	2285448.2	161585.6	1.576	-59.33	184.51	**Normal**	17.80	59.07	72	17
10		22	20.13	2285452.52	161787.62	1.566	2285509.2	161611.4	1.575	-56.67	176.24	**Normal**	14.57	56.43	72	14
10		23	27.27	2285531.39	161829.83	1.567	2285594.5	161633.7	1.579	-63.06	196.12	**Normal**	19.42	62.79	72	17
10		24	26.94	2285617.72	161848.81	1.565	2285688.3	161629.4	1.576	-70.56	219.42	**Normal**	17.80	70.25	72	14
9	1302.65	1	0.00	2288549.64	160029.91	1.554	2288406.0	160079.5	1.577	143.65	-49.59	**Normal**	37.23	46.32	199	39

Appendix 9: Dana Point 3D Seismic Fault Data table (continued).

Fault Name	Total Fault Length (m)	Station #	Distance from last station (m)	Hangingwall Orientation Easting 1 x	Northing 1 y	Hangingwall (s)	Footwall Orientation Easting 2 x2	Northing 2 y2	Footwall (s)	dx Easting	dy Northing	Fault Type	Throw (meters)	Heave (meters)	Rule Fault Fault Strike	dip degrees
9		2	34.24	2288607.05	160126.46	1.553	2288418.8	160191.4	1.578	188.22	-64.98	**Normal**	40.46	60.69	199	34
9		3	35.34	2288608.28	160242.41	1.554	2288433.2	160302.8	1.576	175.08	-60.43	**Normal**	35.61	56.45	199	32
9		4	34.13	2288663.98	160339.54	1.554	2288535.2	160384.0	1.577	128.78	-44.46	**Normal**	37.23	41.53	199	42
9		5	50.48	2288716.32	160496.68	1.554	2288569.2	160562.9	1.576	147.08	-66.23	**Normal**	35.61	49.17	204	36
9		6	33.40	2288758.67	160597.76	1.553	2288606.8	160666.1	1.575	151.89	-68.38	**Normal**	35.61	50.77	204	35
9		7	34.30	2288780.17	160708.22	1.552	2288644.2	160769.5	1.575	135.99	-61.23	**Normal**	37.23	45.46	204	39
9		8	33.41	2288828.81	160806.46	1.552	2288688.2	160869.8	1.575	140.64	-63.32	**Normal**	37.23	47.01	204	38
9		9	33.47	2288880.75	160903.21	1.551	2288740.0	160966.1	1.576	140.79	-62.85	**Normal**	40.46	46.99	204	41
9		10	33.39	2288926.24	161002.87	1.554	2288796.7	161061.2	1.577	129.55	-58.33	**Normal**	37.23	43.30	204	41
9		11	36.02	2289011.61	161084.57	1.553	2288837.4	161163.0	1.577	174.23	-78.45	**Normal**	38.84	58.24	204	34
9		12	52.66	2289056.23	161251.47	1.552	2288888.0	161309.6	1.578	168.26	-58.08	**Normal**	42.08	54.26	199	38
9		13	35.69	2289054.20	161368.54	1.553	2288884.2	161427.2	1.578	169.96	-58.67	**Normal**	40.46	54.80	199	36
9		14	33.68	2289100.00	161469.09	1.554	2288870.6	161548.3	1.578	229.4	-79.2	**Normal**	38.84	73.97	199	28
9		15	15.70	2289116.81	161517.77	1.555	2288969.7	161584.0	1.579	147.09	-66.22	**Normal**	38.84	49.17	204	38
9		16	33.39	2289162.30	161617.43	1.556	2288981.6	161684.3	1.582	180.68	-66.9	**Normal**	42.08	58.73	200	36
9		17	33.87	2289190.25	161724.98	1.555	2289052.8	161786.9	1.583	137.5	-61.91	**Normal**	45.32	45.96	204	45
9		18	35.52	2289199.00	161841.18	1.554	2289077.4	161895.9	1.582	121.6	-54.75	**Normal**	45.32	40.65	204	48
9		19	35.71	2289206.11	161958.12	1.553	2289060.5	162023.7	1.581	145.59	-65.55	**Normal**	45.32	48.67	204	43
9		20	16.41	2289231.65	162005.50	1.553	2289073.1	162060.2	1.58	158.51	-54.72	**Normal**	43.70	51.11	199	41
9		21	33.63	2289259.34	162112.31	1.552	2289115.7	162161.9	1.581	143.65	-49.59	**Normal**	46.94	46.32	199	45
9		22	33.55	2289291.83	162217.47	1.553	2289178.1	162256.7	1.581	113.78	-39.27	**Normal**	45.32	36.69	199	51
9		23	33.53	2289329.42	162320.86	1.553	2289116.4	162394.4	1.578	212.99	-73.53	**Normal**	40.46	68.68	199	31
9		24	36.70	2289319.04	162440.81	1.554	2289187.0	162486.4	1.576	132.04	-45.58	**Normal**	35.61	42.58	199	40
9		25	34.47	2289379.70	162536.24	1.552	2289274.1	162572.7	1.578	105.57	-36.45	**Normal**	42.08	34.04	199	51
9		26	33.80	2289402.44	162644.76	1.554	2289262.2	162693.2	1.577	140.25	-48.42	**Normal**	37.23	45.22	199	39
9		27	35.52	2289401.95	162761.30	1.554	2289273.3	162805.7	1.576	128.63	-44.4	**Normal**	35.61	41.48	199	41
9		28	35.52	2289474.22	162852.72	1.553	2289327.3	162903.4	1.576	146.89	-50.71	**Normal**	37.23	47.36	199	38
9		29	67.89	2289513.04	163072.06	1.554	2289367.7	163122.2	1.576	145.35	-50.18	**Normal**	35.61	46.87	199	37
9		30	33.87	2289534.08	163181.17	1.553	2289443.2	163212.5	1.573	90.87	-31.36	**Normal**	32.37	29.30	199	48
9		31	20.85	2289573.62	163237.00	1.554	2289481.9	163303.0	1.574	91.72	-66.02	**Normal**	32.37	34.45	216	43
9		32	2.76	2289580.98	163231.71	1.554	2289480.4	163304.1	1.574	100.61	-72.41	**Normal**	32.37	37.78	216	41
9		33	32.62	2289627.28	163328.20	1.554	2289534.0	163395.3	1.571	93.25	-67.12	**Normal**	27.51	35.02	216	38
9		34	19.64	2289633.22	163392.37	1.554	2289551.7	163462.8	1.57	81.5	-70.47	**Normal**	25.90	32.84	221	38
9		35	38.11	2289758.02	163384.54	1.552	2289613.4	163519.4	1.57	144.6	-134.87	**Normal**	29.13	60.27	223	26
9		36	30.71	2289821.63	163462.67	1.553	2289753.7	163526.0	1.57	67.94	-63.36	**Normal**	27.51	28.32	223	44
9		37	34.97	2289894.13	163551.61	1.555	2289842.0	163604.9	1.57	52.14	-53.27	**Normal**	24.28	22.72	226	47
9		38	45.38	2290013.40	163640.75	1.556	2289946.6	163709.0	1.567	66.83	-68.26	**Normal**	17.80	29.12	226	31
9		39	48.31	2290159.31	163702.67	1.556	2290082.8	163780.8	1.564	76.51	-78.15	**Normal**	12.95	33.34	226	21
11	1837.79	1	0.00	2287242.10	159666.70	1.551	2287406.4	159612.3	1.575	-164.31	54.41	**Normal**	38.84	52.76	18	36
11		2	33.85	2287292.57	159765.64	1.556	2287387.6	159732.9	1.577	-95	32.79	**Normal**	33.99	30.63	19	48
11		3	34.09	2287309.38	159876.21	1.556	2287490.6	159813.7	1.573	-181.2	62.55	**Normal**	27.51	58.43	19	25
11		4	35.58	2287382.19	159967.45	1.557	2287527.5	159917.3	1.573	-145.33	50.17	**Normal**	25.90	46.86	19	29

Appendix 9: Dana Point 3D Seismic Fault Data table (continued).

Fault Name	Total Fault Length (m)	Station #	Distance from last station (m)	Hangingwall Orientation Easting 1 x	Northing 1 y	Hangingwall (s)	Footwall Orientation Easting 2 x2	Northing 2 y2	Footwall (s)	dx Easting	dy Northing	Fault Type	Throw (meters)	Heave (meters)	Rule Fault Fault Strike	dip degrees
11		5	44.45	2287327.59	160102.67	1.561	2287546.6	160027.1	1.572	-219.05	75.62	**Normal**	17.80	70.63	19	14
11		6	35.83	2287324.27	160220.18	1.561	2287564.7	160137.2	1.576	-240.44	83	**Normal**	24.28	77.53	19	17
11		7	36.78	2287313.29	160340.34	1.564	2287567.1	160252.7	1.575	-253.76	87.6	**Normal**	17.80	81.82	19	12
11		8	83.07	2287537.13	160495.81	1.554	2287696.9	160440.7	1.575	-159.8	55.16	**Normal**	33.99	51.53	19	33
11		9	33.55	2287576.38	160598.63	1.554	2287744.0	160540.8	1.576	-167.66	57.88	**Normal**	35.61	54.06	19	33
11		10	19.41	2287577.00	160662.31	1.552	2287727.9	160584.8	1.576	-150.93	77.48	**Normal**	38.84	51.71	27	37
11		11	33.19	2287626.75	160759.17	1.551	2287777.7	160681.7	1.575	-150.93	77.48	**Normal**	38.84	51.71	27	37
11		12	35.42	2287712.59	160837.51	1.553	2287525.2	160779.7	1.574	187.36	57.83	**Normal**	33.99	59.77	163	30
11		13	19.72	2287708.60	160902.10	1.553	2287849.5	160853.5	1.572	-140.93	48.65	**Normal**	30.75	45.44	19	34
11		14	34.71	2287716.60	161015.70	1.551	2287888.8	160956.3	1.572	-172.18	59.43	**Normal**	33.99	55.52	19	31
11		15	33.56	2287747.99	161121.24	1.552	2287925.7	161059.9	1.57	-177.73	61.36	**Normal**	29.13	57.31	19	27
11		16	34.91	2287814.08	161214.79	1.554	2287963.9	161163.1	1.57	-149.84	51.72	**Normal**	25.90	48.32	19	28
11		17	18.42	2287813.70	161275.23	1.554	2287974.2	161192.8	1.57	-160.5	82.4	**Normal**	25.90	54.99	27	25
11		18	33.43	2287851.69	161378.13	1.552	2287997.3	161303.4	1.57	-145.64	74.77	**Normal**	29.13	49.90	27	30
11		19	40.65	2287951.19	161466.94	1.551	2288053.2	161414.6	1.57	-101.98	52.35	**Normal**	30.75	34.94	27	41
11		20	34.06	2288023.17	161552.40	1.552	2288087.0	161519.6	1.571	-63.8	32.76	**Normal**	30.75	21.86	27	55
11		21	17.58	2288018.22	161609.87	1.552	2288142.2	161567.0	1.571	-123.95	42.86	**Normal**	30.75	39.97	19	38
11		22	33.99	2288071.84	161707.66	1.552	2288216.0	161657.9	1.571	-144.18	49.77	**Normal**	30.75	46.49	19	33
11		23	34.15	2288127.87	161804.69	1.552	2288241.9	161765.3	1.571	-113.98	39.35	**Normal**	30.75	36.75	19	40
11		24	16.76	2288145.81	161856.66	1.552	2288248.9	161803.7	1.572	-103.08	52.92	**Normal**	32.37	35.32	27	43
11		25	33.63	2288211.41	161945.38	1.554	2288285.9	161907.2	1.571	-74.47	38.23	**Normal**	27.51	25.51	27	47
11		26	21.18	2288197.35	162013.44	1.554	2288301.4	161977.5	1.573	-104.02	35.91	**Normal**	30.75	33.54	19	43
11		27	35.34	2288198.65	162129.37	1.553	2288308.2	162091.5	1.573	-109.57	37.83	**Normal**	32.37	35.33	19	42
11		28	33.53	2288236.74	162232.58	1.554	2288332.9	162199.4	1.573	-96.16	33.19	**Normal**	30.75	31.01	19	45
11		29	36.79	2288225.66	162352.78	1.552	2288365.4	162304.5	1.572	-139.78	48.25	**Normal**	32.37	45.07	19	36
11		30	34.02	2288243.66	162462.94	1.554	2288388.0	162413.1	1.572	-144.29	49.81	**Normal**	29.13	46.53	19	32
11		31	33.85	2288294.13	162561.88	1.554	2288417.1	162519.4	1.571	-123	42.46	**Normal**	27.51	39.66	19	35
11		32	36.36	2288286.41	162680.92	1.555	2288411.6	162637.7	1.571	-125.2	43.22	**Normal**	25.90	40.37	19	33
11		33	36.36	2288278.68	162799.96	1.554	2288437.4	162745.2	1.572	-158.76	54.81	**Normal**	29.13	51.19	19	30
11		34	34.15	2288294.45	162910.89	1.556	2288449.8	162857.2	1.572	-155.39	53.65	**Normal**	25.90	50.11	19	27
11		35	33.81	2288343.80	163010.22	1.553	2288516.0	162950.8	1.572	-172.18	59.44	**Normal**	30.75	55.52	19	29
11		36	33.54	2288381.90	163113.44	1.553	2288540.7	163058.6	1.572	-158.75	54.81	**Normal**	30.75	51.19	19	31
11		37	36.36	2288374.17	163232.47	1.555	2288522.9	163181.1	1.572	-148.69	51.33	**Normal**	27.51	47.95	19	30
11		38	33.55	2288413.42	163335.29	1.556	2288548.7	163288.6	1.572	-135.27	46.69	**Normal**	25.90	43.62	19	31
11		39	28.46	2288372.29	163419.10	1.556	2288560.4	163322.5	1.572	-188.11	96.57	**Normal**	25.90	64.45	27	22
11		40	35.82	2288461.32	163495.80	1.558	2288599.5	163424.9	1.572	-138.17	70.93	**Normal**	22.66	47.34	27	26
11		41	34.15	2288534.50	163580.64	1.561	2288644.0	163524.5	1.572	-109.46	56.19	**Normal**	17.80	37.50	27	25
11		42	37.36	2288534.21	163703.20	1.56	2288658.5	163639.4	1.573	-124.31	63.82	**Normal**	21.04	42.59	27	26
11		43	33.26	2288590.34	163796.79	1.561	2288695.5	163742.8	1.574	-105.17	54	**Normal**	21.04	36.03	27	30
11		44	16.24	2288630.06	163832.31	1.56	2288715.7	163772.4	1.573	-85.64	59.94	**Normal**	21.04	31.86	35	33
11		45	34.09	2288660.95	163939.80	1.559	2288768.8	163864.3	1.572	-107.84	75.49	**Normal**	21.04	40.12	35	28
11		46	49.21	2288712.81	164092.71	1.56	2288793.7	164019.2	1.572	-80.91	73.48	**Normal**	19.42	33.31	42	30

Appendix 9: Dana Point 3D Seismic Fault Data table (continued).

Fault Name	Total Fault Length (m)	Station #	Distance from last station (m)	Hangingwall Orientation Easting 1 x	Northing 1 y	Hangingwall (s)	Footwall Orientation Easting 2 x2	Northing 2 y2	Footwall (s)	dx Easting	dy Northing	Fault Type	Throw (meters)	Heave (meters)	Rule Fault Fault Strike	dip degrees
11		47	13.92	2288752.61	164115.11	1.56	2288836.0	164039.4	1.572	-83.41	75.76	**Normal**	19.42	34.34	42	29
11		48	32.03	2288799.37	164209.22	1.561	2288896.1	164121.4	1.57	-96.7	87.82	**Normal**	14.57	39.81	42	20
11		49	34.40	2288904.75	164168.84	1.56	2288981.7	164081.0	1.57	-76.97	87.88	**Normal**	16.18	35.61	49	24
11		50	29.17	2288980.71	164227.07	1.561	2289047.4	164150.9	1.571	-66.73	76.2	**Normal**	16.18	30.87	49	28
11		51	16.78	2289026.58	164257.53	1.561	2289103.6	164169.7	1.571	-76.97	87.88	**Normal**	16.18	35.61	49	24
11		52	31.85	2289071.91	164351.67	1.562	2289167.7	164241.3	1.572	-95.82	110.34	**Normal**	16.18	44.54	49	20
11		53	54.21	2289247.87	164377.62	1.562	2289307.6	164309.4	1.57	-59.73	68.21	**Normal**	12.95	27.63	49	25
11		54	31.59	2289293.19	164470.83	1.563	2289367.1	164386.5	1.567	-73.87	84.35	**Normal**	6.47	34.18	49	11
11		55	29.13	2289362.89	164536.21	1.564	2289433.5	164455.6	1.567	-70.63	80.65	**Normal**	4.86	32.68	49	8
11		56	46.48	2289457.99	164655.43	1.564	2289522.4	164581.9	1.567	-64.37	73.51	**Normal**	4.86	29.78	49	9
12	1331.63	1	0.00	2289972.47	159596.08	1.557	2289998.9	159470.8	1.561	-26.44	125.27	**Normal**	6.47	39.02	78	9
12		2	26.25	2290014.44	159671.27	1.559	2290036.8	159565.5	1.563	-22.32	105.75	**Normal**	6.47	32.94	78	11
12		3	31.83	2290115.98	159646.91	1.559	2290146.8	159501.0	1.564	-30.81	145.96	**Normal**	8.09	45.47	78	10
12		4	30.71	2290215.59	159631.71	1.558	2290236.2	159533.9	1.564	-20.64	97.77	**Normal**	9.71	30.46	78	18
12		5	47.09	2290356.44	159695.16	1.558	2290381.0	159579.1	1.568	-24.51	116.1	**Normal**	16.18	36.17	78	24
12		6	36.82	2290464.32	159640.83	1.558	2290487.3	159531.7	1.568	-23.02	109.09	**Normal**	16.18	33.98	78	25
12		7	20.86	2290532.08	159650.44	1.559	2290540.2	159481.3	1.568	-8.15	169.16	**Normal**	14.57	51.62	87	16
12		8	31.14	2290634.00	159657.36	1.557	2290639.2	159549.4	1.571	-5.2	107.94	**Normal**	22.66	32.94	87	35
12		9	13.26	2290675.53	159644.37	1.555	2290681.0	159531.2	1.571	-5.45	113.18	**Normal**	25.90	34.54	87	37
12		10	49.17	2290817.11	159721.70	1.555	2290819.9	159554.3	1.569	-2.74	167.4	**Normal**	22.66	51.03	89	24
12		11	31.54	2290920.39	159728.26	1.554	2290923.8	159520.7	1.567	-3.4	207.53	**Normal**	21.04	63.26	89	18
12		12	31.90	2291024.02	159713.59	1.554	2291027.1	159523.8	1.567	-3.11	189.84	**Normal**	21.04	57.87	89	20
12		13	31.58	2291127.50	159708.33	1.554	2291130.4	159529.1	1.566	-2.94	179.23	**Normal**	19.42	54.64	89	20
12		14	31.57	2291230.77	159716.10	1.553	2291233.5	159548.7	1.566	-2.74	167.39	**Normal**	21.04	51.03	89	22
12		15	32.85	2291334.63	159687.29	1.553	2291337.7	159502.2	1.564	-3.03	185.09	**Normal**	17.80	56.42	89	18
12		16	31.81	2291437.76	159703.25	1.553	2291440.7	159522.8	1.565	-2.96	180.45	**Normal**	19.42	55.01	89	19
12		17	33.31	2291540.54	159740.43	1.552	2291544.4	159507.0	1.564	-3.83	233.4	**Normal**	19.42	71.15	89	15
12		18	43.78	2291681.95	159715.31	1.55	2291684.7	159545.6	1.564	-2.77	169.72	**Normal**	22.66	51.74	89	24
12		19	35.22	2291786.15	159665.37	1.55	2291789.0	159494.3	1.562	-2.8	171.04	**Normal**	19.42	52.14	89	20
12		20	43.88	2291926.63	159696.86	1.55	2291928.7	159571.9	1.564	-2.04	124.94	**Normal**	22.66	38.09	89	31
12		21	35.61	2292029.10	159752.96	1.549	2292033.2	159504.2	1.563	-4.07	248.78	**Normal**	22.66	75.84	89	17
12		22	9.82	2292054.43	159733.07	1.549	2292052.1	159556.7	1.565	2.3	176.42	**Normal**	25.90	53.78	91	26
12		23	31.82	2292158.46	159741.92	1.549	2292156.6	159567.9	1.563	1.85	174.06	**Normal**	22.66	53.06	91	23
12		24	32.56	2292263.06	159763.60	1.547	2292260.9	159562.5	1.562	2.15	201.09	**Normal**	24.28	61.30	91	22
12		25	39.76	2292366.57	159684.24	1.545	2292364.9	159523.1	1.56	1.71	161.15	**Normal**	24.28	49.12	91	26
12		26	43.43	2292506.03	159713.50	1.546	2292504.3	159550.0	1.561	1.74	163.47	**Normal**	24.28	49.83	91	26
12		27	31.82	2292610.35	159709.37	1.545	2292608.8	159564.7	1.561	1.54	144.72	**Normal**	25.90	44.11	91	30
12		28	32.35	2292714.91	159727.53	1.546	2292713.0	159544.1	1.56	1.96	183.44	**Normal**	22.66	55.92	91	22
12		29	42.42	2292854.00	159722.70	1.548	2292851.6	159495.7	1.559	2.41	227.01	**Normal**	17.80	69.20	91	14
12		30	35.29	2292957.82	159671.47	1.546	2292956.1	159506.9	1.559	1.75	164.57	**Normal**	21.04	50.16	91	23
12		31	38.15	2293072.95	159720.61	1.546	2293076.7	159493.1	1.56	-3.73	227.55	**Normal**	22.66	69.37	89	18
12		32	40.76	2293194.41	159776.56	1.545	2293314.1	159473.7	1.555	-119.64	302.87	**Normal**	16.18	99.26	68	9

Appendix 9: Dana Point 3D Seismic Fault Data table (continued).

Fault Name	Total Fault Length (m)	Station #	Distance from last station (m)	Hangingwall Orientation Easting 1 x	Northing 1 y	Hangingwall (s)	Footwall Orientation Easting 2 x2	Northing 2 y2	Footwall (s)	dx Easting	dy Northing	Fault Type	Throw (meters)	Heave (meters)	Rule Fault Fault Strike	dip degrees
12		33	23.04	2293269.90	159780.30	1.548	2293350.9	159575.3	1.555	-80.99	205.01	**Normal**	11.33	67.19	68	10
12		34	56.85	2293376.11	159933.61	1.545	2293471.7	159691.8	1.553	-95.54	241.84	**Normal**	12.95	79.26	68	9
12		35	32.99	2293472.51	159884.42	1.544	2293524.8	159752.0	1.553	-52.31	132.42	**Normal**	14.57	43.40	68	19
12		36	47.52	2293611.02	159955.96	1.544	2293663.3	159823.5	1.553	-52.31	132.42	**Normal**	14.57	43.40	68	19
12		37	47.73	2293763.18	159992.94	1.546	2293807.3	159881.3	1.552	-44.12	111.69	**Normal**	9.71	36.60	68	15
12		38	26.43	2293849.41	160001.98	1.544	2293907.2	159855.7	1.551	-57.77	146.25	**Normal**	11.33	47.93	68	13
12		39	48.73	2294007.93	160022.86	1.545	2294058.5	159895.0	1.55	-50.52	127.89	**Normal**	8.09	41.91	68	11
13	1241.97	1	0.00	2291458.35	162597.50	1.551	2291457.5	162513.2	1.566	0.9	84.35	**Normal**	24.28	25.71	91	43
13		2	31.81	2291562.70	162596.55	1.55	2291561.7	162503.1	1.564	1	93.43	**Normal**	22.66	28.48	91	39
13		3	33.55	2291667.42	162630.44	1.55	2291666.2	162512.2	1.565	1.26	118.24	**Normal**	24.28	36.04	91	34
13		4	18.30	2291713.39	162669.08	1.553	2291755.8	162550.0	1.566	-42.45	119.11	**Normal**	21.04	38.54	70	29
13		5	25.06	2291793.28	162649.62	1.553	2291854.1	162479.0	1.566	-60.82	170.67	**Normal**	21.04	55.22	70	21
13		6	35.20	2291848.28	162751.16	1.553	2291918.3	162554.7	1.566	-70.01	196.44	**Normal**	21.04	63.56	70	18
13		7	24.51	2291927.02	162734.92	1.553	2291991.7	162553.5	1.566	-64.66	181.44	**Normal**	21.04	58.71	70	20
13		8	12.08	2291938.60	162772.84	1.552	2292010.9	162624.4	1.565	-72.26	148.46	**Normal**	21.04	50.33	64	23
13		9	23.82	2292005.29	162813.55	1.552	2292075.7	162669.0	1.564	-70.36	144.56	**Normal**	19.42	49.00	64	22
13		10	27.78	2292096.03	162804.85	1.553	2292174.9	162642.8	1.564	-78.86	162.02	**Normal**	17.80	54.92	64	18
13		11	30.43	2292138.57	162895.18	1.552	2292214.6	162739.1	1.564	-75.98	156.1	**Normal**	19.42	52.92	64	20
13		12	26.65	2292225.98	162893.31	1.552	2292301.5	162738.1	1.565	-75.55	155.2	**Normal**	21.04	52.61	64	22
13		13	25.09	2292307.71	162903.14	1.551	2292349.3	162817.8	1.565	-41.54	85.34	**Normal**	22.66	28.93	64	38
13		14	30.24	2292350.69	162992.56	1.551	2292430.5	162828.6	1.565	-79.8	163.93	**Normal**	22.66	55.57	64	22
13		15	23.77	2292423.01	163021.71	1.551	2292511.8	162839.3	1.565	-88.78	182.4	**Normal**	22.66	61.83	64	20
13		16	31.30	2292522.29	162995.46	1.551	2292592.2	162851.9	1.565	-69.88	143.56	**Normal**	22.66	48.67	64	25
13		17	23.73	2292593.57	163026.75	1.554	2292660.6	162889.0	1.562	-67.04	137.73	**Normal**	12.95	46.69	64	15
13		18	33.29	2292629.95	163129.73	1.551	2292716.8	162951.2	1.563	-86.88	178.49	**Normal**	19.42	60.51	64	18
13		19	32.78	2292719.42	163189.40	1.549	2292880.8	162934.2	1.563	-161.33	255.25	**Normal**	22.66	92.04	58	14
13		20	45.95	2292858.22	163130.56	1.551	2292964.2	162963.0	1.564	-105.94	167.61	**Normal**	21.04	60.44	58	19
13		21	25.26	2292891.56	163206.43	1.551	2293022.5	162999.3	1.564	-130.89	207.09	**Normal**	21.04	74.67	58	16
13		22	28.27	2292982.85	163222.77	1.551	2293069.3	163086.0	1.564	-86.46	136.8	**Normal**	21.04	49.33	58	23
13		23	36.35	2293059.05	163314.52	1.551	2293115.1	163199.4	1.567	-56.04	115.14	**Normal**	25.90	39.03	64	34
13		24	27.47	2293109.07	163389.48	1.552	2293211.1	163179.8	1.563	-102.07	209.69	**Normal**	17.80	71.08	64	14
13		25	27.28	2293198.38	163383.72	1.551	2293284.0	163207.8	1.563	-85.65	175.96	**Normal**	19.42	59.65	64	18
13		26	13.71	2293240.59	163368.22	1.552	2293281.1	163242.2	1.566	-40.53	126.06	**Normal**	22.66	40.36	72	29
13		27	30.13	2293310.56	163438.07	1.552	2293367.1	163262.2	1.565	-56.54	175.83	**Normal**	21.04	56.30	72	20
13		28	22.45	2293383.40	163427.15	1.552	2293441.3	163247.2	1.563	-57.86	179.93	**Normal**	17.80	57.61	72	17
13		29	27.07	2293463.50	163465.53	1.552	2293516.8	163299.8	1.562	-53.29	165.72	**Normal**	16.18	53.06	72	17
13		30	29.04	2293536.12	163527.18	1.552	2293611.9	163291.4	1.562	-75.82	235.81	**Normal**	16.18	75.50	72	12
13		31	20.91	2293604.69	163529.51	1.554	2293684.8	163280.5	1.562	-80.09	249.06	**Normal**	12.95	79.74	72	9
13		32	27.54	2293682.18	163576.00	1.554	2293760.0	163334.0	1.561	-77.82	242	**Normal**	11.33	77.48	72	8
13		33	52.04	2293851.39	163553.15	1.554	2293867.8	163428.8	1.563	-16.41	124.34	**Normal**	14.57	38.23	82	21
13		34	16.61	2293903.23	163536.34	1.554	2293920.4	163406.1	1.563	-17.19	130.22	**Normal**	14.57	40.04	82	20
13		35	45.03	2293999.97	163648.00	1.555	2294050.4	163455.2	1.562	-50.38	192.78	**Normal**	11.33	60.73	75	11

Appendix 9: Dana Point 3D Seismic Fault Data table (continued).

Fault Name	Total Fault Length (m)	Station #	Distance from last station (m)	Hangingwall Orientation Easting 1 x	Northing 1 y	Hangingwall (s)	Footwall Orientation Easting 2 x2	Northing 2 y2	Footwall (s)	dx Easting	dy Northing	Fault Type	Throw (meters)	Heave (meters)	Rule Fault Fault Strike	dip degrees
13		36	18.65	2294060.20	163658.87	1.555	2294109.1	163471.7	1.562	-48.92	187.2	**Normal**	11.33	58.97	75	11
13		37	23.62	2294123.97	163614.84	1.554	2294208.3	163441.7	1.56	-84.29	173.18	**Normal**	9.71	58.71	64	9
13		38	31.33	2294110.01	163716.69	1.553	2294248.2	163535.1	1.561	-138.14	181.57	**Normal**	12.95	69.54	53	11
13		39	46.50	2294230.64	163810.06	1.554	2294333.2	163675.3	1.556	-102.56	134.79	**Normal**	3.24	51.62	53	4
13		40	18.71	2294275.15	163852.34	1.555	2294431.9	163646.3	1.559	-156.78	206.07	**Normal**	6.47	78.92	53	5
13		41	47.43	2294399.76	163759.13	1.555	2294477.1	163600.3	1.559	-77.32	158.86	**Normal**	6.47	53.85	64	7
13		42	9.50	2294427.67	163773.01	1.553	2294479.6	163611.4	1.558	-51.97	161.62	**Normal**	8.09	51.75	72	9
13		43	30.45	2294496.97	163844.96	1.553	2294572.8	163609.1	1.56	-75.85	235.9	**Normal**	11.33	75.53	72	9
13		44	21.42	2294567.20	163842.14	1.554	2294627.0	163656.1	1.561	-59.82	186.03	**Normal**	11.33	59.56	72	11
13		45	29.85	2294637.83	163909.99	1.554	2294704.2	163703.6	1.56	-66.37	206.44	**Normal**	9.71	66.09	72	8
14	1062.34	1	0.00	2300232.05	160023.57	1.539	2300164.7	160233.1	1.545	67.36	-209.48	**Normal**	9.71	67.07	252	8
14		2	29.98	2300161.73	159954.79	1.538	2300094.6	160163.5	1.547	67.12	-208.73	**Normal**	14.57	66.83	252	12
14		3	19.40	2300116.75	159909.77	1.538	2300059.0	160130.6	1.547	57.71	-220.82	**Normal**	14.57	69.57	255	12
14		4	32.25	2300041.61	159835.29	1.537	2299955.5	160165.0	1.548	86.15	-329.69	**Normal**	17.80	103.86	255	10
14		5	23.92	2299994.97	159898.42	1.537	2299934.0	160088.1	1.548	60.97	-189.63	**Normal**	17.80	60.71	252	16
14		6	26.89	2299913.12	159865.50	1.536	2299849.1	160064.7	1.549	64.04	-199.18	**Normal**	21.04	63.77	252	18
14		7	19.62	2299857.93	159832.39	1.536	2299747.8	160058.7	1.55	110.17	-226.33	**Normal**	22.66	76.72	244	16
14		8	13.53	2299817.70	159813.62	1.536	2299709.5	159989.1	1.55	108.23	-175.48	**Normal**	22.66	62.84	238	20
14		9	33.85	2299844.92	159705.94	1.535	2299716.9	159874.3	1.551	128.07	-168.33	**Normal**	25.90	64.47	233	22
14		10	31.54	2299742.83	159688.97	1.534	2299615.7	159856.1	1.551	127.17	-167.15	**Normal**	27.51	64.02	233	23
14		11	33.53	2299706.94	159584.99	1.534	2299511.2	159842.3	1.549	195.76	-257.29	**Normal**	24.28	98.54	233	14
14		12	33.39	2299670.55	159481.66	1.536	2299463.3	159754.1	1.549	207.28	-272.44	**Normal**	21.04	104.34	233	11
14		13	31.89	2299567.02	159466.58	1.534	2299369.3	159726.4	1.55	197.69	-259.84	**Normal**	25.90	99.52	233	15
14		14	36.15	2299456.16	159508.77	1.534	2299321.2	159655.2	1.551	134.92	-146.45	**Normal**	27.51	60.69	227	24
14		15	37.42	2299495.82	159392.59	1.534	2299336.2	159537.5	1.552	159.6	-144.94	**Normal**	29.13	65.71	222	24
14		16	14.34	2299474.39	159350.71	1.533	2299152.9	159597.3	1.551	321.53	-246.54	**Normal**	29.13	123.50	217	13
14		17	41.10	2299340.38	159365.80	1.536	2299155.2	159507.8	1.552	185.18	-141.99	**Normal**	25.90	71.13	217	20
14		18	26.91	2299383.61	159288.81	1.537	2299139.3	159476.1	1.552	244.3	-187.33	**Normal**	24.28	93.83	217	15
14		19	29.42	2299294.11	159252.69	1.538	2299118.8	159355.4	1.552	175.35	-102.7	**Normal**	22.66	61.94	210	20
14		20	14.26	2299290.23	159206.06	1.538	2299105.7	159298.6	1.552	184.51	-92.55	**Normal**	22.66	62.92	207	20
14		21	14.68	2299253.46	159174.95	1.538	2299075.1	159250.1	1.553	178.36	-75.19	**Normal**	24.28	59.00	203	22
14		22	26.76	2299218.29	159094.49	1.538	2299056.3	159162.8	1.553	161.97	-68.28	**Normal**	24.28	53.58	203	24
14		23	40.95	2299191.60	158962.81	1.539	2299001.2	159043.1	1.554	190.42	-80.27	**Normal**	24.28	62.99	203	21
14		24	31.33	2299159.54	158865.15	1.538	2298923.7	158964.6	1.553	235.86	-99.43	**Normal**	24.28	78.02	203	17
14		25	15.62	2299140.66	158817.51	1.537	2298941.4	158886.3	1.553	199.27	-68.79	**Normal**	25.90	64.25	199	22
14		26	15.78	2299120.13	158770.00	1.538	2298925.3	158823.1	1.552	194.85	-53.06	**Normal**	22.66	61.55	195	20
14		27	16.42	2299093.45	158723.21	1.536	2298902.5	158761.9	1.553	190.97	-38.68	**Normal**	27.51	59.39	191	25
14		28	40.14	2299001.93	158628.52	1.535	2298822.6	158641.4	1.552	179.37	-12.9	**Normal**	27.51	54.81	184	27
14		29	9.16	2299009.91	158599.53	1.535	2298825.3	158612.8	1.551	184.61	-13.28	**Normal**	25.90	56.41	184	25
14		30	18.21	2299040.29	158548.08	1.537	2298841.3	158575.1	1.551	199.02	-27.03	**Normal**	22.66	61.22	188	20
14		31	33.73	2299001.26	158444.53	1.538	2298807.0	158470.9	1.551	194.29	-26.39	**Normal**	21.04	59.76	188	19
14		32	26.82	2298972.57	158361.34	1.538	2298754.9	158390.9	1.551	217.69	-29.57	**Normal**	21.04	66.96	188	17

Appendix 9: Dana Point 3D Seismic Fault Data table (continued).

Fault Name	Total Fault Length (m)	Station #	Distance from last station (m)	Hangingwall Orientation Easting 1 x	Northing 1 y	Hangingwall (s)	Footwall Orientation Easting 2 x2	Northing 2 y2	Footwall (s)	dx Easting	dy Northing	Fault Type	Throw (meters)	Heave (meters)	Rule Fault Fault Strike	dip degrees
14		33	18.98	2298937.67	158309.77	1.536	2298743.7	158349.1	1.552	193.96	-39.29	**Normal**	25.90	60.32	191	23
14		34	16.81	2298939.78	158254.65	1.534	2298768.4	158300.4	1.55	171.34	-45.78	**Normal**	25.90	54.06	195	26
14		35	19.07	2298923.79	158194.16	1.537	2298747.8	158254.9	1.551	175.95	-60.74	**Normal**	22.66	56.74	199	22
14		36	28.73	2298895.22	158104.35	1.537	2298716.0	158138.9	1.55	179.25	-34.57	**Normal**	21.04	55.64	191	21
14		37	17.62	2298877.09	158049.46	1.537	2298749.9	158062.9	1.547	127.15	-13.48	**Normal**	16.18	38.97	186	23
14		38	21.65	2298906.98	157985.04	1.539	2298668.2	157987.6	1.548	238.8	-2.55	**Normal**	14.57	72.79	181	11
14		39	28.34	2298997.87	158004.64	1.539	2298766.5	157974.1	1.548	231.41	30.55	**Normal**	14.57	71.15	172	12
14		40	29.69	2298938.14	157927.70	1.539	2298749.8	157882.7	1.546	188.34	44.96	**Normal**	11.33	59.02	167	11
14		41	10.88	2298963.67	157902.73	1.539	2298807.5	157837.8	1.546	156.14	64.95	**Normal**	11.33	51.54	157	12
14		42	37.55	2298871.33	157821.18	1.539	2298770.3	157772.0	1.546	101.01	49.17	**Normal**	11.33	34.24	154	18
14		43	14.01	2298886.18	157777.68	1.539	2298798.2	157727.3	1.546	88.01	50.34	**Normal**	11.33	30.90	150	20
15	341.37	1	0.00	2303495.12	158159.26	1.537	2303474.0	158319.1	1.546	21.09	-159.79	**Normal**	14.57	49.13	262	17
15		2	24.91	2303425.52	158202.11	1.535	2303440.9	158377.6	1.547	-15.38	-175.46	**Normal**	19.42	53.69	275	20
15		3	18.06	2303403.57	158257.14	1.533	2303415.1	158388.7	1.548	-11.53	-131.57	**Normal**	24.28	40.26	275	31
15		4	11.31	2303379.21	158285.13	1.534	2303414.9	158388.4	1.547	-35.66	-103.3	**Normal**	21.04	33.31	289	32
15		5	33.53	2303275.11	158320.68	1.534	2303311.8	158427.0	1.55	-36.7	-106.33	**Normal**	25.90	34.29	289	37
15		6	33.53	2303171.36	158357.24	1.534	2303207.5	158461.9	1.551	-36.13	-104.65	**Normal**	27.51	33.74	289	39
15		7	22.12	2303103.49	158382.95	1.534	2303173.1	158473.8	1.55	-69.64	-90.83	**Normal**	25.90	34.89	307	37
15		8	44.24	2303150.91	158520.14	1.534	2303243.0	158564.9	1.548	-92.05	-44.8	**Normal**	22.66	31.20	334	36
15		9	30.46	2303051.11	158514.76	1.531	2303138.2	158600.0	1.55	-87.04	-85.2	**Normal**	30.75	37.12	316	40
15		10	16.75	2302999.06	158532.34	1.531	2303034.8	158636.0	1.551	-35.78	-103.64	**Normal**	32.37	33.42	289	44
15		11	33.53	2302895.08	158568.23	1.536	2302930.6	158671.2	1.551	-35.55	-102.98	**Normal**	24.28	33.21	289	36
15		12	17.20	2302842.86	158589.65	1.535	2302827.2	158708.0	1.551	15.63	-118.39	**Normal**	25.90	36.40	262	35
15		13	16.38	2302791.22	158604.47	1.536	2302826.8	158707.5	1.552	-35.55	-102.98	**Normal**	25.90	33.21	289	38
15		14	39.36	2302671.47	158556.17	1.541	2302826.8	158708.2	1.552	-155.3	-152.03	**Normal**	17.80	66.24	316	15
16	798.23	1	0.00	2303735.63	157463.82	1.531	2303911.4	157635.9	1.542	-175.77	-172.07	**Normal**	17.80	74.97	316	13
16		2	32.75	2303763.62	157360.07	1.529	2303933.6	157621.1	1.544	-170.01	-260.99	**Normal**	24.28	94.94	303	14
16		3	12.57	2303803.13	157371.86	1.529	2303902.3	157524.0	1.543	-99.12	-152.15	**Normal**	22.66	55.35	303	22
16		4	29.29	2303891.54	157409.54	1.529	2303927.2	157512.7	1.543	-35.62	-103.2	**Normal**	22.66	33.28	289	34
16		5	16.66	2303942.92	157390.93	1.529	2304004.8	157485.9	1.543	-61.89	-95	**Normal**	22.66	34.56	303	33
16		6	17.09	2303992.36	157364.49	1.53	2304031.4	157477.6	1.543	-39.05	-113.14	**Normal**	21.04	36.48	289	30
16		7	45.46	2304063.47	157233.40	1.528	2304109.6	157366.9	1.542	-46.08	-133.46	**Normal**	22.66	43.04	289	28
16		8	33.53	2304167.87	157198.70	1.53	2304204.6	157305.1	1.545	-36.72	-106.37	**Normal**	24.28	34.30	289	35
16		9	8.37	2304193.68	157189.33	1.53	2304255.6	157284.3	1.545	-61.89	-95	**Normal**	24.28	34.56	303	35
16		10	33.50	2304297.43	157153.09	1.53	2304359.3	157248.1	1.543	-61.87	-94.97	**Normal**	21.04	34.55	303	31
16		11	27.02	2304365.09	157095.82	1.531	2304411.2	157229.3	1.543	-46.08	-133.46	**Normal**	19.42	43.04	289	24
16		12	33.86	2304463.99	157045.20	1.531	2304515.0	157193.0	1.543	-51.01	-147.77	**Normal**	19.42	47.65	289	22
16		13	29.04	2304557.61	157062.81	1.53	2304567.4	157174.5	1.542	-9.79	-111.66	**Normal**	19.42	34.16	275	30
16		14	25.10	2304635.71	157036.73	1.531	2304619.5	157159.6	1.542	16.21	-122.85	**Normal**	17.80	37.77	262	25
16		15	8.44	2304661.59	157026.92	1.53	2304681.5	157253.7	1.541	-19.88	-226.76	**Normal**	17.80	69.38	275	14
16		16	8.31	2304687.62	157018.81	1.53	2304759.8	157228.0	1.542	-72.21	-209.16	**Normal**	19.42	67.44	289	16
16		17	33.53	2304791.74	156983.32	1.53	2304862.6	157188.5	1.543	-70.83	-205.17	**Normal**	21.04	66.16	289	18

Appendix 9: Dana Point 3D Seismic Fault Data table (continued).

Fault Name	Total Fault Length (m)	Station #	Distance from last station (m)	Hangingwall Orientation Easting 1 x	Northing 1 y	Hangingwall (s)	Footwall Orientation Easting 2 x2	Northing 2 y2	Footwall (s)	dx Easting	dy Northing	Fault Type	Throw (meters)	Heave (meters)	Rule Fault Fault Strike	dip degrees
16		18	33.53	2304896.26	156949.00	1.531	2304967.0	157153.8	1.542	-70.7	-204.79	**Normal**	17.80	66.04	289	15
16		19	25.28	2304973.49	156918.78	1.53	2304993.2	157143.8	1.542	-19.73	-225.06	**Normal**	19.42	68.86	275	16
16		20	8.31	2304999.97	156912.32	1.53	2305071.2	157118.7	1.545	-71.24	-206.36	**Normal**	24.28	66.54	289	20
16		21	33.53	2305103.68	156875.64	1.531	2305139.0	156978.0	1.544	-35.34	-102.37	**Normal**	21.04	33.01	289	33
16		22	11.08	2305137.61	156862.59	1.531	2305209.0	156955.7	1.545	-71.37	-93.07	**Normal**	22.66	35.75	307	32
16		23	47.24	2305206.51	156723.77	1.531	2305276.5	156815.1	1.547	-70	-91.29	**Normal**	25.90	35.06	307	36
16		24	33.24	2305308.59	156685.40	1.531	2305380.2	156778.8	1.545	-71.64	-93.43	**Normal**	22.66	35.89	307	32
16		25	32.91	2305408.26	156643.88	1.532	2305475.6	156731.7	1.546	-67.31	-87.79	**Normal**	22.66	33.72	307	34
16		26	11.84	2305425.32	156608.97	1.534	2305518.3	156730.3	1.546	-93	-121.28	**Normal**	19.42	46.58	307	23
16		27	34.19	2305483.08	156512.80	1.534	2305552.3	156603.1	1.544	-69.22	-90.27	**Normal**	16.18	34.67	307	25
16		28	33.49	2305586.81	156476.58	1.535	2305660.6	156572.8	1.541	-73.78	-96.21	**Normal**	9.71	36.95	307	15
16		29	30.32	2305633.91	156388.98	1.535	2305690.0	156551.5	1.541	-56.1	-162.53	**Normal**	9.71	52.41	289	10
16		30	35.15	2305726.60	156320.39	1.532	2305761.8	156422.4	1.538	-35.21	-102	**Normal**	9.71	32.89	289	16
16		31	33.63	2305827.83	156276.54	1.53	2305863.9	156380.9	1.538	-36.04	-104.39	**Normal**	12.95	33.66	289	21
17	357.90	1	0.00	2299340.57	156034.27	1.534	2299257.5	156098.0	1.543	83.06	-63.69	**Normal**	14.57	31.90	217	25
17		2	22.23	2299363.82	156103.39	1.534	2299249.2	156165.6	1.546	114.58	-62.23	**Normal**	19.42	39.74	209	26
17		3	33.75	2299396.23	156209.26	1.535	2299301.7	156260.6	1.545	94.5	-51.33	**Normal**	16.18	32.78	209	26
17		4	17.72	2299454.36	156210.02	1.536	2299325.1	156309.2	1.545	129.31	-99.16	**Normal**	14.57	49.67	217	16
17		5	10.88	2299469.17	156242.50	1.535	2299333.7	156346.4	1.545	135.47	-103.87	**Normal**	16.18	52.03	217	17
17		6	18.66	2299467.56	156303.69	1.535	2299357.9	156415.7	1.546	109.67	-112.03	**Normal**	17.80	47.78	226	20
17		7	31.14	2299557.15	156352.82	1.533	2299374.5	156539.4	1.547	182.65	-186.59	**Normal**	22.66	79.59	226	16
17		8	40.04	2299566.55	156483.86	1.533	2299417.2	156636.4	1.546	149.35	-152.57	**Normal**	21.04	65.08	226	18
17		9	35.80	2299683.46	156472.69	1.533	2299455.1	156647.8	1.547	228.35	-175.1	**Normal**	22.66	87.71	217	14
17		10	32.28	2299732.59	156566.52	1.534	2299499.0	156745.6	1.546	233.58	-179.11	**Normal**	19.42	89.72	217	12
17		11	14.49	2299779.48	156574.40	1.535	2299518.5	156774.5	1.544	260.97	-200.11	**Normal**	14.57	100.24	217	8
17		12	39.08	2299766.14	156701.91	1.534	2299635.7	156835.2	1.542	130.48	-133.29	**Normal**	12.95	56.85	226	13
17		13	29.99	2299836.09	156771.11	1.534	2299689.0	156921.4	1.543	147.12	-150.25	**Normal**	14.57	64.09	226	13
17		14	31.84	2299881.81	156865.05	1.536	2299830.4	156917.6	1.541	51.43	-52.53	**Normal**	8.09	22.41	226	20
18	1277.96	1	0.00	2303162.53	162876.99	1.537	2302959.2	162991.3	1.549	203.31	-114.33	**Normal**	19.42	71.10	209	15
18		2	33.49	2303092.88	162791.99	1.538	2302902.6	162899.0	1.549	190.28	-107	**Normal**	17.80	66.54	209	15
18		3	34.74	2303008.70	162715.17	1.537	2302839.1	162810.6	1.549	169.63	-95.39	**Normal**	19.42	59.32	209	18
18		4	33.85	2302977.41	162608.60	1.537	2302774.0	162723.0	1.549	203.38	-114.37	**Normal**	19.42	71.12	209	15
18		5	35.20	2302889.27	162534.00	1.538	2302734.3	162621.1	1.549	154.95	-87.13	**Normal**	17.80	54.18	209	18
18		6	33.63	2302854.95	162429.13	1.539	2302674.6	162530.6	1.549	180.35	-101.42	**Normal**	16.18	63.07	209	14
18		7	33.91	2302824.38	162322.16	1.537	2302643.3	162424.0	1.549	181.07	-101.82	**Normal**	19.42	63.32	209	17
18		8	34.18	2302796.98	162213.41	1.535	2302611.2	162317.9	1.549	185.75	-104.45	**Normal**	22.66	64.95	209	19
18		9	36.65	2302798.54	162093.19	1.535	2302594.7	162163.6	1.549	203.87	-70.38	**Normal**	22.66	65.74	199	19
18		10	17.85	2302810.83	162035.94	1.535	2302620.0	162083.0	1.549	190.87	-47.06	**Normal**	22.66	59.92	194	21
18		11	15.15	2302797.09	161988.17	1.536	2302596.1	162019.1	1.549	201	-30.9	**Normal**	21.04	61.98	189	19
18		12	34.91	2302817.75	161875.50	1.537	2302626.3	161904.9	1.549	191.45	-29.43	**Normal**	19.42	59.04	189	18
18		13	34.05	2302774.02	161772.72	1.537	2302603.5	161799.0	1.551	170.56	-26.23	**Normal**	22.66	52.60	189	23
18		14	40.47	2302789.87	161640.88	1.539	2302542.8	161678.9	1.551	247.1	-37.99	**Normal**	19.42	76.20	189	14

Appendix 9: Dana Point 3D Seismic Fault Data table (continued).

Fault Name	Total Fault Length (m)	Station #	Distance from last station (m)	Hangingwall Orientation Easting 1 x	Northing 1 y	Hangingwall (s)	Footwall Orientation Easting 2 x2	Northing 2 y2	Footwall (s)	dx Easting	dy Northing	Fault Type	Throw (meters)	Heave (meters)	Rule Fault Fault Strike	dip degrees
18		15	18.35	2302767.03	161585.16	1.538	2302539.9	161641.2	1.552	227.14	-56.01	Normal	22.66	71.31	194	18
18		16	34.07	2302719.26	161484.11	1.539	2302477.8	161543.7	1.554	241.48	-59.54	Normal	24.28	75.81	194	18
18		17	37.22	2302672.94	161371.11	1.539	2302439.8	161478.6	1.554	233.16	-107.52	Normal	24.28	78.26	205	17
18		18	25.59	2302627.50	161300.51	1.539	2302400.4	161433.5	1.554	227.11	-133.01	Normal	24.28	80.22	210	17
18		19	28.34	2302583.64	161218.51	1.538	2302375.0	161378.5	1.554	208.68	-160.01	Normal	25.90	80.15	217	18
18		20	10.61	2302561.54	161191.62	1.54	2302349.3	161354.4	1.554	212.28	-162.77	Normal	22.66	81.53	217	16
18		21	13.05	2302520.55	161179.21	1.538	2302325.7	161328.7	1.554	194.88	-149.44	Normal	25.90	74.85	217	19
18		22	21.21	2302477.06	161124.89	1.538	2302290.9	161267.7	1.554	186.19	-142.77	Normal	25.90	71.51	217	20
18		23	16.16	2302451.06	161078.70	1.539	2302209.4	161193.4	1.554	241.68	-114.69	Normal	24.28	81.54	205	17
18		24	9.55	2302428.14	161057.36	1.539	2302193.2	161138.5	1.554	234.97	-81.11	Normal	24.28	75.77	199	18
18		25	24.56	2302371.63	160999.94	1.539	2302186.0	161091.2	1.554	185.67	-91.24	Normal	24.28	63.06	206	21
18		26	29.57	2302349.98	160905.37	1.539	2302132.3	161057.7	1.555	217.67	-152.36	Normal	25.90	80.98	215	18
18		27	35.94	2302246.51	160848.84	1.539	2302070.0	161029.2	1.556	176.55	-180.35	Normal	27.51	76.93	226	20
18		28	56.02	2302114.99	160720.48	1.539	2302086.0	160940.4	1.555	29.02	-219.88	Normal	25.90	67.60	262	21
18		29	57.51	2302191.47	160892.97	1.54	2302176.7	161004.9	1.556	14.78	-111.9	Normal	25.90	34.40	262	37
18		30	30.88	2302180.27	160792.29	1.537	2302118.1	160985.7	1.556	62.18	-193.37	Normal	30.75	61.91	252	26
18		31	29.19	2302114.73	160722.47	1.539	2302092.7	160889.6	1.554	22.06	-167.12	Normal	24.28	51.38	262	25
18		32	4.49	2302116.66	160707.87	1.539	2302080.4	160982.8	1.555	36.29	-274.91	Normal	25.90	84.52	262	17
18		33	23.27	2302041.00	160697.61	1.539	2301990.4	160937.4	1.554	50.61	-239.77	Normal	24.28	74.69	258	18
18		34	28.81	2301947.44	160684.16	1.54	2301923.4	160798.2	1.552	24.07	-114.01	Normal	19.42	35.52	258	29
18		35	32.25	2302045.09	160643.45	1.537	2301959.5	160755.9	1.552	85.59	-112.49	Normal	24.28	43.08	233	29
18		36	36.67	2302112.75	160742.92	1.541	2301981.7	160814.1	1.554	131.01	-71.15	Normal	21.04	45.44	209	25
18		37	33.85	2302040.16	160658.87	1.539	2301924.9	160721.5	1.552	115.24	-62.59	Normal	21.04	39.97	209	28
18		38	7.84	2302015.46	160651.71	1.54	2301905.0	160711.7	1.551	110.46	-59.99	Normal	17.80	38.31	209	25
18		39	33.38	2301950.58	160563.47	1.539	2301852.2	160616.9	1.551	98.38	-53.43	Normal	19.42	34.12	209	30
18		40	38.68	2301897.98	160447.98	1.54	2301757.5	160524.3	1.55	140.46	-76.29	Normal	16.18	48.72	209	18
18		41	26.38	2301861.67	160369.41	1.54	2301719.0	160478.8	1.55	142.7	-109.42	Normal	16.18	54.81	217	16
18		42	36.75	2301846.09	160249.85	1.538	2301693.9	160366.6	1.547	152.21	-116.72	Normal	14.57	58.46	217	14
18		43	48.97	2301699.93	160316.57	1.54	2301636.6	160392.1	1.547	63.32	-75.48	Normal	11.33	30.03	230	21
18		44	30.72	2301650.49	160228.74	1.539	2301595.9	160293.9	1.544	54.64	-65.14	Normal	8.09	25.91	230	17
19	564.91	1	0.00	2281310.97	173122.44	1.586	2281373.9	173189.9	1.588	-62.89	-67.43	Normal	3.24	28.10	313	7
19		2	53.68	2281485.15	173096.31	1.585	2281607.0	173227.0	1.59	-121.88	-130.66	Normal	8.09	54.46	313	8
19		3	45.45	2281568.20	172972.48	1.584	2281695.5	173109.0	1.59	-127.33	-136.51	Normal	9.71	56.90	313	10
19		4	33.53	2281672.18	172936.59	1.584	2281745.3	173010.7	1.59	-73.14	-74.14	Normal	9.71	31.74	315	17
19		5	19.02	2281692.59	172877.62	1.583	2281757.9	172962.8	1.589	-65.33	-85.2	Normal	9.71	32.72	307	17
19		6	22.08	2281755.17	172841.16	1.584	2281788.0	172936.3	1.589	-32.84	-95.13	Normal	8.09	30.67	289	15
19		7	33.57	2281857.25	172799.77	1.584	2281895.4	172910.4	1.59	-38.18	-110.59	Normal	9.71	35.66	289	15
19		8	39.96	2281937.95	172696.44	1.582	2281988.7	172843.5	1.591	-50.78	-147.1	Normal	14.57	47.43	289	17
19		9	31.11	2281968.69	172599.10	1.581	2282058.5	172745.2	1.59	-89.77	-146.07	Normal	14.57	52.26	302	16
19		10	40.13	2282075.09	172521.58	1.582	2282176.1	172685.9	1.592	-101.02	-164.36	Normal	16.18	58.80	302	15
19		11	40.34	2282195.86	172467.43	1.583	2282293.2	172625.8	1.59	-97.31	-158.33	Normal	11.33	56.64	302	11
19		12	32.78	2282290.43	172416.21	1.582	2282357.6	172525.5	1.59	-67.16	-109.29	Normal	12.95	39.10	302	18

Appendix 9: Dana Point 3D Seismic Fault Data table (continued).

Fault Name	Total Fault Length (m)	Station #	Distance from last station (m)	Hangingwall Orientation Easting 1 x	Northing 1 y	Hangingwall (s)	Footwall Orientation Easting 2 x2	Northing 2 y2	Footwall (s)	dx Easting	dy Northing	Fault Type	Throw (meters)	Heave (meters)	Rule Fault Fault Strike	dip degrees
19		13	39.41	2282344.19	172298.61	1.581	2282460.3	172487.6	1.59	-116.15	-188.98	**Normal**	14.57	67.61	302	12
19		14	33.46	2282447.58	172261.76	1.581	2282553.0	172433.3	1.591	-105.43	-171.55	**Normal**	16.18	61.37	302	15
19		15	33.37	2282550.27	172223.76	1.582	2282621.9	172340.2	1.588	-71.58	-116.47	**Normal**	9.71	41.67	302	13
19		16	34.29	2282659.31	172196.10	1.584	2282742.8	172331.9	1.588	-83.47	-135.82	**Normal**	6.47	48.59	302	8
19		17	32.73	2282751.34	172140.76	1.584	2282817.9	172249.0	1.587	-66.52	-108.23	**Normal**	4.86	38.72	302	7
20	1153.64	1	0.00	2286796.87	171100.62	1.573	2286637.9	171021.5	1.579	159.01	79.17	**Normal**	9.71	54.14	154	10
20		2	47.41	2286864.95	170960.75	1.572	2286755.0	170767.6	1.58	110	193.12	**Normal**	12.95	67.74	120	11
20		3	41.95	2286916.76	170833.25	1.573	2286846.1	170709.1	1.581	70.7	124.12	**Normal**	12.95	43.54	120	17
20		4	33.06	2287015.09	170787.44	1.572	2286910.7	170604.2	1.582	104.35	183.21	**Normal**	16.18	64.26	120	14
20		5	33.53	2287098.97	170716.25	1.572	2287013.9	170566.9	1.582	85.08	149.37	**Normal**	16.18	52.40	120	17
20		6	34.19	2287178.10	170636.73	1.571	2287090.6	170483.1	1.584	87.49	153.59	**Normal**	21.04	53.88	120	21
20		7	33.16	2287278.01	170593.70	1.57	2287191.4	170441.6	1.584	86.65	152.14	**Normal**	22.66	53.37	120	23
20		8	33.29	2287379.59	170553.58	1.569	2287268.0	170357.7	1.583	111.58	195.9	**Normal**	22.66	68.72	120	18
20		9	39.16	2287493.45	170494.07	1.57	2287395.5	170322.1	1.585	97.96	171.97	**Normal**	24.28	60.32	120	22
20		10	36.05	2287611.13	170482.23	1.57	2287497.9	170283.4	1.584	113.24	198.8	**Normal**	22.66	69.74	120	18
20		11	33.29	2287712.70	170442.11	1.57	2287618.7	170277.1	1.584	93.96	164.97	**Normal**	22.66	57.87	120	21
20		12	33.36	2287815.02	170403.30	1.569	2287726.7	170248.3	1.584	88.31	155.05	**Normal**	24.28	54.39	120	24
20		13	34.34	2287924.65	170377.32	1.568	2287829.9	170211.0	1.583	94.72	166.28	**Normal**	24.28	58.33	120	23
20		14	35.46	2288039.85	170361.12	1.57	2287927.4	170163.8	1.583	112.41	197.35	**Normal**	21.04	69.23	120	17
20		15	23.36	2288116.38	170356.90	1.57	2288191.1	170133.8	1.583	-74.74	223.07	**Normal**	21.04	71.71	71	16
20		16	31.00	2288182.43	170434.22	1.571	2288275.9	170155.2	1.583	-93.49	279.03	**Normal**	19.42	89.70	71	12
20		17	44.58	2288327.57	170452.29	1.572	2288217.7	170195.1	1.584	109.88	257.23	**Normal**	19.42	85.26	113	13
20		18	33.53	2288425.31	170401.78	1.57	2288344.9	170213.6	1.582	80.38	188.16	**Normal**	19.42	62.37	113	17
20		19	33.46	2288524.87	170355.54	1.569	2288453.3	170188.1	1.582	71.54	167.48	**Normal**	21.04	55.51	113	21
20		20	33.62	2288621.31	170302.01	1.569	2288552.2	170140.3	1.582	69.07	161.7	**Normal**	21.04	53.59	113	21
20		21	33.50	2288719.64	170252.88	1.569	2288646.2	170081.0	1.581	73.43	171.9	**Normal**	19.42	56.98	113	19
20		22	33.86	2288827.39	170225.80	1.568	2288750.8	170046.5	1.582	76.61	179.34	**Normal**	22.66	59.44	113	21
20		23	34.12	2288937.02	170203.14	1.567	2288851.6	170003.3	1.58	85.38	199.88	**Normal**	21.04	66.25	113	18
20		24	34.84	2289025.34	170130.58	1.565	2288961.9	169982.1	1.579	63.42	148.46	**Normal**	22.66	49.21	113	25
20		25	34.05	2289118.01	170068.22	1.564	2289033.9	169871.2	1.579	84.15	196.99	**Normal**	24.28	65.29	113	20
20		26	19.76	2289149.75	170011.71	1.564	2289070.3	169856.9	1.578	79.47	154.79	**Normal**	22.66	53.03	117	23
20		27	37.96	2289262.67	169959.17	1.565	2289188.4	169814.5	1.579	74.29	144.71	**Normal**	22.66	49.58	117	25
20		28	33.66	2289351.20	169893.18	1.566	2289270.3	169735.6	1.579	80.92	157.61	**Normal**	21.04	54.00	117	21
20		29	33.19	2289447.87	169843.04	1.566	2289360.3	169672.5	1.58	87.54	170.51	**Normal**	22.66	58.42	117	21
20		30	40.23	2289510.66	169726.93	1.567	2289440.0	169589.3	1.581	70.63	137.59	**Normal**	22.66	47.14	117	26
20		31	33.19	2289608.02	169678.14	1.567	2289546.2	169557.8	1.576	61.8	120.39	**Normal**	14.57	41.25	117	19
20		32	33.45	2289698.76	169616.44	1.568	2289610.5	169444.5	1.577	88.3	171.98	**Normal**	14.57	58.93	117	14
20		33	39.77	2289828.47	169630.66	1.567	2289679.9	169341.3	1.577	148.59	289.41	**Normal**	16.18	99.16	117	9
20		34	44.26	2289969.21	169666.38	1.565	2289838.3	169411.4	1.574	130.92	255.02	**Normal**	14.57	87.37	117	9
21	755.35	1	0.00	2290319.99	164213.35	1.559	2290470.3	164127.2	1.564	-150.27	86.16	**Normal**	8.09	52.80	30	9
21		2	105.98	2290530.65	164489.96	1.557	2290661.4	164415.0	1.565	-130.77	74.98	**Normal**	12.95	45.95	30	16
21		3	60.79	2290573.15	164684.82	1.556	2290773.2	164586.5	1.563	-200.04	98.31	**Normal**	11.33	67.94	26	9

Appendix 9: Dana Point 3D Seismic Fault Data table (continued).

Fault Name	Total Fault Length (m)	Station #	Distance from last station (m)	Hangingwall Orientation Easting 1 x	Northing 1 y	Hangingwall (s)	Footwall Orientation Easting 2 x2	Northing 2 y2	Footwall (s)	dx Easting	dy Northing	Fault Type	Throw (meters)	Heave (meters)	Rule Fault Fault Strike	dip degrees
21		4	34.12	2290643.61	164771.81	1.556	2290803.0	164693.5	1.563	-159.38	78.33	**Normal**	11.33	54.13	26	12
21		5	33.57	2290678.45	164876.30	1.555	2290820.6	164806.5	1.563	-142.16	69.85	**Normal**	12.95	48.28	26	15
21		6	66.65	2290763.48	165077.76	1.555	2290912.7	165004.4	1.567	-149.2	73.32	**Normal**	19.42	50.67	26	21
21		7	36.57	2290766.90	165197.69	1.556	2290932.4	165116.4	1.568	-165.49	81.32	**Normal**	19.42	56.20	26	19
21		8	24.39	2290773.06	165277.47	1.556	2290953.4	165232.3	1.566	-180.29	45.2	**Normal**	16.18	56.65	14	16
21		9	65.65	2290806.13	165490.31	1.556	2290940.1	165438.0	1.566	-133.95	52.32	**Normal**	16.18	43.83	21	20
21		10	36.86	2290799.14	165611.04	1.556	2290977.1	165541.6	1.565	-177.91	69.49	**Normal**	14.57	58.22	21	14
21		11	42.33	2290848.71	165740.77	1.556	2291010.4	165662.3	1.566	-161.68	78.46	**Normal**	16.18	54.78	26	16
21		12	33.45	2290905.88	165834.43	1.557	2291009.7	165784.1	1.566	-103.78	50.37	**Normal**	14.57	35.16	26	23
21		13	33.39	2290961.14	165929.01	1.558	2291087.2	165867.8	1.566	-126.1	61.2	**Normal**	12.95	42.72	26	17
21		14	33.34	2291014.29	166024.61	1.56	2291132.3	165967.4	1.567	-118	57.26	**Normal**	11.33	39.98	26	16
21		15	37.45	2291077.96	166129.68	1.56	2291206.1	166067.5	1.568	-128.1	62.17	**Normal**	12.95	43.40	26	17
21		16	40.34	2291147.63	166242.21	1.559	2291292.0	166154.3	1.567	-144.41	87.87	**Normal**	12.95	51.52	31	14
21		17	70.48	2291187.09	166470.05	1.56	2291350.9	166390.6	1.565	-163.78	79.48	**Normal**	8.09	55.49	26	8